2017

# Development and Characterization of Polymer-based Magnetoelectric Nanofibers

Tian Zheng
*University of Wollongong*

**Australian Research Council Centre of Excellence for Electromaterials Science**

**Intelligent Polymer Research Institute**

**Australian Institute for Innovative Materials**

# Development and Characterization of Polymer-based Magnetoelectric Nanofibers

**Tian Zheng**

**This thesis is presented as part of the requirements for the**

**Award of the Degree of Doctor of Philosophy of**

**The University of Wollongong**

**August 2017**

# CERTIFICATION

I, Tian Zheng, declare that this thesis, submitted in fulfilment of the requirements for the award of Doctor of Philosophy, at the Australian Institute for Innovative Materials, University of Wollongong, is wholly my own work except where specific references or acknowledgements are made. The thesis has not been submitted for a degree to any other university or institution.

Tian Zheng

August, 2017

# PUBLICATIONS

1. **T. Zheng**, Z. Yue, G. G. Wallace, Y. Du, P. Martins, S. Lanceros-Mendez and M. J. Higgins, Local probing of magnetoelectric properties of PVDF/$Fe_3O_4$ electrospun nanofibers by piezoresponse force microscopy, ***Nanotechnology***, 2017, 28, 065707.

2. **T. Zheng**, Y. Zong, Z. Yue, G. G. Wallace and M. J. Higgins, Magnetoelectric Composites for Bionics Applications, ***Book Chapter 6b in Magnetoelectric Polymer-Based Composites: Fundamentals and Applications, John Wiley & Sons,*** 2017, 171-195.

3. Y. Zong, **T. Zheng**, P. Martins, S. Lanceros-Mendez, Z. Yue, and M. Higgins, Cellulose-based magnetoelectric composites, ***Nat. Comm.***, 2017, 8, 38.

4. A. Al-Keisy, L. Ren, **T. Zheng**, X. Xu, M. Higgins, W. Hao and Y. Du, Enhancement of charge separation in ferroelectric heterogenerous photocatalyst $Bi_4(SiO_4)_3/Bi_2SiO_5$ nanostructures, ***Dalton Trans.***, 2017, Accepted.

5. R. Goncalves, A. Larrea, **T. Zheng**, M. J. Higgins, V. Sebastian, S. Lanceros-Mendez and P. Martins, Synthesis of highly magnetostrictive nanostructures and their application in a polymer-based magnetoelectric sensing device, ***Eur. Polym. J.***, 2016, 84, 685-692.

6. Y. Ge, R. Jalili, C. Wang, **T. Zheng**, Y. Chao and G. G. Wallace, A robust free-standing $MoS_2$/poly (3,4-ethylenedioxythiophene):poly (styrenesulfonate) film for supercapacitor applications, ***Electrochim. Acta***, 2017, 235, 348-355.

7. A. Sultana, S. K. Ghosh, V. Sencadas, **T. Zheng**, M. J. Higgins, T. R. Middya and D. Mandal, Human skin interactive self-powered wearable piezoelectric bio-e-skin by electrospun poly-L-lactic acid nanofibers for non-invasive physiological signal monitoring, ***J. Mater. Chem. B***, 2017, 5, 7352-7359.

8. Y. Chao, R. Jalili, Y. Ge, C. Wang, **T. Zheng**, K. Shu and G. G. Wallace, Self-assembly of flexible free-standing 3D porous $MoS_2$-reduced graphene oxide structure for high-performance lithium-ion batteries, ***Adv. Funct. Mater.***, 2017, 27, 1700234.

9. H. Feng, J. Zhuang, A. Slattery, L. Wang, Z. Xu, X. Xu, D. Mitchell, **T. Zheng**, S. Li, M. Higgins, L. Ren, Z. Sun, S. Dou, Y. Du and W. Hao, Construction of 2D lateral pseudoheterostructures by strain engineering, ***2D Mater.***, 2017, 4, 025102.

10. J. E. Sader, R. Borgani, C. T. Gibson, D. B. Haviland, M. J. Higgins, J. I. Kilpatrick, J. Lu, P. Mulvaney, C. J. Shearer, A. D. Slattery, P. Thoren, J. Tran, H. Zhang, H. Zhang and **T. Zheng**, A virtual instrument to standardise the calibration of atomic force microscope cantilevers, ***Rev. Sci. Instrum.***, 2016, 87, 093711. (Open access available at https://arxiv.org/abs/1605.07750)

# ABSTRACT

With the rapid development of bionics, where biological systems meet electronics, there is an interest in polymer-based electrode systems that are soft, flexible, easily processed and fabricated. In this research area, magnetoelectric (ME) composites bring new and exciting opportunities, including contactless or "wireless" electrical stimulation, less-invasive integration in the form of dispersible, injectable nanoelectrodes, and applications as biodegradable sensors and bioenergy harvesters in the biomedical field. When ME composites are exposed to a magnetic field, a magnetostrictive (MS) component transfers strain to a piezoelectric (PE) component that generates an output voltage. In doing so, ME composites have the ability to enable magnetic-to-electrical conversion and thus can be utilized to power devices or electrically stimulate tissues or cells from a remote magnetic stimulus. To date, ceramic materials have mostly been applied in nanostructured ME composites, however, these may become fragile and cause deleterious reactions at the interface regions, leading to low electrical resistivity and high dielectric losses and ultimately low output voltage.

To overcome these shortcomings, polymer-based ME composites offer new solutions to develop softer, contactless electrodes, without electrical connections, for easier and unique fabrication approaches (e.g. incorporation into soft gels). Their strain-mediated ME effect in large scale devices has been thoroughly studied both experimentally and theoretically. Polymer-based ME composites have almost exclusively used the PE polymer, poly (vinylidene fluoride) (PVDF), due to its high PE coefficient and as such developments in exploring other types of PE polymers have not been forthcoming. For example, other PE polymers such as poly (vinylidene fluoride-co-hexafluoropropylene) (P(VDF-HFP)) and poly (lactic acid) (PLA) have yet to be investigated though have the potential to bring added-value

and function to polymer-based ME composites. Compared to PVDF and its copolymer P(VDF-TrFE), the piezoelectricity of another copolymer, P(VDF-HFP), is less-well understood. As a biocompatible polymer, PLA has been extensively investigated for applications in drug delivery and tissue engineering. Instead of being used only as a biodegradable and bioactive thermoplastic material, PLA is promising as a PE polymer, which has potential to mimic PE functions of tissues. Thus, in addition to PVDF, the thesis investigates the PE properties of P(VDF-HFP) and PLA and aims to develop ME composite nanofibers based on these polymers.

In future, scaling down polymer-based ME composites to the nanoscale domain is attractive for manufacturing nanoscale devices and other *in vivo* applications such as targeted drug delivery or electrical stimulation at the single cell and molecular level. In the assembly of bulk devices, ME nanocomposites may offer different approaches to manufacturing and provide novel opportunities such as enhancing the magnetic-to-electrical conversion and/or improved mechanical properties. Despite studies on the synthesis of ME nanocomposites, very little is understood on their nanoscale ME properties, which inevitably are critical to their applications. Furthermore, similar nanocomposites based on polymers are only just emerging. This is where recently developed Atomic Force Microscopy-based techniques such as Piezoresponse Force Microscopy (PFM) that can probe both PE and ME response at the nanoscale are expected to play an important role in characterization in this field.

To explore ME nanostructured and nanocomposite systems, electrospinning was used to fabricate nanofibers from different PE polymers, including PVDF, P(VDF-HFP) and biocompatible PLA, of which the latter two have not previously been studied as ME composite materials. More specifically, different magnetic nanoparticles such as magnetite ($Fe_3O_4$) and cobalt ferrite ($CoFe_2O_4$) nanoparticles were incorporated to combine the PE and

MS properties. Their morphological, crystalline and PE properties were characterized using a range of techniques and in particular the PFM to enable quantification of the PE response and domain switching behaviour with nanoscale lateral resolution, as outlined in Chapter 1. Furthermore, the Variable Field Module (VFM) that produces a controllable in-plane magnetic field across a sample was combined with PFM to directly elucidate the nanoscale ME properties of the nanofibers.

In Chapter 2, electrospun PVDF/$Fe_3O_4$ ME composite nanofibers were investigated and the electrospinning was shown to inherently pole and induce the β-phase of the PVDF, demonstrating it to be a useful technique to fabricate PE structures and devices. The butterfly loop, which is typical for PE materials, was observed by PFM measurements, accompanied with a 180-degree switching of dipoles. In addition, PFM measurements revealed that the PE response along a single nanofiber was uniform however significantly greater variation was observed between different nanofibers, with average values of 140.9 ± 84.0 pm at $V_{AC}$ = 500 mV. The addition of $Fe_3O_4$ nanoparticles significantly increased the PE response to 240.5 ± 94.7 pm, suggesting an increase in crystallinity due to the interactions between the PVDF and $Fe_3O_4$. Lastly, when the PVDF/$Fe_3O_4$ ME composite nanofibers were subject to an increasing magnetic field, an opposing decrease in the PE response was observed, confirming a nanoscale ME effect. The mechanism was explained by a published equation which allows for quantitative estimation of effective ME coefficient from the linear change of PE coefficient with the applied magnetic field.

In Chapter 3, P(VDF-HFP), a $d_{31}$ type of PVDF copolymer, was studied as the PE polymer in ME polymer nanocomposites. Unlike PVDF, the PE response of P(VDF-HFP) electrospun nanofibers varied significantly within a single nanofiber, as well as statistical analysis of different nanofibers showing a bimodal distribution in the PE response, perhaps due to the

copolymerization of non-electroactive HFP monomer and electroactive VDF monomer. Furthermore, the average PE response (398.3 ± 222.4 pm at $V_{AC}$ = 200 mV) of the P(VDF-HFP) was greater than PVDF, a finding that was unexpected given that P(VDF-HFP) has a smaller $d_{33}$ value than PVDF. One possible explanation was the $d_{31}$ mode piezoelectricity also contributes to an overall change of height during the PFM measurement. The addition of $Fe_3O_4$ and $CoFe_2O_4$ nanoparticles clearly had an effect on the polymer structure by effectively normalizing the distribution (e.g. unimodal distribution) of the PE response, with the addition of nanoparticles again enhancing the piezoelectricity of P(VDF-HFP). In contrast to the distinct PE response in these P(VDF-HFP) composite nanofibers, a clear trend in the ME nanoscale effect (as a function of the magnetic field strength) was less evident although a significant change in the PE response when subject to a magnetic field was observed in composites with both types of magnetic nanoparticles.

In Chapter 4, the piezoelectricity of the biocompatible and biodegradable polymer PLA was investigated as a potential ME nanocomposite for biomedical applications. A key focus was to quantify the PE properties while tuning the polymer degradability through the addition of faster degrading polymer, PLGA, that is not a PE polymer. Pure PLA nanofibers gave a PE response of 186.0 ± 28.1 pm at $V_{AC}$ = 500 mV, slightly higher than PVDF. Importantly, this PE response persisted with the addition of PLGA albeit showing a decreasing linear dependence with an increase in PLGA content. More specifically, PLA/PLGA (75/25) and PLA/PLGA (50/50) gave values of 88.8 ± 12.3 pm and 49.6 ± 9.1 pm, respectively, while PLA/PLGA (25/75) gave either a very small response or none at all. Nevertheless, the findings were considered significant due to the existence of piezoelectricity in a tuneable biodegradable material that has potential to impart effects, for example, biointeractions with the surrounding biological environment, or drug interactions with the polymer to control the rate of its release. In such applications, there is an opportunity to magnetically control the

piezoelectricity and henceforth PLA/$CoFe_2O_4$ ME nanocomposite nanofibers, with 5% and 10% of $CoFe_2O_4$ nanoparticles, were investigated. Both nanocomposites showed a lower PE response than pure PLA due to the disturbance of polymer chains and dipole moments by the magnetic nanoparticles, in addition to effects from the possible inhomogeneous distribution of $CoFe_2O_4$ nanoparticles.

In the final Chapter 5, having demonstrated an understanding of the PE and ME effect of single nanofibers, the question was posed as to whether such effects at the nanoscale can translate to configurations in macroscale devices. To address this, a home-made macroscale ME testing system, as outlined in Chapter 1, was setup to measure the ME output voltage of laminate composites based on PVDF or PLA electrospun nanofibers and with different configurations, including those with top-and-bottom or interdigitated electrodes. ME laminates consisting of a commercial PVDF sheet and Metglas confirmed the macroscale ME testing system was working properly. Surprisingly, measurements of all electrospun nanofiber based samples showed no typical ME effect. While the exact reasons for these findings were unclear, the observations suggested failure in the PE response of the random fiber sheets and/or mechanical coupling (strain transfer) between the nanofibers and magnetic components. Previous studies have been able to demonstrate good PE responses from electrospun nanofibers, thus further work is required to optimize or configure an ME response from similar types of samples.

In summary, the thesis provides insight into the fundamental PE and ME properties for electrospun polymer nanofibers by PFM/VFM at the nanoscale. Differences in the magnitude and lateral distribution of the PE response are elucidated and shown to depend on the types of polymers and additives. At this stage, translation of nanoscale ME effects to macroscale ME measurement and operation is not straightforward and requires further investigation.

Nevertheless, the ME effect of single nanofibers has been demonstrated and through further optimization could be harnessed in developing nanoscale devices such as magnetic sensors, biosensors and biocompatible contactless electrodes.

# ACKNOWLEDGEMENTS

I would like to express my sincere appreciation to my primary supervisor, Associate Professor Michael Higgins, and co-supervisors, Dr. Zhilian Yue and Professor Gordon Wallace, for their excellent supervision, financial assistance and constant encouragement throughout my PhD study. A special thanks to the Intelligent Polymer Research Institute (IPRI) for providing a prestigious research environment and funding support through the ARC Australian Research Fellowship of Associate Professor Michael Higgins and the Australian Research Council (ARC) Centre of Excellence for Electromaterials Science (ACES).

I would like to thank the group in University of Minho, namely Professor Senentxu Lanceros-Mendez, Dr. Pedro Martins and Dr. Renato Goncalves, for their collaboration and support in undertaking magnetoelectric measurements. I appreciate the time spent with my enthusiastic friends in Portugal.

I would also like to acknowledge the general technical support from Professor Zhenxiang Cheng, Associate Professor Germanas Peleckis, Dr. Yi Du, Dr. Tony Romeo and Dr. David Mitchell from the University of Wollongong.

I am very grateful to all staff members and students of IPRI and ACES for their help and assistance. Thanks to Dr. Javad Foroughi, Dr. Pawel Wagner and Dr. Patricia Hayes for their technical advice. Many thanks to my friends in IPRI, Dr. Kewei Shu, Dr. Qi Gu, Mr. Yu Chen, Ms. Qijie Wu, Ms. Yuqing Liu, Ms. Guanran Zhang, Mr. Yu Ge, Ms. Changchun Yu, Mr Jianfeng Li, Mr Yang Xiao, Mr. Yunfeng Chao and Mr. Liang Wu. Thanks to my team mates, Dr. Paul Molino, Dr. Hongrui Zhang, Mr. Ryan Sullivan, Mr. Yan Zong, Mr. Lei Feng,

Ms. Christina Puckert, Ms. Briana Knowles, Ms. Dan Yang and Mr. Alex Nagle. Working with you is definitely fruitful and enjoyable.

Finally, I would like to express my special thank you to my Mum and Dad for their endless love, motivation and encouragement in my life.

# ABBREVIATIONS

| | |
|---|---|
| AC | Alternating current |
| AFM | Atomic Force Microscopy |
| ANOVA | Analysis of variance |
| $CoFe_2O_4$ | Cobalt ferrite |
| DART | Dual AC Resonance Tracking |
| DC | Direct current |
| DLS | Dynamic light scattering |
| DMAc | N,N-dimethylacetamide |
| DMF | N,N-dimethylformamide |
| DSC | Differential scanning calorimetry |
| $d_{31}$ | Transverse piezoelectric coefficient |
| $d_{33}$ | Longitudinal piezoelectric coefficient |
| E | Electric field |
| EAP | Electroactive polymer |
| EEG | Electroencephalography |
| $Fe_3O_4$ | Magnetite |
| FT-IR | Fourier transform infrared |

| | |
|---|---|
| H | Magnetic field |
| HCl | Hydrochloric acid |
| IE | Interdigitated electrode |
| ME | Magnetoelectric |
| MENs | Magnetoelectric nanoparticles |
| MFM | Magnetic Force Microscopy |
| MLCC | Multilayer ceramic capacitor |
| MS | Magnetostrictive |
| Ms | Saturation magnetization |
| NF | Nanofiber |
| OCP | Organic conducting polymer |
| P | Polarization |
| PBA | Poly (butyl acrylate) |
| PE | Piezoelectric |
| PEDOT | Poly (3,4-ethylenedioxythiophene) |
| PFM | Piezoresponse Force Microscopy |
| PHB | Polyhydroxybutyrate |
| PLA | Poly (lactic acid) |

| | |
|---|---|
| PLGA | Poly (DL-lactide-co-glycolide) |
| PMMA | Poly (methacrylic acid, sodium salt) |
| PPMS | Physical properties measurement system |
| PTX | Paclitaxel |
| PU | Polyurethane |
| PVDF | Poly (vinylidene fluoride) |
| P(VDF-HFP) | Poly (vinylidene fluoride-co-hexafluoropropylene) |
| P(VDF-TrFE) | Poly (vinylidene fluoride-co-trifluoroethylene) |
| PZT | Lead zirconate titanate |
| SEM | Scanning electron microscope |
| SS-PFM | Piezoresponse Force Microscopy switching spectroscopy |
| TBAP | Tetrabutylammonium perchlorate |
| Terfenol-D | $Tb_{1-x}Dy_xFe_2$ |
| VFM | Variable Force Module |
| XRD | X-ray diffraction |
| $\alpha_{ME}$ | ME coefficient |
| $\alpha_{31}$ | Transverse ME coefficient |
| $\alpha_{33}$ | Longitudinal ME coefficient |

# TABLE OF CONTENTS

# LIST OF FIGURES

# LIST OF TABLES

# 1 Introduction

Polymer bionics is where electronics meets biology - softer, more flexible and more processable polymer-based electrode systems that can electrically stimulate living cells. The research area has played an important role in the development of next generation electrode-tissue interfaces. Fundamental to these advances are the polymer's inherent biocompatibility, enhanced electrode properties, ability to perform multiple functions and processing into unique electrode structures. In this chapter, an introduction to bionics was firstly provided and the general attributes of polymer-based electrodes in this field was highlighted.

The chapter introduces magnetoelectric (ME) composites that bring new and exciting opportunities to bionics – these include contactless or "wireless" electrical stimulation and related advances in dispersible, injectable nanoelectrodes. The history of ME materials is discussed with an emphasis on the development of polymer-based ME composites and conventional ME measurements of samples. Then, the ability to fabricate nanostructured ME composites and to probe the ME properties at the nanoscale domain is discussed. This is followed by the potential for exploring the development of ME composites based on biopolymers such as cellulose. Finally, their biocompatibility and applications for the mechanical and electrical stimulation of living cells, as well as the unprecedented capability of using ME composite nanoparticles for stimulating the brain, are presented.

## 1.1 Bionics

### 1.1.1 Implantable Electrode Devices

"Bionics" is the merging of biological and electronic systems and is applicable for the control of electrically excitable tissues such as nerves or muscle tissues within the body [1]. Bionic devices such as the cochlear implant, bionic eye, vagus nerve stimulator and deep brain stimulator require biocompatible electrode interfaces that are vital for communication between the device and the living tissue. The electrodes must be capable of supplying electrical charges [2], should not provoke an inflammatory response, and have low impedance [3]. Low impedance is important for efficient charge transfer at the electrode-tissue interface and decreases the energy required for stimulation (ideal for bionic devices that require a battery). A high charge storage capacity is desirable as the electrode is able to store a relatively large charge without undergoing irreversible, and possibly cytotoxic, Faradaic reactions [4]. Current commercial implantable devices use conventional metal electrodes based on platinum, platinum alloys, and iridium oxide to deliver stimulation [3, 5]. These metals have excellent conductivity, are stable and functional for long-term implants, and do not chemically react with surrounding tissues [3]. For example, platinum is used in cochlear implant electrodes as it is chemically inert, non-toxic, and has low impedance and long-term stability during electrical stimulation [6].

### 1.1.2 Organic Electrode Materials

The hardness of metallic surfaces can have negative effects on surrounding tissues, for example, metals can provoke an inflammatory response during insertion of the electrode or after surgery due to chronic movement of the electrode [7, 8]. This has prompted the

development of organic polymer-based electrodes that have inherent biocompatibility due to their carbonaceous backbone and significantly lower modulus – perceived as ideal properties for bridging the hard-world of electronics with soft biological tissues [9]. The polymer-based electrodes can be defined as Electroactive Polymers (EAPs) and divided into two main classes, dielectric and ionic.

#### *1.1.2.1 Organic Conducting Polymers*

One type of ionic EAP is the organic conducting polymers (OCPs) – OCPs have aromatic backbones and conduct electricity due to delocalized electrons in the conjugated p-orbitals. OCPs act as semiconductors and exhibit both electronic and ionic conductivity and have been extensively investigated as electrodes and electrode coatings in many bionic applications [1, 10-12]. Due to their 3D microtopography and porosity, the surface area of OCPs is much greater than conventional metal electrodes and thus leads to a higher charge density and lower impedance [13]. The charge injection mechanism for OCP electrode materials is more advantageous for biological applications compared to metals; redox reactions occurring within OCPs result in electronic current being converted to ionic current [14]. This electronic-to-ionic conversion of current is seemingly more compatible with living cells that also utilize ionic currents. For example, poly (3,4-ethylenedioxythiophene) (PEDOT) has a high charge injection limit (15 mC $cm^{-2}$) and wide potential limit window compared to metallic materials and has been explored as coatings for neural microelectrodes [15].

The physical properties of OCPs are more advantageous than their metallic counterparts. They are pliable, flexible and lightweight compared to metals, in addition to being inexpensive [16]. The softer surface of these polymers provides inherent compatibility with

biological systems, thus affording them superior biocompatibility compared to conventional metallic electrodes. A supplementary advantage is the potential to incorporate dopants, or other constituents, into the OCP structure. A dopant is a molecule (e.g. biomolecules, drugs) that can be incorporated into the polymer during synthesis. The nature of the dopants (such as size, charge and chemical structure) will modify the properties of the polymers, specifically physical properties [17], surface chemistry [18], and electrical properties [11].

The properties of a polymer-electrode interface – physical, chemical, and electrical – have a direct influence on the proliferation, growth and differentiation of living cells. Cells respond to surface properties through several mechanisms and hence the surface properties of OCPs need to be carefully considered. Their nanotopography and surface chemistry can be used to enhance cell growth or control cell differentiation. Finally, their electrical properties play a very important role and dictate their ability to deliver charges to cells [11, 19], control the release of dopants (e.g. drug molecules) [12], or mechanical stimulation through electro-actuation processes [20].

#### *1.1.2.2 Ferroelectric Polymers*

One group of dielectric EAP's, the ferroelectric polymers, can maintain a permanent electric polarization that can be reversed, or switched, in an external electric field and is described further below in Section 1.2.3. Studies on ferroelectric polymers have long been dominated by the piezoelectric (PE) poly (vinylidene fluoride) (PVDF) and its copolymers. The piezoelectricity of this polymer class arises from the strong molecular dipoles within the polymer chain and resulting change of the dipole density when subjected to a mechanical stimulus. Ferroelectric polymers show moderate PE coefficients in comparison to PE ceramics. However, they are cheaper, lighter and more flexible [21]. Given these advantages,

PE polymers have raised tremendous interest in several applications including hydrophones [22], transducers [23], as well as energy harvesting devices [24].

PE polymers have been utilized as biomaterials or implantable materials, as they are biocompatible and support cell growth and differentiation [25-27]. Early studies have established the use of PE polymers for the electrical stimulation of bone [28-30]. The electrical output induced by mechanical stimulating PVDF has been shown to enhance the growth of different types of cells such as rat spinal cord neurons [31], goat bone marrow cells [32] and osteoblasts [33]. More recently, PE nanogenerators fabricated from electrospun PVDF are efficient at harvesting mechanical vibrations and expected to deliver applications in electrical stimulation of cells and implantable electrode devices [24]. In contrast to OCPs, the stimulation of living cells using PE polymers primarily depends on their intrinsic electrical properties that are induced by mechanical vibrations of the local environment. This is where the advent of ME composites can systematically control the output voltage of a PE polymer through the use of applied magnetic fields.

### 1.1.3 ME Composites - New Opportunities in Bionics

Intimate interactions between the electrode and individual nerves, or specific tissues, are essential to enable effective electrical stimulation [34]. A major roadblock however is that current commercial implantable devices rely on millimeter-sized platinum electrodes which apply the electrical stimulation with brute force, spreading the electrical charges over large areas of tissue and lacking specificity [35, 36]. Due to their large size, there is the perpetual issue of tissue damage and fibrosis [37], which is caused by traumatic surgery and foreign

body responses to the implanted devices including both the electrodes and connecting external wires.

Many bionic devices are progressing rapidly beyond the use of percutaneous cables whose purpose is to connect an external transmitter to its implanted receiver. By eliminating these cables through the use of clever onboard electronics for wireless communication and additional induction coils to provide the necessary power, many of today's devices are less prone to infection and far more comfortable and practical for the recipient. Yet often overlooked in this narrative are the leads that connect the receiver to the electrodes. Therefore, a challenge remains in connecting to the electrodes, which becomes a formidable task as the electrodes can take on very different forms and properties to produce new capabilities, for example, maintaining a connection to soft conductive gels, or liquids, appears inconceivable using conventional electronics.

The next generation electrical stimulation devices demand a huge increase in electrode numbers at nanoscale dimensions to ensure effective communication, for example, the vagus nerve consists of > 40,000 individual fibers [38]. They must also gain easy access to specific regions of the nerve tissue with minimally invasive procedures. In fact, the scaling down of electrode dimensions introduces the challenges of electrically addressing individual electrodes and connecting external wires to the device, primarily due to lack of space and technological advances to implement them.

In light of the above challenges, the field of ME composites brings many exciting opportunities. ME composites can give electrical outputs when subjected to a magnetic stimulus due to coupling between the magnetic and electric order parameters. It is envisaged that they can be developed as infusible and contactless electrodes with potential to enable localized electrical stimulation at the single cell level, or in tissue regions that are difficult to

access in the body, for example, in the form of dispersible nano or microparticles or soft gels, without the need for wire connections (Figure 1.1). Furthermore, the electrode materials can be polymer-based, including the unique prospect of incorporating PE biopolymers to harness their unexploited electrical properties. Finally, remote activation of the electrodes, without the need for onboard wireless circuits or power sources, can be performed via magnetic fields that are well-established in current FDA approved medical and clinical instrumentation. In the next section, the fundamentals of ME materials were introduced and the interesting history of their development was detailed.

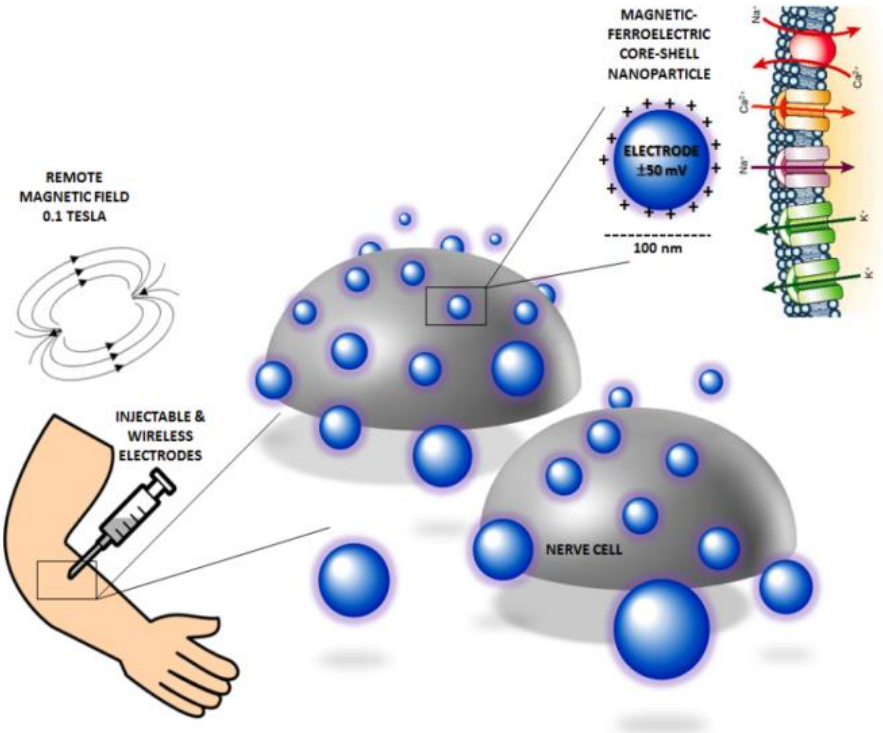


**Figure 1.1** ME composite particles, consisting of ferroelectric and ferromagnetic phases, in the form of dispersible, injectable electrodes for targeting electrical stimulation at level of single cells and cell surface molecules [39].

## 1.2 ME Fundamentals

### 1.2.1 Multiferroics

In ferroic materials, there is a spontaneous internal alignment of ferroic orderings that can be switched by stimuli such as the magnetic field, electric field and stress field. There are three types of ferroics (Figure 1.2): (1) ferromagnetics, in which the alignment of electron spins can be switched by a magnetic field; (2) ferroelectrics, in which electric dipole-moment alignment can be switched by an electric field; (3) ferroelastics, in which strain alignment can be switched by a stress field. Multiferroic materials refer to those combining any two of the ferroic orderings in the same phase (Figure 1.2). The most attractive multiferroic materials are those that display coupling between the ferroelectric and ferromagnetic orders, namely, single-phase ME materials. Conventional applications of ME materials include, but are not limited to, information storage, multiple-state memories, sensors, actuators, transformers, microwave devices and diodes [21, 40].

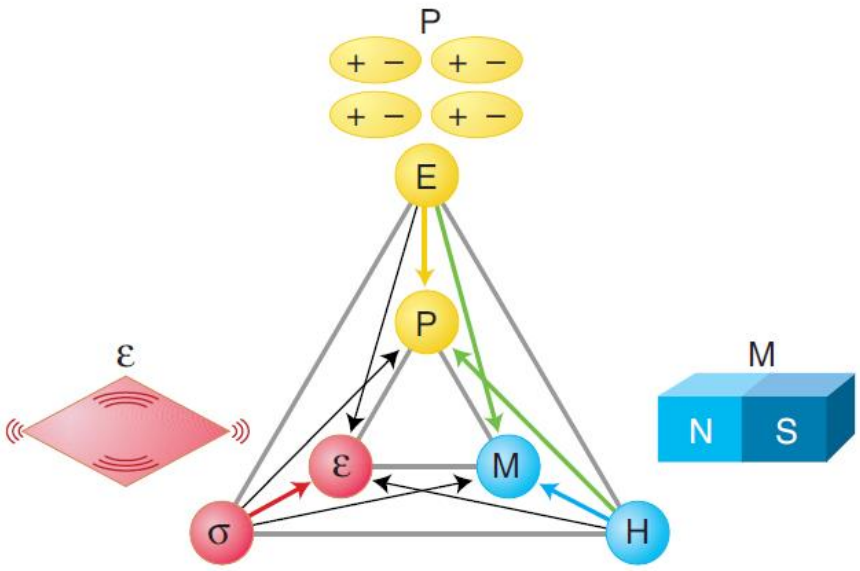


**Figure 1.2** Ferroic orderings and multiferroics [41].

The ME effect was first predicted to occur in the single-phase material, cobalt (III) oxide ($Cr_2O_3$), by Dzyaloshinskii in 1959 [42] and then experimentally confirmed by Astrov in 1961 [43]. More single-phase ME materials such as boracites were also discovered in the ensuing years [44, 45]. Although the intrinsic ME effect exists in single-phase ME materials, most of them exhibit low Curie temperatures (below room temperature), which severely hinder the design and applications of devices. Among families of single-phase ME materials, $BiFeO_3$ is unique with high Curie and Neel temperatures far above room temperature and most widely investigated in recent years [46]. However, $BiFeO_3$ is a G-type antiferromagnetic or only very weak ferromagnetic. To date, a high, inherent ME coupling has not yet been found in single-phase materials, especially above room temperature [41, 47, 48].

Due to the aforementioned limitations in single-phase compounds, the development of ME composites has been of great research interest and offers significant flexibility and advantages when combing different ferroelectric and ferromagnetic materials [49]. In these composites, the ME effect is a product property that results from the cross-interaction between their different ferroelectric and ferromagnetic phases, as proposed by Van Suchtelen in 1972 [50]. The two phases are typically formed in composites by combining magnetostrictive (MS) and PE materials, which are described in more detail below.

### 1.2.2 Magnetostriction

The MS effect was first discovered in 1842 [51], which is the reversible exchange of energy from the magnetic to mechanical form. It can be explained as the rotation of small magnetic domains in a ferromagnetic material when subjected to a magnetic field (Figure 1.3). In the

region 0-1, with a small magnetic field applied, the magnetic domains show a random orientation pattern. In some materials, there may be a small amount of an orientation pattern, which is defined as a permanent magnet bias. In the region 1-2, the relationship between the strain and the magnetic field is almost linear. Beyond point 2, the relationship becomes non-linear again as most of the magnetic domains have been aligned with the magnetic field direction. At point 3, a saturation effect occurs and further strain increase is prevented.

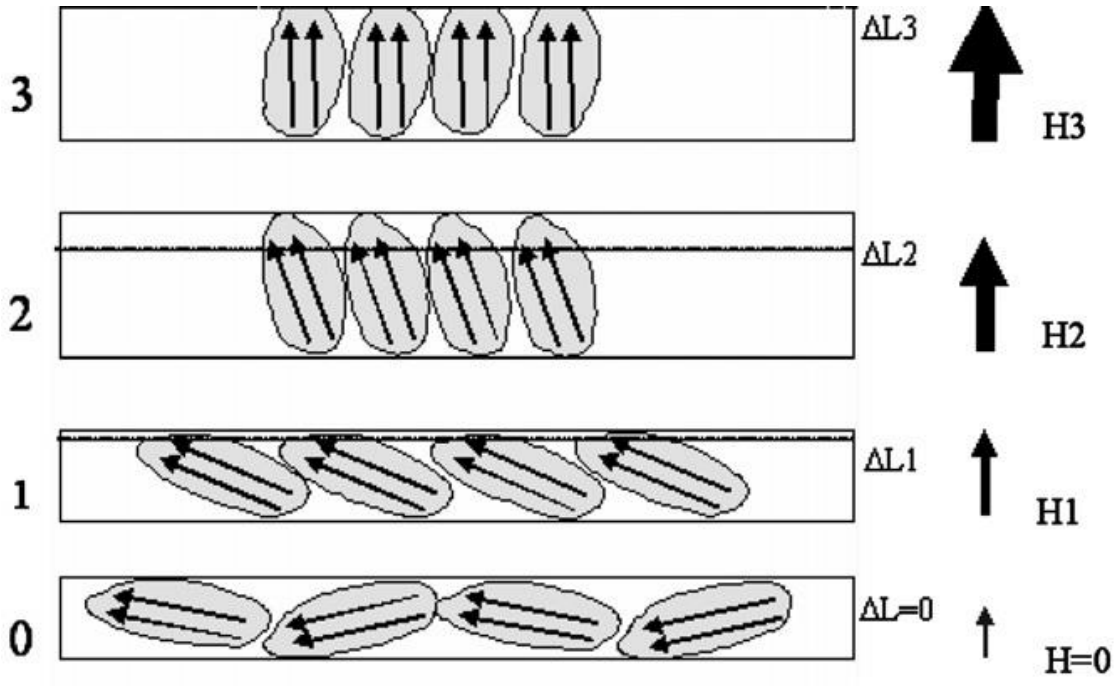


**Figure 1.3** Illustration of the rotation of magnetic domains due to the influence of a magnetic field [52]. The dotted lines in region 1 and region 2 indicated the strain level of the MS materials. The stain level was increased to its maximum in region 3 and overlapped with the upper line of the magnetic domains.

This reorientation induces internal strains, leading to expansion of the material along the direction of the magnetic field while the volume is kept nearly constant (i.e. the Joule Effect). The material shows increasing deformation with stronger magnetic fields, though it eventually reaches saturation at higher fields (Figure 1.4). As the relationship between point 1 and 2 is approximately linear, the behaviour can be predicted easily, hence devices are favourably operated in this region.

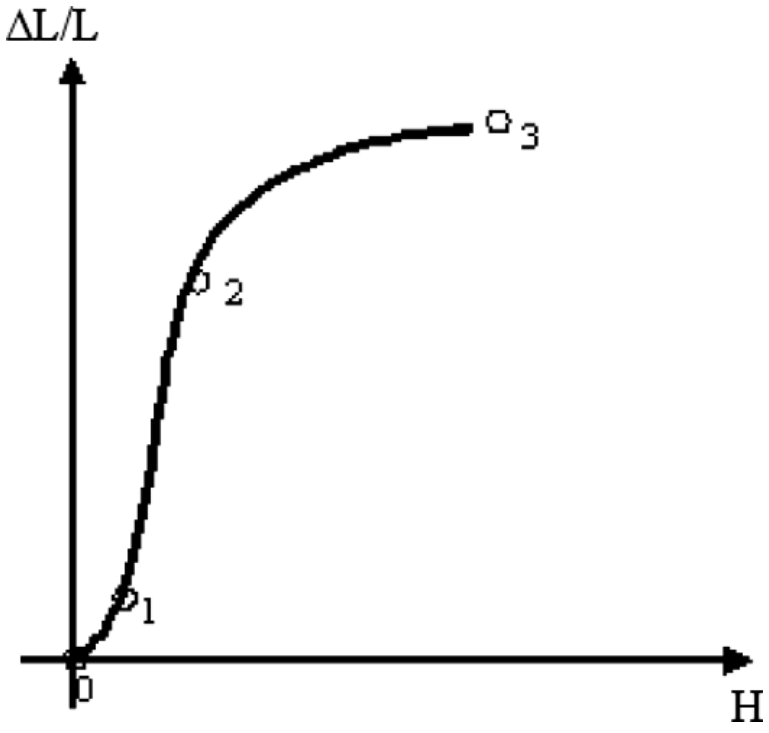


**Figure 1.4** Illustration of an idealised behaviour of deformation of a MS material in magnetic field, presented as strain versus magnetic field [52].

### 1.2.3 Piezoelectricity

Crystalline substances can produce an electric current when subjected to mechanical stress. The phenomenon was discovered in 1880 and named as piezoelectricity [53]. The direct effect of piezoelectricity can be defined as the transformation of mechanical stress to electrical polarization while the converse effect translates an electrical charge into deformation. This property generates due to the lack of an inversion centre of non-centrosymmetric structures of materials, as shown in Figure 1.5. This can be of particular interest due to the great variety of natural materials in the chiral pool. Common PE materials are inorganic crystals and ceramics, for example, $BaTiO_3$ and $Bi_{0.5}Na_{0.5}TiO_3$ [54]. Their diverse mechanical and physical properties are completed by the discovery of soft PE polymers, for example, PVDF, poly (lactic acid) (PLA) and cellulose [55].

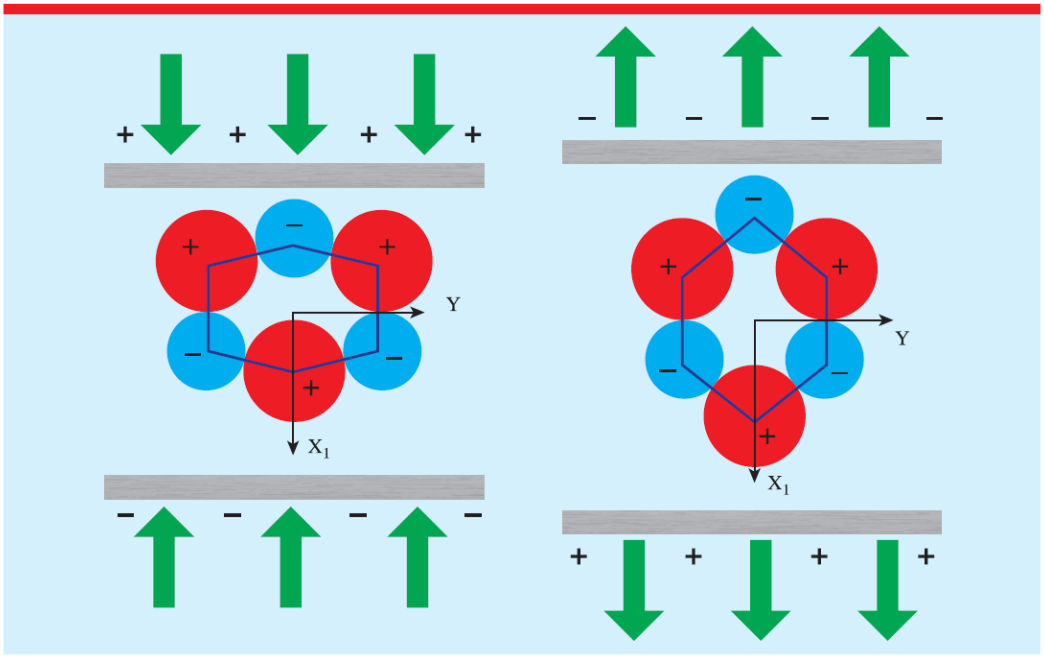


**Figure 1.5** Induction of charges under mechanical stress along the axis $X_1$ in a PE material [56].

The PE strain coefficient $d_{ij}$ is a (3 × 6) tensor which is defined as the electric polarization generated in direction *i* in the material per unit mechanical stress of index *j* applied to it or the induced mechanical strain of index *j* per unit electric field applied in direction *i*. In most PE materials, only 3 or 4 PE coefficient elements are not zero in the (3 × 6) tensor. The two common PE modes are $d_{33}$ and $d_{31}$ (Figure 1.6). The longitudinal coefficient $d_{33}$ describes the electric polarization generated in the same direction as the stress applied. The transverse coefficient $d_{31}$ describes the electric polarization generated in a direction perpendicular to the direction of the applied stress.

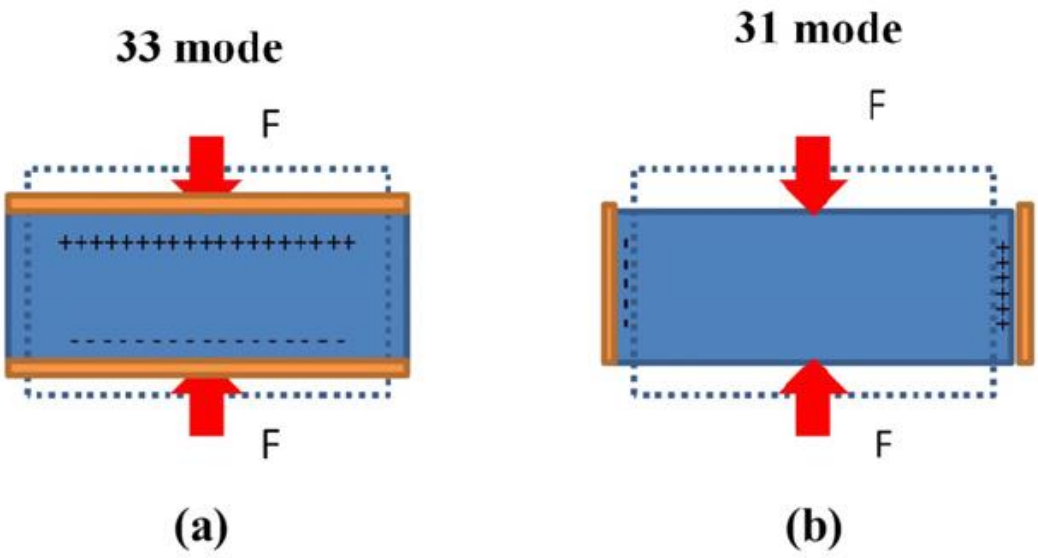


**Figure 1.6** The PE transduction modes [55].

### 1.2.4 ME Effect

Given the definitions of magnetostriction and piezoelectricity, Figure 1.7 illustrates the ME effect in composite systems. The MS effect (magnetic/mechanical effect) in the magnetic

phase and PE effect (mechanical/electrical effect) in the PE phase are combined to produce an ME effect in a composite (Figure 1.7). For direct ME effect, a magnetic field (H) induces strain in the magnetic component due to the MS effect, which is mechanically transferred to the PE component, inducing a dielectric polarization through the PE effect (Figure 1.7a and Equation 1.1) [57]. For a converse ME effect, an electric field (E) induces strain in the PE component due to the inverse PE effect, which is mechanically transferred to the magnetic component and thus induces a change of magnetization (ΔM) or domain reorientation through the piezomagnetic effect (Figure 1.7b and Equation 1.2) [57].

$$Direct\ ME\ effect = \frac{Magnetic}{Mechanical} \times \frac{Mechanical}{Electric} \tag{1.1}$$

$$Converse\ ME\ effect = \frac{Electric}{Mechanical} \times \frac{Mechanical}{Magnetic} \tag{1.2}$$

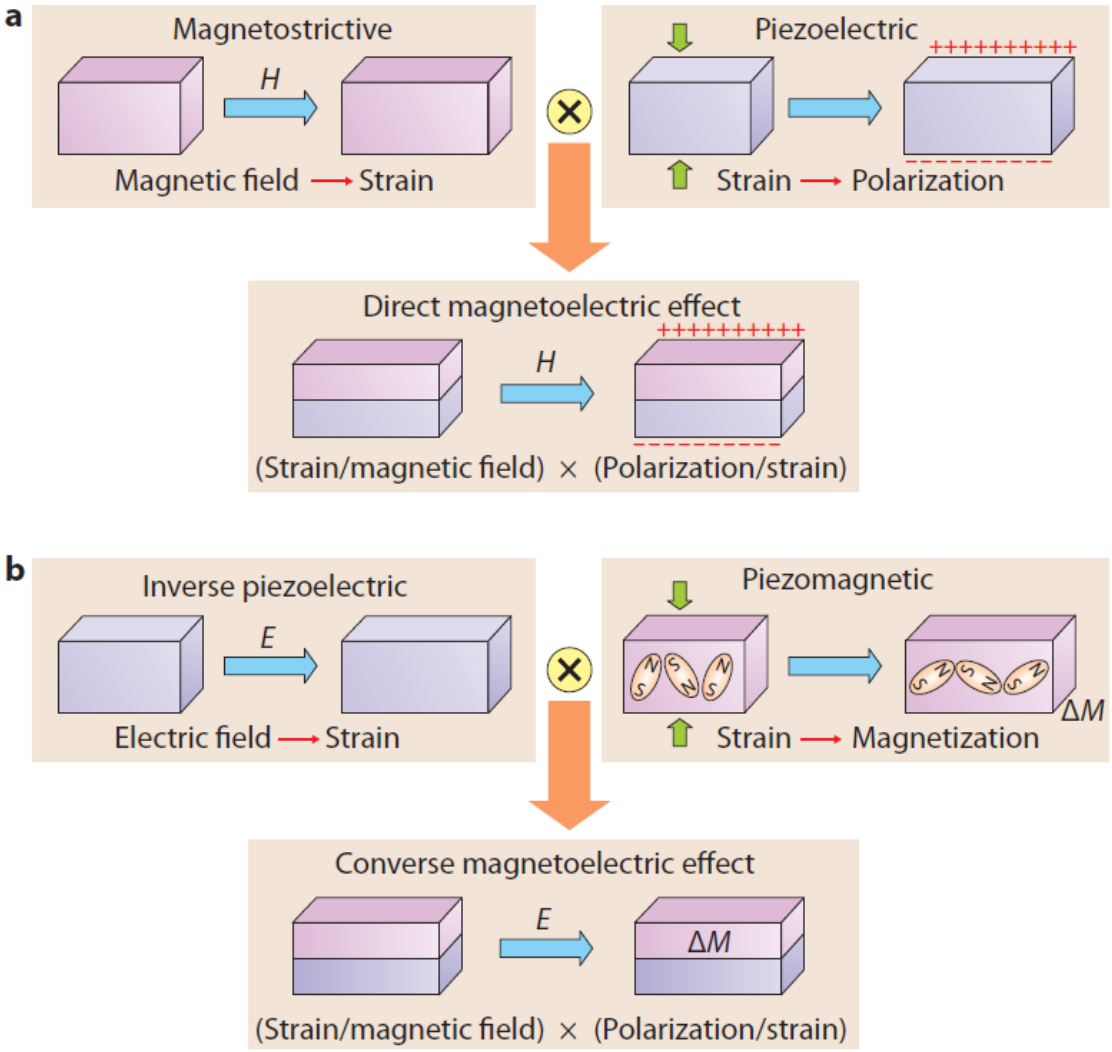


**Figure 1.7** Schematic illustration of strain-mediated ME effect in a composite system. (a) Direct ME effect, (b) Converse ME effect [57].

### 1.2.5 ME Coefficient

The ME effect is defined as the change in dielectric polarization (P) under an applied magnetic field (H) or vice versa [58]. Here, the induced P is related to the applied H by the equation.

$$P = \alpha H \tag{1.3}$$

where $\alpha$ is the second rank ME-susceptibility tensor. Generally, the ME voltage coefficient ($\alpha_{ME}$) is defined as the change in voltage across the sample with the change in applied magnetic field, which can describe the ME response of composite materials as

$$\alpha_{ME} = \frac{dE}{dH} \tag{1.4}$$

where $\alpha = \varepsilon_0 \varepsilon_r \alpha_{ME}$. Here, $\varepsilon_0$ and $\varepsilon_r$ are the vacuum permittivity and the relative permittivity and $\alpha_{ME}$ has a unit of V cm$^{-1}$ Oe$^{-1}$.

Similar to what is defined for PE coefficients $d_{33}$ and $d_{31}$, the measured $\alpha_{ME}$ could fall into two classes, i.e. $\alpha_{33}$ and $\alpha_{31}$. Two different ME laminate modes are distinguished on the basis of the direction of an applied H [59, 60]. The longitudinal ME mode results in longitudinal ME coefficient $\alpha_{33}$, in which H is applied parallel to P. The transverse ME efficient $\alpha_{31}$ can be obtained in transverse ME mode, in which H is applied perpendicular to P.

### 1.2.6 ME Measurement at the Microscale

There are basically three direct methods to measure a macroscale ME effect; they are static [61], quasi-static [62] and dynamic [63] methods. However, these methods may suffer from charge accumulation and improper treatment of zero signals and thus lead to erroneous conclusions. To solve these problems, a new technique with the assistance of a lock-in amplifier has been developed by Duong *et al.* [64].

Figure 1.8a presents a schematic of a ME laminate composite consisting of PE and MS layers. With the application of an in-plane AC and DC magnetic field, the ME output voltage is measured across the top and bottom electrodes. Figure 1.8b shows the experimental setup for

measuring the ME effect using the lock-in technique [64]. A pair of electromagnets is used to supply a DC magnetic field up to 15 kOe driven by a DC power source. A hall probe is placed between the electromagnets to measure the DC magnetic field. Additionally, an AC magnetic field up to 20 Oe ($f$ = 1-10 kHz) is superimposed onto the DC magnetic field. A Helmholtz coil (100 turns, d = 50 mm) is used to supply the AC magnetic field, driven by an AC current generated by a function generator. A multi-meter is connected to the lock-in amplifier (R = 100 MΩ, C = 25 pF) to measure the driving current for calculating the amplitude of the AC magnetic field. The lock-in amplifier isolates the signal of interest, effectively filtering out signals and noise at frequencies other than the specific reference frequency [65]. For the experimental measurement, the sample is placed in the central of the magnetic field. With the sample surface perpendicular or parallel to the field direction, the longitudinal and transverse ME responses, respectively, can be obtained. The ME output voltage at the reference frequency is measured using the lock-in amplifier and then data acquisition is performed by software.

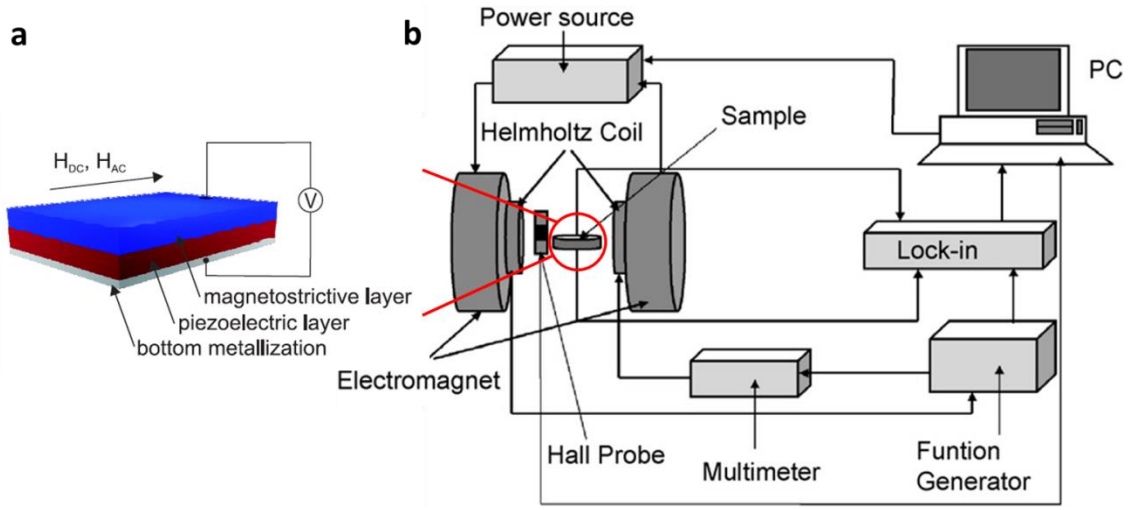


**Figure 1.8** Schematic of (a) a ME laminate composite [66] and (b) macroscale ME testing setup [64].

Physically, the ME coefficient stands for the ability to induce a change in voltage with the applied magnetic field across the sample and has a unit of V $cm^{-1}$ $Oe^{-1}$. In the above mentioned experimental setup, the ME coefficient can be calculated by the following equation [64].

$$ME\ coefficient = \frac{V_{out}}{h_0 d} \tag{1.5}$$

Where $V_{out}$ is the measured output voltage, $h_0$ is the amplitude of AC field and $d$ is the thickness of PE component.

Based on this equation, it is possible to calculate the ME coefficient by the output voltage of the lock-in amplifier. This measurement allows researchers to explore the dependence of the ME effect not only on the DC bias field but also on the frequency of the AC field. It is worth noting that the noise is reduced dramatically and the charge accumulation is avoided as the output signal is obtained at a specific frequency defined by the AC magnetic field. The

system is widely employed in measuring the ME effect of both ceramic and polymer-based laminates and nanocomposites [67-69].

## 1.3 ME Composites

Compared to the single-phase ME materials, ME composites possess the strain-mediated ME effect above room temperature. The separated phases also render ME composites tunable and controllable in manufacturing and processing. In addition, the magnitude of the ME coefficient of most single-phase materials is in the range of 1-20 mV $cm^{-1}$ $Oe^{-1}$ [70] while ME coefficient of composites ranges from 30 mV $cm^{-1}$ $Oe^{-1}$ in modified nickel ferrite/lead zirconate titanate (PZT) bulk composites [71] to giant ME response ($\alpha_{ME}$ > 1 V $cm^{-1}$ $Oe^{-1}$) in $Tb_{1-x}Dy_xFe_2$ (Terfenol-D)/PVDF laminates [72]. Due to these advantages, ME composites are extensively investigated and continue to attract interest in applications such as magnetic field sensors, transducers, oscillators, memory devices and biomedical materials [73, 74].

### 1.3.1 Ceramic ME Composites

Ceramic ME composites consist of ferroelectric oxides and magnetic oxides (mainly ferrites). PZT [75, 76] is widely used as the ferroelectric phase in ME composites due to its marked PE effect whilst ferrites possessing high MS performance, such as $CoFe_2O_4$ [77], $NiFe_2O_4$ [78] and $Ni_{0.8}Zn_{0.2}Fe_2O_4$ [79], are commonly employed as magnetic phase.

In most cases, bulk ME composites are prepared in three connectivity, (0-3) particulate composite, (2-2) laminate composite and (1-3) fiber/rod composite (Figure 1.9). For the (0-3) type particulate composites (Figure 1.9a), it is desired to disperse a high concentration of

ferrite particles into the PE ceramic matrix. However, leakage current always exists as most ferrites are conductive or semi-conductive and can deteriorate the insulation of the composites. Co-sintering at high temperatures is the most commonly applied method for preparing (0-3) type ME particulate composites though may cause atomic interfacial inter-diffusion and thermal expansion mismatch, leading to a much lower ME coefficient than predicted [71, 80]. Recently, chemical solution processing and novel sintering techniques have been employed and some improvements have been achieved [81, 82].

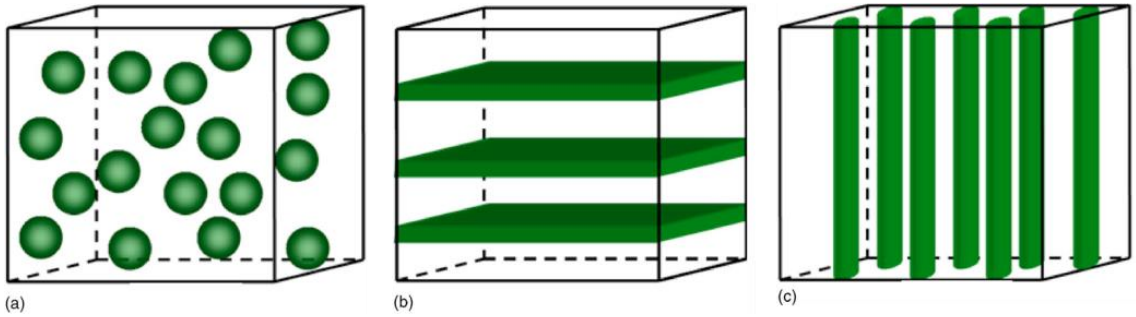


**Figure 1.9** Schematic illustration of three bulk composites with the three common connectivity schemes: (a) (0-3) particulate composite, (b) (2-2) laminate composite, and (c) (1-3) fiber/rod composite [73].

Compared with (0-3) type particulate composites, the (2-2) type laminate composites exhibit superior ME performance due to elimination of the leakage current, as the PE and MS phases are completely separated (Figure 1.9b). However, in laminate composites, the ferrite layers are not highly conductive, resulting in loss of the ME output signal induced from the PE layers. To address this, internal electrodes can be introduced between the PE and MS layers. A good example is the well-commercialized multilayer ceramic capacitors (MLCCs),

consisting of $BaTiO_3$ thin layers and ferromagnetic Ni internal electrodes [83]. Figure1.10 shows the actual size and cost of the $BaTiO_3$/Ni MLCC and structural representation of the device. In its laminate structure, the ME coupling is enhanced due to the Ni internal electrodes. This structure simplifies strain fields and thus enhances coupling with large magnetically-induced output charges generated. Given the high reproducibility of performance and low cost, MLCCs can be used for magnetic-field sensors that do not require electrical power, for example, for underwater, space, health and safety, *in vivo*, teaching or toy applications [83].

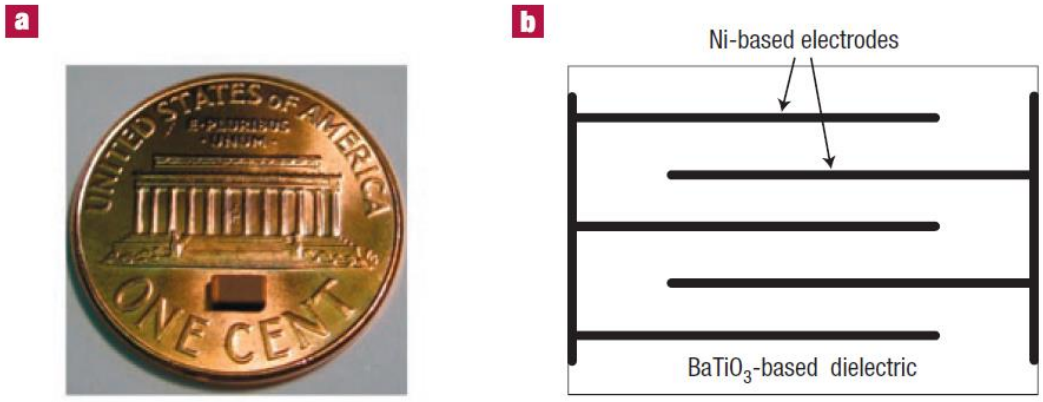


**Figure 1.10** (a) MLCC size and cost comparison, (b) Schematic MLCC cross-section [83].

The (1-3) fiber/rod composite is another connectivity structure (Figure 1.9c). However, in (1-3) ceramic composites, the magnetic phase also causes leakage current during polarization. To overcome this, this type of ME composites usually consist of three phases: PE bulk, MS alloy and insulating polymers [84]. Among the three connectivity of ME composites, the

highest ME coefficient is obtained in (2-2) laminate structures due to the discovery of MS alloy.

In 2001, the development of ceramic ME composites was propelled by the discovery of the giant MS rare-earth-iron alloy Terfenol-D and FeBSiC alloy (Metglas Inc.). The giant ME response (with $\alpha_{ME} > 1$ V cm$^{-1}$ Oe$^{-1}$) of Terfenol-D-based ME composites have been presented both in theoretical [85] and subsequently in experimental works [86, 87]. Further optimization of such composites is still ongoing, for example, a Rosen-type PE transformer bonded to a classical ME sandwich consisting of two Terfenol-D layers and one PMN-PT layer can amplify the output ME voltage up to more than 100 times [67].

Due to the relatively low permeability and high saturation field, Terfenol-D-based ME composites is not suitable for low magnetic field applications. Alternatively, Metglas is an amorphous alloy ribbon manufactured by a rapid solidification process [88] and can be magnetized and demagnetized quickly with high permeability, low coercivity and saturation field. For example, the saturation magnetostriction of the Metglas Inc. is about 30 ppm at $H_{DC} = 10$ Oe, which is much higher than that of Terfenol-D at low fields [89, 90]. A variety of structural and geometrical parameters are investigated to enhance the ME response and field sensitivity of Metglas-based ME composites [91-93].

The laminate composite of PE aluminum nitride (AIN) and amorphous FeCoBSi layers can be fabricated by magnetron sputtering [94]. Figure 1.11 shows the schematic of measuring the output voltage of the device in all three directions and the measured ME coefficient. Symmetric ME behaviour is observed in all the three directions. The laminate shows an extremely high ME coefficient of 737 V cm$^{-1}$ Oe$^{-1}$ on resonance at 753 Hz (black, filled circles), which is the highest value reported so far. In addition, the device shows an anisotropic behavior in resonance in the other two perpendicular axes. For the short axis (red,

crosses), the optimized bias field is 10 Oe, which is slightly larger than that of the long axis (black, filled circles) with 6 Oe. In this direction, the laminate gives a maximum ME coefficient of 49 V $cm^{-1}$ $Oe^{-1}$, while having 32 V $cm^{-1}$ $Oe^{-1}$ at 6 Oe. The bias field is shifted to even higher values in the out-of-plane orientation (blue, open triangles) and the ME coefficient is only 3 V $cm^{-1}$ $Oe^{-1}$ at 6 Oe. Such magnetic anisotropic responses in these composites allow for the realization of a 3D vector field sensor.

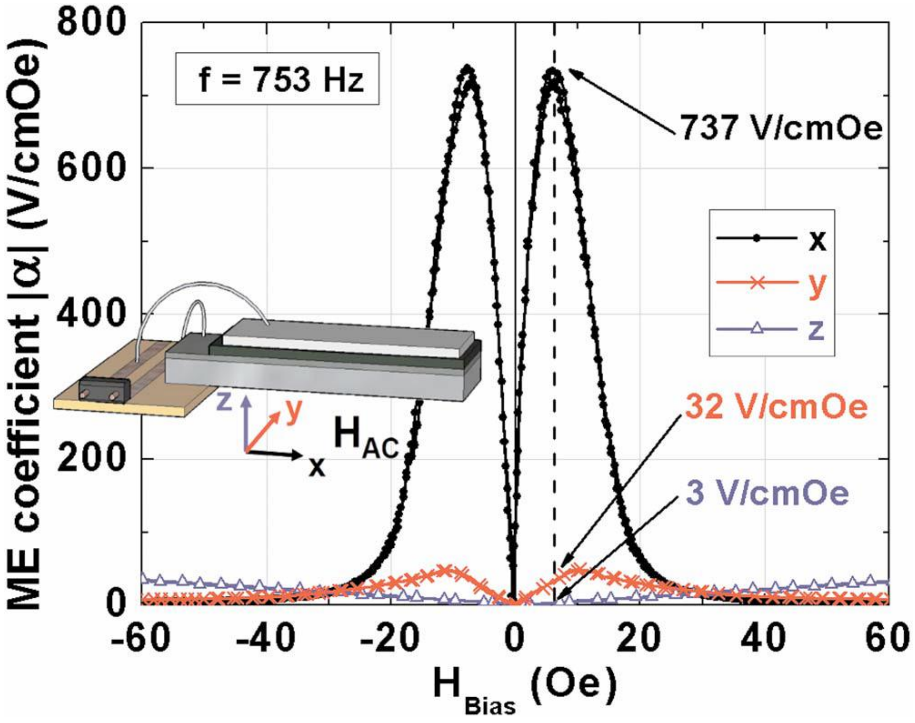


**Figure 1.11** Absolute value of the ME coefficient α of a cantilever with a 1.75 μm FeCoBSi and 1.8 μm AlN film at the resonance frequency of 753 Hz. The ME signal is determined with $H_{AC}$ applied in all three dimensions and shows a clear anisotropy. The maximum ME coefficient of 737 V $cm^{-1}$ $Oe^{-1}$ is achieved in parallel orientation [94].

### 1.3.2 PE Polymers for Polymer-Based ME Composites

Despite the high ME coefficients obtained in ceramic ME composites, these composites may become fragile and cause deleterious reactions at the interface regions, leading to low electrical resistivity and high dielectric losses [95]. Moreover, ceramic composites still have other shortcomings such as being expensive, dense, brittle and toxic [96]. Alternatively, polymer-based ME composites are attractive from a technological point of view, especially in biological applications. In comparison with the ceramic ME composites, PE polymer-based composites can be more easily fabricated and exhibit greatly improved mechanical properties.

#### *1.3.2.1 PVDF*

For years, research on PE polymers has been dominated by PVDF due to its high PE coefficient and well-understood mechanism. The piezoelectricity arises from the strong molecular dipoles within the polymer chain and resulting change of the dipole density upon application of a mechanical stimulus. PE polymers show moderate PE coefficients ($d_{33}$ = 20-30 pC $N^{-1}$) in comparison to PE ceramics.

PVDF is a semicrystalline polymer with five crystalline phases including all trans (TTTT) planar zigzag for the β-phase, TGTG' (trans-gauche-trans-gauche) for the α- and δ-phase and T3GT3G (trans-trans-trans-gauche) for γ- and ε-phase. The most commonly existing crystalline phases of PVDF are α- and β-phase, which are clearly identified by FT-IR and XRD [97]. However, the third discovered phase, γ-phase, has caused some confusion in its identification and has been mistakenly reported as the β-phase [98]. These misinterpretations has persisted for a long time due to the considerable less attention directed to the properties of the γ-phase since, until recently, it is difficult to prepare single-polymorph high γ-phase

content films [99]. Figure 1.12 shows the structures of polymer chains in PVDF with α-, β- and γ-phase [100]. Among these polymorphic crystalline structures, the β-crystalline phase is the most highly polar and desired one in which chains of all-trans conformation pack with dipoles parallel to a common axis in a pseudo-hexagonal configuration. The highly ordered and aligned dipoles in the β-phase give rise to ferroelectric and PE behaviour. The key to achieving excellent piezoelectricity in PVDF is the formation of a high β-phase content and well oriented molecular dipoles within the structure. Conventionally, the former is accomplished by mechanical stretching, while the latter is achieved through an electrical poling treatment [101-104].

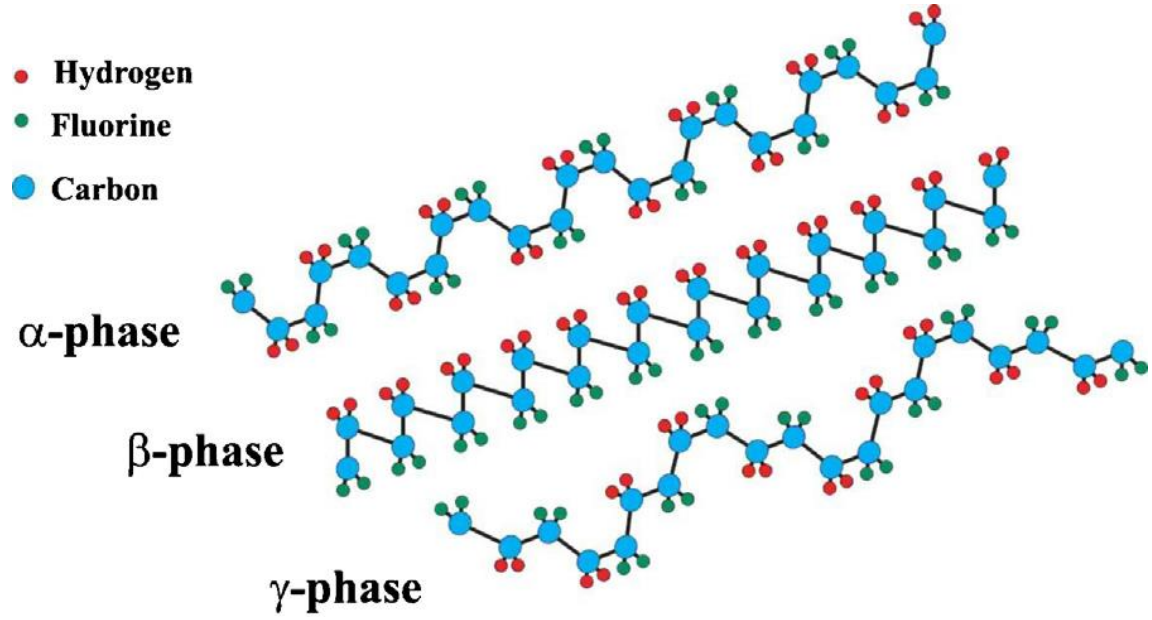


**Figure 1.12** Schematic representation of the chain conformation for the α-, β- and γ-phase of PVDF [100].

#### *1.3.2.2 PVDF Copolymers*

To meet the increasing technological demands, different PE copolymers of PVDF have been developed. Poly (vinylidene fluoride-co-trifluoroethylene), P(VDF-TrFE), is one of the most studied copolymers. The addition of the TrFE monomer unit favours the all-trans conformation due to a large steric hindrance. Compared to PVDF, the higher degree of crystallinity and the preferred orientation of well grown crystallites exhibit higher remnant polarization (~110 mC $m^{-2}$) and higher efficiency in mechanical - electrical transformation [105].

Poly (vinylidene fluoride-co-hexafluoropropene), P(VDF-HFP), consists of the amorphous phase of HFP on the PVDF homopolymer. Compared to PVDF, P(VDF-HFP) is chemically inert and presents a lower crystallinity due to the presence of the bulky $CF_3$ groups [106]. However, the higher PE coefficient ($d_{31}$) of 30 pC $N^{-1}$ presented by this copolymer makes it a promising material in some PE and ferroelectric application areas such as the development of ME sensors and actuators [106]. In addition, PVDF can be modified to form P(VDF-CTFE) [107] and P(VDF-TrFE-CTFE) [108] with designed piezoelectricity.

#### *1.3.2.3 PLA*

In addition to PVDF, other PE polymers include polyurethane (PU) [109], polyhydroxybutyrate (PHB) [110], Polyamide-11 [111], Parylene-C [112] and PLA [113]. As one of the PE polymers, along with PVDF and P(VDF-HFP), studied in this thesis, PLA is an environmentally friendly polymer exhibiting piezoelectricity. Unlike PZT and PVDF, no poling treatment is required to induce piezoelectricity in an entire PLA structure (e.g. casting film) [113]. In other words, the fabrication of a PE PLA film only requires uniaxial

orientation treatment. The piezoelectricity of PLA is due to the cooperative motion of the permanent dipoles in the principal chain molecules [114]. Thus, PLA is not ferroelectric and therefore does not exhibit pyroelectricity which often causes problems in PE devices manufactured from ferroelectrics.

Figure 1.13a shows the helical structure of crystal PLA polymer and Figure 1.13b illustrates the shear piezoelectricity in PLA. When a shear stress is applied to the molecular chain of PLA, all the atoms in the molecular chain will be displaced. The motion causes the rotation on the C-O bond of PLA and thus the change in the polarization. As a result, the change in the polarization is due to the applied shear stress [115]. The macroscopic piezoelectricity is a result of its intrinsic piezoelectricity due to the crystal state. In other words, the mechanism of macroscopic piezoelectricity is made complicated by the existence of a complex high-order structure.

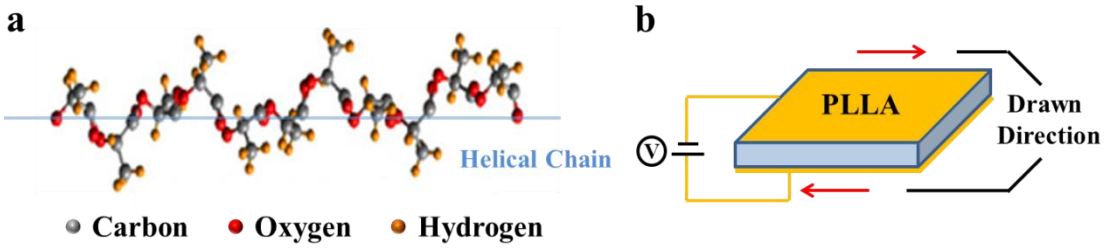


**Figure 1.13** (a) PLA chains formed by covalent bonds between chiral molecules [113]. (b) Illustration of shear piezoelectricity in PLA.

Since an external force does not propagate through the amorphous region, altering the structure in the amorphous region is considered to be a convenient approach to enhance PE

performance. Related to this, the piezoelectricity of PLA films has been found to improve significantly by introducing higher-order structures using additives such as the triblock copolymer, PMMA-b-PBA-b-PMMA, consisting of a soft central block of poly (butyl acrylate) (PBA) and two hard side blocks of poly(methyl methacrylate) (PMMA) (Figure 1.14) [116]. In the PLA film, the PMMA at both ends acts as an anchor between the amorphous region and the crystal region, as shown in Figure 1.14a. To induce piezoelectricity in the PLA film, the film is uniaxially extended, as shown in Figure 1.14b. The stretching of PBA chains may cause residual stress and assist the external force to propagate through the amorphous region and thus the piezoelectricity of a drawn PLA film can be improved. These results suggest that the piezoelectricity of PLA films is strongly affected not by the macroscopic higher-order structure but by the microscopic higher-order structure. In summary, a homogeneous higher-order structure is essential for the piezoelectricity of PLA.

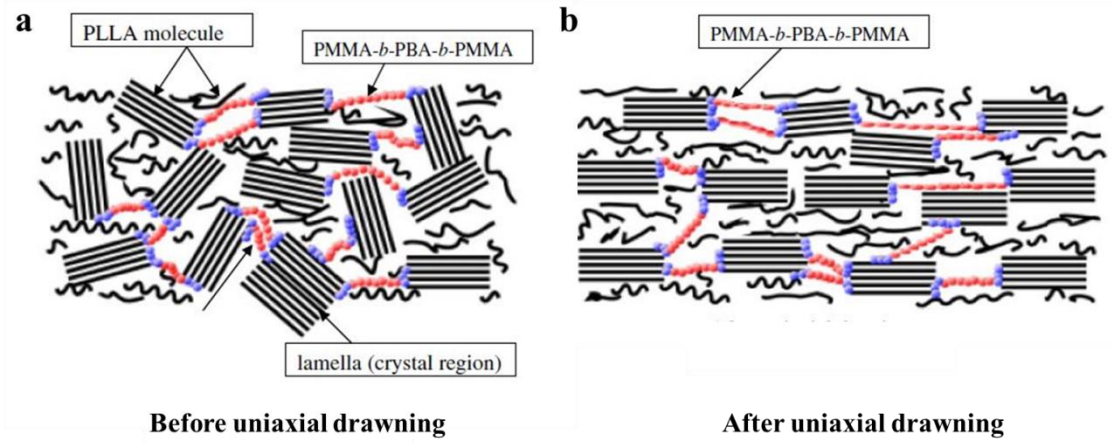


**Figure 1.14** Illustration of higher-order structure before and after drawing PLA/(PMMA-b-PBA-b-PMMA) film [116].

### 1.3.3 Polymer-based ME Composites

Figure 1.15 shows the three main types of polymer-based ME composites: nanocomposites, laminated composites and polymer-as-a-binder composites. Nanocomposites refer to those that consist of MS nanoparticles embedded in polymer matrix (Figure 1.15a). Laminate composites consist of a MS layer and PE polymer layer, which are bonded by epoxy (Figure 1.15b). In the third type of composites, polymers are used as a binder matrix in which both MS and PE particles are dispersed (Figure 1.15c). The fabrication of polymer-based ME composites are dominated by PVDF family with only a few works on PU-based ME materials [109, 117]. In this section, only the former ones are introduced.

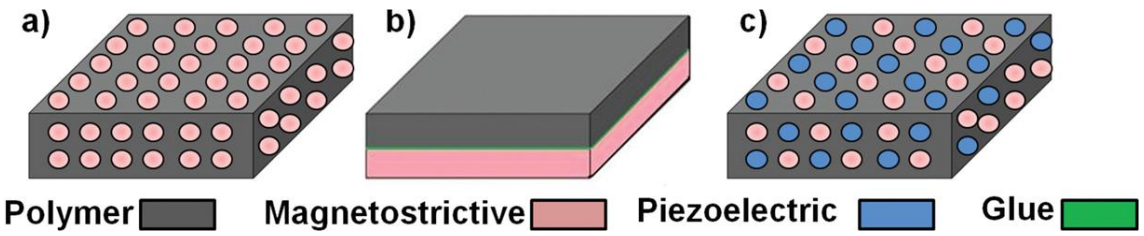


**Figure 1.15** Types of polymer-based ME materials: a) nanocomposites, b) laminate composites, and c) polymer as a binder composites [21].

#### *1.3.3.1 Polymer-based ME Nanocomposites*

Particulate polymer-based ME composites are of technological interest due to their ease of processing. The PVDF family is extensively used as the PE constituent of ME nanocomposites and the theoretical calculations of giant ME on ferromagnetic rare-earth-iron-alloys-filled ferroelectric polymers has been reported in 2001 by Nan *et al.* [85, 118]. The use of P(VDF-TrFE) is also preferred over PVDF since the copolymer can directly

crystallize from the melt into β-phase, which is a key factor for the preparation of polymer-based ME nanocomposites [119].

Martins *et al.* introduced $CoFe_2O_4$ nanoparticles into a polymer matrix of P(VDF-TrFE) [120]. The nanocomposites exhibit ferroelectric, PE, magnetic and ME properties, including a direct ME effect that is dependent on the ferrite loading. The P(VDF-TrFE)/$CoFe_2O_4$ films show saturated hard magnetic properties, improved polarization and a PE response and maximum $\alpha_{ME}$ value of 41.3 mV $cm^{-1}$ $Oe^{-1}$.

#### *1.3.3.2 Polymer-based ME Laminate Compoistes*

Compared to bulk nanocomposites, laminate bilayer or multilayer configurations can efficiently overcome the leakage current. In addition, the PE phase can be electrically poled prior to bonding to the MS phase (e.g. Metglas layer) to enhance the ME coupling. It is also possible to vary the poling and applied field directions to achieve maximum ME coupling. Laminated ME materials consisting of a PZT/PVDF particulate layer sandwiched between two Terfenol-D/PVDF particulate composite layers have been investigated [121]. The maximum ME coefficient $\alpha_{33}$ is improved to 300 mV $cm^{-1}$ $Oe^{-1}$ at a frequency below 50 kHz and about 6 V $cm^{-1}$ $Oe^{-1}$ at the resonance frequency of around 80 kHz. The ME response of such composites is found to be strongly dependent on the applied magnetic field and on the thickness ratio between the Terfenol-D/PVDF layers and the PZT/PVDF layer.

Flexible ME laminate composites (Figure 1.16a) have been fabricated employing Metglas/PVDF with unimorph (Figure 1.16b) and three-layer sandwich (Figure 1.16c) configurations [122]. Those laminates require an applied DC field of only 8 Oe to achieve a maximum ME response. Both laminates exhibit a strong ME enhancement at resonance

frequency of 50 kHz: unimorph composites: $\alpha_{31}$ = 310 V cm$^{-1}$ Oe$^{-1}$; three-layer composites: $\alpha_{31}$ = 238 V cm$^{-1}$ Oe$^{-1}$. At lower frequencies, a maximum value of 7.2 V cm$^{-1}$ Oe$^{-1}$ is obtained for both laminates. This extremely low $H_{DC}$ requirement is an important advantage of Metglas/PVDF laminates over other types of laminates, offering great potential in practical applications in low-magnetic field sensing.

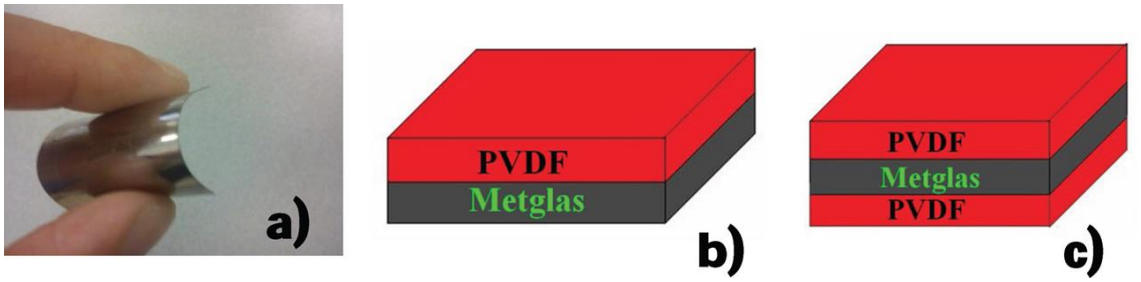


**Figure 1.16** a) Picture of a flexible PVDF/Metglas unimorph laminate, b) unimorph configuration, and c) three-layer laminate [20]. Panels b) and c) are based on the experimental description reported in [122].

After initial studies on Metglas/PVDF laminate nanocomposites [122], several groups have published on these promising ME materials. For example, the chain-end cross-linked ferroelectric P(VDF-TrFE)/Metglas 2605 SA1 composites have demonstrated a superior ME performance (Figure 1.17) [123]. The introduction of chain-end crosslinking and polysilsesquioxane structures leads to the formation of larger crystalline and consequently better PE responses. For the cross-linked P(VDF-TrFE)/Metglas laminates, a $\alpha_{31}$ value of 17.7 V cm$^{-1}$ Oe$^{-1}$ is achieved under a DC magnetic field of 3.79 Oe at 20 Hz, whereas the value obtained for the control sample is only $\alpha_{31}$ = 6.9 V cm$^{-1}$ Oe$^{-1}$ (Figure 1.17a). At a resonance frequency of 65 kHz, the $\alpha_{31}$ values for cross-linked P(VDF-TrFE)/Metglas

laminates can be highly improved to 383 V $cm^{-1}$ $Oe^{-1}$ (Figure 1.17b). The cross-linked laminate composite not only shows the largest value of ME coefficients in polymer-based ME materials but also sheds light on improving the ME response through tuning the PE properties of the PE layer.

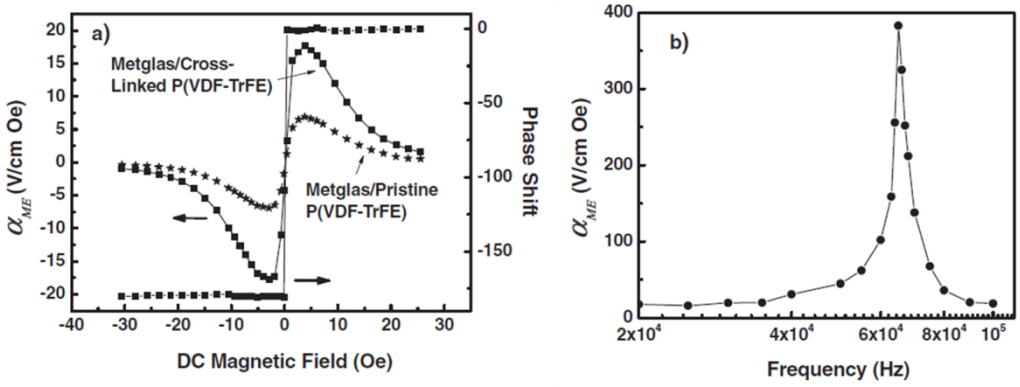


**Figure 1.17** a) The ME voltage coefficient and phase shift of the composites as a function of DC magnetic field measured at 20 Hz and $H_{AC}$ = 0.38 Oe. b) Frequency dependence of the ME voltage coefficient of the cross-linked P(VDF-TrFE)/Metglas laminates measured under $H_{DC}$ = 3.79 Oe and $H_{AC}$ = 0.38 Oe [123].

#### *1.3.3.3 Polymer as a Binder Composites*

In the polymer as a binder composites (Figure 1.15c), the polymer is not used as the PE phase but as a binder for the PE and MS particles that keeps them together and provides the stress coupling. Among the three-phase particulate composites, the system consisting of Tefenol-D alloy, PZT and PVDF is the first to be studied [124], with its structure shown in Figure 1.18. The maximum obtained value for $\alpha_{33}$ is about 42 mV $cm^{-1}$ $Oe^{-1}$ at $H_{DC}$ = 2 kOe. The volume fraction of Terfenol-D (*f*) in the composite is changed to study its influence on the ME

response. When $f$ is lower than 0.07, the composites exhibit good PE and ME responses. Further increasing $f$ to $0.07 \leqslant f \leqslant 0.12$, the PE and ME response sharply drops and disappears at the percolation threshold ($f$ = 0.12), above which the composite becomes a conductor. A conclusion is drawn that the pre-treatment of the Terfenol-D nanoparticles can change the ME coupling. Surfactants are usually used in such a way to improve dispersibility and dispersion stability of nanoparticles in different kind of matrices [125].

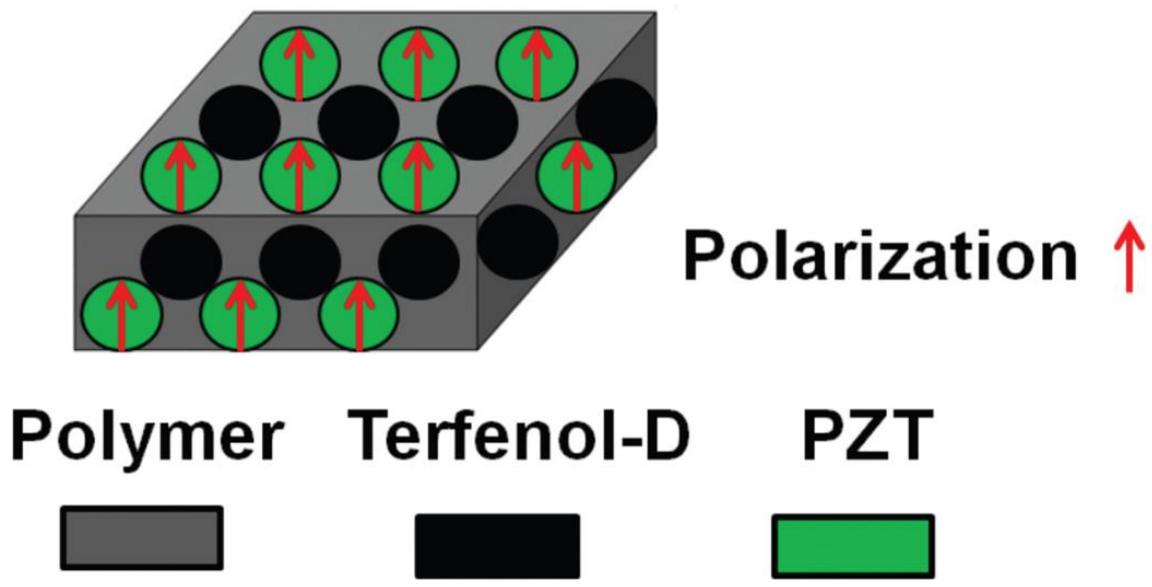


**Figure 1.18** Schematic of the particulate Terfenol-D/PZT/polymer composites [21] based on the experimental description reported in [126].

### 1.3.4 Biopolymers in ME Materials

Although PE biopolymers are a widely distributed resource, the limitation of using raw biomaterials lies in several aspects. One consideration is that most biopolymers cannot easily be moulded into desired form due to poor machinability. Moreover, PE biopolymers usually

coexist with other ingredients; therefore such variations arising from their different sources may hinder the refinement, specification and standardization of final products, especially for clinical applications. For example, wood is interestingly known to exhibit piezoelectricity (from the cellulose) although the mechanical properties of woods vary from species to species and highly depend on environmental parameters such as temperature and humidity, which are likely to influence their PE properties [127-129].

Alternatively, the use of regenerated products brings a supplementary source of PE polymers for biomedical applications. Here, PE polymers can be extracted and purified through dissolution processes and the end-products made suitable for further industrial processes. One example is the regenerated cellulose produced from solution processing with N,N-dimethylacetamide (DMAc)/LiCl that has been used to produce electroactive papers [130]. The regenerated cellulose film can undergo mechanical deformation when an external electrical field is applied [131], and can be configured to make electrical devices such as an actuator [132, 133]. The application of mechanical forces or electrical poling can further increase the degree of crystallinity and enhance the PE properties since the piezoelectricity of cellulose mainly comes from the crystalline structure [134-136]. As a very cheap, renewable, easily processable and degradable substrate, cellulose is developing rapidly as a supporting substrate for flexible and transparent electronics [137, 138], and is expected to have a wider impact in biomedical applications. Hence, exploring novel ME composites based on naturally occurring PE biopolymers is of significant interest.

Our group has pursued this area and recently developed cellulose-based ME composites. The laminates have a bilayered structure consisting of cellulose as the PE phase and Metglas as the MS phase and produce a considerable ME resonance coefficient of ~1.5 V $cm^{-1}$ $Oe^{-1}$ (Figure 1.19A-C). Figure 1.19D shows the $\alpha_{ME}$ dependence on $H_{dc}$. A significant increase in

$\alpha_{ME}$ is observed at the resonance frequency of the MS layer, corresponding to the resonance enhancement effect that is characteristic of an ME effect in laminate structures [49]. Simple solution processing methods induce alignment of cellulose fibrils, leading to amplification of PE domains and the ME coefficient. The study successfully demonstrates the concept of using natural occurring biopolymers which could also extend to other biological PE materials such as proteins (e.g. collagen) as functional electrode interfaces in ME composites.

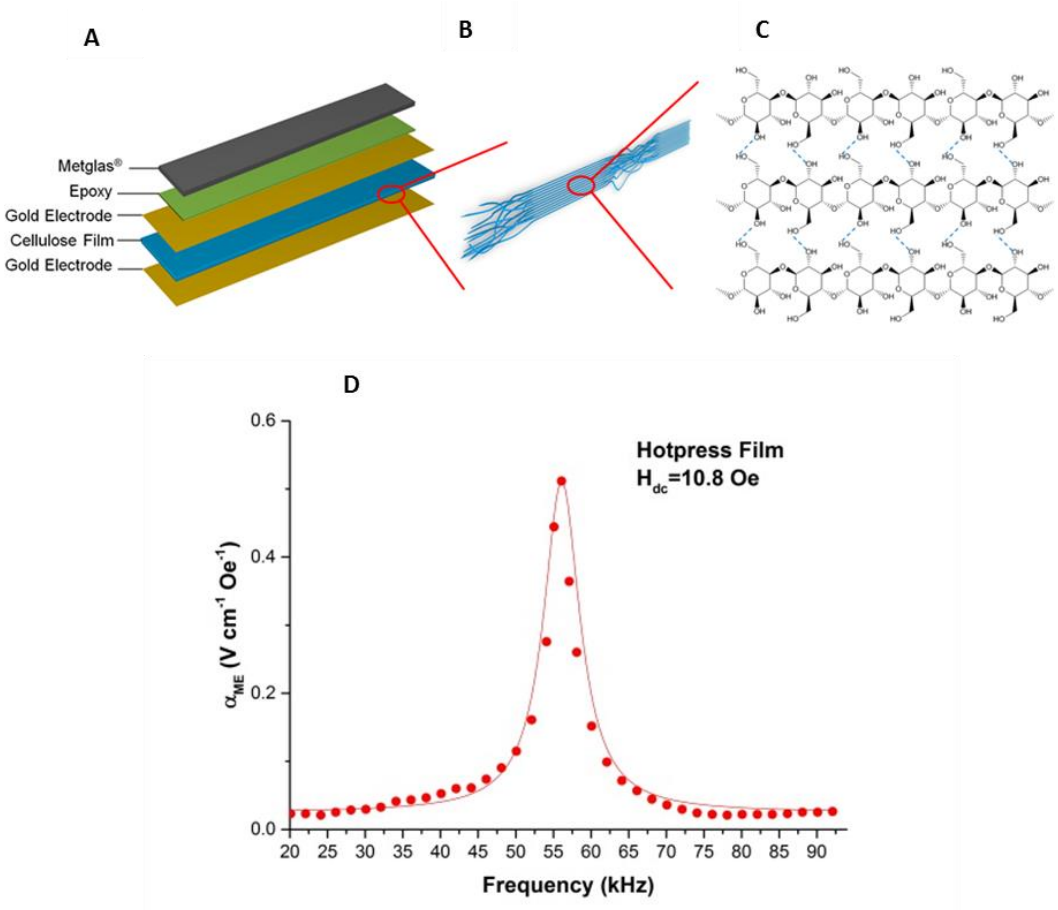


**Figure 1.19** (A) Schematic view of cellulose based ME laminate. The ordered sections cellulose (B) provides crystalline structure in which the aligned dipoles of saccharide (C) arising PE property. (D) Frequency-dependence trace of the ME voltage coefficient hot-press cellulose/Metglas laminate under $H_{dc}$ = 10.8 Oe and $H_{ac}$ = 0.5 Oe [139].

## 1.4 ME at the Nanoscale

### 1.4.1 Nanoscale ME Structures

Here, the thesis has a particular focus on the ME effect at the nanoscale, and the fabrication and characterization of nanostructured and nanoscale ME materials have drawn significant attention in the hope of elucidating remarkable properties (e.g. ME coefficients). Thus, extensive work has been done on the fabrication of spherical core-shell nanoparticles consisting of a MS core and a PE shell (Figure 1.20A), composite nanofibers or core-shell nanofibers with MS core and a PE coating (Figure 1.20B), as well as microspheres of PE polymers with embedded magnetic nanoparticles (Figure 1.20C).

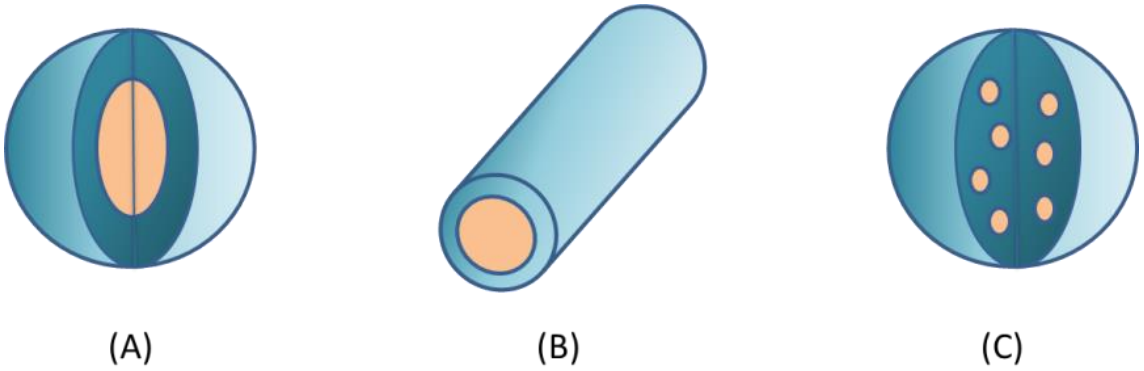


**Figure 1.20** Three types of nanostructured ME materials: (A) spherical core-shell nanoparticles with MS core encapsulated in PE shell, (B) core-shell nanofiber with a MS core and a PE coating and (C) a composite superparticle with MS nanoparticles embedded into PE polymer [39].

These nanostructured materials are expected to possess superior performance compared to their bulk counterpart. Because of the small thickness of the PE shell, the MS stress will be

absorbed by the whole volume of the PE phase (not just the interfacial layer as may occur in bulk ME structures), thus generating larger dipole moments. In addition, substrate clamping effect in the configurations of films and laminates can be overcome in nanoscale ME composites and improved mechanical contact at the interface will benefit transfer of stresses between two different ME components. These composites may use superparamagnetic nanoparticles embedded in the PE polymer, ensuring the ME material is only activated in the presence of a magnetic field and hence switched "off" when not in use. This can also prevent potential problems with particle aggregation. In addition to the aforementioned advantages, studies also reveal that geometrical confinement can greatly influence their physical behaviour, such as crystallization [140] and chain dynamics [141], and thus PE performance. Investigation of unique properties of nanostructures benefits the miniaturization of devices and thus the *in vivo* biological applications.

To date, only ceramic ME nanoparticles have been fabricated due to the need for post-treatment of PE polymers [101, 103]. Pioneer works include the fabrication of $CoFe_2O_4/BaTiO_3$ ME nanoparticles presented by Rodzinski *et al*. [142] and Guduru *et al* [143]. Taking advantage of their small size and moderate ME coefficient, these nanoparticles have been used in drug release and remote stimulation of tissues, which will be discussed further below in Section 1.5.3.

Nanostructured PE polymers are typically synthesized by three main techniques: electrospinning/electrospray [144], template-assisted infiltration [145], and nanoimprinting with a mold [140]. Electrospinning, a widely studied technique, which leads to PVDF and P(VDF–TrFE) nanostructures with at least one feature size below hundreds of nanometers, has a profound influence on the final PE performance. Figure 1.21b shows the schematic of an electrospinning setup [146]. Typically, electrospinning equipment consists of a pump, a

syringe, a high voltage power supply and a collector. The pump connected to the syringe is for controlling the feeding rate of the polymer solution. The power supply is to apply a sufficient high voltage to the polymer solution and thus the dipoles can be aligned along the direction of the electric field during the electrospinning process (Figure 1.21a). Finally, the nanofibers are obtained on a collector. Alternatively, the collector can be changed to a rotary drum for improving the alignment of nanofibers.

Reducing the diameter of the polymer fibers from micrometer to nanometer dimensions gives rise to novel properties, such as large surface area to volume ratio, flexibility in controlling surface functionalities, and superior mechanical performance (stiffness and strength). In particular, preferential crystallization in the polar β-phase has been shown in both P(VDF–TrFE) [147] and PVDF nanowire arrays [148, 149], producing remarkable levels of polarization without the need for further processing with mechanical stretching or electrical poling, as is typically required for bulk ME structures. This represents a great advantage, not only in terms of time and equipment but also because these polymers can be directly fabricated as ready-to-use and device-integrated functional materials without any further processing.

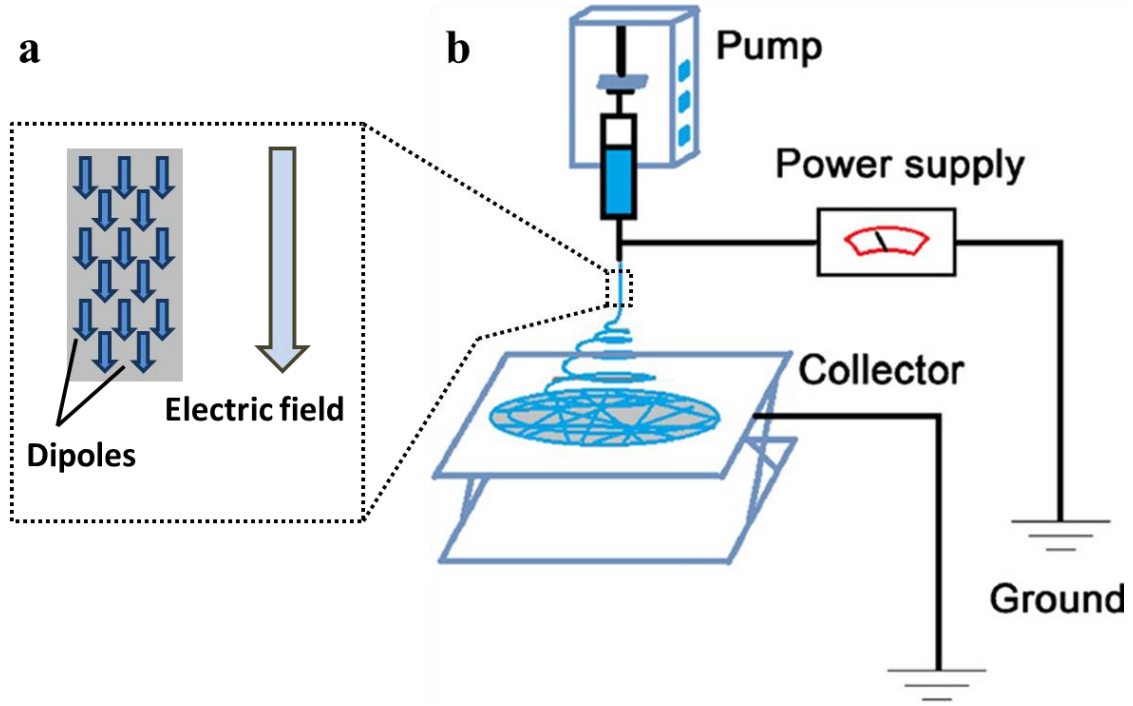


**Figure 1.21** (a) Enlarged view of the induced dipoles in the polymer jet (adjusted from [144]) and (b) schematic of electrospinning equipment [146].

ME composite nanofibers comprising $CoFe_2O_4$ nanoparticles in a PVDF polymer matrix have been prepared by electrospinning [150]. The average diameter of the electrospun composite nanofibers is ~325 nm, independent of the nanoparticle content. The amount of the crystalline polar β-phase is strongly enhanced by the addition of $CoFe_2O_4$ nanoparticles when compared to pristine PVDF polymer nanofibers. The PE response of these electroactive nanofibers is modified by an applied magnetic field, thus evidencing the ME effect of the $CoFe_2O_4$/PVDF 0-1 composites.

In addition to nanoscale ME materials, it is prudent to mention developments in their microscale counterparts that can play a similar role in miniaturized ME devices. For example, $CoFe_2O_4$/PVDF microspheres have been obtained by an electrospray process [151]. Diameters of the spheres vary in the range of 3 to 7 mm, nearly independent of the $CoFe_2O_4$

filler content (Figure 1.22). The interface between $CoFe_2O_4$ nanoparticles and PVDF is found to have a strong influence on the ME response of the $CoFe_2O_4$/PVDF spheres. Increasing the interface value to 55% results in an optimized ME response ($\Delta|d_{33}|$ = 5 pC $N^{-1}$) when a 220 mT DC magnetic field is applied to the $CoFe_2O_4$/PVDF spheres with 21 wt% of ferrite. The overall properties of the ME microspheres and the simplicity of the processing method provide a basis for dispersible, "contactless" polymer-based electrodes for developing novel microelectronic devices. However, the ME measurement still occurs over the bulk of a film even though the particle size is on the order of microns. Nanoscale ME measurements are therefore required to truly measure the properties of such nano- and micro-particulate systems and to lay a solid foundation for determining their practical applications. A technique based on Atomic Force Microscopy, Piezoresponse Force Microscopy, has emerged in recent times to enable such nanoscale characterization of ME properties and is discussed further below.

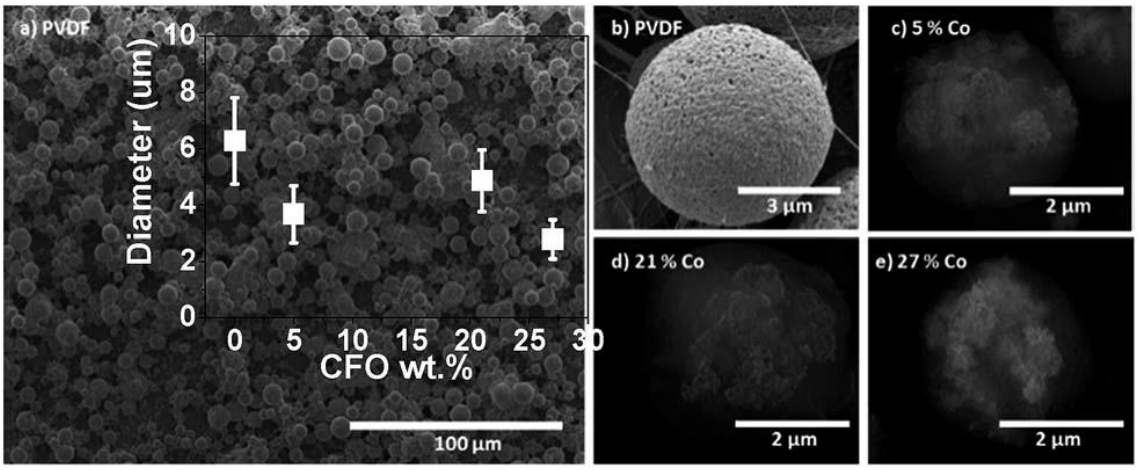


**Figure 1.22** Morphology of (a and b) PVDF polymer and the ME $CoFe_2O_4$/PVDF microspheres with (c) 5 wt%, (d) 21 wt% and (e) 27 wt% $CoFe_2O_4$ nanoparticles [151].

### 1.4.2 PFM Measurement and Switching Spectroscopy

Atomic Force Microscopy (AFM) was invented by Binning, Quate and Gerber in 1986 [152] to broaden surface scanning probe imaging to both conductive and insulating surfaces with an extremely high resolution (0.1 nm in height). More importantly, development of AFM led to a multifunctional research tool for analysing mechanical properties and measuring surface forces at the nanoscale, just to name a few. One of the more recent off-shoots of AFM, Piezoresponse Force Microscopy (PFM), was first demonstrated by Guthner and Dransfeld through a study of domains in a ferroelectric film [153]. The operating principle of PFM is the use of a conductive tip that is brought into contact with a PE material and an AC bias is applied to the tip in order to excite deformation of the sample. The mechanism is based on the coupling between polarization and electromechanical behaviour via the converse PE effect. In this case, the application of a highly localized electric field results in minute deformation of the sample surface, which can be detected in contact-mode imaging with picometer precision. Due to its non-destructive nature and nanoscale spatial resolution, PFM has been widely used in domain characterization of ferroelectrics and multiferroic materials [154-156].

In PFM, a voltage is applied to a conductive tip in contact with a PE material.

$$V_{tip} = V_{DC} + V_{AC} \cos \varpi t \tag{1.6}$$

Here, $V_{DC}$ is the DC bias (switching bias), $V_{AC}$ is the AC bias (probing bias) and ω is the frequency of AC bias (driving frequency). As the sample expands and contracts due to the converse PE effect, the tip deflection is monitored using a lock-in amplifier so that the tip oscillation and hence the sample deformation at the driving frequency of the AC bias is recorded simultaneously with topography. The sample deformation is as follows.

$$A = A_0 + A_{1\varpi} \cos(\varpi t + \varphi) \quad (1.7)$$

Here $A_0$ is the static surface displacement and φ is the phase shift between the driving voltage $V_{AC}$ and the voltage induced deformation $A_{1\varpi}$. The PFM amplitude provides information on the magnitude of the local electromechanical coupling, while the PFM phase image provides information on the ferroelectric domain orientation. For materials with unknown orientation, there can be both an out-of-plane and in-plane PE response. Vertical deflection of the cantilever is induced by an out-of-plane deformation while torsional and buckling deformation of cantilever is induced by the in-plane deformation [157, 158]. The torsional mode results in a "lateral" signal while deflection and buckling result in a "deflection" signal of the AFM position sensor which complicates the analysis of ferroelectric domains in PFM images [159]. Depending on the relative orientations of the applied field and the polarization vector, sample deformation can be in the form of elongation, contraction or shear. Application of the uniform electric field along the polar direction results in the elongation of the domain with polarization parallel to the applied field and in the contraction of the domain with opposite polarization.

In conventional PFM, crosstalk between topography and PFM amplitude is inevitable since the tip is driven at a single frequency, determined by the local interaction between the PFM tip and sample surface. To address this issue, Rodriguez *et al.* has invented a new technique termed Dual AC Resonance Tracking (DART) mode [160] that continually tracks changes in frequency and thus compensates for variations in the contact frequency as the tip scans across the surface. To achieve this, two drive frequencies ($f_1$ and $f_2$) are chosen with a bandwidth of 5-10 kHz and the difference between amplitudes ($A_1$ and $A_2$) at $f_1$ and $f_2$ is used as feedback (Figure 1.23). The resonance frequency is defined as $f_c = (f_1 + f_2) / 2$ and determined by maintaining $A_1 – A_2 = 0$.

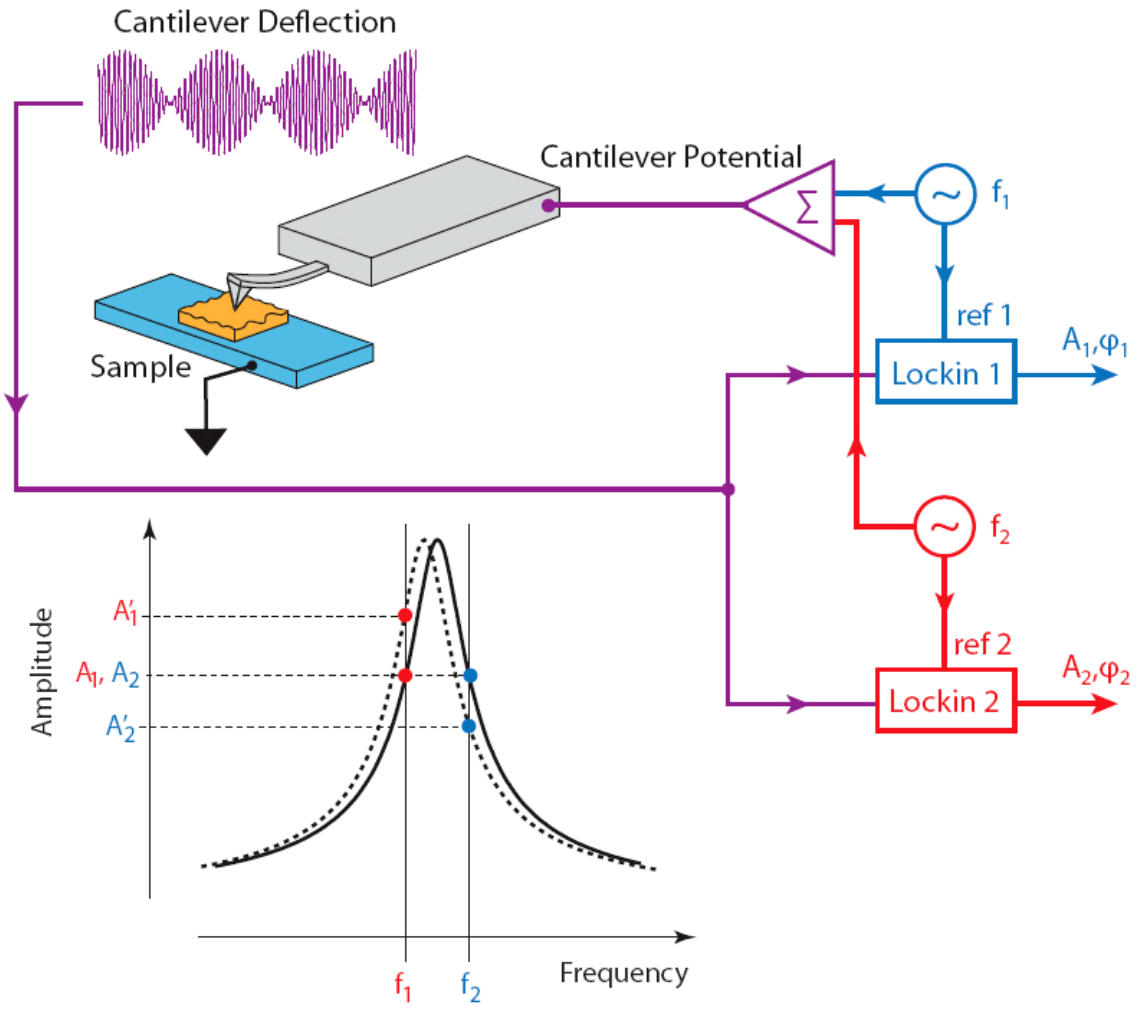


**Figure 1.23** (a) Schematic diagrams of the experimental setup. (b) Principle of the dual-frequency excitation based resonant-amplitude tracking [160].

An alternative approach to study domain dynamics in the PFM experiment is based on local spectroscopic measurements. Domain switching and electromechanical detection are performed simultaneously, yielding local electromechanical hysteresis loops. In this method, the response is measured simultaneously with the application of the DC electric field. Correspondingly, the measured PFM signal contains significant electrostatic (non-hysteretic) contribution to the signal. To solve this problem, a technique to measure remanent loops is reported by Guo *et al.* [161]. In this case, the response is determined after the DC bias is

turned off, minimizing the electrostatic contribution and associated noise to the signal. However, domain relaxation is still possible after the DC bias is turned off.

Recently, PFM spectroscopy has been extended to an imaging mode for fast (30–100 ms) hysteresis loop measurements developed by Jesse *et al.* [162]. In the PFM switching spectroscopy (SS-PFM), hysteresis loops are acquired at each point of the image and analysed to yield 2D maps (Figure 1.24a). The tip approaches the surface vertically in contact mode until the deflection set point is achieved and the signals are acquired at frequencies corresponding to the contact resonances of the cantilever. Figure 1.24b gives the waveform used to trigger the cantilever. The graph is enlarged to show that in each step, a small AC voltage is superimposed on a DC bias switched "on" and "off" for time intervals of $\tau_1$ and $\tau_2$. When DC bias is switched "on", both piezoelectricity and electrostatic force contribute to sample deformation. In contrast, when DC bias is switched "off", charge accumulation is avoided and thus only piezoelectricity induces sample deformation, allowing extracting the real piezoelectricity. As shown in Figure 1.24c, the amplitude butterfly curve and phase hysteresis loop can be achieved on PE materials such as a PVDF thin film using the SS-PFM measurement [163].

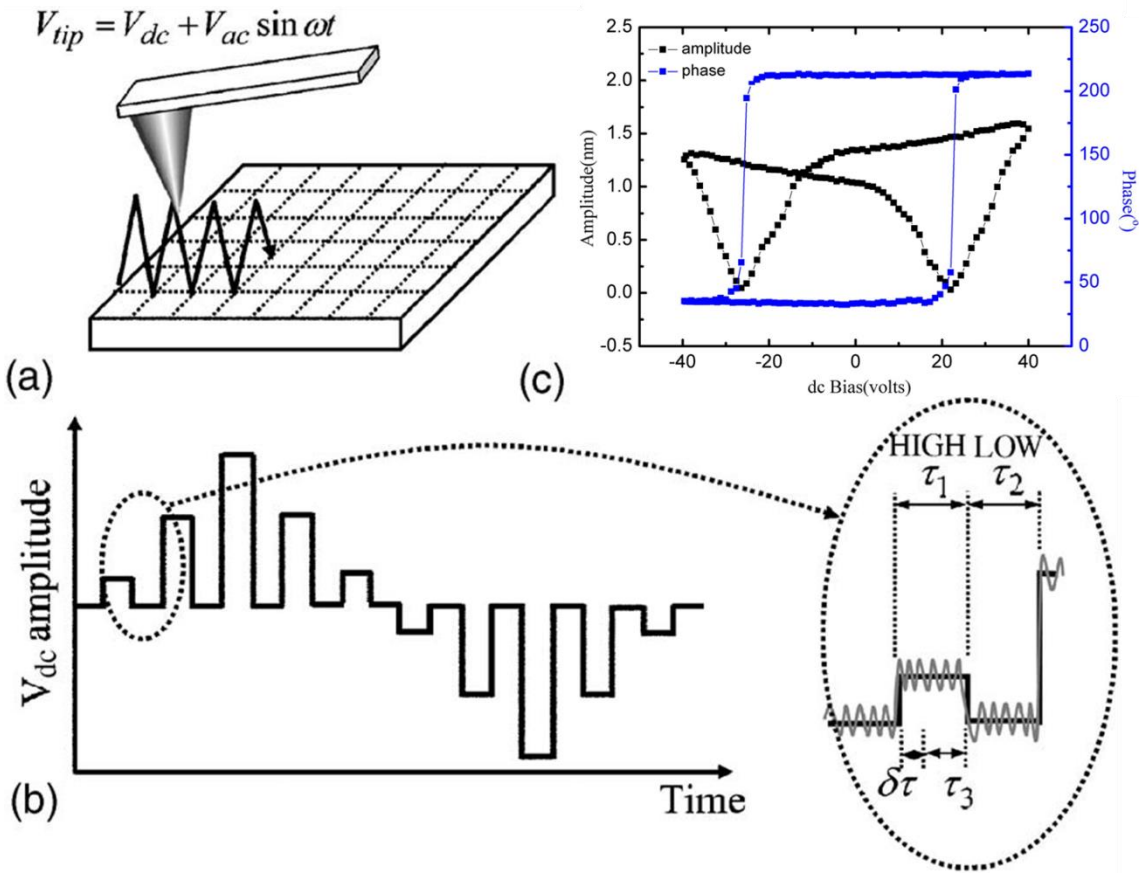


**Figure 1.24** (a) In SS-PFM, local hysteresis loop is collected at each point on N × M mesh. (b) The single-point probing wave form in SS-PFM and data acquisition sequence [162]. (c) Amplitude butterfly curve and phase hysteresis loop of a thin PVDF film [163].

Along with the sequential polarization switching performed with a series of voltage pulses applied to the tip followed by consequent imaging, PFM can be used in a spectroscopy mode when the measurements are done on a fixed tip position (local $d_{33}$ acquisition) under a DC voltage swept in the cyclic manner. It is worth noting that experimental conditions, such as driving voltage, frequency, loading force, cantilever force constant, tip apex radius, ambient environment, as well as physical properties of the samples (thickness, dielectric constants, orientation, defect structure, crystallinity and electrode material) should be taken into account to avoid misinterpretation of the PFM results due to its extremely high sensitivity [164].

### 1.4.3 ME Measurement at the Nanoscale by PFM/VFM

PFM provides insight into nanoscale PE properties with high resolution and has found new application in measuring the ME effect locally by simultaneously applying a magnetic field during the PFM measurement. With the application of a magnetic field, the nanoscale ME effect has been confirmed in various ceramic composite structures such as (1-1) [75, 77], (2-2) [76] and (0-3) [165] type connectivity. For example, ME coupling of $CoFe_2O_4$-PZT [74] and $CoFe_2O_4$-$BaFeO_3$ [77] core–shell nanofibers has been demonstrated by PFM via quantifying the PE response of the composites in the presence of a magnetic field. Changes in the PFM amplitude and phase signals have been observed in nanofibers with an applied magnetic field of 2000 Oe but not in those without a magnetic field. A systematic PFM study of ceramic $PbTiO_3$ (PTO)-$Ni_{0.66}Fe_{2.34}O_4$ (NFO) and PTO-$BaFe_{12}O_{19}$ bilayered structures has been conducted by Caruntu *et al.* [166] showing a magnetic field-dependence of the $d_{33}$ coefficients in the range of 0 to 2000 Oe and 0 to 1500 Oe. Figure 1.25 shows the PFM amplitude dependence of the magnetic field in the ceramic PTO-NFO sample. With the field increasing from 0 to 1500 Oe, the PE response increases from 219 to 250, 288, 307, 385 and 454 pm, indicating that the PE coefficient is magnetic field dependent. Based on the theoretical model proposed by Vopsaroiu *et al.* [167], it is expected that $d_{33}$ is positively and linearly correlated to the magnetic field if the magnetic phase in ME materials possess a negative magnetostriction coefficient. This explains the increasing PE response with an increase in the magnetic field observed by PFM. To date, the only work on polymer-based ME nanofibers is recently done by Martins *et al.* [150] and confirms a linear change in the PE response of PVDF/$CoFe_2O_4$ nanofibers using PFM in the presence of 1000 Oe magnetic field. Despite these observations, the MS mechanism (i.e. of the nanoparticles) acting on the PE response of the nanofiber composites has not been fully explored. In addition, the tip-sample interactions and variations at the nanoscale properties, particularly for PFM measurements on

polymer-based ME composite nanofibers has yet to be studied in detail. PFM will continue to be a particularly useful technique to study ME effects at the nanoscale and future work to shed light on the ME properties of nanostructures and nanocomposites (e.g. nanoparticles) for *in vivo* applications will be important.

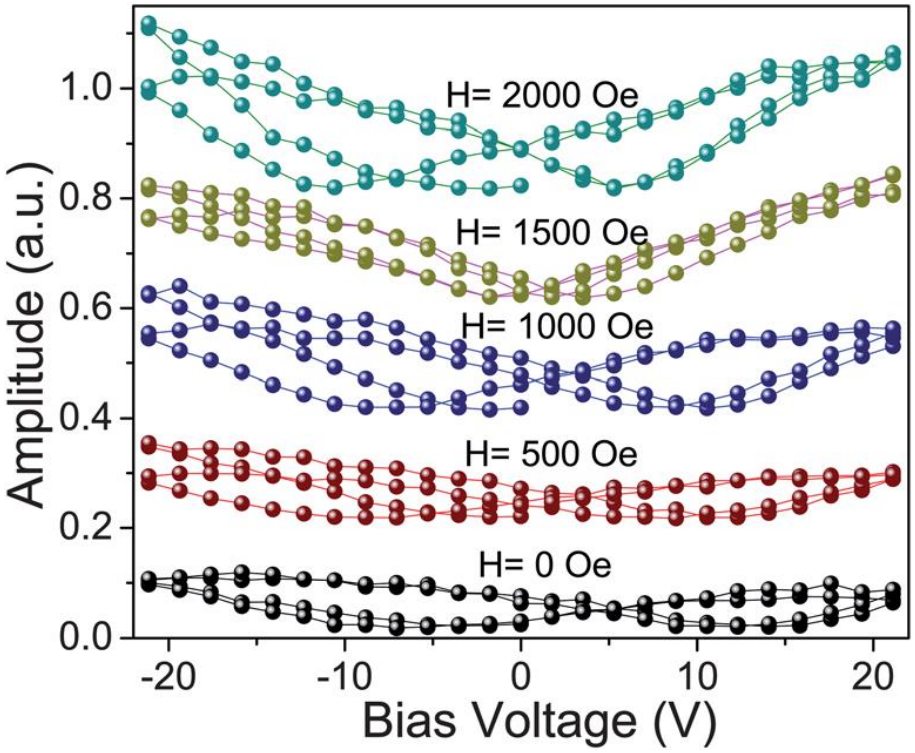


**Figure 1.25** PFM amplitude curves of the PE response of the PTO-NFO bilayered structure collected in DART mode under different magnetic fields. The plots have been translated vertically to increase their visibility [166].

In this thesis, the nanoscale ME measurement is conducted by PFM with a magnetic field applied by Variable Force Module (VFM). Figure 1.26a illustrates the nanoscale ME measurement using PFM/VFM. A DC bias (2.5 V) is generated from the AFM controller and

amplified by ten times through a current amplifier before it is used to stimulate PFM tip in the SS-PFM measurement. At the same time, a small AC voltage (ranging from 200 to 600 mV) is applied to the tip according to the interaction between the tip and sample. A pair of pole pieces is mounted on the sample stage to apply adjustable magnetic fields (ranging from -4000 Oe to 4000 Oe) during the measurement. The photo of a sample on the VFM stage is shown in Figure 1.26b. ME composite nanofibers are directly electrospun on a gold-coated cover slip, which is then mounted on the VFM stage by tiny claps. The variable in-plane magnetic field is applied by a couple of pole pieces and monitored by the magnetic sensor right underneath the sample.

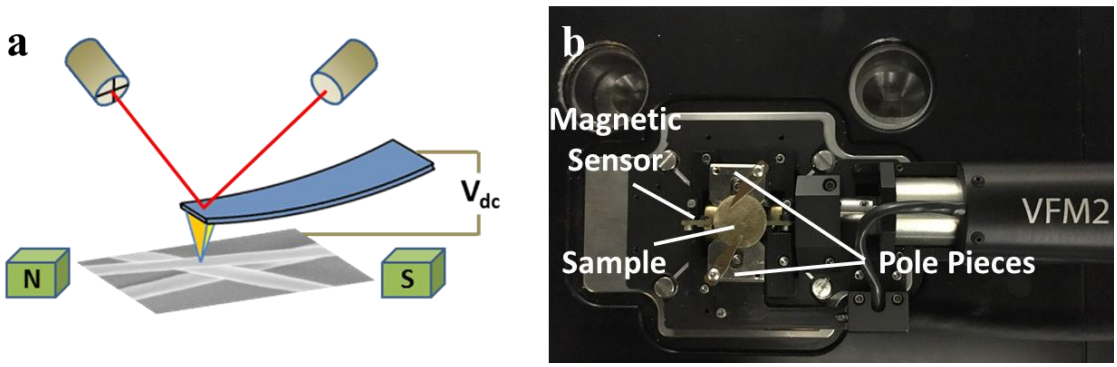


**Figure 1.26** (a) Schematic of nanoscale ME measurement by PFM/VFM [168] and (b) photo of a sample on the VFM stage. Sample, magnetic sensor and pole pieces are indicated by white lines.

## 1.5 Biomedical Applications of ME Materials

Biological tissues such as bone are known to have a close relationship with piezoelectricity [169]. Mechanical energy generated in bone can produce electrical potentials of sufficient magnitude to exert a wide range of effects in living systems such as control of cell nutrition, local pH, enzyme activation or suppression, and specialized functions of cells [169]. Other than bone, a variety of biological materials are demonstrated as PE materials such as collagen [170], polysaccharides [171] and DNA [172]. Given the abundant existence of piezoelectricity in biological systems, early researches mainly focus on exploring the application of PE polymers and more recently ME materials are presenting exciting possibilities in this research area. Here, initial studies were presented demonstrating the biocompatibility and concept of using PE polymers, which are effectively precursors to ME polymer composites. Following this, the demonstrated applications using ME materials are highlighted, in particular the use of nanoparticles for electrical stimulation of biological tissues.

### 1.5.1 Cell Interactions with PE Polymers

Semicrystalline polymers such as PVDF [173], P(VDF-TrFE) [174], PLA [175], and polyamides [176] exhibit excellent piezoelectricity and can be employed in polymer-based ME materials. PVDF can be prepared in the form of films [177], fibers [178] or porous structures [179], allowing the production of materials with a customized micro- or nano-structure for biomedical applications. Previous studies have demonstrated the biocompatibility of PVDF substrates and their interactions with proteins and living cells [31, 180, 181]. The attachment and metabolic activity of murine fibroblasts (L929) cells *in vitro*

on PVDF films shows that α-phase PVDF supports higher cell metabolic activity and cell spreading than β-phase PVDF [182]. However, in another study, β-phase PVDF films show enhanced fibronectin adsorption, supporting more uniform spreading of L929 cells, compared to the α-phase PVDF [183]. Further studies are required to understand these different cell behaviours (e.g. growth and differentiation) and their relationship to interactions of extracellular matrix proteins, which are influenced by the crystalline state of the polymers.

PLA, with a PE constant of 10 pC $N^{-1}$, has been widely established as a bio-friendly material as it promotes bone growth, neural recovery and regeneration [184]. Due to its biocompatibility and biodegradability, PLA has been explored in tissue engineering and other biofunctional devices [184-186]. Despite having PE properties, PLA as yet has not been directly applied for electrical stimulation of cells. However, its composites with other electroactive materials, such as polypyrrole [187] and carbon nanotubes [188], have been used as scaffolding materials for electrical stimulation of cells.

PE polymers have been used for electrical stimulation of cells, namely to promote their growth via mechanically-driven stimulation. Rodrigues *et al.* has described enhanced proliferation and phosphatase alkaline activity of goat bone marrow cells cultured on β-phase PVDF membranes, especially when subjected to agitation, suggesting an effect from the PE property of the material [32]. MC3T3-E1 preosteoblasts subjected to mechanical perturbations can be stimulated by variations in charge density of the PVDF surface to affect cell adhesion, viability and proliferation in an *in vitro* environment. For example, the positive charge of β-phase PVDF has been shown to promote adhesion and proliferation of MC3T3-E1 preosteoblasts (Figure 1.27A-D). With the application of a vibration module (frequency = 1 Hz, amplitude = 1 mm) vertical to the cell culture plates, the poled PVDF film performs

better compared to the non-poled film, indicating that the surface charge under mechanical stimulation improves the growth of osteoblasts [33].

Within a medical implant, PE materials also have the potential to replace cochlear hair cells by mimicking the function of the cochlear sensory epithelium, which converts sound into electrical signals [189]. A PE PVDF membrane is able to induce auditory brainstem responses from sound stimuli in deafened guinea pigs. Sound stimuli can induce the vibration of P(VDF-TrFE) membrane and the output voltage is generated by PE membranes through the application of sound to the middle ear ossicle [190]. These findings establish the fundamental principles for the development of hearing devices based on PE polymers.

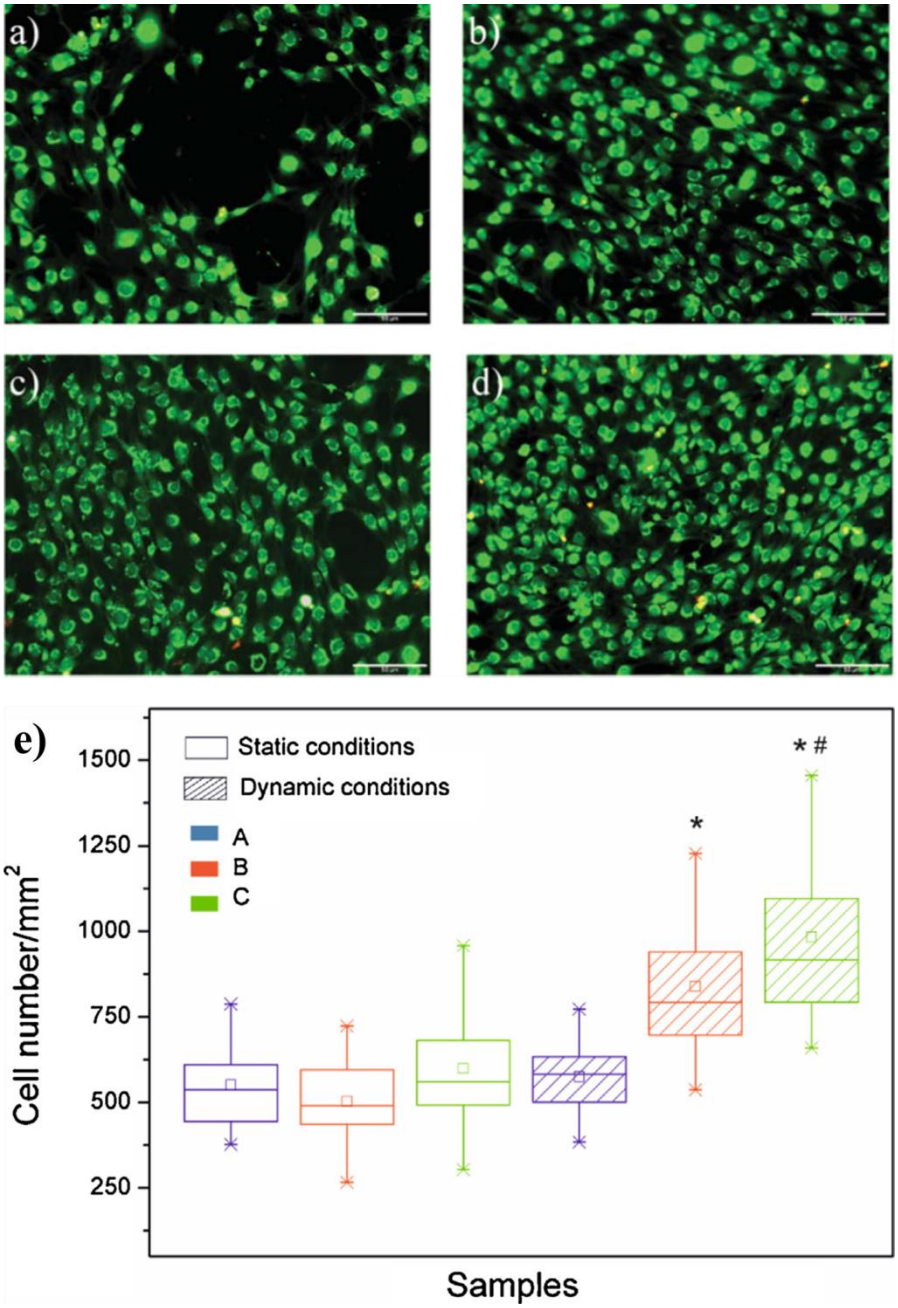


**Figure 1.27** (A-D) LIVE/DEAD staining of MC3T3-E1 preosteoblasts cultured on (A) non-poled PVDF and (B) non-poled PVDF with titanium; (C) poled PVDF and (D) poled PVDF with titanium after cell culture for 3 days. The scale bar is 50 mm for all the images [33]. (E) MC3T3-E1 osteoblast cell density (cell $mm^{-2}$) on the non-poled P(VDF-TrFE) (blue, A), non-poled P(VDF-TrFE)/Terfenol-D (red, B) and poled P(VDF-TrFE)/Terfenol-D) (green, C) under static and dynamic conditions for 72 h [191].

### 1.5.2 Stimulating Cells Using Polymer-based ME Materials

Specific to polymer-based ME composites, Ribeiro *et al.* [191] implements ME stimulation of MC3T3-E1 preosteoblast cells using P(VDF-TrFE)/Terfenol-D composites. These ME composites are able to provide both mechanical and electrical stimuli and can be remotely triggered by an applied magnetic field. Figure 1.27E shows that the highest cell density value is detected on poled P(VDF-TrFE)/Terfenol-D scaffolds under dynamic conditions whereas in static conditions the density of cells is much lower. Under dynamic conditions, both the poled and non-poled P(VDF-TrFE)/Terfenol-D scaffolds show the highest cell densities compared to non-poled ME composites or only P(VDF-TrFE). A reasonable explanation is that the composite scaffolds show preferential areas of cell growth due to local interactions between cells and the mechanical/electrical stimulus (located preferentially close to the magnetic particles). Cell proliferation is increased by up to ≈ 25% when cultured under mechanical (up to 110 ppm) and electrical stimulation (up to 0.115 mV), indicating ME cell stimulation is a novel and feasible approach for cell culture and tissue engineering applications.

### 1.5.3 ME Nanoparticles for Electrical Stimulation of Biological Tissues

Theoretically, the potential generated by micro or nanoparticles depends on the particle size. Nanoparticles as small as 50 nm with ME voltage coefficient of 5 V $cm^{-1}$ $Oe^{-1}$ can generate a voltage of 25 mV when exposed to the field of 100 Oe (or 0.01 T). By increasing the size of the particles to 1 micrometer (which is still a small fraction of the cell size), the output voltage can be much higher by two orders of magnitude, which can be utilized to trigger action potential in nerves [192]. Voltages of at least ~ 15-30 mV are needed to trigger an

action potential and signaling in neurons by driving the cell membrane resting potential (- 65 mV) above its threshold value. Exogenous, electrical signals, as low as 5-10 mV $mm^{-1}$, are also important, particularly in tissue development and regeneration. These processes provide a critical benchmark for determining the voltage ranges that must be delivered by the ME composites in order to electrically stimulate living cells. While the voltages produced by ME composites are small in comparison to those of conventional electrodes, they are ideal for electrical stimulation in the form of nanoparticles and colloids. The ability of nanoparticles to bind cell membranes, or specifically target and dock onto cell surface proteins, means that their close proximity only necessitates the use of small voltages to deliver highly localized electrical stimulation. This provides unprecedented capabilities for targeting of individual molecules, cells or a select group of cells, rather than whole tissues or organs, to enable precise control of neural function using voltages on the order of millivolts. The nanoparticles can be directed to a specific location, either through chemical functionalization of their surface or use of magnetic field gradients to guide them. A visual perspective of this is conveyed in the earlier Figure 1.1 by showing an array of interacting nanoparticle electrodes in 3D space.

Motivated by the advances in multiferroics, ceramic ME nanocomposites have been explored for biomedical applications such as wireless endoscopy, minimally invasive surgical tools [193], and stimulation of functions of living cells [192]. The potential use of ME nanoparticles (MENs) as carriers for on-demand drug release and to artificially stimulate the neural activity deep in the brain has also been suggested [194, 195]. A breakthrough has been made in targeted anticancer drug delivery where controlled release with $CoFe_2O_4$@$BaTiO_3$ nanoparticles is demonstrated in mice tumor [142]. Paclitaxel (PTX)-loaded MENs have been administrated into the circulatory system through an *in vivo* injection. With the application of a specific DC magnetic field, the particles are able to accumulate in the tumor region (Figure

1.28A), and internalized by cancer cells (Figure 1.28B). As an AC magnetic field (100 Hz, 50 Oe) is turned on, PTX can be released in targeted cells with retained anticancer activity.

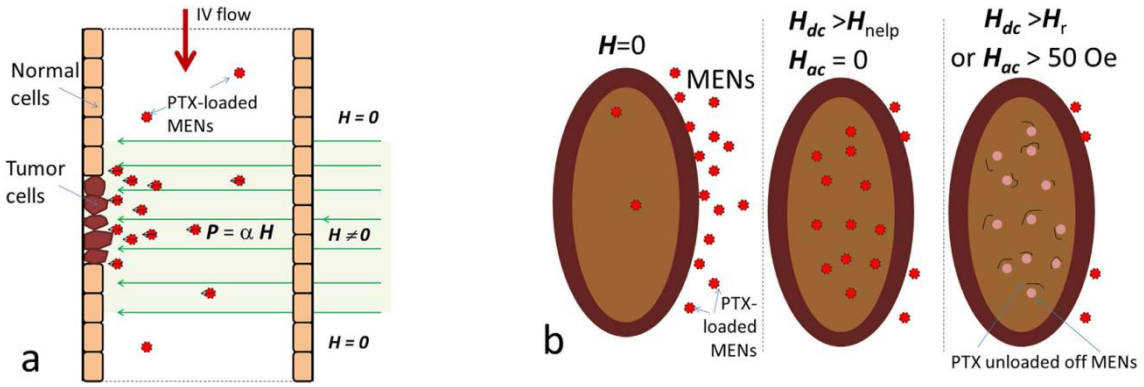


**Figure 1.28** Illustration of a field-controlled targeted drug (PTX) delivery by MENs through a capillary [142].

Very recently, $CoFe_2O_4$-$BaTiO_3$ 30-nm MENs (Figure 1.29A) have been intravenously administration into the tail vein of mice, followed by their forced movement across the blood-brain barrier (BBB) and into the brain by applying a DC field gradient of 3000 Oe $m^{-1}$ [143]. A surgically attached two channel electroencephalography (EEG) headmount is then able to directly measure the modulation of neural brain tissue activity induced by ME stimulation via the nanoparticles (Figure 1.29B). Low AC magnetic fields of 100 Oe with frequencies ranging from 0-20 Hz are applied, with the modulated signals reaching the strength comparable to that of the regular neural activity. This work is of significance, as it opens a pathway to use multifunctional nanoparticles to control intrinsic fields deep in the brain, and the concept is further described in Figure 1.28C. Firstly, MENs are forced into the brain across BBB via application of a DC magnetic field. Secondly, MENs are being distributed

over the entire brain or in selected regions via application of spatially varying DC magnetic field gradients in the brain. The presence of MENs effectively creates a "new brain microenvironment", in which the intrinsic electric signals due to the neural activity are strongly coupled at the subneuronal level to the external magnetic fields generated by remote sources. Finally, such coupling can be used for non-invasive high-efficacy stimulation of selected regions deep in the brain via application of focused and relatively low (~ 100 Oe) near DC (<1000 Hz) magnetic field.

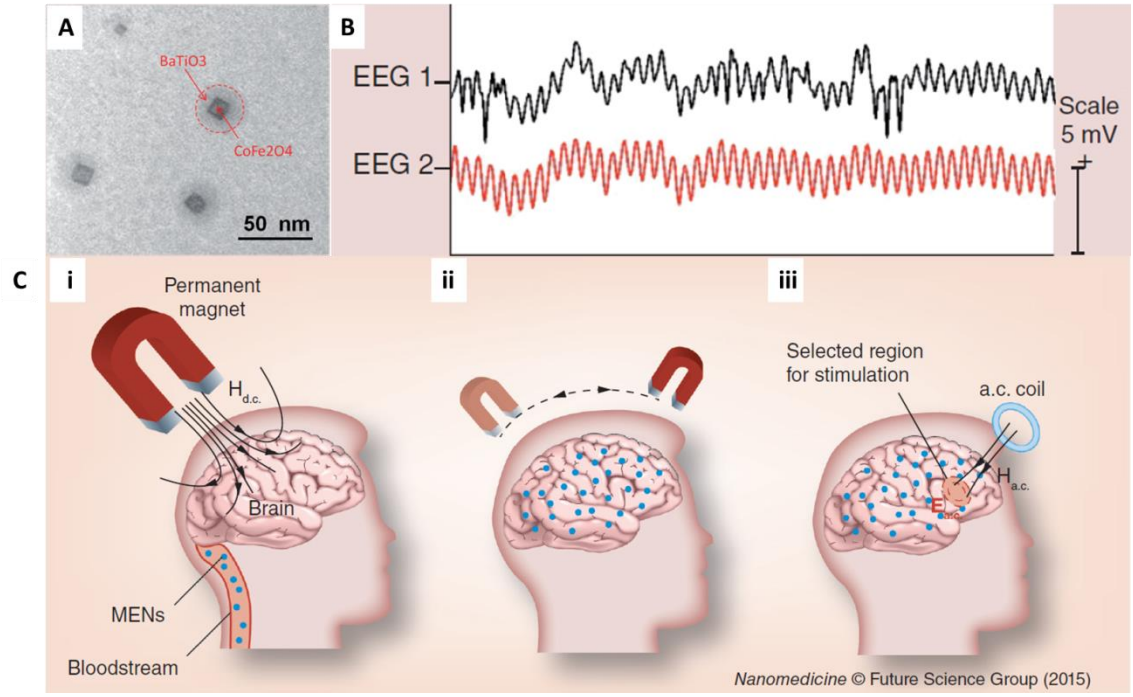


**Figure 1.29** (A) TEM image of core-shell MENs. (B) EEG waveforms from the two EEG channels with MENs in the brain under exposure to an external 100 Oe AC magnetic field at a frequency of 10 Hz. The vertical scale bar for the waveform signal is 5 mV. (C) Schematic illustration of the novel concept to use MENs for "mapping" the brain for non-invasive electric field stimulation of selected regions deep in the brain [143].

## 1.6 References


1. Wallace, G.G., et al., *Organic bionics*. 2012: John Wiley & Sons.
2. Weiland, J.D., et al., *In vitro electrical properties for iridium oxide versus titanium nitride stimulating electrodes.* IEEE Transactions on Biomedical Engineering, 2002. **49**(12): p. 1574-1579.
3. Geddes, L., et al., *Criteria for the selection of materials for implanted electrodes.* Annals of Biomedical Engineering, 2003. **31**(7): p. 879-890.
4. Merrill, D.R., et al., *Electrical stimulation of excitable tissue: design of efficacious and safe protocols.* Journal of Neuroscience Methods, 2005. **141**(2): p. 171-198.
5. Polikov, V.S., et al., *Response of brain tissue to chronically implanted neural electrodes.* Journal of Neuroscience Methods, 2005. **148**(1): p. 1-18.
6. Green, R.A., et al., *Conducting polymers for neural interfaces: challenges in developing an effective long-term implant.* Biomaterials, 2008. **29**(24): p. 3393-3399.
7. Wallace, G.G., et al., *Conducting polymers: a bridge across the bionic interface.* Australian Institute for Innovative Materials-Papers, 2007.
8. Hassler, C., et al., *Polymers for neural implants.* Journal of Polymer Science Part B: Polymer Physics, 2011. **49**(1): p. 18-33.
9. Balint, M.L.A., et al., *Conductive polymers: towards a smart biomaterial for tissue engineering.* Acta Biomaterialia, 2014. **10**(6): p. 2341-2353.
10. Gilmore, K.J., et al., *Skeletal muscle cell proliferation and differentiation on polypyrrole substrates doped with extracellular matrix components.* Biomaterials, 2009. **30**(29): p. 5292-5304.
11. Liu, X., et al., *Electrical stimulation promotes nerve cell differentiation on Polypyrrole/Poly (2-methoxy-5 aniline sulfonic acid) composites.* Journal of Neural Engineering, 2009. **6**(6): p. 065002.
12. Thompson, B.C., et al., *Conducting polymers, dual neurotrophins and pulsed electrical stimulation - dramatic effects on neurite outgrowth.* Journal of Controlled Release, 2010. **141**(2): p. 161-167.

13. Ludwig, K.A., et al., *Chronic neural recordings using silicon microelectrode arrays electrochemically deposited with a Poly(3,4-ethylenedioxythiophene) (PEDOT) film.* Journal of Neural Engineering, 2006. **3**(1): p. 59-70.

14. Khodagholy, D., et al., *Highly conformable conducting polymer electrodes for in vivo recordings.* Advanced Materials, 2011. **23**(36): p. H268-H272.

15. Cogan, S.F., *Neural stimulation and recording electrodes.* Annual Review of Biomedical Engineering, 2008. **10**: p. 275-309.

16. Guimard, N.K., et al., *Conducting polymers in biomedical engineering.* Progress in Polymer Science, 2007. **32**(8-9): p. 876-921.

17. Cui, X.Y., et al., *Surface modification of neural recording electrodes with conducting polymer/biomolecule blends.* Journal of Biomedical Materials Research, 2001. **56**(2): p. 261-272.

18. Ateh, D.D., et al., *Polypyrrole-based conducting polymers and interactions with biological tissues.* Journal of the Royal Society Interface, 2006. **3**(11): p. 741-752.

19. Schmidt, C.E., et al., *Stimulation of neurite outgrowth using an electrically conducting polymer.* Proceedings of the National Academy of Sciences, 1997. **94**(17): p. 8948-8953.

20. Svennersten, K., et al., *Mechanical stimulation of epithelial cells using polypyrrole microactuators.* Lab on a Chip, 2011. **11**(19): p. 3287-3293.

21. Martins, P., et al., *Polymer-based magnetoelectric materials.* Advanced Functional Materials, 2013. **23**(27): p. 3371-3385.

22. Kharat, D.K., et al., *Polymeric piezoelectric transducers for hydrophone applications.* Defence Science Journal, 2007. **57**(1): p. 7-22.

23. Lu, Y., et al., *Fabrication of broadband poly(vinylidene difluoride-trifluroethylene) line-focus ultrasonic transducers for surface acoustic wave measurements of anisotropy of a (100) silicon wafer.* Ultrasonics, 2014. **54**(1): p. 296-304.

24. Chang, J., et al., *Piezoelectric nanofibers for energy scavenging applications.* Nano Energy, 2012. **1**(3): p. 356-371.

25. Lee, Y.S., et al., *Neurite extension of primary neurons on electrospun piezoelectric scaffolds.* Acta Biomaterialia, 2011. **7**(11): p. 3877-3886.

26. Lee, Y.S., et al., *The influence of piezoelectric scaffolds on neural differentiation of human neural stem/progenitor cells.* Tissue Engineering Part A, 2012. **18**(19-20): p. 2063-2072.

27. Ribeiro, C., et al., *Piezoelectric polymers as biomaterials for tissue engineering applications.* Colloids and Surfaces B: Biointerfaces, 2015. **136**: p. 46-55.

28. Ikada, Y., et al., *Enhancement of bone formation by drawn poly(L-lactide).* Journal of Biomedical Materials Research, 1996. **30**(4): p. 553-558.

29. Prabhakaran, M.P., et al., *Electrospun nanostructured scaffolds for bone tissue engineering.* Acta Biomaterialia, 2009. **5**(8): p. 2884-2893.

30. Damaraju, S.M., et al., *Structural changes in PVDF fibers due to electrospinning and its effect on biological function.* Biomedical Materials, 2013. **8**(4): p. 045007.

31. Royo-Gascon, N., et al., *Piezoelectric substrates promote neurite growth in rat spinal cord neurons.* Annals of Biomedical Engineering, 2013. **41**(1): p. 112-122.

32. Rodrigues, M.T., et al., *β-PVDF membranes induce cellular proliferation and differentiation in static and dynamic conditions.* Materials Science Forum, 2008. **587-588**: p. 72-76.

33. Ribeiro, C., et al., *Enhanced proliferation of pre-osteoblastic cells by dynamic piezoelectric stimulation.* RSC Advances, 2012. **2**(30): p. 11504-11509.

34. Jin, G., et al., *Tissue engineering bioreactor systems for applying physical and electrical stimulations to cells.* Journal of Biomedical Materials Research Part B-Applied Biomaterials, 2015. **103**(4): p. 935-948.

35. Park, S., et al., *Nanoporous Pt microelectrode for neural stimulation and recording: in vitro characterization.* The Journal of Physical Chemistry C, 2010. **114**(19): p. 8721-8726.

36. Li, M., et al., *Nanostructured porous platinum electrodes for the development of low-cost fully implantable cortical electrical stimulator.* Sensors and Actuators B: Chemical, 2015. **221**: p. 179-186.

37. Barrese, J.C., et al., *Scanning electron microscopy of chronically implanted intracortical microelectrode arrays in non-human primates.* Journal of Neural Engineering, 2016. **13**(2): p. 026003.

38. Mei, N., et al., *The composition of the vagus nerve of the cat.* Cell and Tissue Research, 1980. **209**(3): p. 423-431.

39. Zheng, T., et al. *Magnetoelectric composites for bionics applications.* Magnetoelectric Polymer-Based Composites: Fundamentals and Applications, 2017: p. 171-195.

40. Ma, J., et al., *Recent progress in multiferroic magnetoelectric composites: from bulk to thin films.* Advaced Materials, 2011. **23**(9): p. 1062-1087.

41. Spaldin, N.A., et al., *The renaissance of magnetoelectric multiferroics.* Science, 2005. **309**(5733): p. 391-392.

42. Dzyaloshinskii, I., *On the magneto-electrical effect in antiferromagnets.* Soviet Physics JETP-Ussr, 1960. **10**(3): p. 628-629.

43. Astrov, D., *Magnetoelectric effect in antiferromagnetic $Cr_2O_3$.* Soviet Physics JETP, 1961. **13**(2).

44. Ascher, E., et al., *Some properties of ferromagnetoelectric Nickel-Iodine Boracite $Ni_3B_7O_{13}I$.* Journal of Applied Physics, 1966. **37**(3): p. 1404-1405.

45. Astrov, D., et al., *Spontaneous magnetoelectric effect.* Soviet Journal of Experimental and Theoretical Physics, 1969. **28**: p. 1123.

46. Catalan, G., et al., *Physics and applications of bismuth ferrite.* Advanced Materials, 2009. **21**(24): p. 2463-2485.

47. Fiebig, M., *Revival of the magnetoelectric effect.* Journal of Physics D: Applied Physics, 2005. **38**(8): p. R123-R152.

48. Eerenstein, W., et al., *Multiferroic and magnetoelectric materials.* Nature, 2006. **442**(7104): p. 759-765.

49. Srinivasan, G., *Magnetoelectric composites.* Annual Review of Materials Research, 2010. **40**(1): p. 153-178.

50. Van Suchtelen, J., *Product properties: a new application of composite materials.* Philips Research Reports, 1972. **27**(1): p. 28-37.

51. Joule, J., *On a new class of magnetic forces.* Ann. Electr. Magn. Chem, 1842. **8**(1842): p. 219-224.

52. Olabi, A.G., et al., *Design and application of magnetostrictive materials.* Materials & Design, 2008. **29**(2): p. 469-483.

53. Curie, J., et al., *Development by pressure of polar electricity in hemihedral crystals with inclined faces.* Bull. soc. min. de France, 1880. **3**: p. 90.

54. Panda, P.K., *Review: environmental friendly lead-free piezoelectric materials.* Journal of Materials Science, 2009. **44**(19): p. 5049-5062.

55. Ramadan, K.S., et al., *A review of piezoelectric polymers as functional materials for electromechanical transducers.* Smart Materials and Structures, 2014. **23**(3): p. 033001.

56. Erhart, J., *Experiments to demonstrate piezoelectric and pyroelectric effects.* Physics Education, 2013. **48**(4): p. 438.

57. Wang, Y., et al., *Multiferroic magnetoelectric composite nanostructures.* NPG Asia Materials, 2010. **2**(2): p. 61-68.

58. Park, C.S., et al., *Quantitative understanding of the elastic coupling in magnetoelectric laminate composites through the nonlinear polarization–magnetic (P–H) response.* Smart Materials and Structures, 2011. **20**(8): p. 082001.

59. Dong, S., et al., *Longitudinal and transverse magnetoelectric voltage coefficients of magnetostrictive/piezoelectric laminate composite: Theory.* IEEE Transactions on Ultrasonics, Ferroelectrics, and Frequency Control, 2003. **50**(10): p. 1253-1261.

60. Dong, S., et al., *Longitudinal and transverse magnetoelectric voltage coefficients of magnetostrictive/piezoelectric laminate composite: Experiments.* IEEE Transactions on Ultrasonics, Ferroelectrics, and Frequency Control, 2004. **51**(7): p. 794-799.

61. Singh, R.S., et al., *Dielectric and magnetoelectric properties of $Bi_5FeTi_3O_{15}$.* Solid State Communications, 1994. **91**(7): p. 567-569.

62. Rivera, J.P., *On definitions, units, measurements, tensor forms of the linear magnetoelectric effect and on a new dynamic method applied to Cr-Cl boracite.* Ferroelectrics, 1994. **161**(1): p. 165-180.

63. Kumar, M.M., et al., *An experimental setup for dynamic measurement of magnetoelectric effect.* Bulletin of Materials Science, 1998. **21**(3): p. 251-255.

64. Duong, G.V., et al., *The lock-in technique for studying magnetoelectric effect.* Journal of Magnetism and Magnetic Materials, 2007. **316**(2): p. 390-393.

65. Braun, D., et al., *Computer-based photon-counting lock-in for phase detection at the shot-noise limit.* Optics Letters, 2002. **27**(16): p. 1418-1420.

66. Marauska, S., et al., *MEMS magnetic field sensor based on magnetoelectric composites.* Journal of Micromechanics and Microengineering, 2012. **22**(6): p. 065024.

67. Jia, Y., et al., *Giant magnetoelectric response from a piezoelectric/magnetostrictive laminated composite combined with a piezoelectric transformer.* Advanced Materials, 2008. **20**(24): p. 4776-4779.

68. Silva, M., et al., *Optimization of the magnetoelectric response of Poly(vinylidene fluoride)/Epoxy/Vitrovac laminates.* ACS Applied Materials & Interfaces, 2013. **5**(21): p. 10912-10919.

69. Martins, P., et al., *Large linear anhysteretic magnetoelectric voltage coefficients in $CoFe_2O_4$/Polyvinylidene fluoride 0-3 nanocomposites.* Journal of Nanoparticle Research, 2013. **15**(8): p. 1825.

70. Ryu, J., et al., *Magnetoelectric effect in composites of magnetostrictive and piezoelectric materials.* Journal of Electroceramics, 2002. **8**(2): p. 107-119.

71. Petrov, V.M., et al., *Magnetoelectric effects in porous ferromagnetic-piezoelectric bulk composites: Experiment and theory.* Physical Review B, 2007. **75**(17): p. 174422.

72. Mori, K., et al., *Magnetoelectric coupling in Terfenol-D/polyvinylidenedifluoride composites.* Applied Physics Letters, 2002. **81**(1): p. 100-101.

73. Nan, C.W., et al., *Multiferroic magnetoelectric composites: historical perspective, status, and future directions.* Journal of Applied Physics, 2008. **103**(3): p. 031101.

74. Scott, J., *Applications of magnetoelectrics.* Journal of Materials Chemistry, 2012. **22**(11): p. 4567-4574.

75. Xie, S., et al., *Multiferroic $CoFe_2O_4$-$Pb(Zr_{0.52}Ti_{0.48})O_3$ core-shell nanofibers and their magnetoelectric coupling.* Nanoscale, 2011. **3**(8): p. 3152-3158.

76. Khodaei, M., et al., *Nanoscale magnetoelectric coupling study in (111)-oriented PZT-Co ferrite multiferroic nanobilayer thin film using piezoresponse force microscopy: Effect of Co ferrite composition.* Sensors and Actuators a-Physical, 2016. **242**: p. 92-98.

77. Zhu, Q., et al., *Multiferroic $CoFe_2O_4$–$BiFeO_3$ core–shell nanofibers and their nanoscale magnetoelectric coupling.* Journal of Materials Research, 2014. **29**(05): p. 657-664.

78. Gorige, V., et al., *Strain mediated magnetoelectric coupling in a $NiFe_2O_4$-$BaTiO_3$ multiferroic composite.* Journal of Physics D-Applied Physics, 2016. **49**(40): p. 405001.

79. Rani, J., et al., *Structural, dielectric and magnetoelectric studies of $0.5Ba(Zr_{0.2}Ti_{0.8})O_3$-$0.5(Ba_{0.7}Ca_{0.3})TiO_3$-$Ni_{0.8}Zn_{0.2}Fe_2O_4$ multiferroic composites.* Journal of Alloys and Compounds, 2017. **696**: p. 266-275.

80. Ren, S.Q., et al., *$BaTiO_3$/$CoFe_2O_4$ particulate composites with large high frequency magnetoelectric response.* Journal of Materials Science, 2005. **40**(16): p. 4375-4378.

81. Jiang, Q., et al., *Multiferroic properties of $Bi_{0.87}La_{0.05}Tb_{0.08}FeO_3$ ceramics prepared by spark plasma sintering.* Applied Physics Letters, 2007. **91**(2): p. 022914.

82. Agrawal, S., et al., *Magnetoelectric properties of microwave sintered particulate composites.* Materials Letters, 2009. **63**(26): p. 2198-2200.

83. Israel, C., et al., *A one-cent room-temperature magnetoelectric sensor.* Nature Materials, 2008. **7**(2): p. 93-94.

84. Shi, Z., et al., *Magnetoelectric properties of multiferroic composites with pseudo-1-3-type structure.* Journal of Applied Physics, 2006. **99**(12): p. 124108.

85. Nan, C.W., et al., *Calculations of giant magnetoelectric effects in ferroic composites of rare-earth–iron alloys and ferroelectric polymers.* Physical Review B, 2001. **63**(14): p. 144415.

86. Ryu, J., et al., *Effect of the magnetostrictive layer on magnetoelectric properties in Lead Zirconate Titanate/Terfenol‐D laminate composites.* Journal of the American Ceramic Society, 2001. **84**(12): p. 2905-2908.

87. Dong, S., et al., *Enhanced magnetoelectric effects in laminate composites of Terfenol-D/Pb (Zr, Ti) $O_3$ under resonant drive.* Applied Physics Letters, 2003. **83**(23): p. 4812-4814.

88. Liebermann, H., et al., *Production of amorphous alloy ribbons and effects of apparatus parameters on ribbon dimensions.* IEEE Transactions on Magnetics, 1976. **12**(6): p. 921-923.

89. Zhai, J., et al., *Magnetoelectric laminate composites: an overview.* Journal of the American Ceramic Society, 2008. **91**(2): p. 351-358.

90. Dong, S., et al., *Tunable features of magnetoelectric transformers.* IEEE Transactions on Ultrasonics, Ferroelectrics, and Frequency Control, 2009. **56**(6).

91. Das, J., et al., *Enhancement in the field sensitivity of magnetoelectric laminate heterostructures.* Applied Physics Letters, 2009. **95**(9): p. 092501.

92. Park, C.S., et al., *Design and characterization of broadband magnetoelectric sensor.* Journal of Applied Physics, 2009. **105**(9): p. 094111.

93. Park, C.S., et al., *Dimensionally gradient magnetoelectric bimorph structure exhibiting wide frequency and magnetic dc bias operating range.* Journal of Applied Physics, 2009. **106**(11): p. 114101.

94. Greve, H., et al., *Giant magnetoelectric coefficients in $(Fe_{90}Co_{10})_{78}Si_{12}B_{10}$-AlN thin film composites.* Applied Physics Letters, 2010. **96**(18): p. 182501.

95. Nan, C.W., *Magnetoelectric effect in composites of piezoelectric and piezomagnetic phases.* Physical Review B, 1994. **50**(9): p. 6082.

96. Jiansirisomboon, S., et al., *Mechanical properties and crack growth behavior in poled ferroelectric PMN–PZT ceramics.* Current Applied Physics, 2006. **6**(3): p. 299-302.

97. Salimi, A., et al., *FTIR studies of beta-phase crystal formation in stretched PVDF films.* Polymer Testing, 2003. **22**(6): p. 699-704.

98. Ince-Gunduz, B.S., et al., *Impact of nanosilicates on poly (vinylidene fluoride) crystal polymorphism: part 2. Melt-crystallization at low supercooling.* Journal of Macromolecular Science, Part A: Pure and Applied Chemistry, 2010. **47**(12): p. 1208-1219.

99. Prest, W.M., et al., *Formation of gamma-phase from alpha-polymorphs and beta-polymorphs of polyvinylidene fluoride.* Journal of Applied Physics, 1978. **49**(10): p. 5042-5047.

100. Martins, P., et al., *Electroactive phases of Poly(vinylidene fluoride): determination, processing and applications.* Progress in Polymer Science, 2014. **39**(4): p. 683-706.

101. Mohammadi, B., et al., *Effect of tensile strain rate and elongation on crystalline structure and piezoelectric properties of PVDF thin films.* Polymer Testing, 2007. **26**(1): p. 42-50.

102. Alamusi, et al., *Evaluation of piezoelectric property of reduced graphene oxide (rGO)–poly(vinylidene fluoride) nanocomposites.* Nanoscale, 2012. **4**(22): p. 7250-7255.

103. Mahadeva, S.K., et al., *Effect of poling time and grid voltage on phase transition and piezoelectricity of Poly(vinyledene fluoride) thin films using corona poling.* Journal of Physics D: Applied Physics, 2013. **46**(28): p. 285305.

104. Ouyang, Z.W., et al., *Enhanced piezoelectric responses and crystalline arrangement of electroactive polyvinylidene fluoride/magnetite nanocomposites.* Journal of Applied Polymer Science, 2014. **131**(20): p. 40941.

105. Koga, K., et al., *Piezoelectricity and related properties of vinylidene fluoride and trifluoroethylene copolymers.* Journal of Applied Physics, 1986. **59**(6): p. 2142-2150.

106. Neese, B., et al., *Piezoelectric responses in poly(vinylidene fluoride/hexafluoropropylene) copolymers.* Applied Physics Letters, 2007. **90**(24): p. 242917.

107. Li, Z., et al., *Electromechanical properties of poly (vinylidene-fluoride-chlorotrifluoroethylene) copolymer.* Applied Physics Letters, 2006. **88**(6): p. 062904.

108. Bauer, F., et al. *Advances in relaxor ferroelectric terpolymer: new applications*. in *Applications of Ferroelectrics (ISAF/PFM), 2011 International Symposium on and 2011*

*International Symposium on Piezoresponse Force Microscopy and Nanoscale Phenomena in Polar Materials*. 2011. IEEE.

109. Guyomar, D., et al., *Magnetoelectricity in polyurethane films loaded with different magnetic particles.* Materials Letters, 2009. **63**(6): p. 611-613.

110. Malmonge, J., et al., *Piezo and dielectric properties of PHB–PZT composite.* Polymer Composites, 2009. **30**(9): p. 1333-1337.

111. Frübing, P., et al., *Relaxation processes at the glass transition in polyamide 11: From rigidity to viscoelasticity.* The Journal of Chemical Physics, 2006. **125**(21): p. 214701.

112. Kim, J.Y.H., et al., *Cantilever actuated by piezoelectric Parylene-C*. in *Micro Electro Mechanical Systems (MEMS), 2012 IEEE 25th International Conference on*. 2012. IEEE.

113. Tajitsu, Y., *Development of environmentally friendly piezoelectric polymer film actuator having multilayer structure.* Japanese Journal of Applied Physics, 2016. **55**(4): p. 04EA07.

114. Fukada, E., *Recent developments of polar piezoelectric polymers.* IEEE Transactions on Dielectrics and Electrical Insulation, 2006. **13**(5): p. 1110-1119.

115. Tajitsu, Y., *Piezoelectricity of chiral polymeric fiber and its application in biomedical engineering.* IEEE Transactions on Ultrasonics, Ferroelectrics, and Frequency Control, 2008. **55**(5).

116. Shiomi, Y., et al., *Improvement of piezoelectricity of Poly(L-lactide) film by using acrylic symmetric block copolymer as additive.* Japanese Journal of Applied Physics, 2013. **52**(9): p. 09KE02.

117. Guyomar, D., et al., *Two-phase magnetoelectric nanopowder/polyurethane composites.* Journal of Applied Physics, 2008. **104**(7): p. 074902.

118. Nan, C.W., et al., *Possible giant magnetoelectric effect of ferromagnetic rare-earth–iron-alloys-filled ferroelectric polymers.* Applied Physics Letters, 2001. **78**(17): p. 2527-2529.

119. Sencadas, V., et al., *Behaviour of the ferroelectric phase transition of P(VDF/TrFE)(75/25) with increasing deformation.* Ferroelectrics, 2004. **304**(1): p. 23-26.

120. Martins, P., et al., *Optimizing piezoelectric and magnetoelectric responses on $CoFe_2O_4$/P(VDF-TrFE) nanocomposites.* Journal of Physics D-Applied Physics, 2011. **44**(49): p. 495303.

121. Nan, C.W., et al., *Large magnetoelectric response in multiferroic polymer-based composites.* Physical Review B, 2005. **71**(1): p. 014102.

122. Zhai, J., et al., *Giant magnetoelectric effect in Metglas/Polyvinylidene-fluoride laminates.* Applied Physics Letters, 2006. **89**(8): p. 083507.

123. Jin, J., et al., *Multiferroic polymer composites with greatly enhanced magnetoelectric effect under a low magnetic bias.* Advanced Materials, 2011: p. 3853-3858.

124. Nan, C.W., et al., *A three-phase magnetoelectric composite of piezoelectric ceramics, rare-earth iron alloys, and polymer.* Applied Physics Letters, 2002. **81**(20): p. 3831-3833.

125. Pyun, J., *Nanocomposite materials from functional polymers and magnetic colloids.* Polymer Reviews, 2007. **47**(2): p. 231-263.

126. Shi, Z., et al., *Influence of mechanical boundary conditions and microstructural features on magnetoelectric behavior in a three-phase multiferroic particulate composite.* Physical Review B, 2004. **70**(13): p. 134417.

127. Fukada, E., *Vibrational study of the wood used for the sound boards of pianos.* Nature, London, 1950. **166**(4227): p. 772-773.

128. Fukada, E., et al., *Effect of temperature on piezoelectricity in wood.* Journal of Polymer Science Part C: Polymer Symposia, 1968. **23**(2): p. 509-517.

129. Maeda, H., et al., *Effect of bound water on piezoelectric, dielectric, and elastic properties of wood.* Journal of Applied Polymer Science, 1987. **33**(4): p. 1187-1198.

130. Kim, J., et al., *Discovery of cellulose as a smart material.* Macromolecules, 2006. **39**(12): p. 4202-4206.

131. Kim, J., et al., *Blocked force measurement of electro-active paper actuator by micro-balance.* Sensors and Actuators A: Physical, 2007. **133**(2): p. 401-406.

132. Jaehwan, K., et al., *Electro-active paper actuators.* Smart Materials and Structures, 2002. **11**(3): p. 355.

133. Yun, G.Y., et al., *Effect of aligned cellulose film to the performance of electro-active paper actuator.* Sensors and Actuators A: Physical, 2008. **141**(2): p. 530-535.

134. Yun, S., et al., *Alignment of cellulose chains of regenerated cellulose by corona poling and its piezoelectricity.* Journal of Applied Physics, 2008. **103**(8): p. 083301.

135. Sungryul, Y., et al., *Electrically aligned cellulose film for electro-active paper and its piezoelectricity.* Smart Materials and Structures, 2009. **18**(11): p. 117001.

136. Yang, C., et al., *Piezoelectricity of wet drawn cellulose electro-active paper.* Sensors and Actuators A: Physical, 2009. **154**(1): p. 117-122.

137. Nogi, M., et al., *Transparent nanocomposites based on cellulose produced by bacteria offer potential innovation in the electronics device industry.* Advanced Materials, 2008. **20**(10): p. 1849-1852.

138. Zhu, H., et al., *Biodegradable transparent substrates for flexible organic-light-emitting diodes.* Energy & Environmental Science, 2013. **6**(7): p. 2105-2111.

139. Zong, Y., et al., *Cellulose-based magnetoelectric composites.* Nature Communications, 2017. **8**: p. 38.

140. Hu, Z., et al., *Regular arrays of highly ordered ferroelectric polymer nanostructures for non-volatile low-voltage memories.* Nature Materials, 2009. **8**(1): p. 62-67.

141. Liu, Y., et al., *Rapid nanoimprinting and excellent piezoresponse of polymeric ferroelectric nanostructures.* ACS Nano, 2010. **4**(1): p. 83-90.

142. Rodzinski, A., et al., *Targeted and controlled anticancer drug delivery and release with magnetoelectric nanoparticles.* Scientific Reports, 2016. **6**: p. 2204.

143. Guduru, R., et al., *Magnetoelectric 'spin' on stimulating the brain.* Nanomedicine, 2015. **10**(13): p. 2051-2061.

144. Mandal, D., et al., *Origin of piezoelectricity in an electrospun poly(vinylidene fluoride-trifluoroethylene) nanofiber web-based nanogenerator and nano-pressure sensor.* Macromolecular Rapid Communications, 2011. **32**(11): p. 831-837.

145. Oh, S., et al., *Fabrication of vertically well-aligned P(VDF-TrFE) nanorod arrays.* Advanced Materials, 2012. **24**(42): p. 5708-5712.

146. Dong, Z., et al., *Electrospinning materials for energy-related applications and devices.* Journal of Power Sources, 2011. **196**(11): p. 4886-4904.

147. Lutkenhaus, J.L., et al., *Confinement effects on crystallization and Curie transitions of Poly(vinylidene fluoride-co-trifluoroethylene).* Macromolecules, 2010. **43**(8): p. 3844-3850.

148. Cauda, V., et al., *Confinement in oriented mesopores induces piezoelectric behavior of polymeric nanowires.* Chemistry of Materials, 2012. **24**(21): p. 4215-4221.

149. Cauda, V., et al., *Nanoconfinement: an effective way to enhance PVDF piezoelectric properties.* ACS Applied Materials & Interfaces, 2013. **5**(13): p. 6430-6437.

150. Goncalves, R., et al., *Magnetoelectric $CoFe_2O_4$/Polyvinylidene fluoride electrospun nanofibres.* Nanoscale, 2015. **7**(17): p. 8058-8061.

151. Goncalves, R., et al., *Development of magnetoelectric $CoFe_2O_4$/Poly(vinylidene fluoride) microspheres.* RSC Advances, 2015. **5**(45): p. 35852-35857.

152. Binnig, G., et al., *Atomic Force Microscope.* Physical Review Letters, 1986. **56**(9): p. 930-933.

153. Guthner, P., et al., *Local poling of ferroelectric polymers by Scanning Force Microscopy.* Applied Physics Letters, 1992. **61**(9): p. 1137-1139.

154. Gruverman, A., et al., *Piezoresponse force microscopy and recent advances in nanoscale studies of ferroelectrics.* Journal of Materials Science, 2006. **41**(1): p. 107-116.

155. Kalinin, S.V., et al., *Nanoscale electromechanics of ferroelectric and biological systems: a new dimension in Scanning Probe Microscopy.* Annual Review of Materials Research, 2007. **37**(1): p. 189-238.

156. Balke, N., et al., *Electromechanical imaging and spectroscopy of ferroelectric and piezoelectric materials: state of the art and prospects for the future.* Journal of the American Ceramic Society, 2009. **92**(8): p. 1629-1647.

157. Kalinin, S.V., et al., *Vector piezoresponse force microscopy.* Microscopy and Microanalysis, 2006. **12**(3): p. 206-220.

158. Soergel, E., *Piezoresponse Force Microscopy (PFM).* Journal of Physics D: Applied Physics, 2011. **44**(46): p. 464003.

159. Wang, W.B., et al., *Quantitative measurements of shear displacement using atomic force microscopy.* Applied Physics Letters, 2016. **108**(12): p. 122901.

160. Rodriguez, B.J., et al., *Dual-frequency resonance-tracking atomic force microscopy.* Nanotechnology, 2007. **18**(47): p. 475504.

161. Guo, H.Y., et al., *Study of domain stability on $(Pb_{0.76}Ca_{0.24})TiO_3$ thin films using piezoresponse microscopy.* Applied Physics Letters, 2002. **81**(4): p. 715-717.

162. Jesse, S., et al., *Switching spectroscopy piezoresponse force microscopy of ferroelectric materials.* Applied Physics Letters, 2006. **88**(6): p. 062908.

163. Miao, H., et al., *Piezoelectricity and ferroelectricity of cellular polypropylene electrets films characterized by piezoresponse force microscopy.* Journal of Applied Physics, 2014. **116**(6): p. 066820.

164. Kalinin, S.V., et al., *Imaging mechanism of piezoresponse force microscopy of ferroelectric surfaces.* Physical Review B, 2002. **65**(12): p. 125408.

165. Li, L.L., et al., *Direct observation of magnetic field induced ferroelectric domain evolution in self-assembled quasi (0-3) $BiFeO_3$-$CoFe_2O_4$ thin films.* ACS Applied Materials & Interfaces, 2016. **8**(1): p. 442-448.

166. Caruntu, G., et al., *Probing the Local strain-mediated magnetoelectric coupling in multiferroic nanocomposites by magnetic field-assisted Piezoresponse Force Microscopy.* Nanoscale, 2012. **4**(10): p. 3218-3227.

167. Vopsaroiu, M., et al., *Experimental determination of the magnetoelectric coupling coefficient via piezoelectric measurements.* Measurement Science and Technology, 2008. **19**(4): p. 045106.

168. Zheng, T., et al., *Local probing of magnetoelectric properties of PVDF/$Fe_3O_4$ electrospun nanofibers by piezoresponse force microscopy*. Nanotechnology, 2017. **28**(6): p. 065707.

169. Bassett, C.A.L., *Biologic significance of piezoelectricity.* Calcified Tissue Research, 1968. **1**(4): p. 252-272.

170. Di Lullo, G.A., et al., *Mapping the ligand-binding sites and disease-associated mutations on the most abundant protein in the human, type I collagen.* Journal of Biological Chemistry, 2002. **277**(6): p. 4223-4231.

171. Rinaudo, M., *Chitin and chitosan: properties and applications.* Progress in Polymer Science, 2006. **31**(7): p. 603-632.

172. Ando, Y., et al., *Piezoelectric properties of oriented deoxyribonucleate films.* Journal of Polymer Science: Polymer Physics Edition, 1976. **14**(1): p. 63-79.

173. Karan, S.K.,et al., *Self-powered flexible Fe-doped RGO/PVDF nanocomposite: an excellent material for a piezoelectric energy harvester.* Nanoscale, 2015. **7**(24): p. 10655-10666.

174. Hong, C.C., et al., *Enhanced piezoelectricity of nanoimprinted sub-20 nm poly(vinylidene fluoride–trifluoroethylene) copolymer nanograss.* Macromolecules, 2012. **45**(3): p. 1580-1586.

175. Lee, S.J., et al., *Piezoelectric properties of electrospun poly(l-lactic acid) nanofiber web.* Materials Letters, 2015. **148**: p. 58-62.

176. Liu, M., et al., *Synthesis of a novel aromatic-aliphatic hyperbranched polyamide and its application in piezoelectric immunosensors.* Polymer International, 2007. **56**(11): p. 1432-1439.

177. Martins, P., et al., *On the origin of the electroactive poly(vinylidene fluoride) β-phase nucleation by ferrite nanoparticles via surface electrostatic interactions.* CrystEngComm, 2012. **14**(8): p. 2807-2811.

178. Ribeiro, C., et al., *Influence of processing conditions on polymorphism and nanofiber morphology of electroactive Poly(vinylidene fluoride) electrospun membranes.* Soft Materials, 2010. **8**(3): p. 274-287.

179. California, A., et al., *Tailoring porous structure of ferroelectric poly(vinylidene fluoride-trifluoroethylene) by controlling solvent/polymer ratio and solvent evaporation rate.* European Polymer Journal, 2011. **47**(12): p. 2442-2450.

180. Ribeiro, C., et al., *Fibronectin adsorption and cell response on electroactive poly(vinylidene fluoride) films.* Biomedical Materials, 2012. **7**(3): p. 035004.

181. Guo, H.F., et al., *Piezoelectric PU/PVDF electrospun scaffolds for wound healing applications.* Colloids and Surfaces B-Biointerfaces, 2012. **96**: p. 29-36.

182. Low, Y.K., et al., *Alpha- and beta-poly(vinylidene fluoride) evoke different cellular behaviours.* Journal of Biomaterials Science, Polymer Edition, 2011. **22**(12): p. 1651-1667.

183. Low, Y.K., et al., *Beta-phase poly(vinylidene fluoride) films encouraged more homogeneous cell distribution and more significant deposition of fibronectin towards the cell-material interface compared to alpha-phase poly(vinylidene fluoride) films.* Materials Science and Engineering: C, 2014. **34**: p. 345-353.

184. Ni, P., et al., *Preparation of poly(ethylene glycol)/polylactide hybrid fibrous scaffolds for bone tissue engineering.* International Journal of Nanomedicine, 2011. **6**: p. 3065-3075.

185. Haaparanta, A.M., et al., *Preparation and characterization of collagen/PLA, chitosan/PLA, and collagen/chitosan/PLA hybrid scaffolds for cartilage tissue engineering.* Journal of Materials Science-Materials in Medicine, 2014. **25**(4): p. 1129-1136.

186. Bago, J.R., et al., *Electrospun nanofibrous scaffolds increase the efficacy of stem cell-mediated therapy of surgically resected glioblastoma.* Biomaterials, 2016. **90**: p. 116-125.

187. Xie, J.W., et al., *Conductive core-sheath nanofibers and their potential application in neural tissue engineering.* Advanced Functional Materials, 2009. **19**(14): p. 2312-2318.

188. Shao, S., et al., *Osteoblast function on electrically conductive electrospun PLA/MWCNTs nanofibers.* Biomaterials, 2011. **32**(11): p. 2821-2833.

189. Ashmore, J., *Cochlear outer hair cell motility.* Physiological Reviews, 2008. **88**(1): p. 173-210.

190. Inaoka, T., et al., *Piezoelectric materials mimic the function of the cochlear sensory epithelium.* Proceedings of the National Academy of Sciences of the United States of America, 2011. **108**(45): p. 18390-18395.

191. Ribeiro, C., et al., *Proving the suitability of magnetoelectric stimuli for tissue engineering applications.* Colloids and Surfaces B-Biointerfaces, 2016. **140**: p. 430-436.

192. Kargol, A.M., et al., *Biomedical applications of multiferroic nanoparticles.* In Advanced Magnetic Materials; Dr Malkinski, L., (Ed.) InTech: Rijeka, Croatia,, 2012: p. 89-118.

193. Paluszek, M.A., et al., *Magnetoelectric composites for medical application.* In Composite Magnetoelectrics, Srinivasan, G., Priya, S., Sun, N. X., Eds.; Woodhead Publishing: Cambridge, UK,, 2015: p. 297-327.

194. Yue, K., et al., *Magneto-electric nano-particles for non-invasive brain stimulation.* Plos One, 2012. **7**(9): p. e44040.

195. Guduru, R., et al., *Magneto-electric nanoparticles to enable field-controlled high-specificity drug delivery to eradicate ovarian cancer cells.* Scientific Reports, 2013. **3**.

# Overarching Aims

Nanoscale and nanostructured ME materials have potential to bring advantages into biomedical applications. To date, ceramics have dominated this research field, with only few studies on polymer-based ME nanocomposites emerging in recent times. Here, PVDF/$CoFe_2O_4$ electrospun nanofibers represent the first exploration into polymer-based ME nanocomposites and offer exciting possibilities in the aforementioned applications, especially bionics, yet their PE and ME properties and such properties in general at the nanoscale have not been studied. Understanding these properties is critical to fabricating structures, interfaces, films, coatings and components in ME devices with controllable and desirable properties. To address this, the thesis aims to:

**Aim 1: Investigating the properties of PE polymers at the nanoscale**

Although PE polymers have been extensively studied for their bulk PE properties, fewer studies have focused on their PE behaviour at the nanoscale level. Critically, nanoscale PE properties are a "precursor" to the ME effect and therefore aim (1) attempts to address this by employing electrospinning to produce PE nanofibers from a range of different polymers, including PVDF, P(VDF-HFP) copolymer and biodegradable PLA. The nanofibers provide a system to enable investigation of nanoscale PE properties that was specifically probed using Piezoresponse Force Microscopy (PFM).

**Aim 2: Investigating the nanoscale ME effect of polymer-based ME nanofibers**

Having investigated the nanoscale piezoelectricity of electrospun polymer nanofibers, the incorporation of magnetic nanoparticles is required for the ME properties. Aim (2) attempts to address this by employing the MS $Fe_3O_4$ and $CoFe_2O_4$ nanoparticles in the electrospinning

and investigating their effect on the PE properties of the nanofibers using PFM. Importantly, the Variable Magnetic Field Module is combined with the PFM to quantify the PE response of the nanofibers in response to applied magnetic fields, effectively elucidating their ME properties. Directly measuring the ME properties at the nanoscale on single nanofibers can provide a fundamental understanding of the ME effect and potentially give rise to information on configuring nanostructured polymer-based ME materials and their use as components in ME devices.

**Aim 3: Investigating the ability to configure ME nanocomposites as components in macroscale ME devices**

As the development of nanostructured polymer-based ME composites continues to emerge, it will be important to understand how to translate, preserve or even enhance their nanoscale ME properties within components of macroscale ME devices to enable a broader range of applications including sensing and memory devices. Aim (3) attempts to address this by developing a macroscale ME testing system based on the lock-in technique to quantify the ME output voltage from macroscale devices furnished from electrospun nanofiber sheets. In particular, different types of ME composites devices are fabricated, including laminate and nanocomposite sheets, with different electrode configurations such as top-and-bottom and interdigitated electrodes.

# 2 Local Probing of Magnetoelectric Properties of PVDF/$Fe_3O_4$ Electrospun Nanofibers by PFM/VFM

## 2.1 Introduction

### 2.1.1 ME Composites

Magnetoelectric (ME) materials have great potential in the fabrication of multifunctional devices, such as broadband magnetic sensors, multiple-state memory elements, electric field controlled ferromagnetic resonance devices, and actuators [1-4]. This is due to their ability to either undergo a dielectric polarization in response to an applied magnetic field, or induce magnetization by an external electric field [5]. The early studies on single phase ME materials (e.g. single crystal $Cr_2O_3$ [6], $DyMn_2O_5$ [7] and $TbMn_2O_5$ [8]) demonstrate limited practical applications due to small ME coupling and low operating temperatures [9]. A renaissance in the field has ensued from the discovery of ME composites.

ME composites consist of two separate piezoelectric (PE) and magnetostrictive (MS) phases, with their ME effect regarded as a "product" property mediated by strain coupling. Strain coupling induced ME effects have given rise to extraordinary ME properties, particularly in the polymer-based composites that combine the PE poly (vinylidene fluoride) (PVDF) with ME materials such as Terfernol-D [10] or Metglas [11]. This has led to the generation of ME coefficients of up to 370 V $cm^{-1}$ $Oe^{-1}$ [11] under an externally applied magnetic field, thus making these ME composites promising candidates for a wide range of device applications [4, 12, 13].

### 2.1.2 Piezoelectricity of PVDF

PVDF is a well-established biocompatible material and has been widely used in tissue engineering due to its flexibility and facile processing techniques [14, 15]. Given these advantages, the exploration of PVDF-based ME composites will shed light on new applications for functional biomaterials. Among all the crystalline phases of PVDF, β-phase (all-trans planar zigzag) possesses the highest PE coefficient, in which chains of all-trans conformation pack with dipoles parallel to a common axis in a pseudo-hexagonal configuration. To promote the formation of β-phase while processing, electrospinning is extensively employed [16-18]. In this case, a PVDF solution is subject to both electrical poling and uniaxial stretching in a single step, which helps to overcome energy barriers of the molecular chain configuration to form polar β-crystals, thus enhancing the piezoelectricity.

### 2.1.3 Nanoscale ME Measurement of ME Composites

The strain-mediated ME effect at the macroscale has been thoroughly studied in both laminates [4, 19, 20] and nanocomposites [21-23]. Recently, the ability to fabricate the ME nanofibers via electrospinning and advances in characterization techniques such as Piezoresponse Force Microscopy (PFM) have enabled studies at the nanoscale. In particular, PFM offers a new approach to measuring nanoscale PE properties in the presence of magnetic fields. For example, ME coupling of $CoFe_2O_4$–$PbZr_{0.52}Ti_{0.48}O_3$ [24] and $CoFe_2O_4$-$BaFeO_3$ [25] core–shell nanofibers has been confirmed by changes in the PFM amplitude and phase signals when a magnetic field of 2000 Oe is applied. A systematic PFM study has been conducted on ceramic $PbTiO_3$ (PTO)–$Ni_{0.66}Fe_{2.34}O_4$ and PTO–$BaFe_{12}O_{19}$ bilayered structures [26], which shows a magnetic field-dependence of the $d_{33}$ coefficient in the range of 0 to

2000 Oe and 0 to 1500 Oe. Recently, Martins *et al.* [27] presents the first study of polymer-based ME nanofibers and confirms a change in the PE response of PVDF/$CoFe_2O_4$ nanofibers using PFM in the presence of 1000 Oe magnetic field. Despite these observations, the tip-sample interactions and variations in the local, nanoscale PE and ME properties, particularly for PFM measurements on nanofiber polymer-based ME composites, have yet to be studied in detail.

In this chapter, the previous studies were extended with electrospun PVDF composites by incorporating degradable, non-toxic $Fe_3O_4$ nanoparticles to study ME properties using PFM. Given that PFM performs highly localized nanoscale measurements, the lateral nanometer variations in PE and ME properties were likely to arise due to variations in nanofiber morphology, PVDF crystallinity and distribution of the magnetic nanoparticles. This also considered the undertaking of measurements for statistical analysis such as multiple PFM measurements on single nanofibers and between different nanofibers. In doing so, tip-sample variations in properties but also interactions were observed, such as mechanical plastic deformation, specific to PFM measurements on nanoscale polymer structures.

## 2.2 Experimental

### 2.2.1 Materials

Ferric chloride ($FeCl_3 \cdot 6H_2O$), ferrous chloride ($FeCl_2 \cdot 4H_2O$), poly (methacrylic acid, sodium salt) solution (PMMA), tetrabutylammonium perchlorate (TBAP) and PVDF with average molecular weight of 275,000 (g $mol^{-1}$) were purchased from Aldrich. Ammonia solution ($NH_3 \cdot H_2O$) (28% w/w) was purchased from Ajax Finechem. Hydrochloric acid (HCl), N,N-

dimethylformamide (DMF) and acetone were purchased from Chem Supply. All the chemicals were used without further purification.

### 2.2.2 Synthesis of PMMA-$Fe_3O_4$ Nanoparticles

PMMA-$Fe_3O_4$ nanoparticles were synthesized using a co-precipitation method [28] (Figure 2.1). In a typical procedure, Fe precursor solution was prepared by dissolving 1.08 mmol $FeCl_3 \cdot 6H_2O$ and 0.54 mmol $FeCl_2 \cdot 4H_2O$ in 2 mL diluted HCl (pH=2.0). 100 mL PMMA aqueous solution (0.768 mmol $L^{-1}$, pH=4.9) was purged with argon and heated under reflux in a three-neck round-bottom flask. The Fe precursor solution was then injected into the PMMA solution in one shot, followed by the addition of 30 mL $NH_3 \cdot H_2O$. The whole injection process took less than 5 s to ensure the homogeneous nucleation of $Fe_3O_4$ nanoparticles. The resulted solution was kept under reflux for another 2 h. The nanoparticles were purified by dialysis against deionized water for three days. The dialyzed solution was then transferred into centrifuge tubes, stored in fridge overnight and freeze dried.

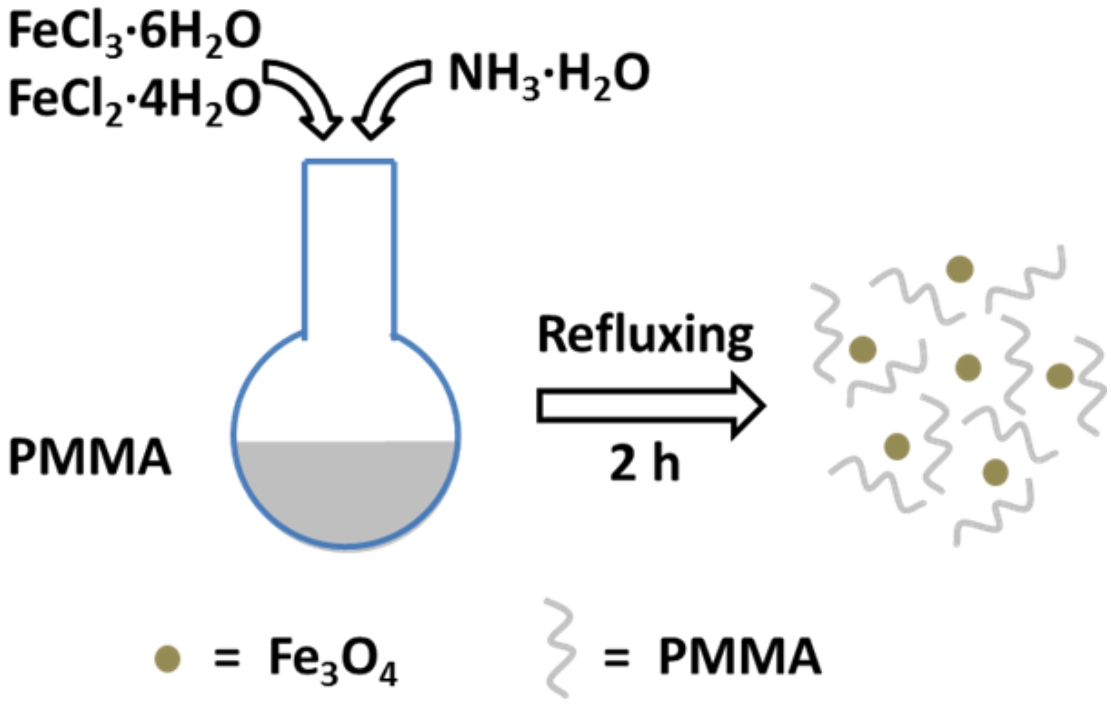


**Figure 2.1** Schematic of the preparation of PMMA-$Fe_3O_4$ nanoparticles.

### 2.2.3 Fabrication of PVDF and PVDF/$Fe_3O_4$ Nanofibers by Electrospinning

PVDF pellets were dissolved in mixed organic solvents (DMF/acetone = 7/3 by weight) at 12 wt%, 16 wt% and 20 wt%, respectively. To obtain better morphology, a small amount of TBAP (0.5 wt% of PVDF) was added to increase the conductivity of the PVDF solution. The mixture was then heated at 70 $^{o}$C for 4 h and left at room temperature to achieve complete dissolution of the PVDF pellets. The solution was stirred overnight at room temperature to reach thermal equilibrium. A NANON electrospinning system (MECC Co. Ltd, Japan) was used for electrospinning process. The PVDF solution was placed in a plastic syringe fitted with a 25 G needle and electrospun at 28 kV. A syringe pump was used to feed the polymer solution into the needle tip at a rate of 0.5 mL $h^{-1}$. The distance between the needle and collector plate was 15 cm. For fabrication of PVDF/$Fe_3O_4$ nanofibers, PMMA-$Fe_3O_4$

nanoparticles (10 wt% of PVDF) were added into the 16 wt% solution followed by sonication for 3 h. The solution was then electrospun using the same parameters as those for pure PVDF solutions.

### 2.2.4 Physico-Chemical Characterization of Nanofibers

X-ray diffraction (XRD) measurements were carried out using a powder XRD system (GBC MMA, Cu Kα radiation, λ = 0.15418 nm) at a scanning rate of 5° $min^{-1}$. Dynamic light scattering (DLS) was conducted by ZetaSizer (Malvern Instruments). The morphology of the nanofibers was characterized by field emission scanning electron microscope (SEM) (JEOL JSM-7500FA), with an accelerating voltage of 5.0 kV and an emission current of 10 mA. The nanofibers were directly electrospun on a silicon wafer and then coated with a 15 nm gold layer (Edwards Sputter Coater) for SEM testing. Fourier transform infrared spectroscopy (FT-IR) was performed using the Shimadzu AIM8000 FT-IR spectrometer. Magnetic property under different magnetic fields was carried out on a 14 T physical properties measurement system (PPMS).

### 2.2.5 Atomic Force Microscopy (AFM) and Piezoresponse Force Microscopy (PFM)

For imaging of $Fe_3O_4$ nanoparticles, tapping mode was used by AFM (Park Systems, Korea). The images were obtained in air using a silicon AFM tip (Type: NCHR, Nanoworld) with resonance frequency of 320 kHz and scan rate set at 0.5 Hz. For PFM measurements, the composite nanofibers were electrospun on gold coated cover slips. The topography images were obtained in AC mode with an MFP-3D AFM (Asylum Research, CA). Scan rate was set

at 0.5 Hz in air. For measuring the local ME effect, Dual AC Resonance Tracking (DART) Mode PFM was used with the assistance of the Variable Field Module (VFM) for monitoring the vertical deformation of the composite nanofibers under different in-plane magnetic fields. Typically, a Pt/Ir coated silicon tip (Type: EFM, Nanoworld) with force constant of 2.8 N $m^{-1}$ and gold layer (50 nm) and the gold-coated substrate were used as top and bottom electrodes. The tip-sample contact frequency varied due to slightly changes on sample surface from point to point. A small AC voltage of 200-600 mV was applied to oscillate the tip during the measurements. For PFM switching spectroscopy (SS-PFM) measurement, a sweeping DC bias with frequency of 0.2 Hz and range of ± 25 V was applied to the tip to offer the nanofiber with an electric field higher than the coercive field of PVDF. During acquisition of a single curve, 5 cycles of sweeping triangle/square waves were applied to obtain reproducible results. VFM was used to apply magnetic fields to nanofibers samples during SS-PFM testing. Asylum Research MFP-3D software within the Igor Pro 6.36 Software was used to obtain the butterfly loops and analyse data.

## 2.3 Results and Discussion

### 2.3.1 Synthesis of PMMA-$Fe_3O_4$ Nanoparticles

The XRD patterns and relative intensities of all diffraction peaks for the synthesized magnetic nanoparticles (Figure 2.2a) agreed well with those previously reported for $Fe_3O_4$ nanoparticles [28, 29]. The average diameter was ~ 8 nm as measured by DLS (Figure 2.2b) and AFM imaging confirmed a spherical morphology of the nanoparticles, with the surrounding structures identified as PMMA that was included in the synthesis to prevent aggregation of the $Fe_3O_4$ nanoparticles (Figure 2.2c). Cross-sectional AFM analysis gave

larger particle diameters of ~ 50 nm, most likely due to the presence of the PMMA and known tip broadening effects associated with AFM (Figure 2.2d).

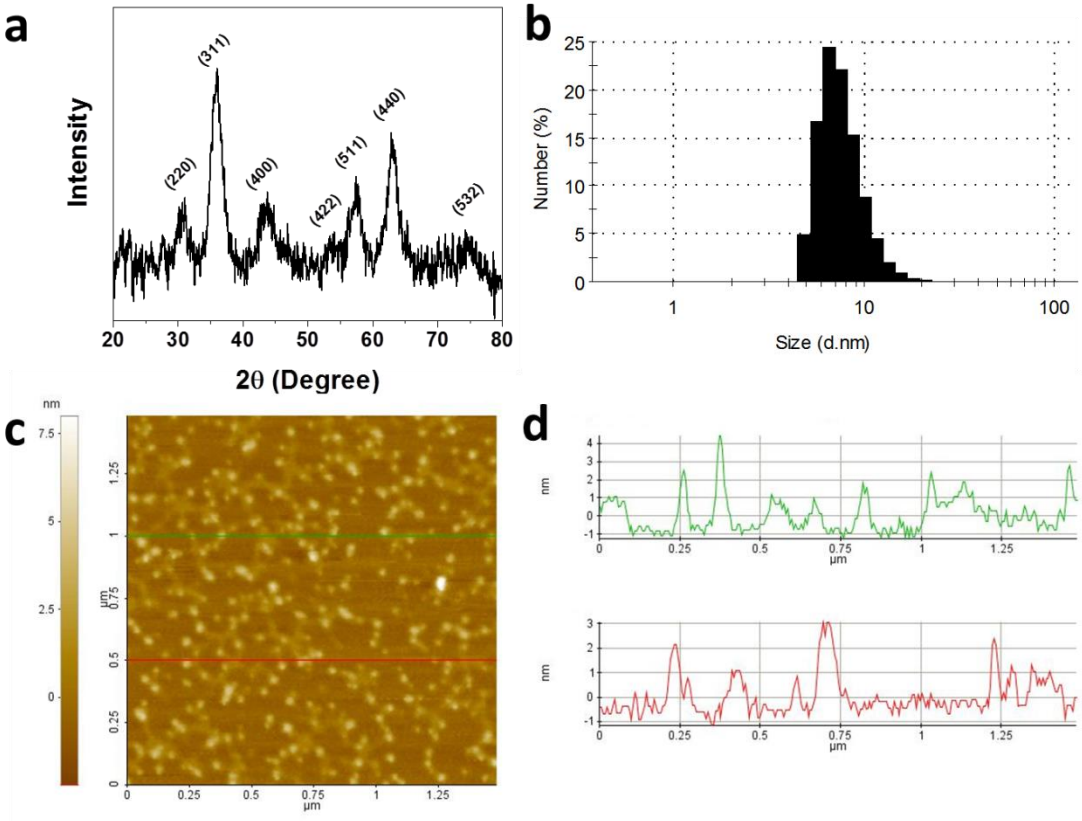


**Figure 2.2** (a) XRD pattern, (b) histogram of the particle size by DLS, (c) AFM image of PMMA-$Fe_3O_4$ nanoparticles and (d) profiles of two representative lines which are shown in (c).

### 2.3.2 Morphology of PVDF and PVDF/$Fe_3O_4$ Nanofibers

SEM images showing the size and morphology of the PVDF nanofibers and PVDF/$Fe_3O_4$ composite nanofibers are presented in Figure 2.3. For each sample, 100 nanofibers were measured for statistical analysis. Histograms showed that with increasing PVDF concentration, the average diameter of the nanofibers increased from 59 ± 19 nm (mean ± s.e.) (12 wt%) to 116 ± 23 nm (16 wt%) and to 184 ± 61 nm (20 wt%) (Figure 2.3e-g). At a low PVDF concentration, beaded structures were obtained due to the low viscosity of solution (Figure 2.3a). The nanofibers were observed to undergo twisting when the PVDF concentration reached 20 wt% (Figure 2.3c), which was attributed to the difficulty of solvent evaporation. The nanofibers obtained from 16 wt% PVDF solution had more uniform morphology without twisting and beaded structures (Figure 2.3b) and as such this PVDF concentration was chosen to fabricate the composite nanofibers. With incorporation of the $Fe_3O_4$ nanoparticles, the average diameter of the nanofibers increased from 116 ± 23 nm to 142 ± 29 nm (Figure 2.3d and 2.3h).

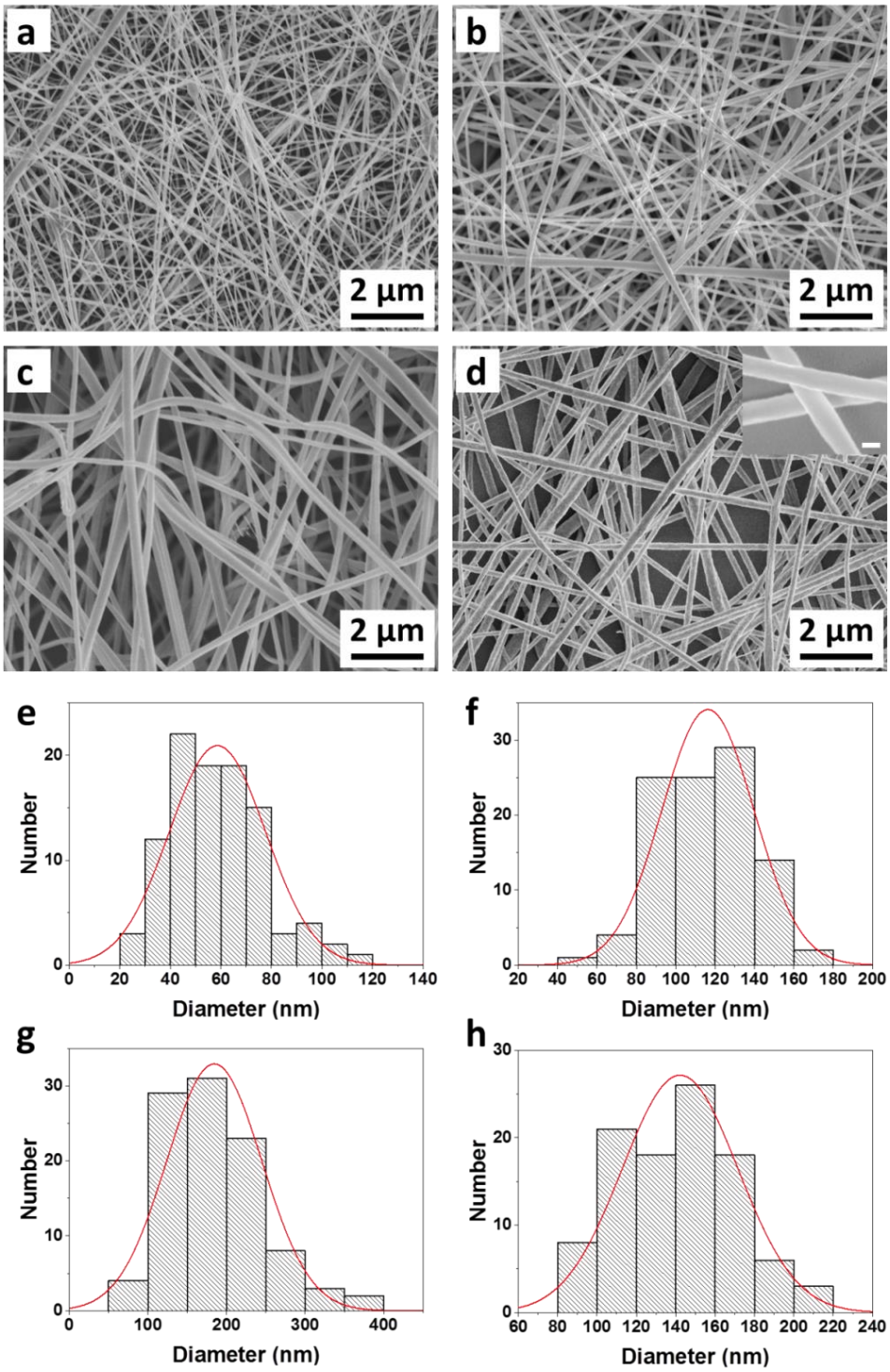


**Figure 2.3** (a, b, c, d) SEM images and (e, f, g, h) histograms of size of (a, e) 12 wt%, (b, f) 16 wt%, (c, g) 20 wt% pristine PVDF nanofibers and (d, h) 16 wt% PVDF/$Fe_3O_4$ composite nanofibers. Insert: magnified SEM image of the PVDF/$Fe_3O_4$ composite nanofibers (Scale bar: 100 nm).

### 2.3.3 Characterization of PVDF and PVDF/$Fe_3O_4$ Nanofibers

To confirm the formation of the electroactive phase induced by electrospinning, XRD and FT-IR measurements were conducted on the macroscale nanofiber sheets. Figure 2.4a shows the corresponding XRD patterns of electrospun nanofibers as well as a commercial PVDF film for comparison. For the commercial PVDF film, the peaks occurring at 18.92$^o$ and 26.74$^o$ corresponded to the (020) and (021) crystalline planes of α-phase. All of the electrospun samples showed a significant peak at 2θ=20.6$^o$ attributed to the (200)/(110) reflections of the β-phase. However, the reflections of the α- and γ-phase may overlap, thus XRD was unable to clearly identify the crystal structure of PVDF nanofibers exclusively [30]. As a result, FT-IR was used to further identify the crystalline structure in the electrospun nanofibers. In the FT-IR spectra (Figure 2.4b), the absorption bands at 840 $cm^{-1}$ and 1275 $cm^{-1}$ were attributed to the β-phase. Two significant bands at 763 $cm^{-1}$ and 795 $cm^{-1}$, associated with the α-phase, were observed in the commercial PVDF film but not in electrospun nanofibers. Only in the 20 wt% PVDF nanofibers that a small band at 1234 $cm^{-1}$ was observed and attributed to the γ-phase. These observations further confirmed the promotion of β-phase via electrospinning. The fraction of β-phase in PVDF/$Fe_3O_4$ composite nanofibers was calculated as 95.1%, according to equation established by Gregorio *et al.* [31]:

$$F(\beta) = \frac{A_\beta}{(K_\beta/K_\alpha)A_\alpha + A_\beta} \tag{2.1}$$

where F(β) is the β-phase content; $A_\alpha$ and $A_\beta$ are the absorbance at 763 and 840 $cm^{-1}$; $K_\alpha$ and $K_\beta$ are the absorption coefficients at the respective wavenumber, which have values of 6.1 × $10^4$ and 7.7 × $10^4$ $cm^2$ $mol^{-1}$, respectively. This β-phase fraction of 95% was similar to ≈ 90 % previously reported for similar electrospun PVDF/$CoFe_2O_4$ nanofibers when the wt% of $CoFe_2O_4$ magnetic nanoparticle reached 5% [27].

The magnetic properties of $Fe_3O_4$ nanoparticles and composite nanofibers were confirmed by magnetization isotherms at room temperature (Figure 2.4c and 2.4d). Due to their nanometer dimensions, the $Fe_3O_4$ nanoparticles exhibited superparamagnetic properties (Figure 2.4c) and this was maintained in the composite nanofibers (Figure 2.4d). The saturation magnetization ($M_S$) of the $Fe_3O_4$ nanoparticles was 29.68 emu $g^{-1}$, which is lower than that previously reported due to the inclusion of PMMA in the particles [29, 32]. In comparison, the $M_S$ of the composite nanofibers was significantly lower with a value of 1.79 emu $g^{-1}$. The fraction of $Fe_3O_4$ nanoparticles was less than 10 wt% in the nanofibers, calculated by Equation 2.2 [33]. This was because the dispersed nanoparticles may not be uniformly distributed in the solution during the electrospinning process, resulting in a lower fraction of nanoparticles than the theoretical values. According to the values, it is estimated that the PVDF/$Fe_3O_4$ nanofibers contained ~ 6 wt% nanoparticles.

$$nanoparticle\ wt\%_{composite} = \frac{Satruation\ Magnetization_{composite}}{Satruation\ Magnetization_{nanoparticle}} \times 100\% \qquad (2.2)$$

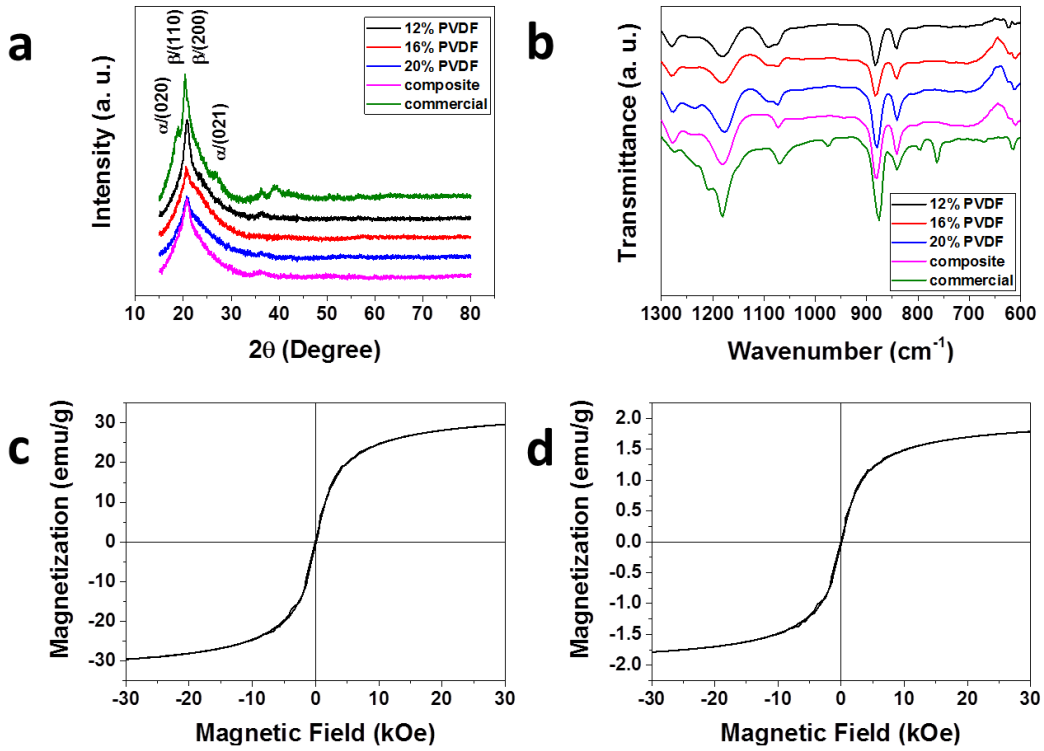


**Figure 2.4** (a) XRD patterns, (b) FT-IR spectra of different nanofibers and room-temperature magnetization isotherms of (c) $Fe_3O_4$ nanoparticles and (d) PVDF/$Fe_3O_4$ composite nanofibers.

### 2.3.4 PFM Study of PVDF and PVDF/$Fe_3O_4$ Nanofibers

The PE properties of the composite nanofibers were characterized using SS-PFM. In our initial attempts, imaging of the nanofibers after performing multiple switching spectroscopy curves revealed that in some cases the polymer had undergone localized deformation at the X-Y position of the curves. As a high voltage (± 25 V) was applied to the conducting tip during the measurement, heating of the tip was generated and could induce localized deformation of the polymer surface. Melting of the polymer may also result in adhesion of the polymer to the tip and uncertainty in the measurements. To address this, the

measurements were limited to only one switching spectroscopy curve at an X-Y position on a nanofiber alleviated this effect.

To obtain a good butterfly loop from the SS-PFM measurement, different measuring conditions were taken into consideration. For a single measurement on one spot, the initial change in contact frequency as a function of the DC bias waveform (five cycles) and whilst applying different AC modulating potentials to the conductive PFM tip are shown in Figure 2.5. The grey line shows the corresponding DC bias during the measurement. It is observed that the contact frequency between the PFM tip and sample was not stable and continued to increase during the first two cycles. From the third cycle, the contact frequency became stable to ensure reliable SS-PFM measurements. Thus, the data obtained from the third cycle was used in the following experiments.

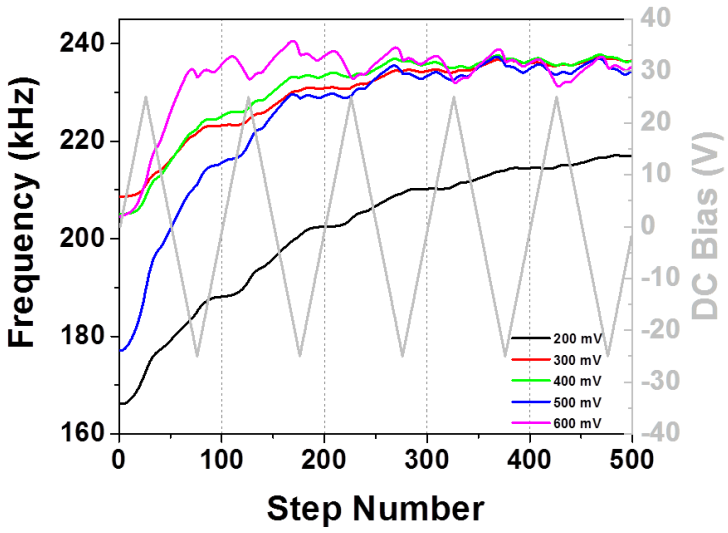


**Figure 2.5** Change in the tip-sample contact frequency during application of a DC and AC bias for a SS-PFM measurement.

In addition to ascertaining a constant contact frequency, another factor to be considered is the effect of the AC voltage applied to the PFM tip. Figure 2.6 showed the dependence of PE response and phase change on the applied AC voltage. Five different AC voltages from 200 mV to 600 mV were tested and the PE response was found to increase with an increase in the AC voltage (Figure 2.6a), as expected [34]. In contrast, the phase change was independent of the AC voltage although the noise of the phase signal decreased with an increase in the AC voltage, as the tip effectively pushed harder into the surface (Figure 2.6b). Based on these observations, an AC bias of 500 mV was chosen for the SS-PFM experiments, ensuring good sensitivity and signal-to-noise while avoiding causing too much damage to the tip.

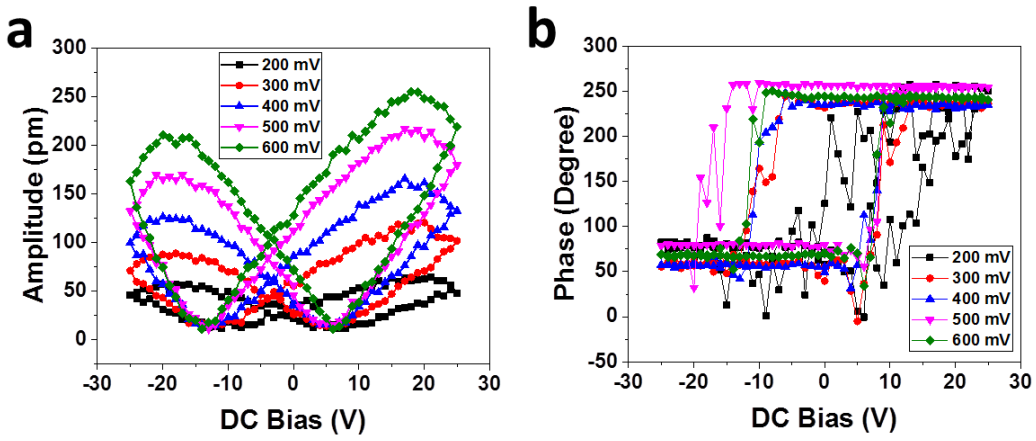


**Figure 2.6** SS-PFM curves showing the PE response (a) amplitude signal and (b) phase change in PFM measurement with different AC voltages.

For statistical analysis, switching spectroscopy curves were performed on 20 different nanofibers (n = 20). Along each nanofiber, only 1 curve was performed at 3 different X-Y positions, giving a total of 60 curves. Figure 2.7a shows an AFM height image of a single

composite nanofiber, indicating the location of three X-Y positions where the switching spectroscopy curves were performed. Figure 2.7b and 2.7c show the typical amplitude versus applied voltage curves (i.e. butterfly loops) and corresponding phase signals obtained on the aforementioned three positions. The coercive bias was about ± 10 V, where the nanofibers exhibited a minima in the PE response. In this case, the effective PE response was zero, showing that responses from the nascent domain generated by the tip bias and the surrounding material were compensating each other [35]. This voltage was the same voltage at which the phase changed by 180 degrees, indicating the dipoles localized under the tip were switched by the external electric field. This also confirmed that the response of the sample was due to the electromechanical contribution instead of long range electrostatic forces [36]. Whilst the amplitude response in each X-Y position was similar (Figure 2.7b), the corresponding phase curves showed different starting values (Figure 2.7c), indicating differences in the arrangement of individual dipoles (e.g. in the case of ferroelectric domains, $0^o$ represents for pointing down and $180^o$ represents for pointing up [37]). One possibility of the shift for spot 1 could relate to artefact of tuning the contact resonance frequency and centring of the phase signal, which was undertaken prior to each measurement on a nanofiber. In this case, changes in the sample properties (e.g. roughness, stiffness) could have an effect on the tip-sample interactions and thus on the contact-resonance frequency and corresponding phase. Alternatively, similar to variations in the PFM amplitude, any observed shifts in the phase could correspond to nanoscale lateral variations in the PE properties along a single nanofiber that could be easily detected by the highly localized measurements of the PFM probe.

Further to this, a statistical approach to the switching spectroscopy showed a significant variation in the PE response for different nanofibers. The maximum value of each butterfly loop was taken as the PE response. A histogram of the PE response collected from 20

nanofibers gave a peak distribution value of 240.5 ± 94.7 pm (N = 20) and values ranged from 100 to 450 pm (Figure 2.7d). Some nanofibers even showed no PE response. Whilst significant variation occurred among different nanofibers, the PE responses at different positions along a single nanofiber were similar, as evident in the butterfly loops in Figure 2.7b. These observations of the amplitude response within the same nanofiber and among different nanofibers, as well as their respective phase signals, are highlighted in Figure 2.8. Though not entirely clear, local variations in the PE response may be explained by heterogeneity in the electrospinning process, including changes in the expelled droplet size and composition (e.g. fraction of nanoparticles), which may lead to significant variations in morphology and crystallinity of the PVDF over time and hence across different nanofibers.

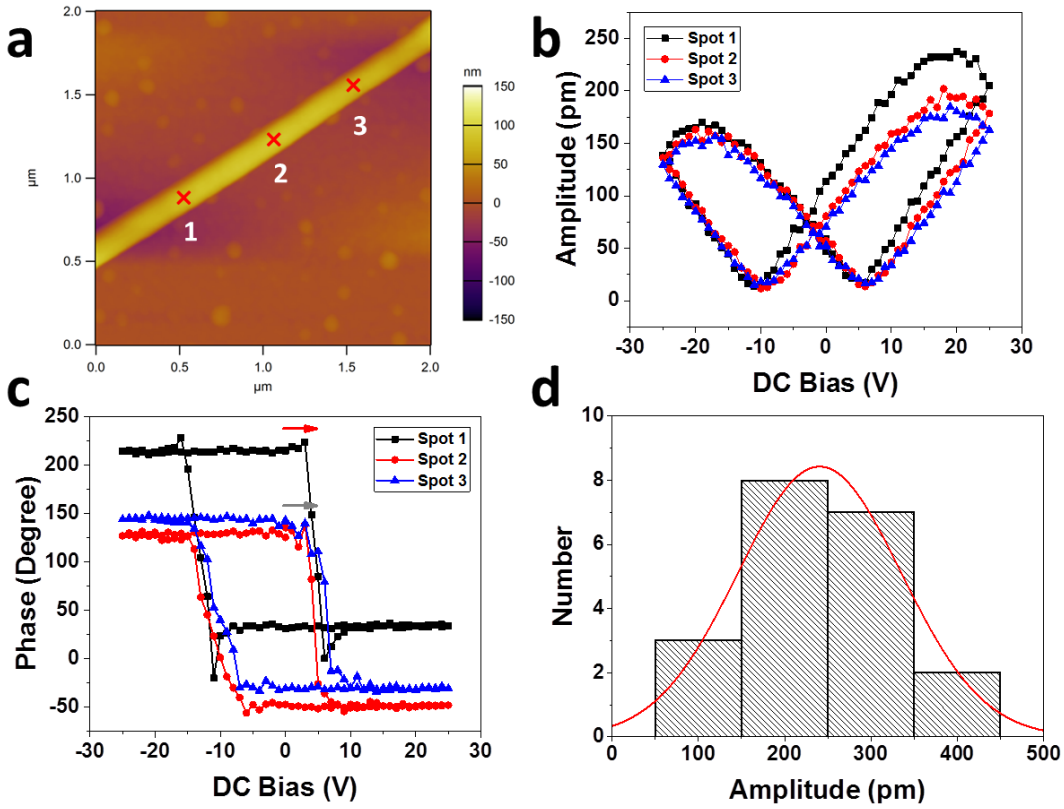


**Figure 2.7** (a) Topography image, (b) butterfly loops, (c) phase changing curves of a single composite nanofiber and (d) PE response histogram of composite nanofibers. All SS-PFM measurements start from 0 V and arrows indicate the direction (red arrow for Spot 1 and grey arrow for Spot 2 and 3).

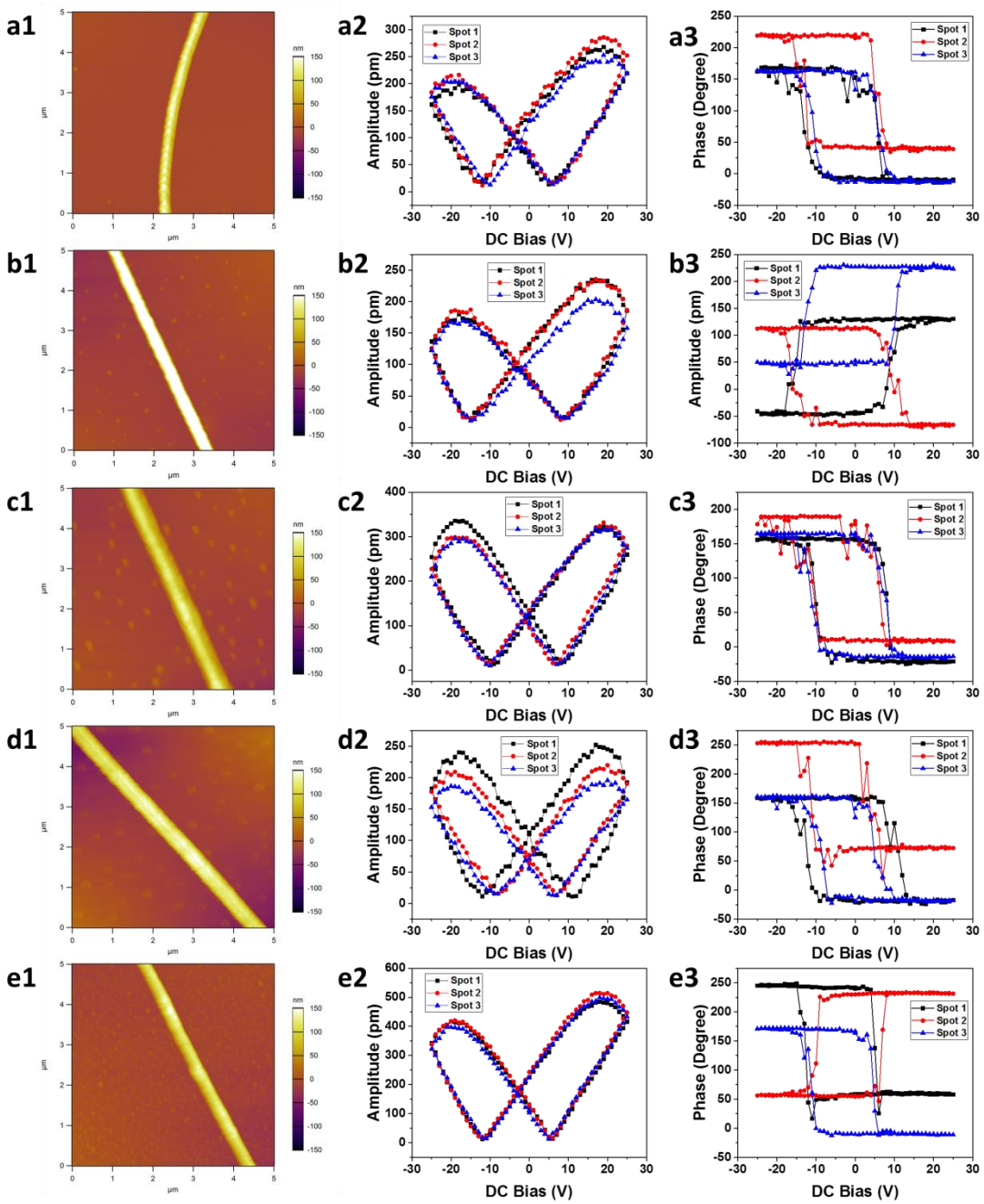


**Figure 2.8** (a1, b1, c1, d1, e1) Topography image, (a2, b2, c2, d2, e2) butterfly loops and (a3, b3, c3, d3, e3) phase changing curves of different PVDF/$Fe_3O_4$ composite nanofibers.

A similar statistical analysis was undertaken for switching spectroscopy curves on pristine PVDF nanofibers (without magnetic nanoparticles). In these nanofibers, a histogram of the PE response gave a peak distribution value of 140.9 ± 84.0 pm (N = 20) (Figure 2.9), indicating that the incorporation of the $Fe_3O_4$ nanoparticles enhanced the PE properties of the PVDF nanofibers. Here and in other work the introduction of the magnetic nanoparticles enhanced in volume fraction of the electroactive β-phase when compared to pure electrospun PVDF nanofibers [27]. This was explained by the interaction between the negatively charged surface of the nanoparticles and the positively charged polymer $CH_2$ groups, which promoted nucleation of the polar β-phase [38].

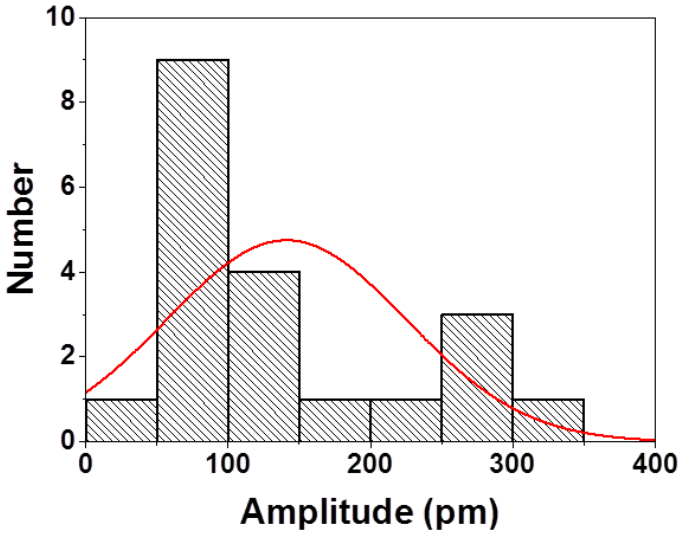


**Figure 2.9** PE response histogram of pristine PVDF nanofibers.

### 2.3.5 ME Effect of PVDF/$Fe_3O_4$ Nanofibers

PFM with the assistance of a magnetic field in the range of 0 to 2000 Oe was employed to better elucidate the localized ME effect of the nanofibers. For a single nanofiber, a topography image was taken prior to performing a switching spectroscopy measurement. With the application of external magnetic fields of 0 Oe, 500 Oe, 1000 Oe, 1500 Oe and 2000 Oe, switching spectroscopy measurements were obtained at five different X-Y positions along a nanofiber. The same procedure was then conducted on a pristine PVDF nanofiber for comparison. Figure 2.10 shows the PFM butterfly loops and the effect of the applied magnetic field. For both nanofibers, the amplitude curves exhibited entire butterfly loops with full switching of dipoles in all magnetic fields. In measurements on three different composite nanofibers, the PE response decreased with an increasing magnetic field (Figure 2.10a). This was further shown with the average maximum values of the butterfly loops plotted as a function of magnetic field in Figure 2.10c. Taking fiber #1 for example, the amplitudes of the PE signal decreased from 205.8 ± 11.9 pm to 173.6 ± 10.2 pm, 132.2 ± 4.8 pm, 110.5 ± 3.9 pm and 87.1 ± 3.3 pm with a magnetic field of 0 Oe, 500 Oe, 1000 Oe, 1500 Oe and 2000 Oe, respectively, suggesting a PE coefficient dependence on the magnetic field. The composite nanofibers underwent a linear decrease with an increase of magnetic field strength. To ensure that the PVDF had no response to magnetic stimulation, ME measurement was also conducted on pure PVDF nanofibers subjected to a magnetic field (Figure 2.10b and 2.10d). In the range of 0 to 2000 Oe, the PE response of pristine PVDF nanofibers only showed minor variation without significant change. The results confirmed it was the presence of the $Fe_3O_4$ nanoparticles and not the PVDF on its own that resulted in the change in PE response with magnetic field, giving rise to a nanoscale ME effect.

According to Vopsaroiu's work on a trilayered Permendur-(CoFeV)-PZT-Permendur ME structure, the thermodynamic treatment of ME coupling allows for quantitative estimation of effective ME coefficient from the linear change of PE coefficient with the applied magnetic field [39]:

$$d_{33}^{eff} = \frac{D_3}{\sigma_3} - \frac{\alpha_{33}}{\sigma_3} H_1 \tag{2.2}$$

where $\alpha_{33}$ is the effective ME coefficient, $D_3$ is the displacement, $\sigma_3$ is the mechanical stress, $d_{33}^{eff}$ is the PE coefficient and $H_1$ is the magnetic field. Since Permendur has a positive MS coefficient associated with a positive stress $\sigma_3$, the variation of $d_{33}^{eff}$ has a negative slope. In general, ferrites have negative MS coefficient. However, the signs of its tensor components are strongly dependent on the crystallographic direction along which they are measured [26]. In our case, the PE response decreased with the magnetic field, which also indicated a negative slope of $d_{33}^{eff}$. This may be due to the domination of a positive MS coefficient.

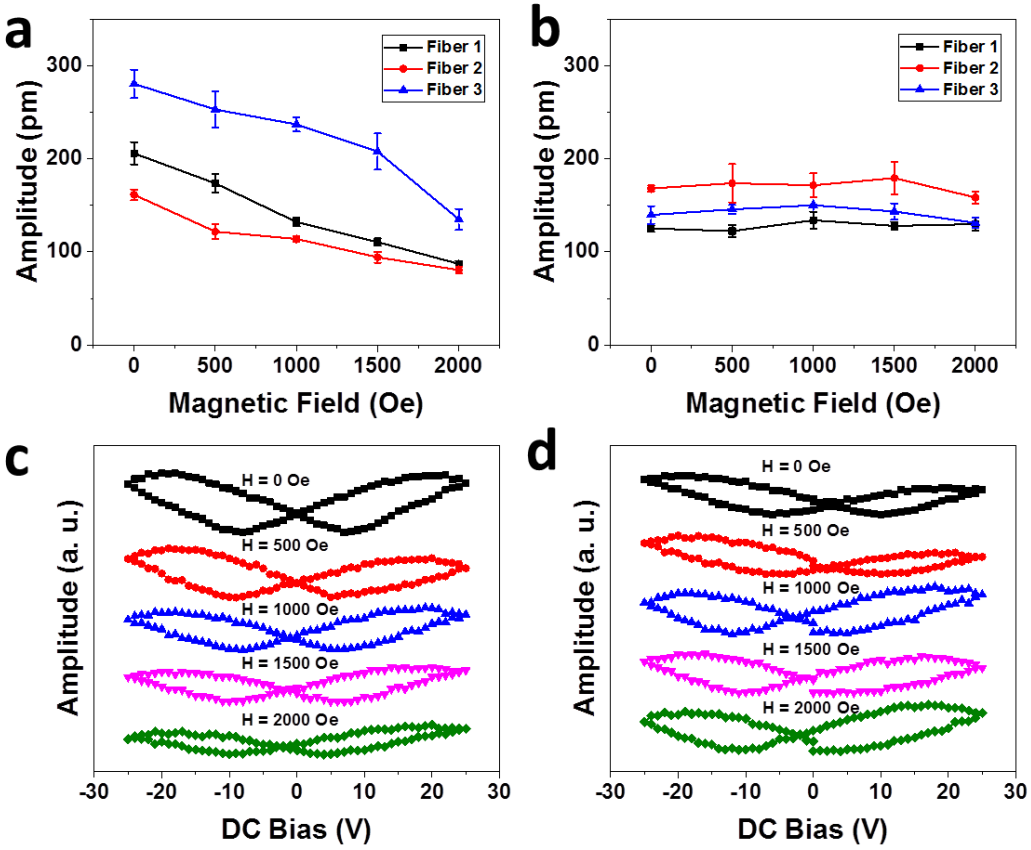


**Figure 2.10** (a, b) PE response dependence on magnetic field strength and (c, d) PFM butterfly loops obtained in (a, c) PVDF/$Fe_3O_4$ composite nanofibers and (b, d) pristine PVDF nanofibers.

## 2.4 Conclusions

PMMA-$Fe_3O_4$ nanoparticles with an average size of 8 nm were fabricated by a co-precipitation method. With the incorporation of magnetic nanoparticles, PVDF/$Fe_3O_4$ nanofibers were fabricated by electrospinning, which proved to be a useful technique for promoting the formation of β-phase PVDF, hence enhancing its PE property. At a highly localized nanoscale level, PFM measurements showed the PE response was similar along the length of a single nanofiber but varied between different nanofibers. With the application of

an external magnetic field, the change in the PFM amplitude of single PVDF/$Fe_3O_4$ nanofibers indicated the magnetic field had a significant effect on the PE response and confirmed a nanoscale ME effect, which was becoming of significant interest for the ME stimulation of neural cells and tissues for biomedical applications [40].

## 2.5 References


1. Eerenstein, W., et al., Multiferroic and magnetoelectric materials. Nature, 2006. **442**(7104): p. 759-765.

2. Zheng, H., et al., *Self-assembled growth of $BiFeO_3$-$CoFe_2O_4$ Nanostructures.* Advanced Materials, 2006. **18**(20): p. 2747-2752.

3. Levin, I., et al., *Design of self-assembled multiferroic nanostructures in epitaxial films.* Advanced Materials, 2006. **18**(15): p. 2044-2047.

4. Jin, J., et al., *Multiferroic polymer laminate composites exhibiting high magnetoelectric response induced by hydrogen-bonding interactions.* Advanced Functional Materials, 2014. **24**(8): p. 1067-1073.

5. Jia, Y., et al., *Giant magnetoelectric response from a piezoelectric/magnetostrictive laminated composite combined with a piezoelectric transformer.* Advanced Materials, 2008. **20**(24): p. 4776-4779.

6. Borisov, P., et al., *Magnetoelectric switching of exchange bias.* Physical Review Letters, 2005. **94**(11): p. 117203.

7. Hur, N., et al., *Colossal magnetodielectric effects in $DyMn_2O_5$.* Physical Review Letters, 2004. **93**(10): p. 107207.

8. Chapon, L.C., et al., *Structural anomalies and multiferroic behavior in magnetically frustrated $TbMn_2O_5$.* Physical Review Letters, 2004. **93**(17): p. 177402.

9. Nan, C.W., et al., *Multiferroic magnetoelectric composites: historical perspective, status, and future directions.* Journal of Applied Physics, 2008. **103**(3): p. 031101.

10. Lu, M.C., et al., *Enhancing the magnetoelectric response of Terfenol-D/Polyvinylidene fluoride/Terfenol-D Laminates by exploiting the shear mode effect.* Applied Physics Letters, 2015. **106**(11): p. 112905.

11. Zhai, J., et al., *Giant magnetoelectric effect in Metglas/Polyvinylidene-fluoride laminates.* Applied Physics Letters, 2006. **89**(8): p. 083507.

12. Martins, P., et al., *Correlation between crystallization kinetics and electroactive polymer phase nucleation in ferrite/Poly(vinylidene fluoride) magnetoelectric nanocomposites.* Journal of Physics Chemistry B, 2012. **116**(2): p. 794-801.

13. Carvell, J., et al., *Induced magneto-electric coupling at ferroelectric/ferromagnetic interface.* Journal of Applied Physics, 2013. **113**(17): p. 17C715.

14. Tschoeke, B., et al., *Development of a composite degradable/nondegradable tissue-engineered vascular graft.* Artificial Organs, 2008. **32**(10): p. 800-809.

15. Correia, D.M., et al., *Strategies for the development of three dimensional scaffolds from piezoelectric Poly(vinylidene fluoride).* Materials & Design, 2016. **92**: p. 674-681.

16. Zheng, J., et al., *Polymorphism control of Poly(vinylidene fluoride) through electrospinning.* Macromolecular Rapid Communications, 2007. **28**(22): p. 2159-2162.

17. Andrew, J.S., et al., *Effect of electrospinning on the ferroelectric phase content of polyvinylidene difluoride fibers.* Langmuir, 2008. **24**(3): p. 670-672.

18. Baji, A., et al., *Electrospinning induced ferroelectricity in Poly(vinylidene fluoride) fibers.* Nanoscale, 2011. **3**(8): p. 3068-3071.

19. Lu, S.G., et al., *Large magnetoelectric coupling coefficient in Poly(vinylidene fluoride-hexafluoropropylene)/Metglas laminates.* Journal of Applied Physics, 2011. **110**(10): p. 104103.

20. Silva, M., et al., *Optimization of the magnetoelectric response of Poly(vinylidene fluoride)/Epoxy/Vitrovac laminates.* ACS Applied Materials & Interfaces, 2013. **5**(21): p. 10912-10919.

21. Wong, C.K., et al., *Effect of inclusion deformation on the magnetoelectric effect of particulate magnetostrictive/piezoelectric composites.* Journal of Applied Physics, 2007. **102**(6): p. 063908.

22. Martins, P., et al., *Optimizing piezoelectric and magnetoelectric responses on $CoFe_2O_4$/P(VDF-TrFE) nanocomposites.* Journal of Physics D-Applied Physics, 2011. **44**(49): p. 495303.

23. Martins, P., et al., *Large linear anhysteretic magnetoelectric voltage coefficients in $CoFe_2O_4$/Polyvinylidene Fluoride 0-3 nanocomposites.* Journal of Nanoparticle Research, 2013. **15**(8): p. 1825.

24. Xie, S., et al., *Multiferroic $CoFe_2O_4$-$Pb(Zr_{0.52}Ti_{0.48})O_3$ core-shell nanofibers and their magnetoelectric coupling.* Nanoscale, 2011. **3**(8): p. 3152-3158.

25. Zhu, Q., et al., *Multiferroic $CoFe_2O_4$–$BiFeO_3$ core–shell nanofibers and their nanoscale magnetoelectric coupling.* Journal of Materials Research, 2014. **29**(05): p. 657-664.

26. Caruntu, G., et al., *Probing the local strain-mediated magnetoelectric coupling in multiferroic nanocomposites by magnetic field-assisted Piezoresponse Force Microscopy.* Nanoscale, 2012. **4**(10): p. 3218-3227.

27. Goncalves, R., et al., *Magnetoelectric $CoFe_2O_4$/Polyvinylidene Fluoride electrospun nanofibres.* Nanoscale, 2015. **7**(17): p. 8058-8061.

28. Li, Z., et al., *Direct coprecipitation route to monodisperse dual-functionalized magnetic iron oxide nanocrystals without size selection.* Small, 2008. **4**(2): p. 231-239.

29. Cheng, F.Y., et al., *Characterization of aqueous dispersions of $Fe_3O_4$ nanoparticles and their biomedical applications.* Biomaterials, 2005. **26**(7): p. 729-738.

30. Martins, P., et al., *Electroactive phases of Poly(vinylidene fluoride): determination, processing and applications.* Progress in Polymer Science, 2014. **39**(4): p. 683-706.

31. Gregorio, R., et al., *Effect of crystallization temperature on the crystalline phase content and morphology of Poly(vinylidene fluoride).* Journal of Polymer Science Part B-Polymer Physics, 1994. **32**(5): p. 859-870.

32. Hong, X., et al., *Fabrication of magnetic luminescent nanocomposites by a layer-by-layer self-assembly approach.* Chemistry of Materials, 2004. **16**(21): p. 4022-4027.

33. Goncalves, R., et al., *Development of magnetoelectric $CoFe_2O_4$/Poly(Vinylidene Fluoride) microspheres.* RSC Advances, 2015. **5**(45): p. 35852-35857.

34. Xie, S., et al., *High resolution quantitative Piezoresponse Force Microscopy of $BiFeO_3$ nanofibers with dramatically enhanced sensitivity.* Nanoscale, 2012. **4**(2): p. 408-413.

35. Jesse, S., et al., *Switching Spectroscopy Piezoresponse Force Microscopy of ferroelectric materials.* Applied Physics Letters, 2006. **88**(6): p. 062908.

36. Kalinin, S.V., et al., *Contrast mechanism maps for Piezoresponse Force Microscopy.* Journal of Materials Research, 2002. **17**(5): p. 936-939.

37. Soergel, E., *Piezoresponse Force Microscopy (PFM).* Journal of Physics D: Applied Physics, 2011. **44**(46): p. 464003.

38. Martins, P., et al., *Role of nanoparticle surface charge on the nucleation of the electroactive beta-Poly(vinylidene fluoride) nanocomposites for sensor and actuator applications.* Journal of Physical Chemistry C, 2012. **116**(29): p. 15790-15794.

39. Vopsaroiu, M., et al., *Experimental determination of the magnetoelectric coupling coefficient via piezoelectric measurements.* Measurement Science and Technology, 2008. **19**(4): p. 045106.

40. Ribeiro, C., et al., *Proving the suitability of magnetoelectric stimuli for tissue engineering applications.* Colloids and Surfaces B-Biointerfaces, 2016. **140**: p. 430-436.

# 3 Probing of Piezoelectric and Magnetoelectric Properties of P(VDF-HFP)/$CoFe_2O_4$ and P(VDF-HFP)/$Fe_3O_4$ Nanofibers by PFM/VFM

## 3.1 Introduction

### 3.1.1 Piezoelectricity of P(VDF-HFP)

The use of piezoelectric (PE) polymers gives rise to the development of magnetoelectric (ME) composites. In contrast to their ceramic counterparts, PE polymers, such as poly (vinylidene fluoride) (PVDF) and its copolymers poly (vinylidene fluoride-co-trifluoroethylene) (P(VDF-TrFE)) and poly (vinylidene fluoride-co-hexafluoropropylene) (P(VDF-HFP)), exhibit easy processing, light weight and good flexibility [1]. Due to its high PE coefficient, PVDF has been used extensively in polymer-based ME composites for decades [1]. The copolymer, P(VDF-TrFE), possesses the highest $d_{33}$ PE coefficient and has also been widely used in the fabrication of ME composites with a variety of magnetic materials (e.g. Co [2], $CoFe_2O_4$ [3], Terfenol-D [4] and Metglas [5]).

However, the other member of the PVDF family of PE polymers, P(VDF-HFP), hasn't attracted as much attention for ME composites, perhaps due to its unique properties compared to most other PE polymers. For instance, P(VDF-HFP) possesses a higher transverse $d_{31}$ PE coefficient compared to its longitudinal $d_{33}$ PE coefficient [6]. The origin of such PE responses is believed to occur from a reversible change between a poled α-like structure and β-like structure. In addition, P(VDF-HFP) is attractive from the viewpoint of real applications due to its improved chemical and thermal stability and longer lifetimes [7]. To date, only a

few ME composites have been developed based on P(VDF-HFP) [8, 9] and as such further investigation of their use in this research field is warranted.

### 3.1.2 Magnetostriction of $CoFe_2O_4$

$CoFe_2O_4$ has been an important magnetic constituent in ME composites due to their high magnetostrictive (MS) coefficient ($\lambda_S = -110\times10^{-6}$ at 300 K), high Curie temperature (above 700 K), moderate saturation magnetization, high coercivity at room temperature, high electrical resistivity and good thermal stability [10-13]. From a structural point of view, $CoFe_2O_4$ exhibits a cubic spinel structure ($AB_2O_4$) in which both of tetrahedral (A) and octahedral (B) sites exist. The cations $Co^{2+}$ and $Fe^{3+}$ have the tendency to occupy either tetrahedral or octahedral sites [12]. The large magnetization comes from the possibility of atomic rearrangements in the spinel structure. Namely, Co ions from the B sublattice replace Fe ions in the A sublattice and vice versa. In this case, the moment of the Fe ions no longer compensates each other and the magnetization can increase dramatically [14]. Owing to its good magnetic properties, $CoFe_2O_4$ nanoparticles have been widely employed in the fabrication of both ceramic and polymeric ME composites such as $Bi_4Ti_3O_{12}/CoFe_2O_4$ composite films [15], $CoFe_2O_4/BiFeO_3$ core-shell nanofibers [16], $CoFe_2O_4$/PVDF composite nanofibers [17] and $CoFe_2O_4$/P(VDF-TrFE) nanocomposites [3, 18]. In addition to excellent MS properties, $CoFe_2O_4$ nanoparticles also possess a relatively high remanence ratio [19] which is believed to enhance the ME response during mechanical coupling in magnetically isotropic samples [3].

Following on from Chapter 2, this study investigates the PE properties and ME effect of P(VDF-HFP)/$CoFe_2O_4$ and P(VDF-HFP)/$Fe_3O_4$ electrospun nanofibers using Piezoresponse

Force Microscopy combined with the application of a magnetic field. The electrospun conditions and ensuing properties, for example the morphology and crystallinity, of pristine P(VDF-HFP) nanofibers were firstly shown followed by the electrospinning of composite nanofibers. For the latter, the effects of the $CoFe_2O_4$ and $Fe_3O_4$ magnetic nanoparticles on the PE and ME response of the composite nanofibers were compared. Experimental data suggested that the P(VDF-HFP) nanofibers possess a higher PE response than PVDF nanofibers. In addition, the PE properties could be further enhanced with the addition of magnetic nanoparticles, as observed in the previous Chapter 2. However, the ME effect of the P(VDF-HFP)-based composite nanofibers was more complex and less evident compared to PVDF-based composite nanofibers, probably due to the copolymerization nature and the large transverse piezoelectricity of P(VDF-HFP). Despite this, the addition of magnetic nanoparticles had an effect on the PE response of composite nanofibers when subjected to different DC magnetic fields. This indicated an ME coupling effect in the P(VDF-HFP)/$CoFe_2O_4$ and P(VDF-HFP)/$Fe_3O_4$ nanofibers though the exact underlying mechanism was still not clear.

## 3.2 Experimental

### 3.2.1 Materials

PMMA-$Fe_3O_4$ nanoparticles were prepared using the same method in Chapter 2. $CoFe_2O_4$ nanoparticles (30 nm), tetrabutylammonium perchlorate (TBAP) and P(VDF-HFP) with average molecular weight of 400, 000 (g $mol^{-1}$) were purchased from Aldrich. N,N-dimethylformamide (DMF) and acetone were purchased from Chem Supply. All the chemicals were used without further purification.

### 3.2.2 Fabrication of P(VDF-HFP) Nanofibers

P(VDF-HFP) pellets were dissolved in mixed organic solvents (DMF/acetone = 3/7, 5/5 and 7/3 by volume) at 12% w/v, 15% w/v and 18% w/v. To obtain better morphology, a small amount of TBAP (0.5 wt% of P(VDF-HFP)) was added to increase the conductivity of the polymer solution. The mixture was heated at 70 $^{o}$C for 4 h, and then left at room temperature to achieve complete dissolution of the P(VDF-HFP) pellets. To reach thermal equilibrium, the solution was stirred overnight at room temperature. A commercial system (NANON electrospinning system, MECC Co. Ltd, Japan) was used for electrospinning. The solution was placed in a plastic syringe fitted with a 25 G needle and electrospun at 20 kV. A syringe pump was used to feed the polymer solution into the needle tip at a rate of 0.5 mL $h^{-1}$. The distance between the needle and collector plate was 11.5 cm.

### 3.2.3 Fabrication of P(VDF-HFP)/$CoFe_2O_4$ and P(VDF-HFP)/$Fe_3O_4$ Nanofibers

Based on structural characterization, a 15% w/v P(VDF-HFP) solution in DMF/Acetone (ratio 3/7) was used to fabricate composite nanofibers. To obtain P(VDF-HFP)/$CoFe_2O_4$ and P(VDF-HFP)/$Fe_3O_4$ solutions, $CoFe_2O_4$ and PMMA-$Fe_3O_4$ nanoparticles (10 wt% of P(VDF-HFP)) were added into the polymer solution followed by sonication for 3 h. The solutions were then electrospun using the same parameters as those for pure P(VDF-HFP) solutions.

### 3.2.4 Physico-Chemical Characterization of Nanofibers

Field emission scanning electron microscope (SEM) (JEOL JSM-7500FA) was used to characterize the morphology of nanofibers, with an accelerating voltage of 5.0 kV and an

emission current of 10 mA. The nanofibers were directly electrospun on a silicon wafer. Then, a thin layer of gold was sputtered on the sample (15 nm, Edwards Sputter Coater) for SEM testing. Fourier transform infrared spectroscopy (FT-IR) was performed using the Shimadzu AIM8000 FT-IR spectrometer. X-ray diffraction (XRD) measurements were carried out using a powder XRD system (GBC MMA, Cu Kα radiation, $\lambda = 0.15418$ nm) at a scanning rate of 5° $min^{-1}$. Differential scanning calorimetry (DSC) data were collected on a TA Q100 calorimeter under a dry nitrogen environment. The measured heat flow was obtained in the conventional mode at heating and cooling temperature ramps of 10 $^{o}C$ $min^{-1}$. The temperature accuracy was 0.1 $^{o}C$. For the data analysis, the TA universal analysis 2000 software was used. Magnetic property under different magnetic fields was carried out on a 14 T physical properties measurement system (PPMS).

### 3.2.5 Atomic Force Microscopy (AFM) and Piezoresponse Force Microscopy (PFM)

For AFM and PFM measurement, the substrate was a cover slip with a 50 nm gold layer applied using a sputter coater (Edwards Sputter Coater). Then, the nanofibers were directly electrospun on the substrate. The topography images were obtained in AC mode with an MFP-3D AFM (Asylum Research, CA). Scan rate was set as 0.5 Hz in air. For measuring ME effect locally, Dual AC Resonance Tracking (DART) Mode PFM was used with the assistance of the Variable Field Module (VFM), monitoring the PE response of the composite nanofibers under different in-plane magnetic fields. Typically, a Pt/Ir coated silicon tip with force constant of 2.8 N $m^{-1}$ and gold layer on the substrate were used as top and bottom electrodes. The tip-sample contact frequency changed from 320 kHz to 340 kHz due to slight variations across the sample surface. An AC voltage of 200 mV was applied to oscillate the tip during the measurements. A sweeping DC bias with a frequency of 0.2 Hz and in the

range of ± 25 V was applied to the tip to offer the nanofiber with an electric field higher than its coercive field. During acquisition of a single curve, 5 cycles of the sweeping triangle/square waveform were applied to the tip. Data analysis was carried out using Asylum Research software within Igor Pro 6.36 Software (Wavemetrics). To identify the statistical significance of amplitudes, ANOVA was performed using statistical packages of OriginPro 9.2.

## 3.3 Results and Discussion

### 3.3.1 Morphology of P(VDF-HFP) Nanofibers

Figure 3.1 shows the SEM images of P(VDF-HFP) nanofibers electrospun with different polymer concentrations and different solvents. Figure 3.2 shows the effect of polymer concentrations and solvents on the diameters of obtained nanofibers, calculated from 100 individual nanofibers for each sample. Table 3.1 shows the diameters of all samples. With the same solvent, 15% w/v P(VDF-HFP) nanofibers possessed the largest diameter (Figure 3.1d, 3.1e and 3.1f). With the same polymer concentration, the diameter of P(VDF-HFP) nanofibers decreased with increasing DMF/Acetone ratio. Compared to acetone, DMF was less likely to facilitate the evaporation of solvent, which promoted the elongation of polymer solution by prolonging the solidification time. Thus, higher DMF/Acetone ratio resulted in the formation of thinner nanofibers (Figure 3.1c, 3.1f and 3.1i). In a low polymer concentration (12% w/v) (Figure 3.1a-c), the electrospun nanofibers may encounter a beading problem whilst some nanofibers were found to be much thinner than others in a high polymer concentration (18% w/v) (Figure 3.1g-i), which was attributed to the unstable electrospinning process of solution with high viscosity.

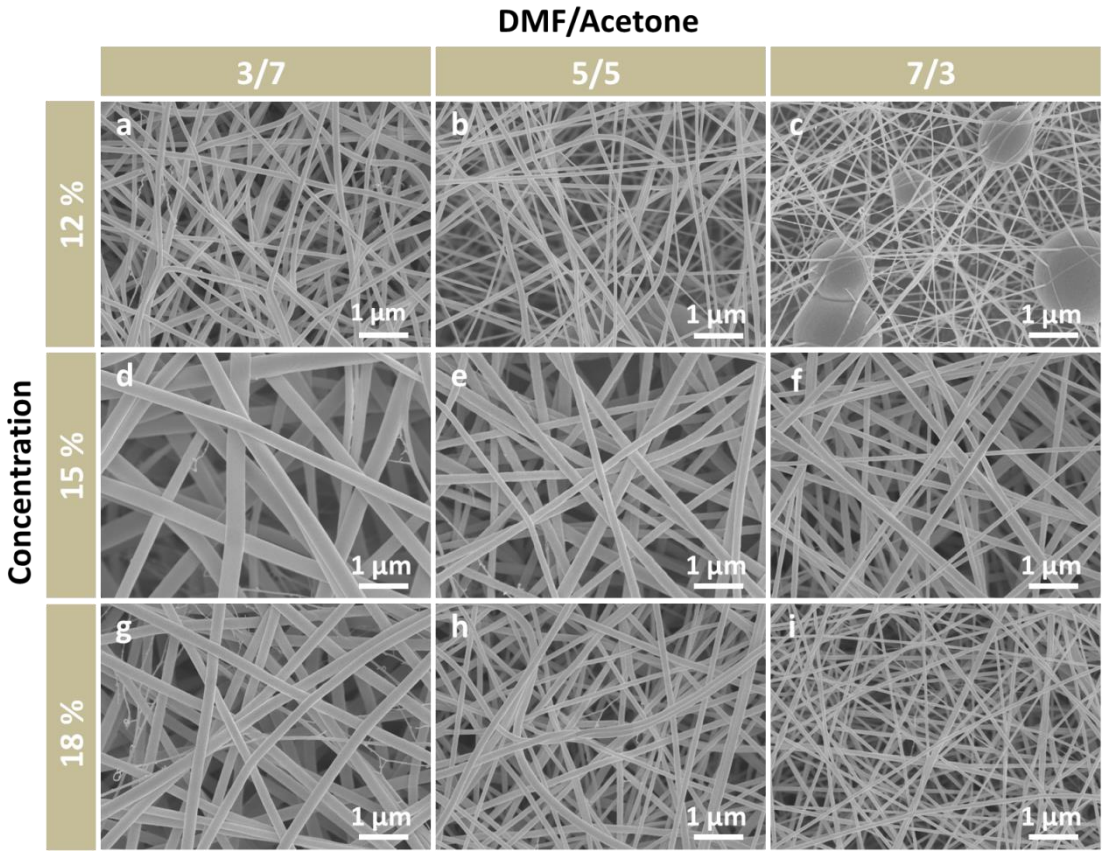


**Figure 3.1** SEM images of P(VDF-HFP) nanofibers with different concentrations: (a, b, c) 12% w/v, (d, e, f) 15% w/v and (g, h, i) 18% w/v electrospun from solvents with different DMF/Acetone ratios: (a, d, g) 3/7, (b, e, h) 5/5 and (c, f, i) 7/3.

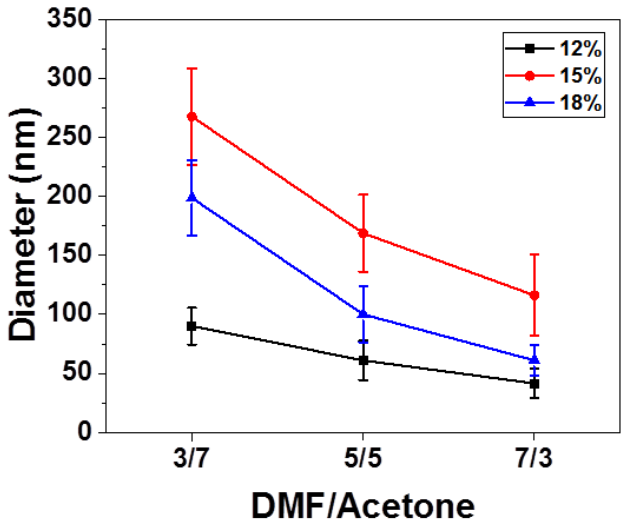


**Figure 3.2** Relation between the diameter of P(VDF-HFP) nanofibers and DMF/Acetone ratio in different polymer concentrations.

**Table 3.1** Diameter of electrospun P(VDF-HFP) nanofibers

| Sample* | Diameter (mean ± s.e.) (nm) |
|---|---|
| 12-3-7 | 90 ± 16 |
| 12-5-5 | 61 ± 17 |
| 12-7-3 | 42 ± 13 |
| 15-3-7 | 268 ± 41 |
| 15-5-5 | 169 ± 33 |
| 15-7-3 | 116 ± 34 |
| 18-3-7 | 199 ± 32 |
| 18-5-5 | 100 ± 24 |
| 18-7-3 | 61 ± 13 |

*A-B-C: A is the concentration of P(VDF-HFP), B/C is the DMF/Acetone ratio.

### 3.3.2 Characterization of P(VDF-HFP) Nanofibers

The formation of the electroactive phase induced by electrospinning was identified by physical characterization of macroscale nanofiber sheets. Figure 3.3 shows FT-IR and XRD measurements conducted on all the samples. In the FT-IR spectra, the peaks of different samples had similar positions and transmittance (Figure 3.3a). Similar to that previously observed for PVDF, no absorption band was found at 763 $cm^{-1}$ and 795 $cm^{-1}$, which were associated with the α-phase. The absorption bands at 840 $cm^{-1}$ and 1275 $cm^{-1}$ showed the existence of β-phase in P(VDF-HFP). Note that there was no band at 1234 $cm^{-1}$ (γ-phase), indicating that the β-phase existed in the electrospun nanofibers exclusively. This was also confirmed by XRD results (Figure 3.3b). All of the samples showed a significant peak at $2\theta=20.6^{o}$ attributed to the (200)/(110) reflections of the β-phase and there was no peak corresponding to α-phase at $18.92^{o}$ and $26.74^{o}$. Unlike the similarity of absorption peaks in FT-IR, the intensity of peaks in XRD showed greater variation among the different samples. In a low polymer concentration (12% w/v), the intensity of peaks was not as strong as others, indicating that the degree of crystallinity may be lower due to the higher mobility of polymer chains.

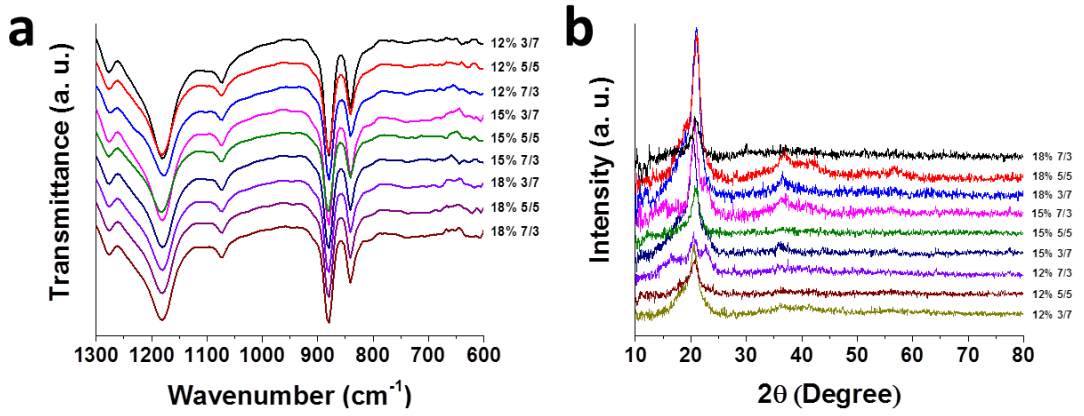


**Figure 3.3** (a) FT-IR spectra and (b) XRD patterns of different P(VDF-HFP) nanofibers.

DSC thermograms of (PVDF-HFP) nanofibers were recorded to further study the effect of solvents and polymer concentrations on the melting temperature and the degree of crystallinity (Figure 3.4). The films showed melting endotherms ranging from 143.3 $^{o}$C to 152.3 $^{o}$C. Apart from this observation, there was no other significant change in the heat flow signal, indicating that the polymer concentrations and solvent ratios didn't have a significant influence on the melting peak and thermal stability. The degree of crystallinity was given in Table 3.2 and calculated using the following equation:

$$X_c = \left(\frac{\Delta H_f}{\Delta H_f^0} \times 100\right) \tag{3.1}$$

where $\Delta H_f$ is the enthalpy of the sample being measured and $\Delta H_f^0$ is the enthalpy of fusion of 100% crystalline P(VDF-HFP), which has a value of 104.7 J g$^{-1}$ [20]. The degree of crystallinity was found to be significantly affected by the polymer concentration. Electrospun nanofibers from 15% w/v polymer solution showed relatively high degree of crystallinity regardless of the solvent ratio. Among the three samples with 15% w/v, the highest degree of crystallinity (53.6%) was obtained when DMF/Acetone ratio was 3/7. It had been widely

published that increasing the degree of crystallinity will enhanced the piezoelectricity of P(VDF-HFP) [21-24]. On the basis of these observations, the P(VDF-HFP) concentration and DMF/Acetone ratio were set as 15% w/v and 3/7, respectively, to fabricate the composite nanofibers.

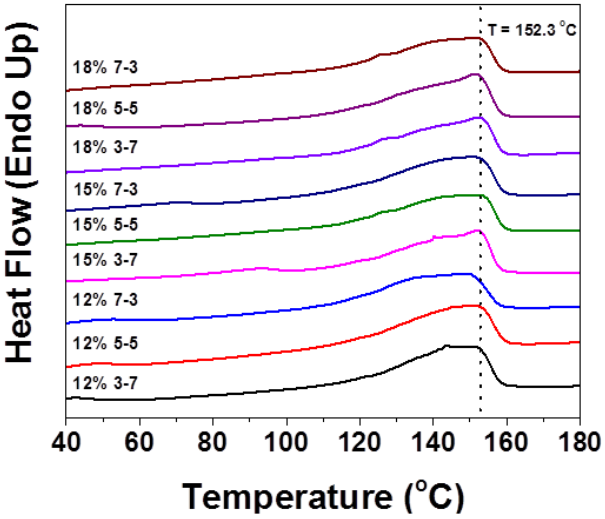


**Figure 3.4** DSC thermograms during heating for (PVDF-HFP) nanofibers.

**Table 3.2** Crystallinity of P(VDF-HFP) nanofibers

| Sample* | $T_m$ ($^oC$) | $\Delta H_m$ (J/g) | Crystallinity (%) |
|---|---|---|---|
| 12-3-7 | 143.3 | 51.4 | 49.1 |
| 12-5-5 | 150.4 | 49.9 | 47.7 |
| 12-7-3 | 148.5 | 48.7 | 46.5 |
| 15-3-7 | 152.3 | 56.0 | 53.5 |
| 15-5-5 | 150.9 | 55.3 | 52.8 |
| 15-7-3 | 150.4 | 54.3 | 51.9 |
| 18-3-7 | 151.5 | 46.0 | 43.9 |
| 18-5-5 | 144.2 | 50.9 | 48.6 |
| 18-7-3 | 146.6 | 53.9 | 51.5 |

*A-B-C: A is the concentration of P(VDF-HFP), B/C is the DMF/Acetone ratio.

### 3.3.3 Fabrication of P(VDF-HFP)/$CoFe_2O_4$ and P(VDF-HFP)/$Fe_3O_4$ Nanofibers

P(VDF-HFP)/$CoFe_2O_4$ and P(VDF-HFP)/$Fe_3O_4$ nanofibers were electrospun by incorporating $CoFe_2O_4$ and PMMA-$Fe_3O_4$ nanoparticles into 15% w/v P(VDF-HFP) solution. Their morphology was characterized by SEM (Figure 3.5). Compared to P(VDF-HFP)/$Fe_3O_4$ nanofibers, P(VDF-HFP)/$CoFe_2O_4$ nanofibers exhibited a rougher surface, which may be due to the bigger size of $CoFe_2O_4$ nanoparticles. Other than that, both electrospun nanofibers showed beadless and uniform morphology.

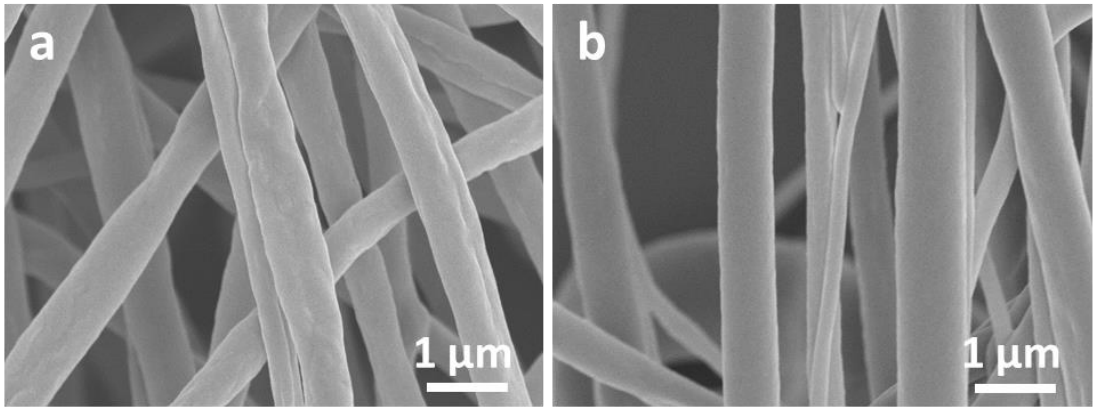


**Figure 3.5** SEM images of (a) P(VDF-HFP)/$CoFe_2O_4$ and (b) P(VDF-HFP)/$Fe_3O_4$ nanofibers.

### 3.3.4 Characterization of P(VDF-HFP)/$CoFe_2O_4$ and P(VDF-HFP)/$Fe_3O_4$ Nanofibers

Figure 3.6a shows the FT-IR spectra for the P(VDF-HFP)/$Co_2Fe_2O_4$ and P(VDF-HFP)/$Fe_3O_4$ nanofibers. There was no peak attributed to α-phase in both composite nanofibers indicating the exclusive existence of β-phase, which was also confirmed by XRD patterns (Figure 3.6b). The XRD pattern of commercial $CoFe_2O_4$ nanoparticles corresponded to standard cubic spinel structure of $CoFe_2O_4$ (JCPDS card: 22-1086) [25]. Compared with pristine P(VDF-HFP) nanofibers, a higher peak occurred at $2\theta=20.6^o$ in both composite nanofibers associating with stronger (200)/(110) reflections of the β-phase. P(VDF-HFP)/$CoFe_2O_4$ nanofibers presented some high-intensity peaks of $CoFe_2O_4$ nanoparticles, while P(VDF-HFP)/$Fe_3O_4$ showed no peak except for P(VDF-HFP). This was due to the PMMA surrounding of $Fe_3O_4$ nanoparticles, which decreased the reflection intensity of pure nanoparticles. Magnetization curves of $CoFe_2O_4$ and $Fe_3O_4$ nanoparticles and corresponding composite nanofibers are shown in Figure 3.6c and 3.6d. The saturation magnetization ($M_S$) of the $CoFe_2O_4$ and $Fe_3O_4$ nanoparticles was 59.99 emu $g^{-1}$ and 26.39 emu $g^{-1}$. The $CoFe_2O_4$ nanoparticles possessed a higher coercive field since more domain walls existed in larger

nanoparticles, whilst $Fe_3O_4$ nanoparticles exhibited superparamagnetic properties. $M_S$ of P(VDF-HFP)/$CoFe_2O_4$ and P(VDF-HFP)/$Fe_3O_4$ nanofibers was much lower with values of 4.53 emu $g^{-1}$ and 1.97 emu $g^{-1}$. The contents of $CoFe_2O_4$ and $Fe_3O_4$ nanoparticles were about 7.6 wt% and 7.5 wt% of P(VDF-HFP), calculated by Equation 2.2. It was believed that, due to the gravity differentiation, sedimentation of dispersed nanoparticles occurred during electrospinning process, leading to a lower fraction of nanoparticles than expected.

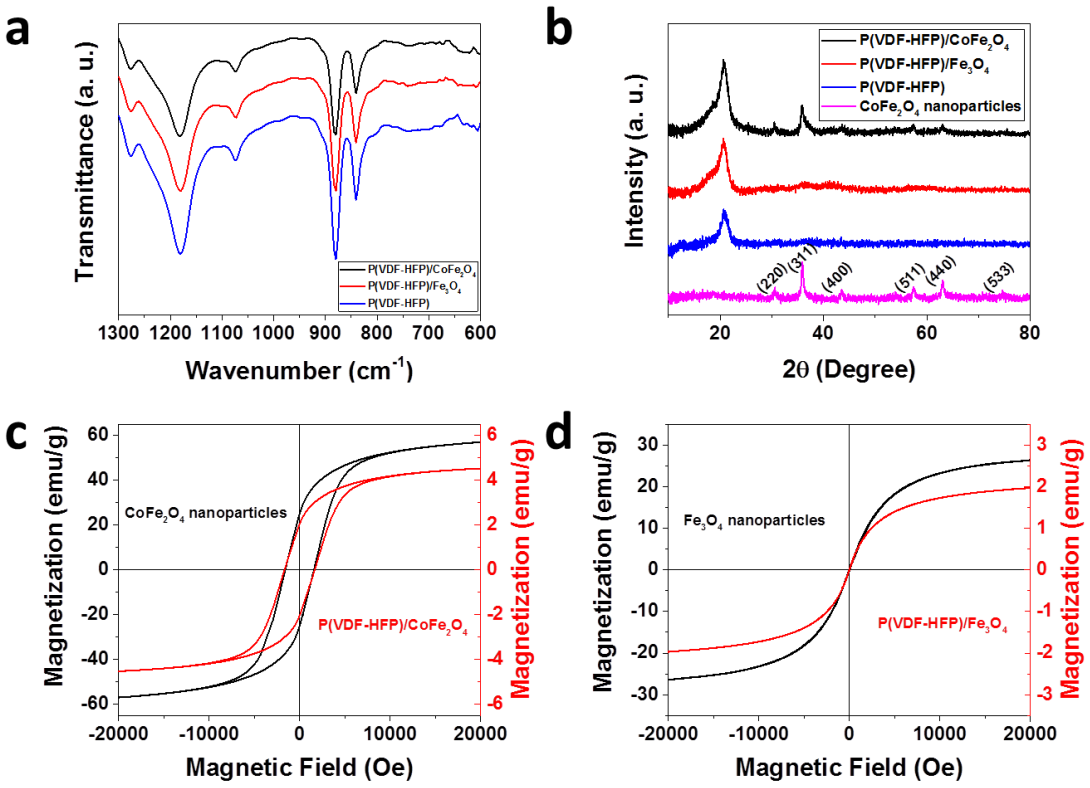


**Figure 3.6** (a) XRD patterns, (b) FT-IR spectra of different nanofibers and room-temperature magnetization isotherms of (c) $CoFe_2O_4$ nanoparticles and P(VDF-HFP)/$CoFe_2O_4$ composite nanofibers (d) $Fe_3O_4$ nanoparticles and PVDF/$Fe_3O_4$ composite nanofibers.

### 3.3.5 PFM Study of P(VDF-HFP) and Composite Nanofibers

The PE properties of the nanofibers were characterized using PFM switching spectroscopy (SS-PFM). Following the same procedure in Chapter 2, SS-PFM measurements were restricted to only one switching spectroscopy curve at any given X-Y position on a nanofiber to alleviate the tip-heating problem. The measurements were first carried out on pristine P(VDF-HFP) nanofibers. Along each nanofiber, only one curve was performed at five different X-Y positions. Figure 3.7 presents the butterfly loops and corresponding phase changing curves measured on three nanofibers as an example. All the amplitude curves showed entire butterfly loops indicating the piezoelectricity of P(VDF-HFP) nanofibers. In some cases, different X-Y positions along the same nanofiber showed significant variations in the butterfly loops (Figure 3.7a, 3.7c and 3.7e) whilst the phase change was more or less consistent (Figure 3.7 b, 3.7d and 3.7f).

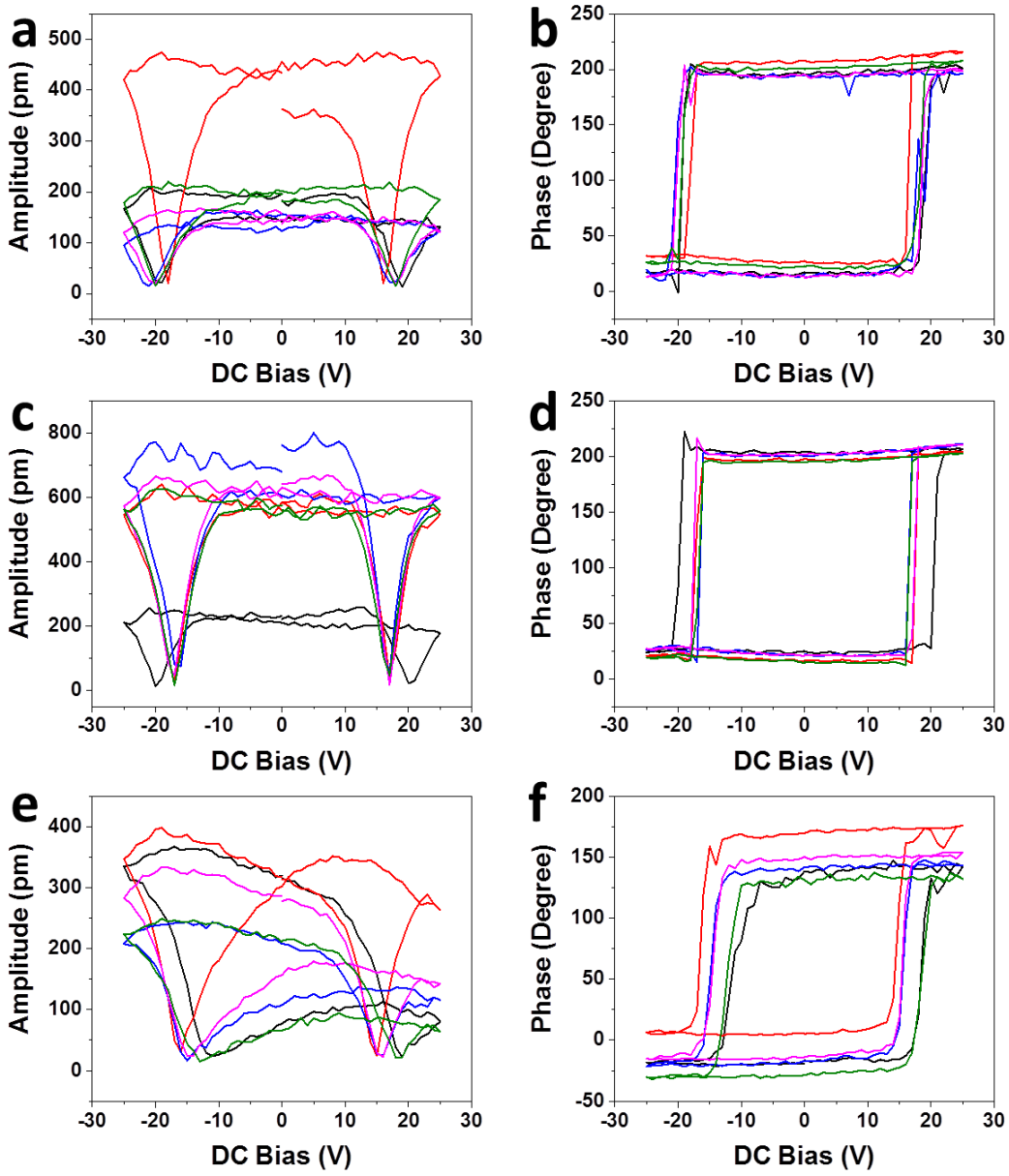


**Figure 3.7** (a, c, e) Butterfly loops and (b, d, f) corresponding phase changing curves of different P(VDF-HFP) nanofibers.

For statistical analysis, switching spectroscopy curves were performed on 12 different nanofibers, giving a total of 60 curves with 5 different X-Y positions along each nanofiber. The maximum value of each butterfly loop was taken as the PE response. The average PE response of each nanofiber is shown in Figure 3.8a, of which the error bar was calculated

from all five spots. Significant variations were found in some nanofibers, indicating the spatial distribution dependence of the P(VDF-HFP) nanofiber PE response. Unlike PVDF, the PE response of P(VDF-HFP) nanofibers was not uniform. Furthermore, there appeared to be two distinct populations of nanofibers exhibiting either higher amplitudes of ≈ 600 pm or lower amplitudes of ≈ 200-300 pm. Even on the same nanofiber, different X-Y positions showed large variations in the PE response. These observations were attributed to the copolymerization of P(VDF-HFP), consisting of two kinds of monomers, VDF and HFP. Figure 3.9 shows the schematic representation of the P(VDF-HFP) repeat units [26]. The VDF component possesses piezoelectricity because of the difference in electronegativity between the hydrogen and fluorine atoms. In contrast, there is no significant difference in electronegativity within the HFP component and thus the piezoelectricity of the HFP component is much lower. Since the PFM measurements are highly localized (i.e. tip radius of < 10 nm), probing of the surface may therefore lead to lateral nanoscale variations in the PE response. Figure 3.8b shows the histogram of the PE response, giving a bimodal distribution with peaks at 253.2 pm and 647.7 pm. Similarly, this correlated to the amplitude values in Figure 3.8a and may be due to the copolymerization of P(VDF-HFP) as mentioned above. The amplitude values ranged from 100 pm to 1000 pm and the average value was 398.3 ± 222.4 pm. Despite the bimodal distribution, the PE response of P(VDF-HFP) was much higher than that of PVDF. According to the mechanism of SS-PFM measurement, this amplitude related to the longitudinal deformation of tested samples generated by an electric field, i.e. $d_{33}$. However, any deformation caused by $d_{31}$ piezoelectricity could also translate to a change in the amplitude in these PFM measurements [27]. Therefore, the higher PE response measured for P(VDF-HFP) was explained by its higher $d_{31}$ coefficient, yet comparable $d_{33}$ coefficient [6], compared to that of the PVDF nanofibers.

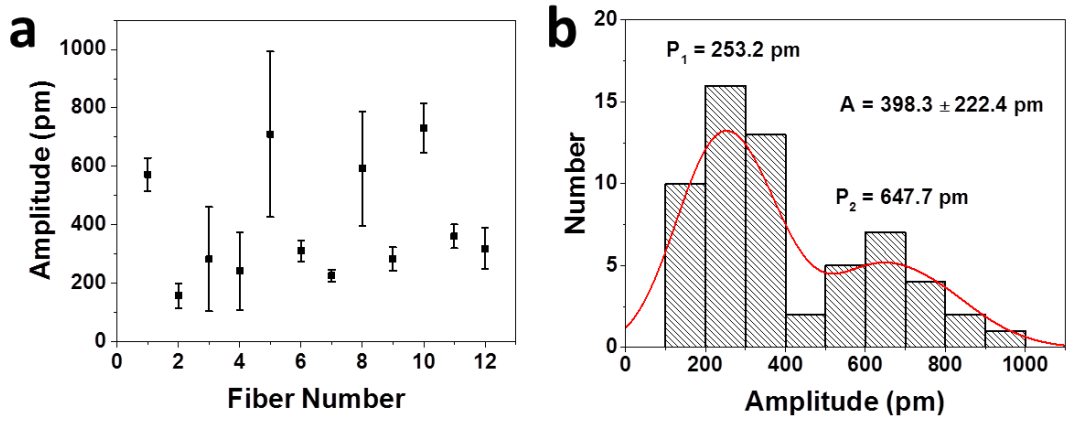


**Figure 3.8** (a) Average PE response of 12 different P(VDF-HFP) nanofibers and (b) PE response histogram of P(VDF-HFP) nanofibers. "A" stands for average value. "$P_1$" and "$P_2$" stand for individual peak values.

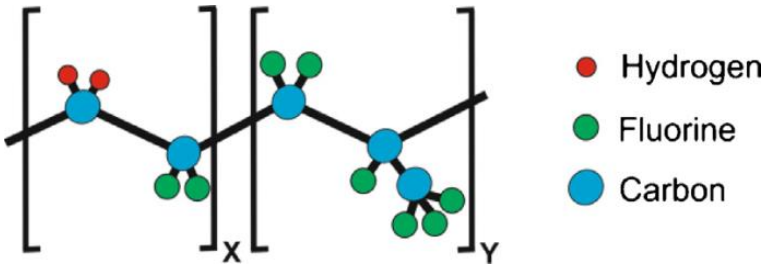


**Figure 3.9** Schematic representation of the P(VDF-HFP) repeat units [26].

After evaluating the PE response of pristine P(VDF-HFP) nanofibers, the same measurements were also carried out on P(VDF-HFP)/$CoFe_2O_4$ and P(VDF-HFP)/$Fe_3O_4$ composite nanofibers and the results are shown in Figure 3.10. Figure 3.10a and 3.10b show the butterfly loops and corresponding phase changing curves obtained on five X-Y positions along a P(VDF-HFP)/$CoFe_2O_4$ nanofiber and Figure 3.10c and 3.10d are for a P(VDF-HFP)/$Fe_3O_4$ nanofiber. Similar to the pristine nanofibers, the butterfly loops for the ME

composite nanofibers showed variations at different X-Y positions whilst the phase changes were similar. However, it was observed that the voltages at which the phase changed by 180 degrees were lower compared to pristine P(VDF-HFP). The coercive bias decreased to 10-15 V for both ME composite nanofibers (Figure 3.10b and 3.10d) as opposed to higher voltages of ≈ 20 V for the pristine P(VDF-HFP) (Figure 3.7b, 3.7d and 3.7f). Since the switching of dipoles only occured when the applied electric field was higher than the coercive field, the lower coercive bias for the composite nanofibers indicated their enhanced piezoelectriciy. This also correlated with their higher PFM amplitude values, which were discussed and shown further below in Figure 3.11.

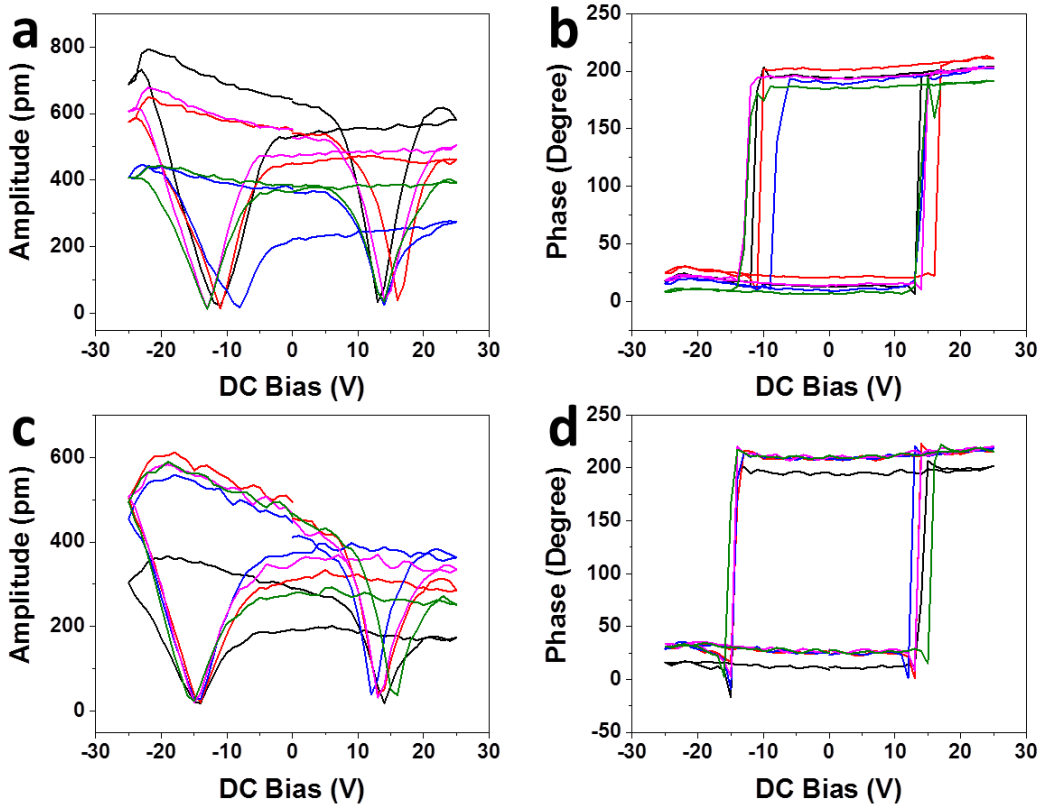


**Figure 3.10** (a, c) Butterfly loops and (b, d) corresponding phase changing curves of (a, b) P(VDF-HFP)/$CoFe_2O_4$ and (c, d) P(VDF-HFP)/$Fe_3O_4$ composite nanofibers.

Following the same statistical analysis method for P(VDF-HFP), Figure 3.11a and 3.11b show that, along a single nanofiber, the variation (i.e. error bars) of the PE response was comparable for both composite nanofibers with $CoFe_2O_4$ (Figure 3.11a) and $Fe_3O_4$ (Figure 3.11b) nanoparticles and the observed variation in a majority of the composite nanofibers was greater than that of the pristine P(VDF-HFP) nanofibers (Figure 3.8a). The incorporation of the nanoparticles could induce such variations through effects on 1) the formation of nanofibers during the electrospinng process, such as interuption of solvent evaporation and crystalline phase formation, 2) the PE response of the P(VDF-HFP) due to physical interactions between the nanoparticles and polymer, or 3) the measured PFM amplitude for an X-Y position where the PFM tip is located in the vicinity of a distributed nanoparticle(s) within the nanofiber (e.g. a nanoparticle positioned directly under the PFM tip). Interestingly, despite the variation in amplitude along a single nanofiber, the incorporation of magnetic nanoparticles did not result in two different PE responses, as shown in Figure 3.8a for the pristine P(VDF-HFP) nanofibers. This was confirmed in the histograms of P(VDF-HFP)/$CoFe_2O_4$ and P(VDF-HFP)/$Fe_3O_4$ nanofibers (Figure 3.11c and 3.11d) that showed a unimodal distribution, with peak distributions of 519.8 ± 148.2 pm and 413.3 ± 146.3 pm, respectively. The results indicated two findings, firstly that the addition of $CoFe_2O_4$ nanoparticles further enhanced the PE response of P(VDF-HFP) compared to $Fe_3O_4$ nanoparticles and secondly the addition of both types of magnetic nanoparticles modified the polymer structure to produce homogeneous (i.e. unimodal distribution) PE properties.

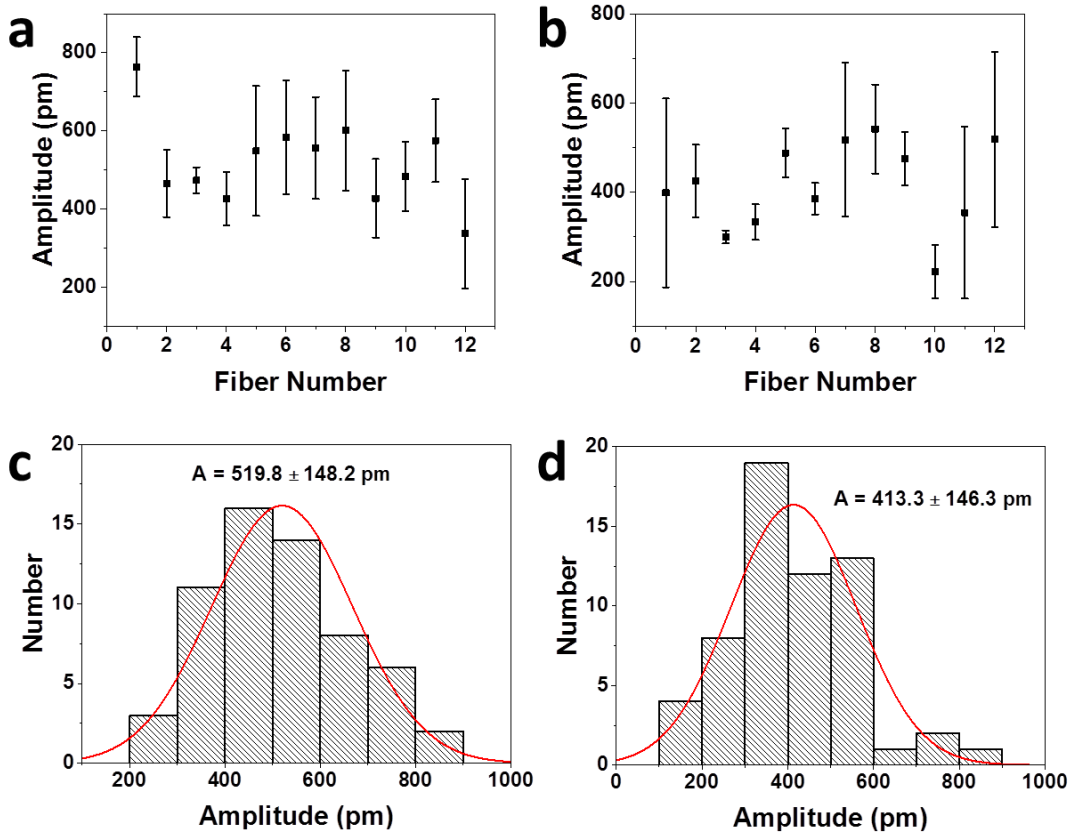


**Figure 3.11** (a, b) Average PE response and (c, d) PE response histograms of (a, c) P(VDF-HFP)/$CoFe_2O_4$ and (b, d) P(VDF-HFP)/$Fe_3O_4$ composite nanofibers.

### 3.3.6 ME effect of P(VDF-HFP)/$CoFe_2O_4$ and P(VDF-HFP)/$Fe_3O_4$ Nanofibers

To explore the localized ME effect of composite nanofibers, PFM/VFM was used to measure the change of PE response in different magnetic fields ranging from -2000 Oe to 2000 Oe. For a single nanofiber, a topography image was taken prior to performing a switching spectroscopy measurement. With the application of external magnetic fields of 0 Oe, 500 Oe, 1000 Oe, 1500 Oe and 2000 Oe, switching spectroscopy measurements were obtained at five different X-Y positions along a nanofiber. The magnetic field was then switched to 0 Oe and another set of measurement was carried out at 0 Oe, -500 Oe, -1000 Oe, -1500 Oe and -2000

Oe. The same procedure was conducted on pristine P(VDF-HFP) and both composite nanofibers for comparison.

Figure 3.12 shows the effect of the applied magnetic field on the PE response for all three samples in both directions of the magnetic field. For the pristine P(VDF-HFP) nanofibers (Figures 3.12a), all five X-Y positions showed random variations as a function of the magnetic field increasing in the positive direction. However, when the magnetic field was applied in the opposite direction toward the negative (Figures 3.12b), the amplitude signal appeared to show a slight decrease for all X-Y positions. Since the pristine P(VDF-HFP) should not respond to the magnetic field, the change of amplitude may be attributed to a change of tip position on the nanofiber that resulted in a different PE response, as discussed above in Section 3.3.5. However, the exact reason was still unclear. In addition, the decrease in the amplitude as the magnetic field was change from 0 to -2000 Oe is ≈ 100-200 pm. Given the observed variations, the statistical significance of this decrease was further analysed below in Figure 3.13 to rationalize the shift with both composites. Figure 3.12c and 3.12d were obtained from the P(VDF-HFP)/$CoFe_2O_4$ composite nanofibers. The PE response showed a clear decreasing trend in the positive direction (Figure 3.12c) while in the negative direction the most significant change occurred at -500 Oe for all five spots (Figure 3.12d). Beyond -500 Oe, there was no significant change in the amplitude signal (Figure 3.12d). Figure 3.12e and 3.12f were obtained from P(VDF-HFP)/$Fe_3O_4$ composite nanofibers, showing that the PE response decreased in the positive direction of the applied magnetic field (Figure 3.12e), which was similar to the P(VDF-HFP)/$CoFe_2O_4$ nanofibers (Figure 3.12c) and in agreement with the previous PFM/VFM measurements on PVDF/$Fe_3O_4$ nanofibers in Chapter 2. In contrast, the PE response in the negative direction is again more complex, showing significant variations and no clear trend (Figure 3.12f). Similar to that previously discussed in Chapter 2, one approach to explain the observed decrease in the PE response as

the magnetic field increases in the positive direction is proposed by Vopsaroiu *et al.* [28]. Further to this, however, the decreasing trend for both the P(VDF-HFP)/$CoFe_2O_4$ and P(VDF-HFP)/$Fe_3O_4$ nanofibers is not plausible given that the MS coefficients of the $Fe_3O_4$ and $CoFe_2O_4$ have opposite signs.

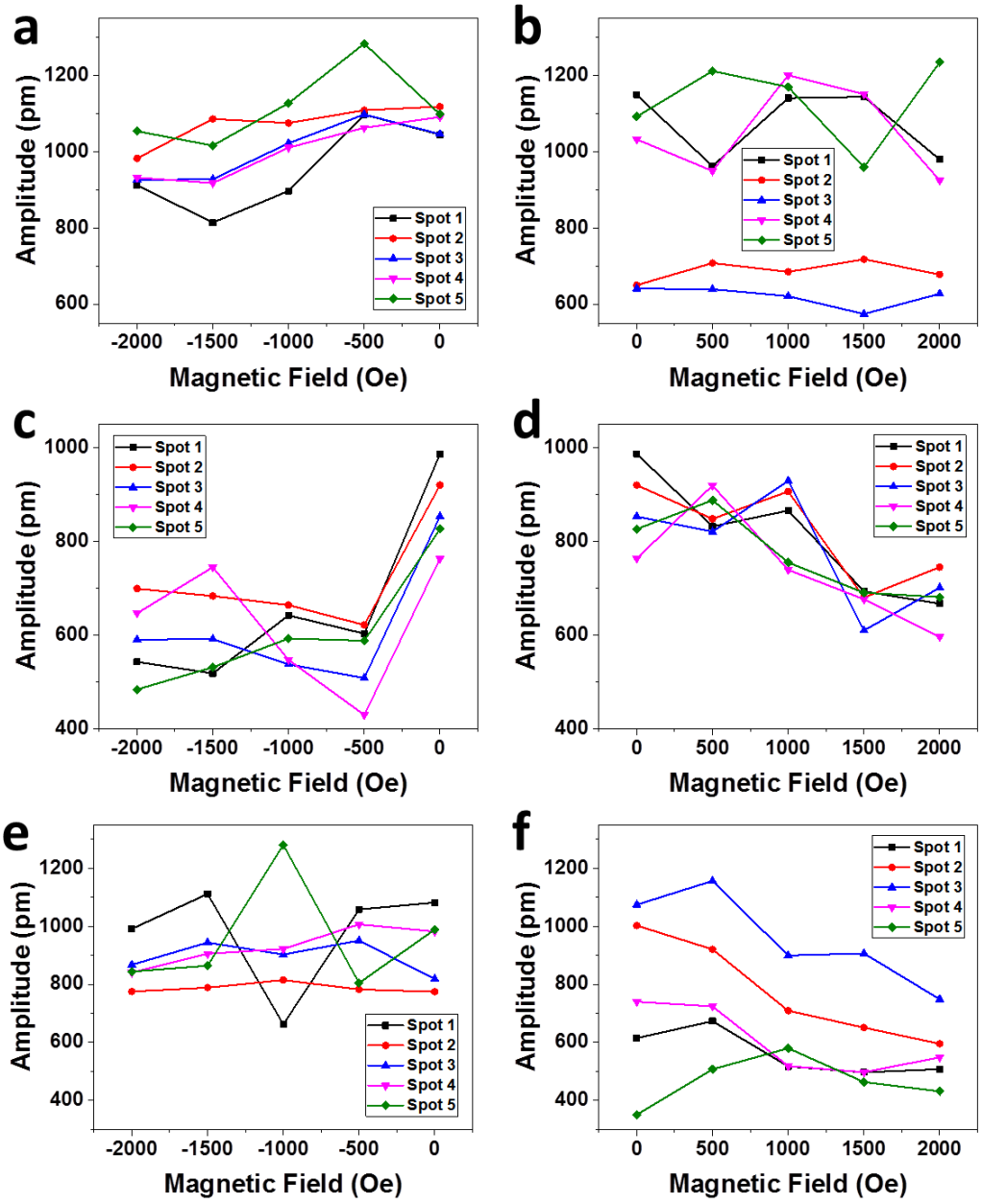


**Figure 3.12** PE response dependence on (a, c, e) positive and (b, d, f) negative magnetic field strength obtained in (a, b) P(VDF-HFP), (c, d) P(VDF-HFP)/$CoFe_2O_4$ and (e, f) P(VDF-HFP)/$Fe_3O_4$ nanofibers.

To more closely examine the shifts in the amplitude between the pristine and composite nanofibers, particularly using a statistical analysis, the maximum change of PE response

($A_{max}$ - $A_{min}$) observed with the entire range of the applied magnetic field was compared using box-and-whisker plots in Figure 3.13. Six boxes showed the data collected on pristine P(VDF-HFP), P(VDF-HFP)/$Fe_3O_4$ and P(VDF-HFP)/$CoFe_2O_4$ nanofibers in both the positive and negative directions of the applied magnetic field. For each set of data, a total of 20 different X-Y positions were sampled on four different nanofibers. The upper and lower edges of the box showed the third quartile and first quartile. The solid line and the open square in the box showed the median and mean values, which were also displayed in Table 3.3. Comparing the median and mean values of three samples, P(VDF-HFP)/$Fe_3O_4$ composite nanofibers possessed the highest change of PE response in the positive direction while P(VDF-HFP)/$CoFe_2O_4$ composite nanofibers gave the most significant change in the negative direction.

Analysis of variance (ANOVA) test was carried between different columns to compare the shifts of different samples. In the positive direction of magnetic field, the data collected from pristine P(VDF-HFP) and P(VDF-HFP)/$Fe_3O_4$ nanofibers were statistically significant ($P<0.05$). However, the shifts of two composite samples showed no significant difference ($P\geq0.05$). In the negative direction, only the shift of P(VDF-HFP)/$CoFe_2O_4$ was considered as different with that of P(VDF-HFP). In addition, the two composite nanofibers showed significant difference, which may be due to the interaction between polymer matrix and magnetic nanoparticles. Combined with observations in Figure 3.12, a conclusion was drawn that the addition of $CoFe_2O_4$ and $Fe_3O_4$ nanoparticles did have interactions with P(VDF-HFP) and ME effect existed in both composite nanofibers as their PE response was more responsive to magnetic field when compared with P(VDF-HFP) nanofibers.

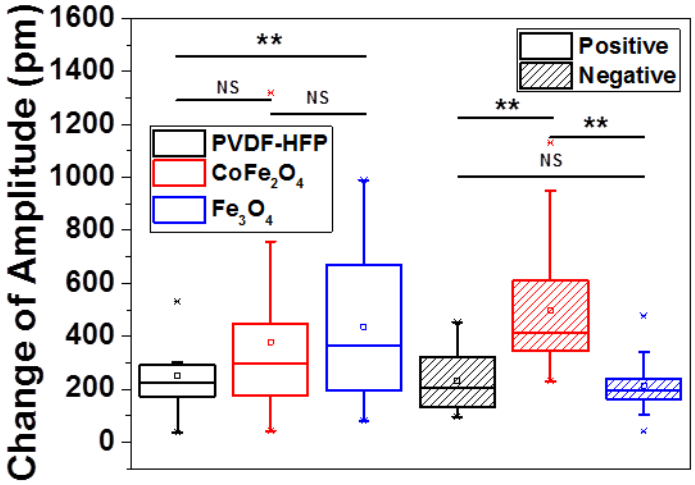


**Figure 3.13** Change of amplitude in P(VDF-HFP) and composite nanofibers. Statistical significances were calculated with ANOVA test. ** very significant, P<0.01; * significant , P<0.05; NS, non-significant, P≥0.05.

**Table 3.3** Statistics for pristine P(VDF-HFP) and composite nanofibers

| | Median (pm) | | Mean (pm) | |
|---|---|---|---|---|
| | Positive | Negative | Positive | Negative |
| P(VDF-HFP) | 224.2 | 204.7 | 251.1 | 232.1 |
| P(VDF-HFP)/$CoFe_2O_4$ | 298.2 | 411.1 | 377.3 | 496.1 |
| P(VDF-HFP)/$Fe_3O_4$ | 365.2 | 195.0 | 435.0 | 214.3 |

## 3.4 Conclusions

As an extension work of Chapter 2, P(VDF-HFP) nanofibers were fabricated by electrospinning method. Based on the same solution and electrospinning parameters, P(VDF-HFP)/$CoFe_2O_4$ and P(VDF-HFP)/$Fe_3O_4$ composite nanofibers were electrospun with the incorporation of $CoFe_2O_4$ and PMMA-$Fe_3O_4$ nanoparticles. Compared to PVDF nanofibers, the PE properties of P(VDF-HFP) increased significantly which was attributed to a higher $d_{31}$ coefficient. However, the histogram of PFM amplitude showed a bimodal distribution due to its copolymerization and possible cross-talk existing between the $d_{33}$ and $d_{31}$ during PFM measurements. Both composite nanofibers were found to have higher PE and more uniform responses than pristine P(VDF-HFP) nanofibers as revealed by PFM measurements.

Finally, the magnetic field dependence of PE response for both composite nanofibers was estimated by SS-PFM measurements under different in-plane magnetic fields. The amplitudes of both composites were found to decrease with the magnetic fields in the positive direction. Compared to P(VDF-HFP), the impact of magnetic field on PE response of composite nanofibers was statistically significant as revealed by ANOVA test. Though the mechanism was not clear enough, the nanoscale ME effect was confirmed in both P(VDF-HFP)/$CoFe_2O_4$ and P(VDF-HFP)/$Fe_3O_4$ composite nanofibers.

## 3.5 References


1. Martins, P., et al., *Polymer-based magnetoelectric materials.* Advanced Functional Materials, 2013. **23**(27): p. 3371-3385.

2. Mardana, A., et al., *Magnetoelectric effects in ferromagnetic Cobalt/ferroelectric copolymer multilayer films.* Applied Physics Letters, 2010. **97**(11): p. 112904.

3. Zhang, J.X., et al., *The effect of magnetic nanoparticles on the morphology, ferroelectric, and magnetoelectric behaviors of CFO/P(VDF-TrFE) 0–3 nanocomposites.* Journal of Applied Physics, 2009. **105**(5): p. 054102.

4. Fang, F., et al., *A multipeak phenomenon of magnetoelectric coupling in Terfenol-D/P(VDF-TrFE)/Terfenol-D laminates.* Journal of Applied Physics, 2010. **108**(10): p. 104505.

5. Kulkarni, A., et al., *Giant magnetoelectric effect at low frequencies in polymer-based thin film composites.* Applied Physics Letters, 2014. **104**(2): p. 022904.

6. Neese, B., et al., *Piezoelectric responses in Poly(vinylidene fluoride/hexafluoropropylene) copolymers.* Applied Physics Letters, 2007. **90**(24): p. 242917.

7. Wegener, M., et al., *Ferroelectric polarization in stretched piezo- and pyroelectric Poly(vinylidene fluoride-hexafluoropropylene) copolymer films.* Journal of Applied Physics, 2002. **92**(12): p. 7442-7447.

8. Liu, X., et al., *Magnetoelectricity in $CoFe_2O_4$ nanocrystal-P(VDF-HFP) thin films.* Nanoscale Research Letters, 2013. **8**(1): p. 374.

9. Jin, J., et al., *Multiferroic polymer laminate composites exhibiting high magnetoelectric response induced by hydrogen-bonding interactions.* Advanced Functional Materials, 2014. **24**(8): p. 1067-1073.

10. Zi, Z., et al., *Synthesis and magnetic properties of $CoFe_2O_4$ ferrite nanoparticles.* Journal of Magnetism and Magnetic Materials, 2009. **321**(9): p. 1251-1255.

11. Nongjai, R., et al., *Magnetic and electrical properties of in doped cobalt ferrite nanoparticles.* Journal of Applied Physics, 2012. **112**(8): p. 084321.

12. Vadivel, M., et al., *Role of SDS surfactant concentrations on the structural, morphological, dielectric and magnetic properties of $CoFe_2O_4$ nanoparticles.* RSC Advances, 2015. **5**(34): p. 27060-27068.

13. Long, N.V., et al., *Related magnetic properties of $CoFe_2O_4$ cobalt ferrite particles synthesised by the polyol method with $NaBH_4$ and heat treatment: new micro and nanoscale structures.* RSC Advances, 2015. **5**(70): p. 56560-56569.

14. Luders, U., et al., *$NiFe_2O_4$: A versatile spinel material brings new opportunities for spintronics.* Advanced Materials, 2006. **18**(13): p. 1733-1736.

15. Tang, Z.H., et al., *Magnetoelectric coupling effect in lead-free $Bi_4Ti_3O_{12}/CoFe_2O_4$ composite films derived from chemistry solution deposition.* Smart Materials and Structures, 2016. **25**(8): p. 085020.

16. Zhu, Q., et al., *Multiferroic $CoFe_2O_4$–$BiFeO_3$ core–shell nanofibers and their nanoscale magnetoelectric coupling.* Journal of Materials Research, 2014. **29**(05): p. 657-664.

17. Goncalves, R., et al., *Magnetoelectric $CoFe_2O_4$/Polyvinylidene Fluoride electrospun nanofibres.* Nanoscale, 2015. **7**(17): p. 8058-8061.

18. Martins, P., et al., *Optimizing piezoelectric and magnetoelectric responses on $CoFe_2O_4$/P(VDF-TrFE) nanocomposites.* Journal of Physics D-Applied Physics, 2011. **44**(49): p. 495303.

19. Liu, B.H., et al., *Strain-induced high coercivity in $CoFe_2O_4$ powders.* Applied Physics Letters, 2006. **88**(4): p. 042506.

20. Rudhziah, S., et al., *Conductivity and structural studies of Poly(vinylidene fluoride co-hexafluoropropylene)/Polyethyl Methacrylate blend doped with Ammonium Triflate.* International Journal of Electrochemical Science, 2013. **8**(1): p. 421-434.

21. He, X., et al., *Phase transition and properties of a ferroelectric Poly(vinylidene fluoride-hexafluoropropylene) copolymer.* Journal of Applied Physics, 2005. **97**(8): p. 084101.

22. Wang, F.P., et al., *Enhanced polarization in melt-quenched and stretched Poly(vinylidene fluoride-hexafluoropropylene) films.* Ieee Transactions on Dielectrics and Electrical Insulation, 2010. **17**(4): p. 1088-1095.

23. Mandal, D., et al., *Improved performance of a polymer nanogenerator based on Silver nanoparticles doped electrospun P(VDF-HFP) nanofibers.* Physical Chemistry Chemical Physics, 2014. **16**(22): p. 10403-10407.

24. Adhikary, P.,et al., *The co-operative performance of a hydrated salt assisted sponge like P(VDF-HFP) piezoelectric generator: an effective piezoelectric based energy harvester.* Physical Chemistry Chemical Physics, 2015. **17**(11): p. 7275-7281.

25. Wang, H., et al., *A facile synthesis of monodisperse $CoFe_2O_4/SiO_2$ nanoparticles.* Applied Surface Science, 2011. **257**(16): p. 7107-7112.

26. Martins, P., et al., *Electroactive phases of Poly(vinylidene fluoride): determination, processing and applications.* Progress in Polymer Science, 2014. **39**(4): p. 683-706.

27. Kalinin, S.V., et al., *Imaging mechanism of piezoresponse force microscopy in capacitor structures.* Applied Physics Letters, 2008. **92**(15): p. 152906.

28. Vopsaroiu, M., et al., *Experimental determination of the magnetoelectric coupling coefficient via piezoelectric measurements.* Measurement Science and Technology, 2008. **19**(4): p. 045106.

# 4 Investigation of Piezoelectricity of PLA-based Magnetoelectric Nanofibers by PFM

## 4.1 Introduction

### 4.1.1 Piezoelectricity of PLA

Poly (lactic acid) (PLA) as a renewable resource is very low cost, environmentally friendly and due to it biocompatibility has become a very important polymer in biomedical applications [1]. When a helical PLA molecule is subjected to a shear strain in the direction of the helix axis, the permanent dipole of the C=O bond rotates slightly and induces a change in the polarization perpendicular to the plane of the shear strain, as illustrated in Section 1.3.2.3 [2]. Unlike the poly (vinylidene fluoride) (PVDF) family of piezoelectric (PE) polymers, the piezoelectricity of PLA is generated from its ordered structure and thus does not show a pyroelectric effect when operating as a PE material [2-4]. This unique property is important in applications where these two types of effects need to be separated.

PLA fibers have shown a large PE strain constant due to their ultimate uniaxial alignment [5]. In this work, an axis-oriented PLA fiber with a drawing ratio of 10 and a diameter of 10 μm is obtained by a high-speed spinning process. A soft sensor has been fabricated with the helical torsion of a single PLA fiber coil, demonstrating a new technique for realizing sensing using a PLA fiber with shear piezoelectricity [5]. Electrospinning is a simple approach for fabricating fibers with uniaxially aligned dipoles due to the electrostatic forces applied during fiber formation [6]. Recently, electrospun PLA nanofibers have been used to power LEDs via the PE effect [7]. During electrospinning, the helical PLA nanofibers exhibit angled and preferential orientation of C=O dipoles along its helical direction aided by the poling effect

[7]. Nanoscale piezoelectricity of PLA microfibers has been demonstrated by Sencadas *et al.*, confirming that the dipole switching can be achieved by *in situ* electric poling using PFM [8]. As shown in Figure 4.1c, two PE response loops are obtained on PLA microfibers of which the PE coefficient increases with increased poling voltages from 100 V (Figure 4.1a) to 200 V (Figure 4.1b).

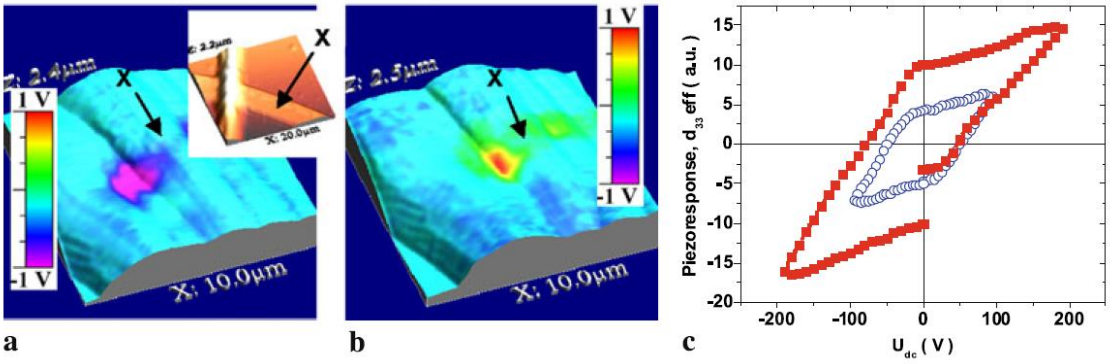


**Figure 4.1** PLA fiber surfaces poled at (a) 100 and (b) 200 V. (c) measured PE response loops recorded in locations shown by x in (a) and (b) [8].

### 4.1.2 PLA with Biodegradable PLGA

Poly (DL-lactide-co-glycolide) (PLGA) is composed of lactic acid and glycolic acid monomer units and has wide applications in drug delivery, tissue engineering, and modification of biological interfaces [9, 10]. The degradation, mechanical and chemical properties of PLGA can be tuned by adjusting the ratio of the two monomers [11]. PLGA is not a PE material but shows better biocompatibility and shorter degradation time [12, 13], whereas PLA has a higher breaking strength and initial modulus [14]. Combining PLA and PLGA is of great interest when considering applications that require control over the function

efficiency and the degradation rate. For example, the highest drug encapsulation efficiency is found in PLA/PLGA (50/50) [15], while a higher content of PLGA in PLA/PLGA composites shortens the degradation time [16]. Further tuning of the piezoelectricity in combination with the degradation is less well understood though may well broaden the *in vivo* applications of PLA, including harvesting energy from the motions of biological tissues, producing electrical outputs to promote cell growth in tissue engineering [17] or electrically controlling the drug delivery process [18].

### 4.1.3 PLA with Magnetic Nanoparticles

In addition to PLGA, incorporating magnetic nanoparticles into PLA is an emerging research area [19-21]. A $Fe_3O_4$/PLA microsphere structure has been developed as a magnetic targeted drug delivery system, offering a new approach to localized drug release [19, 20]. Many studies have looked into the synthesis [20, 22], stability [23], or biocompatibility [21] of PLA/$Fe_3O_4$ or PLA/$CoFe_2O_4$ systems for targeting of *in vivo* applications in biomedicine. Despite not being the focus of studies, these PLA/magnetic nanoparticle composites are expected to possess magnetoelectric (ME) properties that have potential to contribute to new functions in many of the current applications involving this polymer.

Therefore, the PE behaviour of biocompatible PLA-based ME nanocomposites was investigated in this chapter. The trade-off between controlling degradation versus the piezoelectricity of biocompatible materials was also assessed by measuring the PE response of PLA nanofibers incorporating different amount of PLGA. Finally, magnetic $CoFe_2O_4$ nanoparticles were incorporated into the PLA nanofibers to produce ME composites, which

like recent studies on ceramic ME nanocomposites could be used as *in vivo* contactless electrodes [24, 25].

## 4.2 Experimental

### 4.2.1 Materials

$CoFe_2O_4$ nanoparticles (30 nm), were purchased from Aldrich. PLA and PLGA were purchased from PURAC, Netherland. DMF and chloroform ($CHCl_3$) were purchased from Chem Supply. All the chemicals were used without further purification.

### 4.2.2 Fabrication of PLA and PLA/PLGA Nanofibers

PLA powders were dissolved in mixed organic solvents (DMF/$CHCl_3$ = 1/3 by volume) at 6% w/v, 9% w/v 12% w/v and 15% w/v. The mixture was stirred overnight at room temperature to achieve complete dissolution of PLA powders. A NANON electrospinning system (MECC Co. Ltd, Japan) was used for electrospinning process. The solution was placed in a plastic syringe fitted with a 25 G needle, and electrospun at 20 kV. A syringe pump was used to feed the polymer solution into the needle tip at a rate of 0.5 mL/h. The distance between the needle and collector plate was 15 cm.

To fabricate PLA/PLGA nanofibers, PLA and PLGA powders were dissolved in mixed organic solvents (DMF/$CHCl_3$ = 1/3 by volume). The whole PLA/PLGA concentration was set as 6% w/v, 9% w/v and 12% w/v. The ratio of PLA/PLGA was set as 75/25, 50/50 and 25/75 by weight. For the electrospinning, all the parameters were set as same as those used

for fabricating PLA nanofibers. The electrospun nanofibers were named as PLA/PLGA (75/25), PLA/PLGA (50/50) and PLA/PLGA (25/75).

### 4.2.3 Fabrication of PLA/$CoFe_2O_4$ Nanofibers

Based on the morphology of PLA nanofibers, the 12% w/v PLA solution (DMF/$CHCl_3$ = 1/3 by volume) was used to fabricate composite nanofibers for PE response measurement by PFM. To obtain PLA/$CoFe_2O_4$ solutions, $CoFe_2O_4$ nanoparticles (5 wt% and 10 wt% of PLA) were added into the polymer solution, followed by sonication for 4 h. The solutions were then electrospun using the same parameters as those for pure PLA solutions. The obtained nanofibers were named as PLA-5 and PLA-10 respectively.

### 4.2.4 Physico-Chemical Characterization of Nanofibers

To characterize the morphology of nanofibers, field emission scanning electron microscope (FE-SEM, JEOL JSM-7500FA) was used with an accelerating voltage of 5.0 kV and an emission current of 10 mA. The nanofibers were directly electrospun on a silicon wafer with a thin layer of sputter gold (15 nm, Edwards Sputter Coater). Fourier transform infrared spectroscopy (FT-IR) was performed using the Shimadzu AIM8000 FT-IR spectrometer. X-ray diffraction (XRD) measurements were carried out using a powder XRD system (GBC MMA, Cu Kα radiation, $\lambda$ = 0.15418 nm) at a scanning rate of 5° $min^{-1}$. Magnetic property under different magnetic fields was carried out on a 14 T physical properties measurement system (PPMS).

### 4.2.5 Atomic Force Microscopy (AFM) and Piezoresponse Force Microscopy (PFM)

For AFM and PFM measurement, the substrate used was a glass cover slip with a 50 nm gold layer applied using sputter coating (Edwards Sputter Coater) and the nanofibers were then directly electrospun onto the substrate. AFM topography images in air were obtained in AC mode at a scan rate of 0.5 Hz using a MFP-3D AFM (Asylum Research, CA). For measuring piezoelectricity of the nanofibers, PFM switching spectroscopy (SS-PFM) was used to monitor the vertical deformation of the composite nanofibers. Typically, a Pt/Ir coated silicon tip with force constant of 2.8 N/m and gold layer on the substrate were used as top and bottom electrodes. Before SS-PFM measurements, AC voltages (200-500 mV) were applied to oscillate the tip to obtain the resonance frequency. The contact frequency varied from 300 kHz to 310 kHz due to slightly variations across the sample surface. During the SS-PFM measurements, a sweeping DC bias (Frequency = 0.2 Hz) in the range of ± 25 V was applied to the tip to stimulate the PE response. During acquisition of a single SS-PFM curve, 5 cycles of a sweeping triangle/square wave were applied to the tip to obtain trustable results. For statistical study, SS-PFM measurements were carried on 20 different nanofibers for each sample and three X-Y positions for each nanofiber, giving an overall data points of 60 (N = 60). Data analysis was carried out on Igor Pro 6.36 Software.

## 4.3 Results and Discussion

### 4.3.1 Fabrication of PLA Nanofibers

Figure 4.2 shows SEM images of PLA nanofibers electrospun with different polymer concentrations. Among the four samples, 6% w/v PLA nanofibers exhibited the smallest diameter (Figure 4.2a). Beaded structures were observed in both 6% w/v and 9% w/v PLA

nanofibers due to the low viscosity of the polymer solution (Figure 4.2a and 4.2b), while in higher concentrations, the nanofibers showed uniform morphology without beads (Figure 4.2c and 4.2d). When the concentration increased to 15% w/v, instability was induced as curved nanofibers appeared (Figure 4.2d). Therefore, further structural characterizations and PFM measurements were carried on 12% w/v PLA nanofibers. Figure 4.3a-d gives the histograms for diameters of PLA nanofibers (N=100) at different concentrations and Figure 4.3e shows the average values. From 6% w/v to 15% w/v, the average diameter increased from 224.2 ± 31.7 nm, to 469.1 ± 57.6 nm, to 903.9 ± 105.3 nm and to 987.8 ± 144.4 nm.

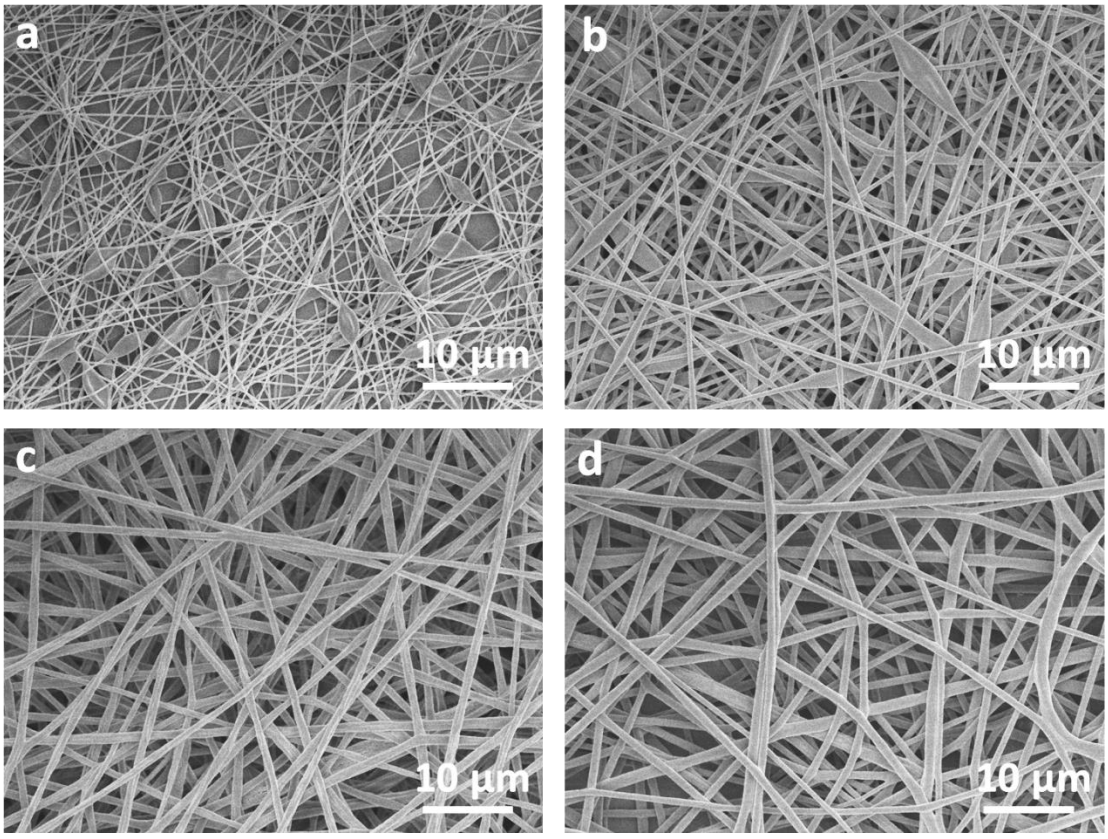


**Figure 4.2** SEM images of PLA nanofibers with different concentrations: (a) 6% w/v, (b) 9% w/v, (c) 12% w/v and (d) 15% w/v.

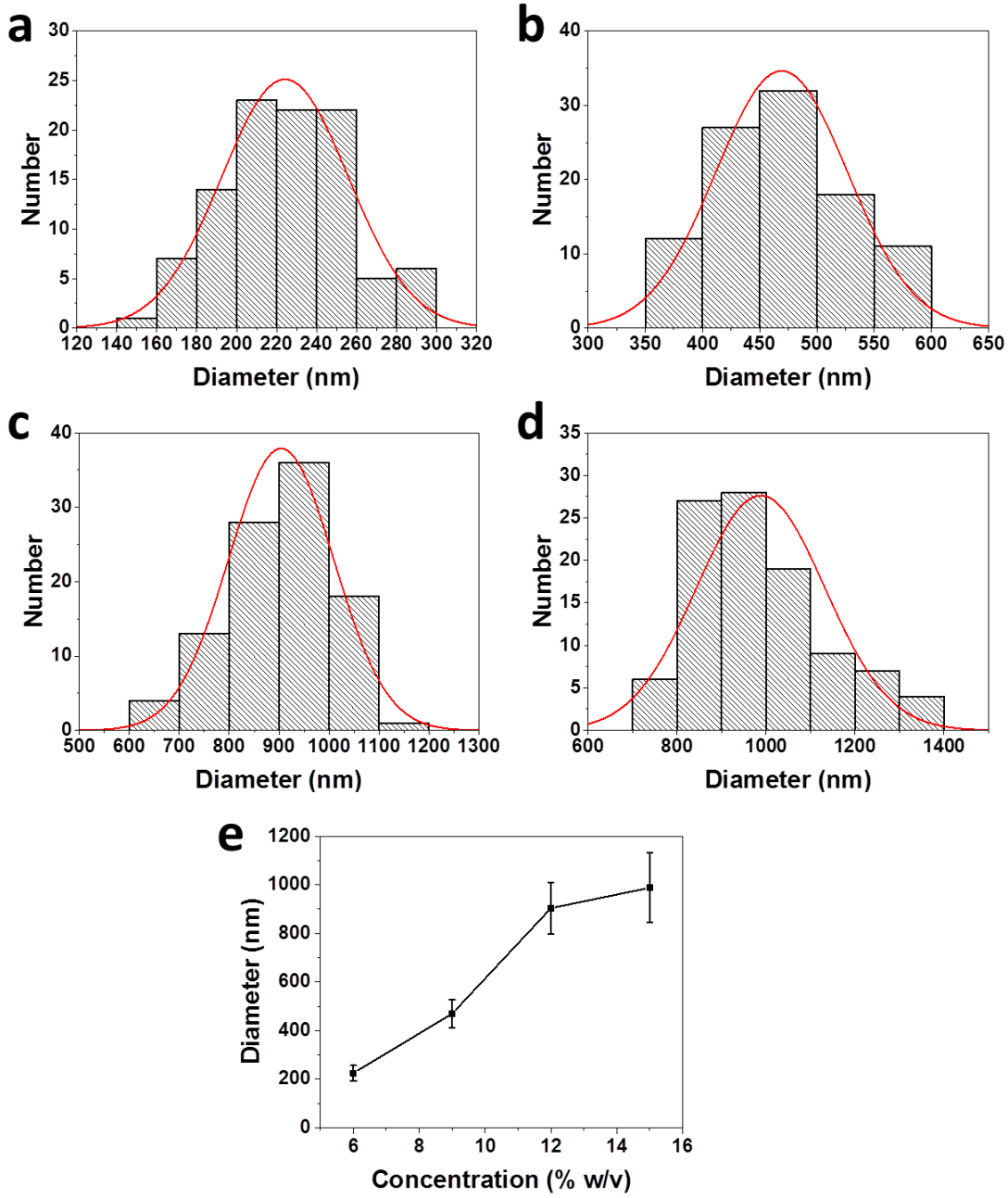


**Figure 4.3** Histograms of diameters of PLA nanofibers with different concentrations: (a) 6% w/v, (b) 9% w/v, (c) 12% w/v and (d) 15% w/v. (e) Average diameter of PLA nanofibers versus PLA concentration.

### 4.3.2 Fabrication of PLA/PLGA Nanofibers

To investigate the effect of PLGA content on the PE performance of PLA/PLGA nanofibers, PLA/PLGA solutions were electrospun with different ratios of 75/25, 50/50 and 25/75. Figure 4.4 shows the SEM images of the PLA/PLGA composite nanofibers. With the same PLGA content, an increase in PLA/PLGA concentration from 6% w/v (Figure 4.4a-c), to 9% w/v (Figure 4.4d-f) and to 12% w/v (Figure 4.4g-i) facilitated the electrospinning process and resulted in more uniform morphology of composite nanofibers. The beading effect was observed less as the viscosity of the polymer solution increased. With the same PLA/PLGA concentration, the increase in the PLGA content induced bead-like structures more frequently in PLA/PLGA (25/75) compared to the other two samples. This could be explained by that the DMF/$CHCl_3$ ratio needed further optimization for PLGA-rich polymer solutions. Due to the less beaded structures, 12% w/v PLA/PLGA composite nanofibers were used for further characterizations, including piezoelectricity evaluation by PFM. Figure 4.5a-c shows the histograms of diameters of 12% w/v PLA/PLGA nanofibers with different PLA/PLGA ratios. The average nanofiber diameters were 985.5 ± 185.3 nm, 622.2 ± 143.0 nm, and 606.8 ± 133.6 nm for PLA/PLGA (75/25), PLA/PLGA (50/50) PLA/PLGA (25/75) in 12% w/v (Figure 4.5d).

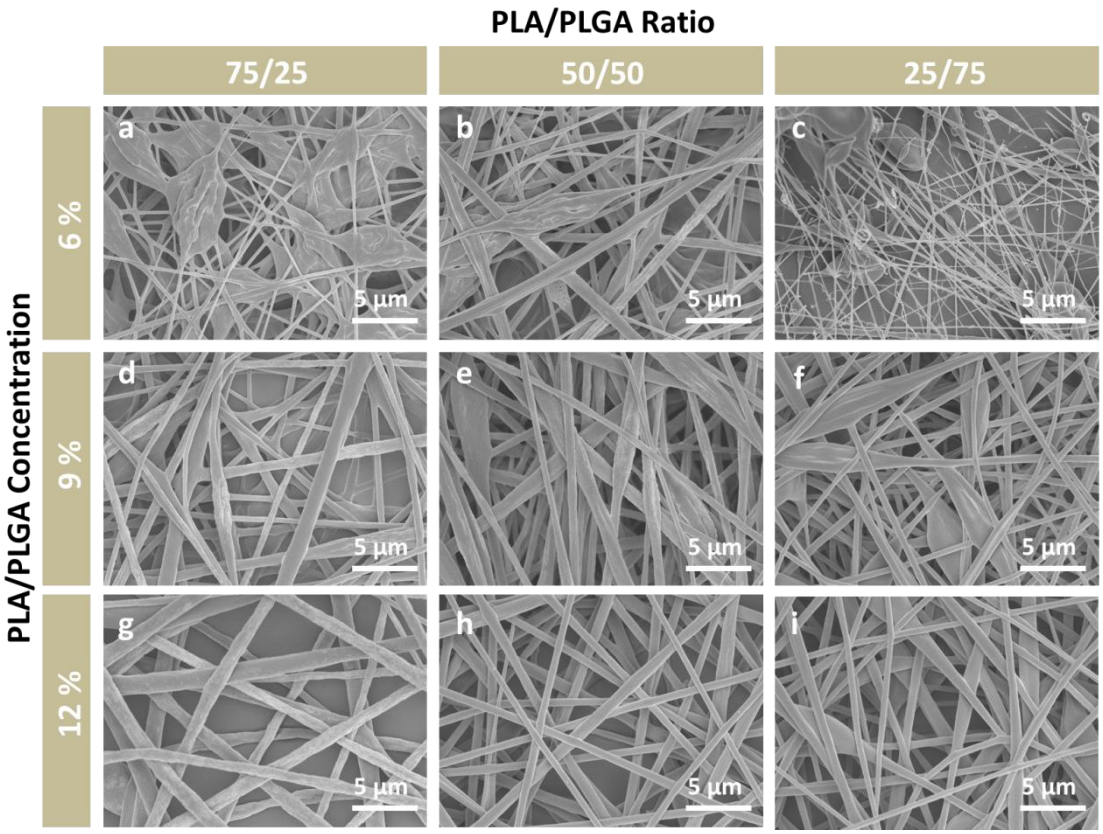


**Figure 4.4** SEM images of (a, d, g) PLA/PLGA (75/25), (b, e, h) PLA/PLGA (50/50) and (c, f, i) PLA/PLGA (25/75) nanofibers with different PLA/PLGA concentrations: (a, b, c) 6% w/v, (d, e, f) 9% w/v, (g, h, i) 12% w/v.

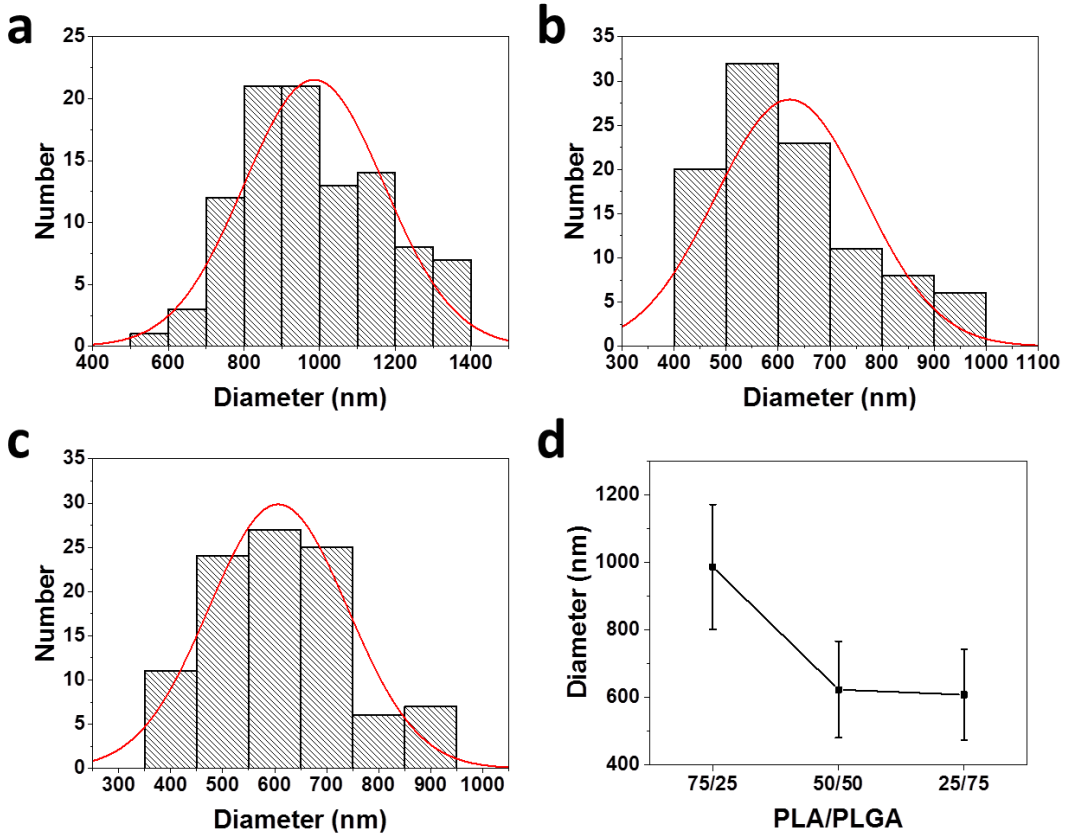


**Figure 4.5** Histograms of diameters of 12% w/v PLA/PLGA nanofibers with different PLA/PLGA ratios: (a) 75/25, (b) 50/50 and (c) 25/75. (d) Average diameter of PLA/PLGA nanofibers versus PLA/PLGA ratio.

### 4.3.3 Characterization of PLA and PLA/PLGA Nanofibers

Figure 4.6 presents the XRD patterns and FT-IR spectra of electrospun PLA and PLA/PLGA nanofibers. There was no sharp peak in XRD patterns for all the four samples, indicating that the degree of crystallinity was not high enough to be detected (Figure 4.6a). In FT-IR spectra (Figure 4.6b), similar characteristic peaks were observed in all the four samples. The peaks at 1751 $cm^{-1}$, 1454 $cm^{-1}$, 1385 $cm^{-1}$, and 1184 $cm^{-1}$ corresponded to stretching vibration of C=O bonds, bending vibration of C-H bonds, symmetrical bending vibration of $CH_3$ bonds and

stretching vibration of C-O bonds, respectively [16]. The peak occurred at 1088 $cm^{-1}$ was attributed to the C-O asymmetric group of ester groups [26]. With an increasing content of the PLGA component from 25% to 75%, a gradual decrease in the intensity of all these characteristic absorption was observed as expected, due to the relatively lower content of these bonds in PLGA compared to PLA [16].

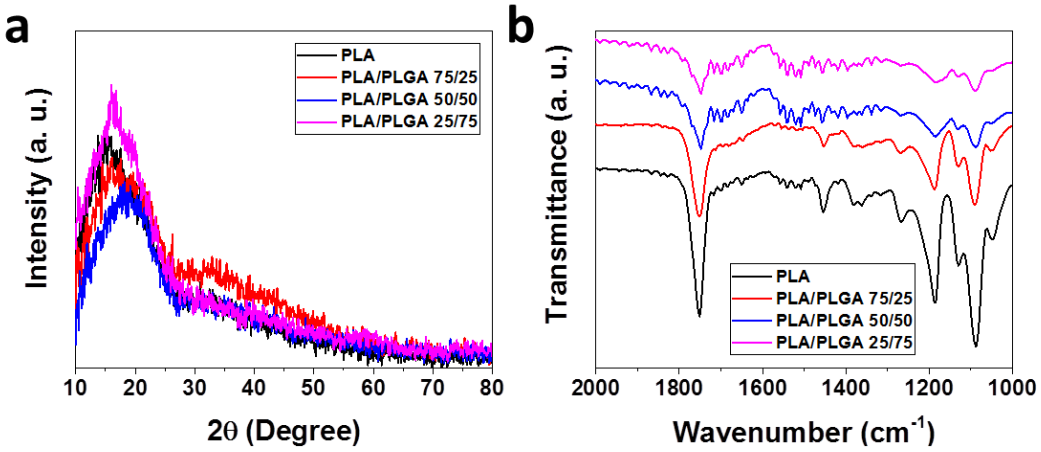


**Figure 4.6** (a) XRD patterns and (b) FT-IR spectra of PLA and PLA/PLGA nanofibers.

### 4.3.4 PFM Study of PLA and PLA/PLGA Nanofibers

The polymer solutions were directly electrospun onto a gold coated cover slip for PFM measurement. Different parameters such as the contact frequency and the AC voltage for oscillating the PFM tip were first assessed in order to optimize the SS-PFM measurements of PLA nanofibers (Figure 4.7). For a single spectroscopy curve at one X-Y position, the change in contact frequency (red, blue, black and pink curves) as a function of the sweeping DC bias waveform (grey curve, five cycles) was recorded whilst applying different AC modulating potentials to the conductive PFM tip (Figure 4.7a). When the AC voltage was set as 200 mV

(black curve), the contact frequency showed a decrease within five cycles of the DC bias. For AC voltages of 300 mV (red curve) and 400 mV (blue curve), the contact frequencies showed an opposing increase during the same period. For an AC voltage of 500 mV (pink curve), the contact frequency between the PFM tip and sample initially showed a sharp decrease, then an increase, within the first couple of cycles of the DC bias, as was observed for the other voltages. However, at an AC voltage of 500 mV the contact frequency became stable after approximately the third cycle and provided good indication for reliability in the SS-PFM measurements. Figure 4.7b and 4.7c show the amplitude signals and phase changes with different AC voltages. From 200 mV to 500 mV, all the amplitude signals showed entire butterfly loops. The response increased linearly with voltage as expected, which was actually validation of the PE response of PLA nanofibers. Also, all phase values showed a 180-degree change and the voltage did not change the phase, indicating entire switching of PLA dipoles had been achieved. Based on these observations, 500 mV was used to oscillate the tip to ensure a stable contact frequency signal during measurement. Data obtained from the third DC bias cycle was used for analysis.

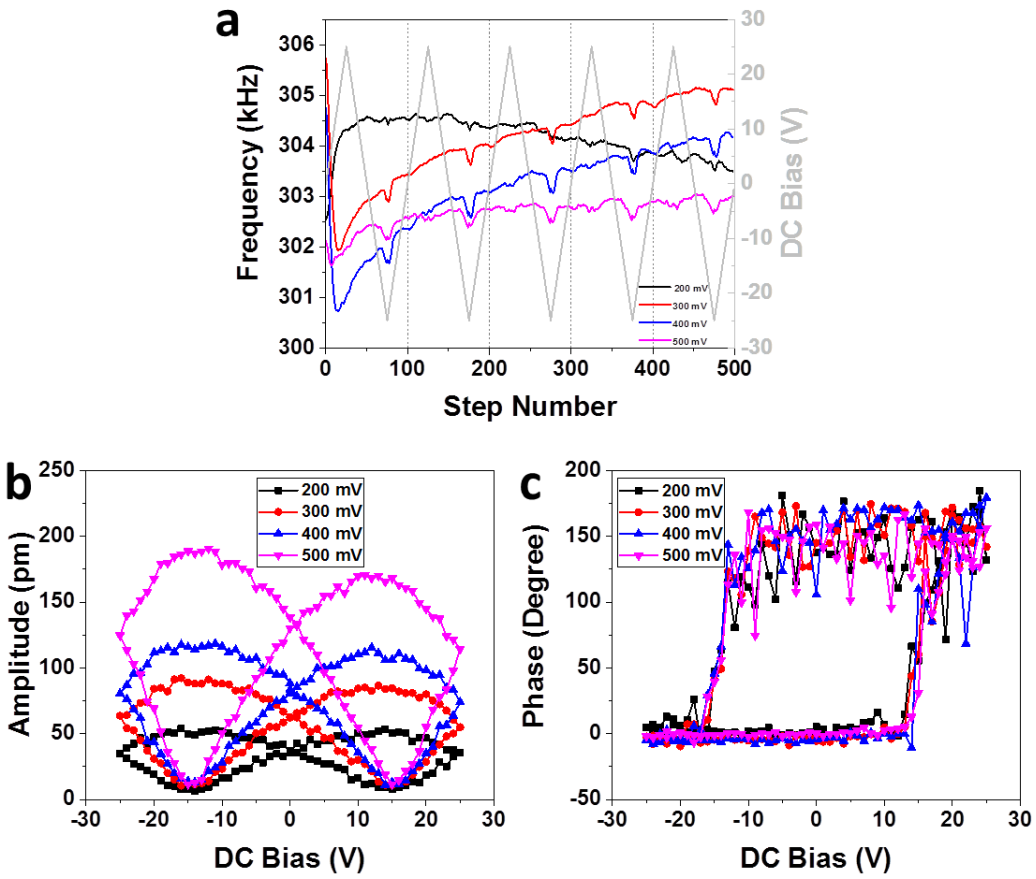


**Figure 4.7** (a) Change in the tip-sample contact frequency during the application of DC and AC bias for a SS-PFM measurement. SS-PFM curves showing the PE response (b) amplitude signal and (c) phase change in PFM measurement with different AC voltages.

Figure 4.8a and 4.8b show the PFM butterfly loops and phase curves obtained from three X-Y positions of a PLA nanofiber. The PE response in butterfly loops showed minimal variation within one single nanofiber, with the corresponding phase curves all showing a 180-degree switching that start and end at the same values. In each butterfly loop, the PE response was obtained using same method used for analysing butterfly loops for PVDF in Chapter 2 and P(VDF-HFP) in Chapter 3. The PE response analysed from 60 butterfly loops taken from 20 different PLA nanofibers showed significantly greater variation, as depicted by the

histogram of the average amplitude signals which showed a general Gaussian distribution with a peak value of 186.0 ± 28.1 pm (Figure 4.8c). Interestingly, this PE response of PLA was higher compared to PVDF (140.9 ± 84.0 pm) even though the known PE coefficient of PLA is lower [27, 28]. The reason for this was not clear as PLA has shear piezoelectricity [2]. During the electrospinning process, the polymer chains were subjected to a stretching force and an electric field, forcing the polymer chains aligned and thus the alignment of permanent dipolar C=O bond could be achieved. As reported, the piezoelectricity of PLA was explained by the rotation of the permanent dipolar C=O bond [2].

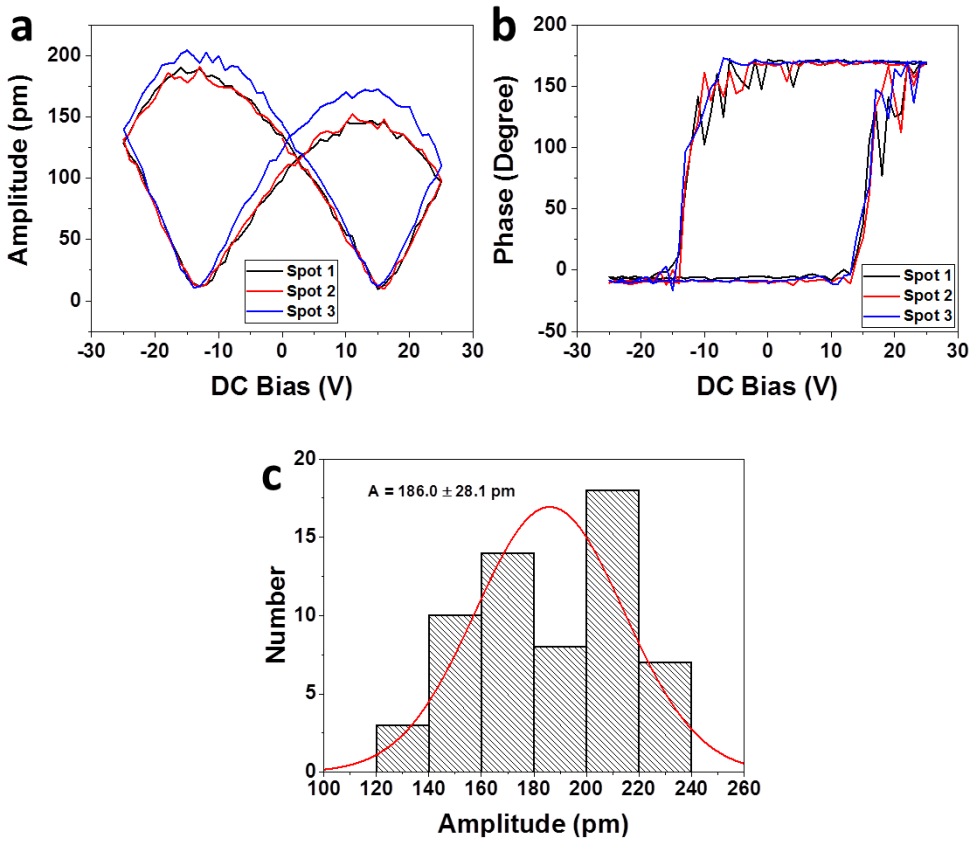


**Figure 4.8** (a) Butterfly loops, (b) phase changing curves and (c) histogram of PLA nanofibers PE response.

Following the same procedures as for PLA nanofibers, PFM measurements were carried out on PLA/PLGA (75/25), PLA/PLGA (50/50) and PLA/PLGA (25/75) nanofibers for comparison. Figure 4.9 shows the PFM results of PLA/PLGA (75/25), PLA/PLGA (50/50). Similar to PLA nanofibers, the amplitude obtained on single nanofibers were similar, indicating that there appeared to be minimal variation in the PE response along a single nanofiber (Figure 4.9a and 4.9b). Both PLA/PLGA (75/25) and PLA/PLGA (50/50) nanofibers showed a phase change of 180 degrees (Figure 4.9c and 4.9d), indicating the butterfly loops came from the true PE response as stated for PVDF in Chapter 2 and P(VDF-HFP) in Chapter 3, not from the electrostatic force. Figure 4.9e and 4.9f show histograms of the PE response from 60 X-Y positions for PLA/PLGA (75/25) and PLA/PLGA (50/50) nanofibers. Compared to PLA nanofibers, both composites showed a significantly lower PE response of 88.8 ± 12.3 pm and 49.6 ± 9.1 pm for PLA/PLGA (75/25) and PLA/PLGA (50/50) nanofibers, respectively (Figure 4.9g). For PLA/PLGA (25/75) nanofibers, only very few nanofibers exhibited a low response of 28.8 pm (Figure 4.10a and 4.10b) while most showed no response (Figure 4.10c and 4.10d) and thus a statistical analysis was not undertaken on this sample. Overall, an increasing PLGA content caused a decrease in the PE response, thus an expected trade-off existed between the biodegradability versus piezoelectricity of the PLA/PLGA that was dependent on their content ratio. As reported, PLGA microspheres have a much shorter breakdown time (56 days) than PLA microspheres (360 days) [12, 13]. Despite the decrease in PE response, a reasonable PE effect is preserved in PLA/PLGA (75/25) and PLA/PLGA (50/50) and is promising for applications such as bone morphogenetic protein delivery system [29] where faster degradation of carriers is preferred.

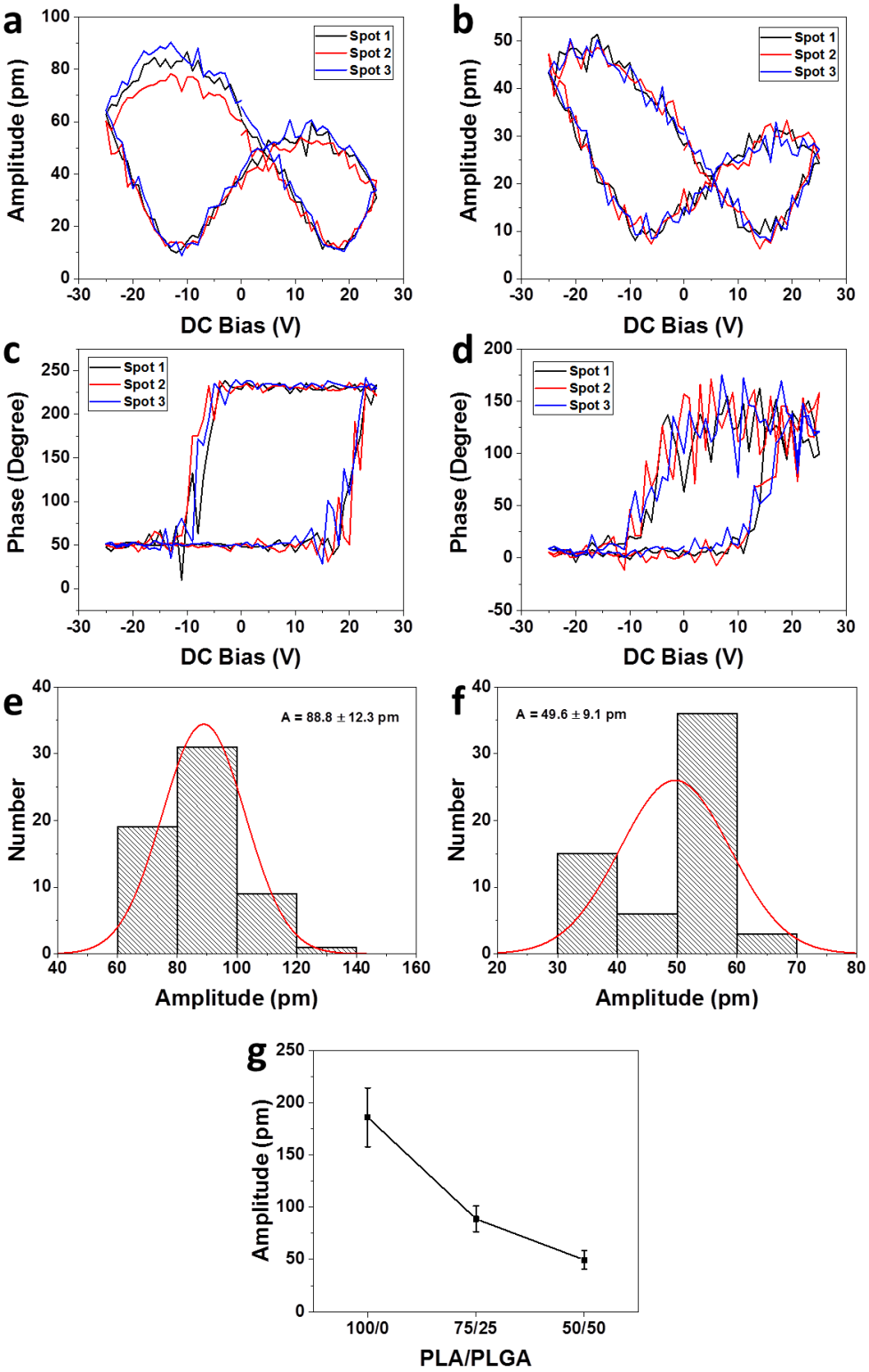


**Figure 4.9** (a, b) Butterfly loops, (c, d) phase changing curves, (e, f) PE response histograms of (a, c, e) PLA/PLGA (75/25) and (b, d, f) PLA/PLGA (50/50) nanofibers. (g) Relation between average PE response and PLA/PLGA ratio.

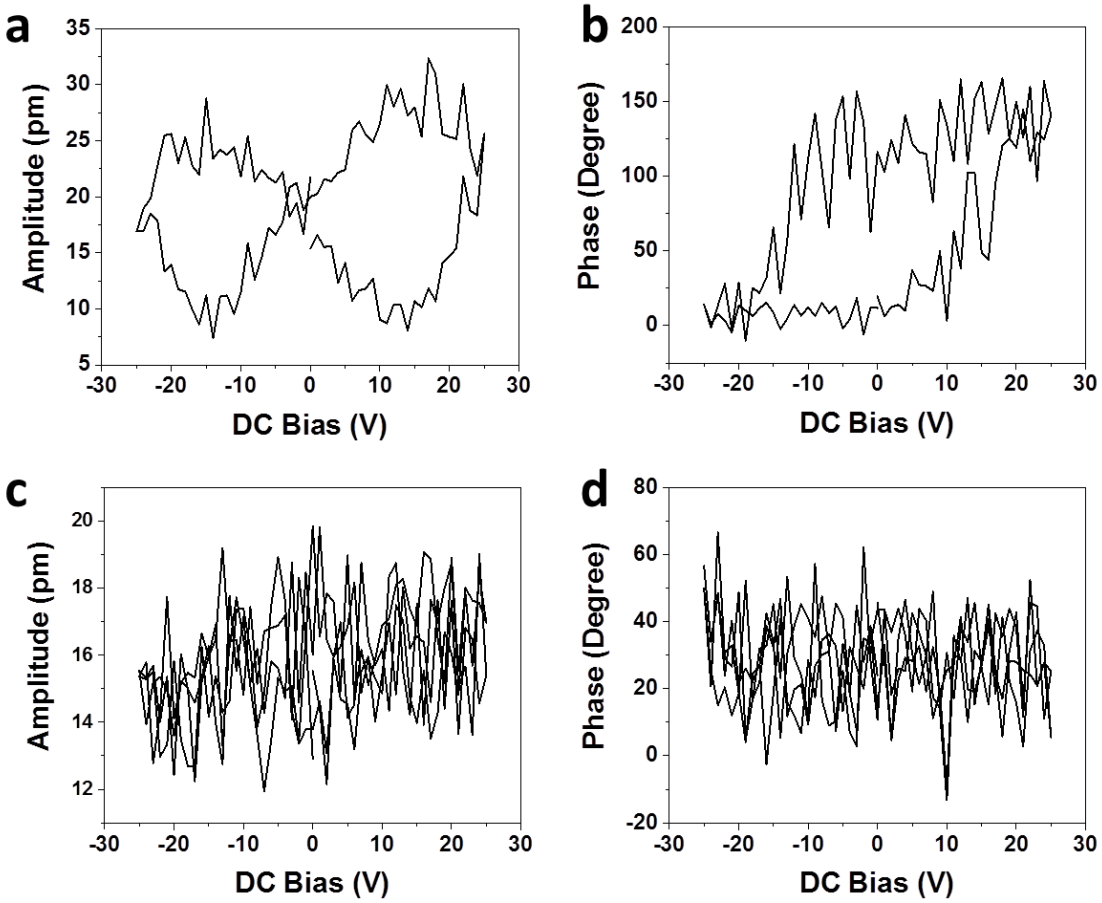


**Figure 4.10** (a, c) Butterfly loops and (b, d) corresponding phase changing curves of PLA/PLGA (25/75) nanofibers.

### 4.3.5 Fabrication of PLA/$CoFe_2O_4$ Composite Nanofibers

Following the PE measurement on PLA nanofibers, the effect of magnetic $CoFe_2O_4$ nanoparticles on the PE response of PLA/$CoFe_2O_4$ composite nanofibers was studied. PLA/$CoFe_2O_4$ composite nanofibers with 5% and 10% $CoFe_2O_4$ nanoparticles, named as PLA-5 and PLA-10, were fabricated using electrospinning under the same conditions as for 12% w/v PLA nanofibers in Section 4.2.2. SEM images are shown in Figure 4.11a and 4.11b with both composite nanofibers displaying uniform morphology without beaded structures.

Histograms of nanofiber diameters indicated that the incorporation of nanoparticles slightly increased the diameter from 903.9 ± 105.3 nm of PLA nanofibers to 965.1 ± 116.3 nm and 1102.0 ± 110.4 nm for PLA-5 and PLA-10 nanofibers, respectively (Figure 4.11c and 4.11d).

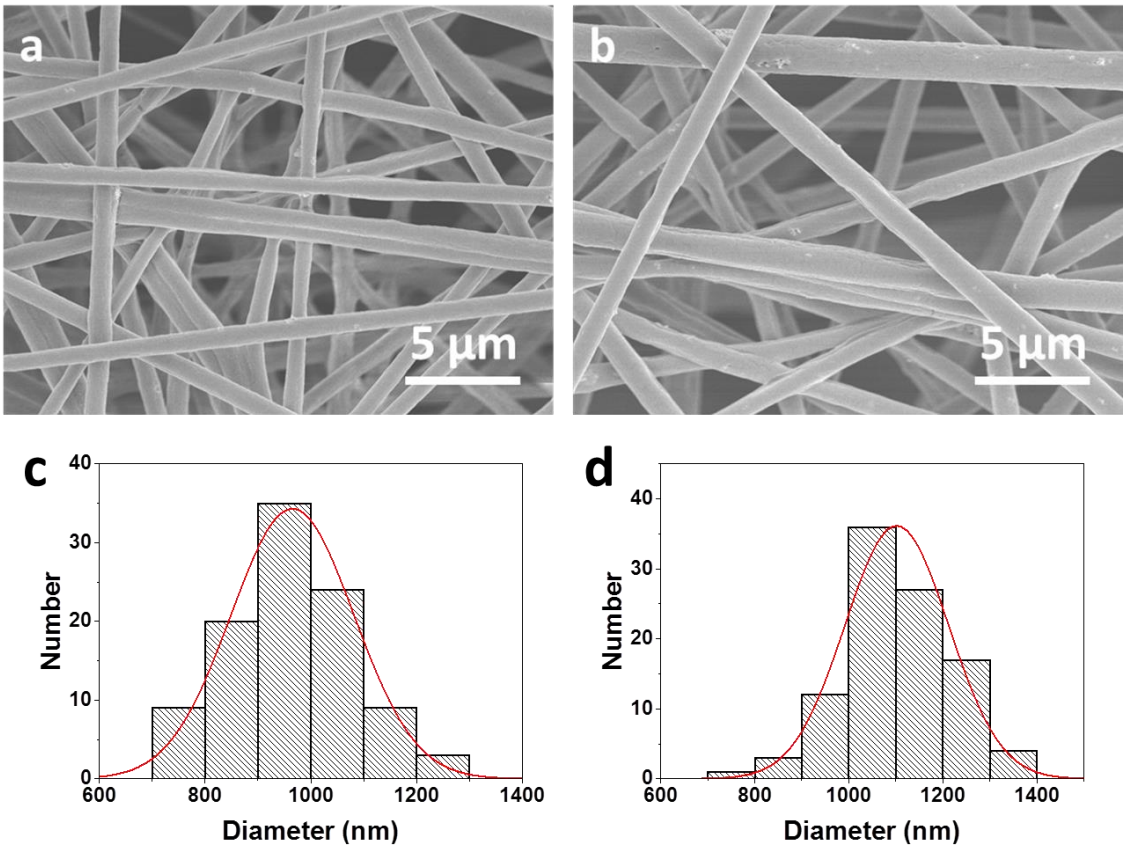


**Figure 4.11** (a, b) SEM images and (c, d) histograms of diameters of (a, c) PLA-5 and (b, d) PLA-10 nanofibers.

### 4.3.6 Characterization of PLA and PLA/$CoFe_2O_4$ Composite Nanofibers

Figure 4.12a shows the XRD patterns of $CoFe_2O_4$ nanoparticles and both PLA/$CoFe_2O_4$ composite nanofiber samples. The XRD pattern of commercial $CoFe_2O_4$ nanoparticles corresponded to the standard cubic spinel structure of $CoFe_2O_4$ (JCPDS card: 22-1086) [30]. However, due to the PLA surrounding of $CoFe_2O_4$ nanoparticles in both composites, the reflection intensity of pure nanoparticles decreased and only the strongest peak at $2\theta=35.9^o$ (reflection of (311) crystal plane) was observed in both composite nanofibers. The broad peak was attributed to the PLA component. The comparison of FT-IR spectra between pure PLA and PLA/$CoFe_2O_4$ nanofibers is presented in Figure 4.12b. Characteristic peaks of the PLA were also observed in composite nanofibers although their intensity decreased due to the incorporation of $CoFe_2O_4$ nanoparticles. To determine the actual amount of $CoFe_2O_4$ nanoparticles, magnetization measurement was carried on at room temperature (Figure 4.12c). The magnetization values of $CoFe_2O_4$ nanoparticles, PLA-5 and PLA-10 were 56.99 emu $g^{-1}$, 2.32 emu $g^{-1}$ and 4.06 emu $g^{-1}$. The fractions of $CoFe_2O_4$ nanoparticles in composite nanofibers were calculated by Equation 2.2. From these values, it was estimated that the fractions of $CoFe_2O_4$ nanoparticles in PLA-5 and PLA-10 were 4.1% and 7.1%, respectively. Due to the gravity differentiation, sedimentation of dispersed nanoparticles occurred during electrospinning process leading to fractions slightly lower than expected.

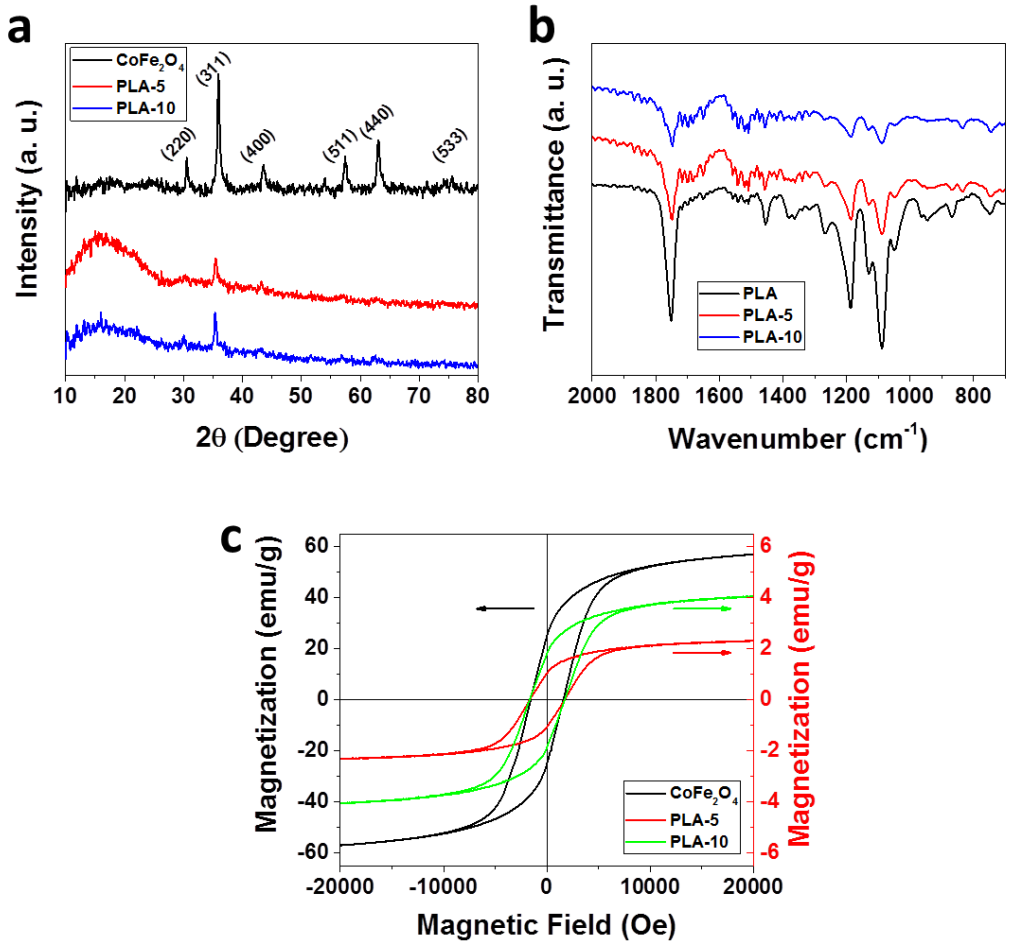


**Figure 4.12** (a) XRD patterns, (b) FT-IR spectra and (c) room-temperature magnetization isotherms of $CoFe_2O_4$ nanoparticles and PLA/$CoFe_2O_4$ composite nanofibers.

### 4.3.7 PFM Study of PLA/$CoFe_2O_4$ Composite Nanofibers

The PE response of PLA-5 and PLA-10 samples was measured using SS-PFM according to the same procedures described above for PLA nanofibers. Again, the SS-PFM measurement was performed on 20 different nanofibers with three X-Y positions on each (N=60). Figure 4.13 shows the PE response histograms for both samples. The average PE response of PLA-5 and PLA-10 was 140.7 ± 28.2 pm and 143.4 ± 43.7 pm, respectively, indicating that the addition of $CoFe_2O_4$ nanoparticles lowered the PE response by most likely perturbing the

ordered structure of the PLA. It was worth noting that the PE response of PLA-5 had a unimodal distribution while the PE response of PLA-10 had a bimodal distribution with peaks at 89.8 pm and 170.8 pm, referred to as the low-response group and the high-response group, respectively.

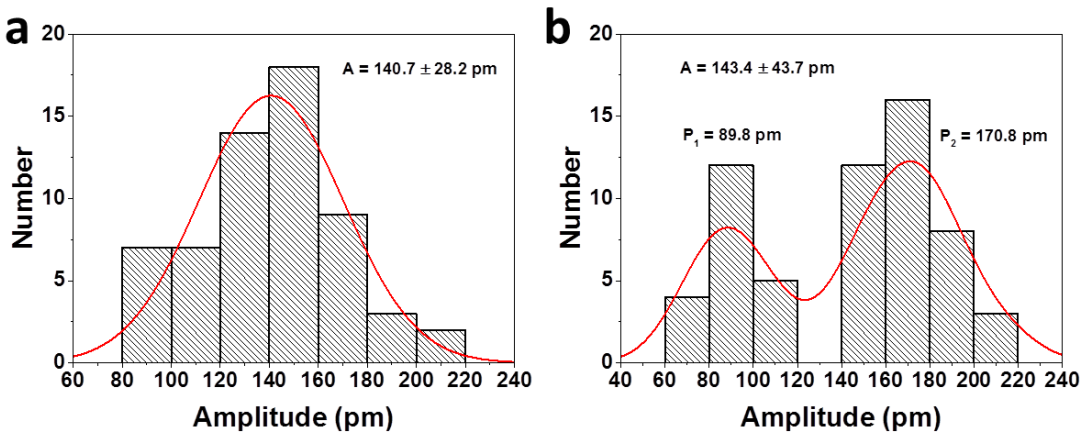


**Figure 4.13** PE response histograms of (a) PLA-5 and (b) PLA-10 nanofibers. "A" stands for average value. "$P_1$" and "$P_2$" stand for individual peak values.

Figure 4.14 shows the butterfly loops and corresponding phase changing curves obtained from PLA-5, low-response PLA-10 and high-response PLA-10 nanofibers. All three samples exhibited a phase change of 180 degrees (Figure 4.14b, 4.14d and 4.14f). For both PLA-5 (Figure 4.14a and 4.14b) and low-response PLA-10 (Figure 4.14c and 4.14d) samples, the butterfly loops were qualitatively similar to that of pure PLA nanofibers, only with lower peak values. However, the butterfly loop of high-response PLA-10 showed a narrower "coercive" field exclusively, which meant a smaller electric field could be used to switch the polarization and generate a PE response (Figure 4.14e and 4.14f). These effects may be due

to the inhomogeneous distribution of $CoFe_2O_4$ nanoparticles in the nanofibers. $CoFe_2O_4$ may interfere with the order structure of PLA and decrease its piezoelectricity, as the case in PLA-5. Alternatively, the conductive $CoFe_2O_4$ nanoparticles may decrease the "coercive" field, as the case in high-response PLA-10, though the exact reason for the latter is unclear.

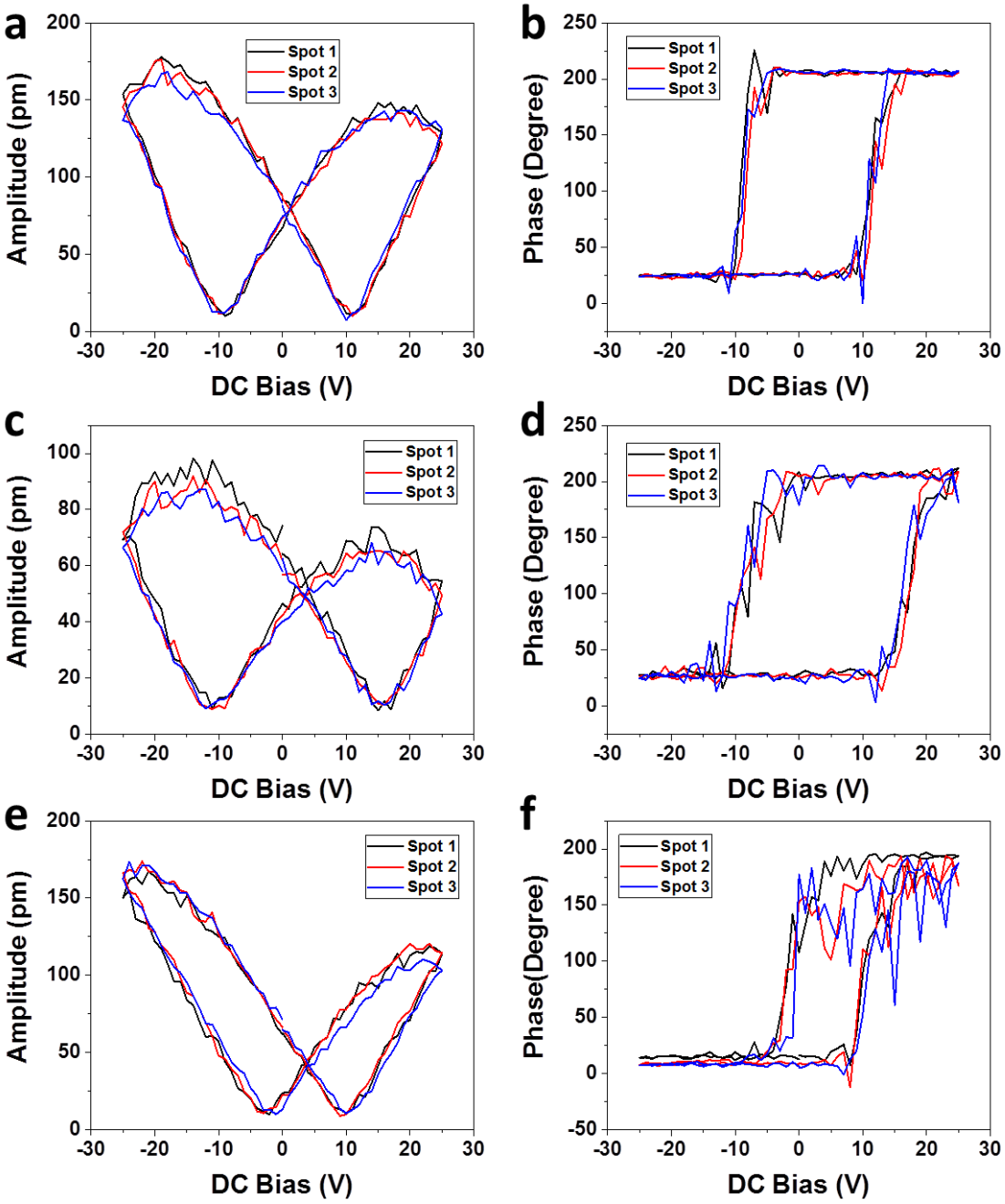


**Figure 4.14** (a, c, e) Butterfly loops and (b, d, f) phase changing curves of (a, b) PLA-5, (c, d) low-response PLA-10 and (e, f) high-response PLA-10 nanofibers.

## 4.4 Conclusions

Uniform PLA nanofibers and PLA/PLGA nanofibers with different PLA/PLGA ratios were fabricated using electrospinning. The PE response decreased with increasing PLGA content, from 186.0 ± 28.1 pm for pure PLA to 88.8 ± 12.3 pm for PLA/PLGA (75/25) and to 49.6 ± 9.1 pm for PLA/PLGA (50/50). For PLA/PLGA (25/75), the nanofibers showed low PE response or even no response. Nevertheless, reasonable PE responses remained at PLA/PLGA (75/25) and PLA/PLGA (50/50), which are polymers commonly used in many biomedical applications requiring short to mid-term degradability. Therefore, an interesting question is what role the PE properties can play in these applications, for example, in drug release applications where the mechanical motion of the PLA/PLGA will induce polarization and in turn have potential effects on the interaction between the polymer and drug (e.g. rate of drug release). Beyond this, the piezoelectricity of PLA/PLGA can also be controlled by magnetic stimuli and used as biocompatible electrodes if integrated into PLA-based ME materials.

Moreover, the PE properties of PLA/$CoFe_2O_4$ nanofibers were studied in different concentrations of $CoFe_2O_4$ nanoparticles. Both PLA-5 and PLA-10 showed lower PE response than pure PLA due to the disturbance of ordered structure by the magnetic nanoparticles. Further to this, $CoFe_2O_4$ nanoparticles were found to have effect on the PE response of PLA-10. Despite the lower PE response of PLA/$CoFe_2O_4$ composites, the study on incorporating magnetic nanoparticles provided a foundation for fabricating PLA-based ME materials in the future. Since $CoFe_2O_4$ nanoparticles are cytotoxic, the commonly used, non-toxic $Fe_3O_4$ nanoparticles or other biocompatible magnetic nanomaterials can be a promising substitution. Inspired by this work, a fully degradable ME electrode based on PLA/$Fe_3O_4$ is of significant interest from the viewpoint of *in vivo* applications.

## 4.5 References


1. Lasprilla, A.J.R., et al., *Poly-lactic acid synthesis for application in biomedical devices - a review.* Biotechnology Advances, 2012. **30**(1): p. 321-328.
2. Ando, M., et al., *Pressure-sensitive touch panel based on piezoelectric Poly (L-lactic acid) film.* Japanese Journal of Applied Physics, 2013. **52**(9S1): p. 09KD17.
3. Ando, M., et al., *Film sensor device fabricated by a piezoelectric Poly (L-lactic acid) film.* Japanese Journal of Applied Physics, 2012. **51**(9S1): p. 09LD14.
4. Tajitsu, Y., *Fundamental study on improvement of piezoelectricity of Poly (L-lactic acid) and its application to film actuators.* IEEE Transactions on Ultrasonics, Ferroelectrics, and Frequency Control, 2013. **60**(8): p. 1625-1629.
5. Ito, S., et al., *Sensing using piezoelectric chiral polymer fiber.* Japanese Journal of Applied Physics, 2012. **51**(9S1): p. 09LD16.
6. Smyth, M., et al., *Electrospinning highly oriented and crystalline Poly(lactic acid) fiber mats.* Journal of Materials Science, 2014. **49**(6): p. 2430-2441.
7. Lee, S.J., et al., *Piezoelectric properties of electrospun Poly(L-lactic acid) nanofiber web.* Materials Letters, 2015. **148**: p. 58-62.
8. Sencadas, V., et al., *Local piezoelectric activity of single Poly(L-lactic acid) (PLLA) microfibers.* Applied Physics A, 2012. **109**(1): p. 51-55.
9. Danhier, F., et al., *PLGA-based nanoparticles: an overview of biomedical applications.* Journal of Controlled Release, 2012. **161**(2): p. 505-522.
10. Gentile, P., et al., *An overview of Poly(lactic-co-glycolic) acid (PLGA)-based biomaterials for bone tissue engineering.* International Journal of Molecular Sciences, 2014. **15**(3): p. 3640-3659.
11. Anderson, J.M., et al., *Biodegradation and biocompatibility of PLA and PLGA microspheres.* Advanced Drug Delivery Reviews, 2012. **64**: p. 72-82.
12. Visscher, G., et al., *Biodegradation of and tissue reaction to 50: 50 Poly (DL-lactide-co-glycolide) microcapsules.* Journal of Biomedical Materials Research Part A, 1985. **19**(3): p. 349-365.
13. Visscher, G., et al., *Biodegradation of and tissue reaction to Poly (DL-lactide) microcapsules.* Journal of Biomedical Materials Research, 1986. **20**(5): p. 667-676.

14. Okamoto, M., et al., *Synthetic biopolymer nanocomposites for tissue engineering scaffolds.* Progress in Polymer Science, 2013. **38**(10-11): p. 1487-1503.

15. Liu, R., et al., *Preparation of Insulin-loaded PLA/PLGA microcapsules by a novel membrane emulsification method and its release in vitro.* Colloids and Surfaces B-Biointerfaces, 2006. **51**(1): p. 30-38.

16. Liu, H., et al., *Controllable structure, properties, and degradation of the electrospun PLGA/PLA-blended nanofibrous scaffolds.* Journal of Applied Polymer Science, 2012. **125**: p. E468-E476.

17. Santoro, M., et al., *Poly(lactic acid) nanofibrous scaffolds for tissue engineering.* Advanced Drug Delivery Reviews, 2016. **107**: p. 206-212.

18. Hu, J., et al., *Novel controlled drug delivery system for multiple drugs based on electrospun nanofibers containing nanomicelles.* Journal of Biomaterials Science-Polymer Edition, 2014. **25**(3): p. 257-268.

19. Li, F., et al., *Preparation of magnetic polylactic acid microspheres and investigation of its releasing property for loading Curcumin.* Journal of Magnetism and Magnetic Materials, 2011. **323**(22): p. 2770-2775.

20. Zhang, X., et al., *Effects of surface modification on the properties of magnetic nanoparticles/PLA composite drug carriers and in vitro controlled release study.* Colloids and Surfaces A: Physicochemical and Engineering Aspects, 2013. **431**: p. 80-86.

21. Correia, D.M., et al., *Processing and size range separation of pristine and magnetic Poly (L-lactic acid) based microspheres for biomedical applications.* Journal of Colloid and Interface Science, 2016. **476**: p. 79-86.

22. Chen, F., et al., *Synthesis of magnetite core–shell nanoparticles by surface-initiated ring-opening polymerization of L-lactide.* Journal of Magnetism and Magnetic Materials, 2008. **320**(13): p. 1921-1927.

23. Gomez-Lopera, S.A., et al., *Colloidal stability of magnetite/Poly (lactic acid) core/shell nanoparticles.* Langmuir, 2006. **22**(6): p. 2816-2821.

24. Guduru, R., et al., *Magnetoelectric 'spin' on stimulating the brain.* Nanomedicine, 2015. **10**(13): p. 2051-2061.

25. Rodzinski, A., et al., *Targeted and controlled anticancer drug delivery and release with magnetoelectric nanoparticles.* Scientific Reports, 2016. **6**: p. 2204-2204.

26. Valapa, R.B., et al., *Fabrication and characterization of sucrose palmitate reinforced Poly(lactic acid) bionanocomposite films.* Journal of Applied Polymer Science, 2015. **132**(3): p. 41320.

27. Neese, B., et al., *Piezoelectric responses in Poly(vinylidene fluoride/hexafluoropropylene) copolymers.* Applied Physics Letters, 2007. **90**(24): p. 242917.

28. Ribeiro, C., et al., *Piezoelectric polymers as biomaterials for tissue engineering applications.* Colloids and Surfaces B-Biointerfaces, 2015. **136**: p. 46-55.

29. Agrawal, V., et al., *A review on carrier systems for bone morphogenetic Protein-2.* Journal of Biomedical Materials Research Part B-Applied Biomaterials, 2017. **105**(4): p. 904-925.

30. Wang, H., et al., *A facile synthesis of monodisperse $CoFe_2O_4/SiO_2$ nanoparticles.* Applied Surface Science, 2011. **257**(16): p. 7107-7112.

# 5 Macroscale Magnetoelectric Measurements of Magnetoelectric Composites from Electrospun Piezoelectric Nanofibers

## 5.1 Introduction

### 5.1.1 ME Effect in Macroscale ME materials

Macroscale magnetoelectric (ME) effects have been widely measured in polymer-based composites using a lock-in technique, as described in Chapter 1, Section 1.2.6. Particulate ME composites, comprising polymer matrices with dispersed magnetic nanoparticles, generate ME coefficients in the range of ~ 1-100 mV $cm^{-1}$ $Oe^{-1}$. For example, an optimal ME coefficient ($\alpha_{ME}$) of 7.5 mV $cm^{-1}$ $Oe^{-1}$ is observed in PVDF/$CoFe_2O_4$ nanocomposite films with a $CoFe_2O_4$ filler concentration of 10% [1] while the highest ME response of 41.3 mV $cm^{-1}$ $Oe^{-1}$ is found in the copolymer PVDF-TrFE/$CoFe_2O_4$ nanocomposites with 72 wt% $CoFe_2O_4$ nanoparticles [2]. Giant ME responses ($\alpha_{ME}$ > 1 V $cm^{-1}$ $Oe^{-1}$) up to 383 V $cm^{-1}$ $Oe^{-1}$ [3] have been observed in ME laminate structures consisting of a piezoelectric (PE) PVDF film adhered to ferromagnetic alloy film with highly magnetostrictive (MS) responses such as Terfenol-D [4, 5] and Metglas [3, 6].

### 5.1.2 Fabrication of Polymer-based ME Nanocomposites

The fabrication of ME devices are typically limited to continuous films [7] via drop casting, followed by post-poling of the PE layer [8, 9]. Abridging the manufacturing process by fabricating ready-to-use ME composites has the potential to provide practical advantages and

introduce new material properties (e.g. flexibility, transparency) to benefit applications in magnetic field sensors, memory devices and biomedical materials [10, 11]. This is where electrospinning, as demonstrated in previous chapters and by others [12, 13], is a flexible approach that can inherently produce PE nanostructures and films in different configurations. For example, poly (vinylidene fluoride) (PVDF) and poly (vinylidene fluoride-co-trifluoroethylene) (P(VDF-TrFE)) nanofiber sheets have been developed as flexible pressure sensors and nano-energy harvesters [14-16] by taking advantage of the induced electroactive phase induced by electrospinning. Recently, the first study on the piezoelectricity of poly (lactic acid) (PLA) nanofiber sheets has revealed that they can operate as an effective sensor with an optimized PE output voltage of 7.2 V [17]. Comparing to simple folding the nanofiber sheets by three layers with a configuration of top-and-bottom electrodes, connecting the electrodes in serial or parallel is shown to effectively enhance the outputs from 1.7 V to 5.5 V or 7.2 V [17].

In addition to electrospinning [13-16, 18, 19], PE polymer nanostructures can be achieved by a variety of techniques including electrospray [20], nanoconfinement [21] and nanoimprinting [22], offering great flexibility for developing and patterning polymer-based ME nanocomposites. Recently, PVDF/$CoFe_2O_4$ nanofibers and microspheres have been developed by electrospinning [23] and electrospray [24]. The use of new fabrication techniques (e.g. inkjet printing of ME dispersions) and emergence of ME nanocomposites provide new possibilities for assembling macroscale devices (e.g. from the bottom-up or top-down strategy). Compared to their bulk counterparts, ME nanocomposites may also provide a larger surface area to volume ratio. In particular, some bulk devices such as sensing and memory devices can be manufactured from ME nanocomposites for better performance such as higher sensitivity or larger memory capacity [10, 11].

A premise is that nanoscale ME properties of ME nanocomposites, as observed in studies using a PFM-based technique [25, 26], can be imparted in the final assembled component or device. However, ensuring that the nanoscale ME properties are preserved is critical to configuring macroscale devices from nanocomposites, yet has been little work done on this development of ME devices. Therefore, in this chapter, a serial of experiments was carried out to investigate whether the nanoscale ME properties of nanofibers observed in the previous chapters could be translated when in the form of a macroscopic ME device. To do this, various macroscale ME devices furnished from the electrospun nanofibers were assembled, including a ME laminate of electrospun PVDF nanofiber sheet/Metglas and ME nanofiber sheets of PVDF/$Fe_3O_4$ or PLA/$CoFe_2O_4$ in different electrode configurations (top-and-bottom electrodes and interdigitated electrodes). A macroscale ME testing system was setup to measure the ME output voltage based on the lock-in technique [27].

## 5.2 Experimental

### 5.2.1 Materials

PVDF with average molecular weight of 275,000 (g $mol^{-1}$) and $CoFe_2O_4$ nanoparticles (30 nm) were purchased from Aldrich. PLA was purchased from PURAC, Netherland. $Fe_3O_4$ nanoparticles were synthesized by a co-precipitation method in Chapter 2. Commercial poled PVDF film (28 μm, Cu/Ni coated) were purchased from Measurement Specialties (China) Ltd. Iron-based Metglas 2605 SA1 (20 μm) was contributed by our Portuguese collaborators, which has a composition of FeBSiC and saturation magnetostriction of 27 ppm.

### 5.2.2 Top-and-bottom Electrode Configuration for ME Devices

Throughout this chapter, all devices are configured in top-and-bottom electrodes or interdigitated electrodes. Figure 5.1 shows the schematic illustration of Metglas/electrospun nanofibers laminates with a configuration of top-and-bottom electrodes. A 50 nm gold layer was sputtered as top and bottom electrodes onto an electrospun porous sheet. Metglas (27 mm × 3 mm × 0.020 mm) was cut slightly smaller than electrospun nanofiber sheet or the commercial PVDF sheet (30 mm × 5 mm × 0.028 mm) so that wires could be connected onto the gold electrodes using silver paste (Figure 5.1a). Then, epoxy was used to combine the PE electrospun nanofiber sheet to Metglas, as shown in Figure 5.1b.

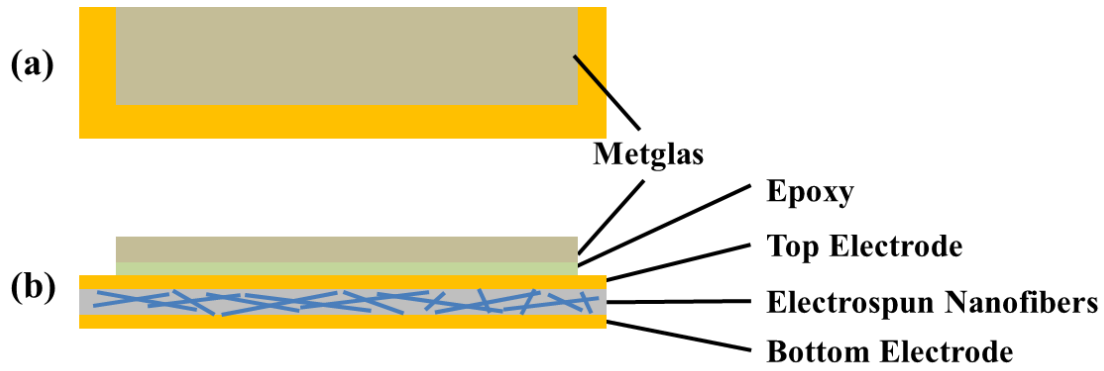


**Figure 5.1** (a) Top view and (b) side view of Metglas-based laminates. A 50 nm gold layer was sputter coated onto both sides of electrospun nanofiber sheets as top and bottom electrodes. The laminate was obtained by combining Metglas and nanofiber sheets using epoxy. Dimentions: Metglas (27 mm × 3 mm × 0.020 mm), the electrospun nanofiber sheet or the commercial PVDF sheet (30 mm × 5 mm × 0.028 mm).

### 5.2.3 Interdigitated Electrode Configuration for ME Devices

Figure 5.2 illustrates the configuration with interdigitated electrodes. To enable a comparison, both the electrospun nanofiber sheet and commercial PVDF sheet had the same dimensions (30 mm × 5 mm × 0.020 mm). The bare interdigitated electrodes (Figure 5.2a) were made from gold mylar by laser cutting. Both random (Figure 5.2b) and aligned (Figure 5.2c) nanofibers were prepared on the interdigitated electrodes by adjusting electrospinning process, as described further below.

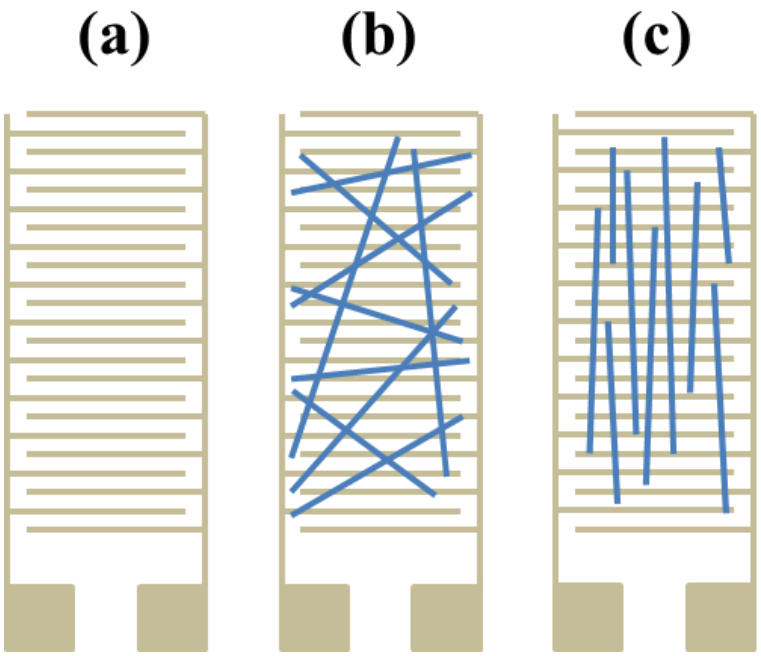


**Figure 5.2** Schematic illustration of (a) bare interdigitated electrodes (30 mm × 5 mm), (b) random and (c) aligned electrospun nanofibers on interdigitated electrodes. Electrodes had a dimension of 4 mm × 250 μm with a spacing of 500 μm.

### 5.2.4 Preparation of Electrospun PVDF-based ME Materials

Electrospinning of PVDF and PVDF/$Fe_3O_4$ was done following the method in Chapter 2. For microscale ME testing, A commercial PVDF sheet (not electrospun) on Metglas (PVDF sheet/Metglas) was developed in top-and-bottom electrodes as a control sample, as illustrated in Figure 5.1a. For devices furnished form electrospun samples, an electrospun PVDF nanofiber sheet without magnetic nanoparticles was fixed onto Metglas as a laminate structure (PVDF-NF/Metglas), with the same configuration in Figure 5.1b. The ME nanofiber sheets comprised of electrospun PVDF/$Fe_3O_4$ nanofibers were prepared in either top-and-bottom electrodes (PVDF/$Fe_3O_4$-NF) or randomly distributed onto interdigitated electrodes (IE PVDF/$Fe_3O_4$-NF) (Figure 5.2b). Finally, a single PVDF nanofiber sheet was also sputtered gold on both sides to enable ME testing (PVDF-NF).

### 5.2.5 Preparation of Electrospun PLA-based ME Materials

Both random and aligned electrospun PLA/$CoFe_2O_4$ nanofibers on interdigitated electrodes were fabricated with different $CoFe_2O_4$ concentrations, as illustrated in Figure 5.2b and 5.2c. Random and aligned PLA nanofibers with 5% $CoFe_2O_4$ nanoparticles were named as PLA/$CoFe_2O_4$ 5-R and PLA/$CoFe_2O_4$ 5-A. Similarly, PLA/$CoFe_2O_4$ 10-R and PLA/$CoFe_2O_4$ 10-A referred to those samples prepared from random and aligned PLA nanofibers, respectively, both with 10% $CoFe_2O_4$ nanoparticles. To align the PLA nanofibers, the plate collector of the electrospinning setup was changed to a rotatory drum. The PLA solution was prepared as same as used in Chapter 4. Since a short fiber-travelling distance facilitated the alignment [28], the tip-to-receptor distance was lowered to 7.5 cm and the applied voltage was lowered to 10 kV correspondingly to keep the electric field constant. The rotating speed

of the drum was set as 500, 1000 and 1500 rpm. The morphology of the aligned PLA fibers was characterized by field emission scanning electron microscope (FE-SEM, JEOL JSM-7500FA) with an accelerating voltage of 5.0 kV and an emission current of 10 mA.

### 5.2.6 Macroscale ME Testing

Based on previous experimental setups [27, 29], a similar ME testing system was built for measuring the output voltage of the samples. A schematic of the experimental setup and image of macroscale ME testing system are shown in Figure 5.3 and Figure 5.4. In the home-made system, DC and AC magnetic fields are supplied by electromagnets and Helmholtz coils (Dexing Magnet Tech. Co., Ltd). The pole pieces of the electromagnets have a diameter of 50 mm and supply a DC field up to 5000 Oe driven by a DC power supply. The Helmholtz coils have a diameter of 70 mm and supply an AC field up to 20 Oe driven by an AC power, with waveforms produced by a function generator (generating a sin waveform with frequencies ranging from 1 to 100 kHz) and magnified by a current amplifier. A Gauss meter is placed in between the electromagnets to measure the strength of both DC and AC fields. The voltage generated across the sample is transferred through a coaxial cable to the lock-in amplifier that monitors the reference frequency from the function generator. Finally, the user-end interface shows the output voltage and the ME coefficient is calculated according to the theory in Section 1.2.6 [27].

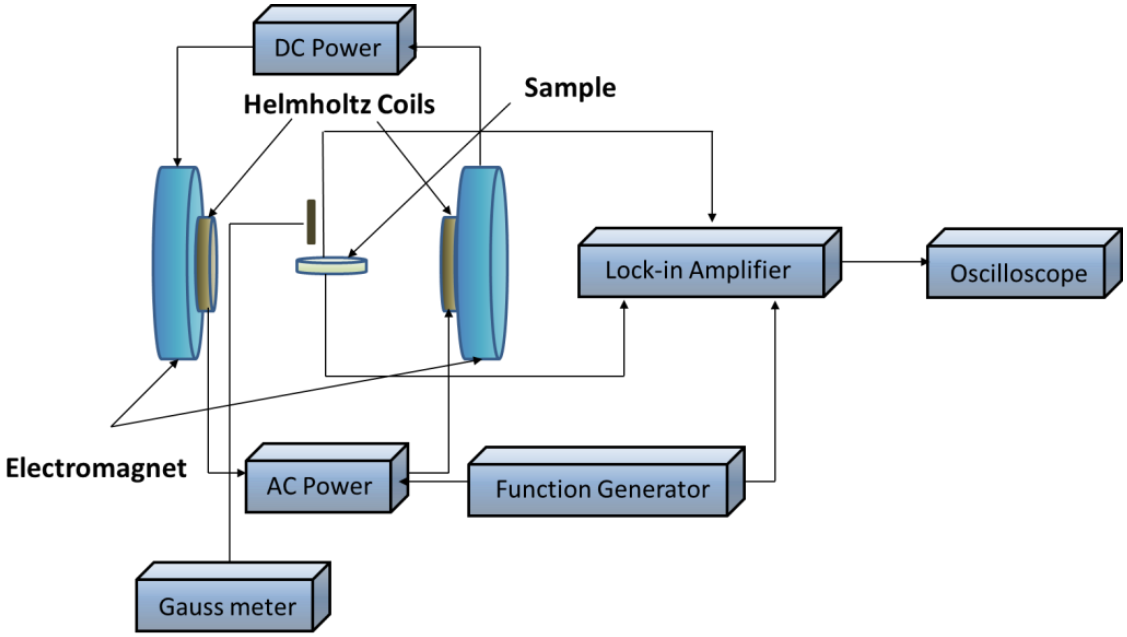


**Figure 5.3** Schematic of home-made experimental setup.

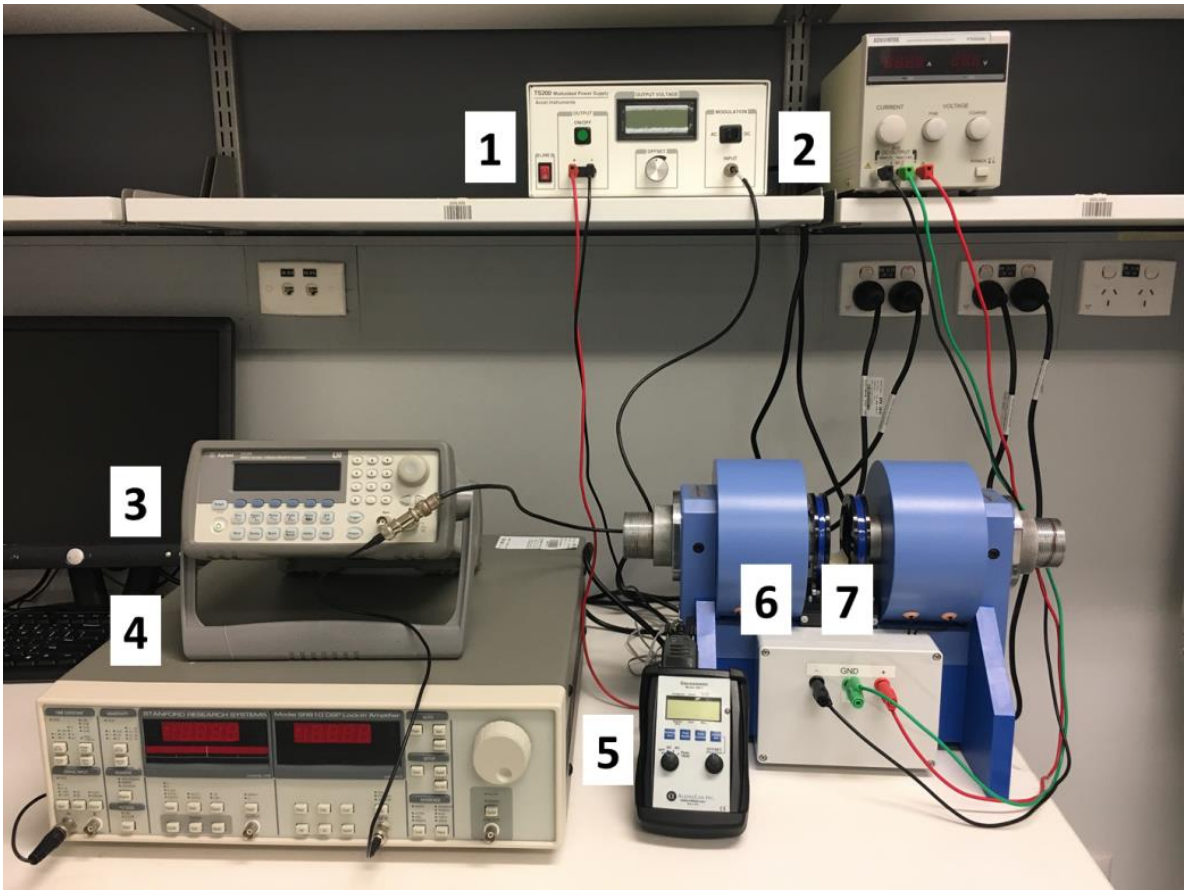


**Figure 5.4** Photograph of home-made macroscale ME testing system: (1) current amplifier (2) DC power supply (3) function generator (4) lock-in amplifier (5) Gauss meter (6) DC electromagnets (7) Helmholtz coils.

## 5.3 Results and Discussion

### 5.3.1 Fabrication of PVDF-based Samples

PVDF-based samples were prepared using two different electrode configurations, the top-and-bottom and interdigitated electrodes. Figure 5.5a shows the commercial PVDF sheet/Metglas laminate in top-and-bottom electrode configuration, which is used as a reference sample. In contrast, a photograph of the bare interdigitated electrodes is given in

Figure 5.5b. By mounting the interdigitated electrodes directly onto the collector of electrospinning instrument, PVDF/$Fe_3O_4$ electrospun nanofibers can be directly deposited on the electrode substrate. Figure 5.5c confirms that the electrospun nanofiber sheet adheres closely to the substrate due to the high electric field applied between the electrospinning needle and interdigitated electrodes.

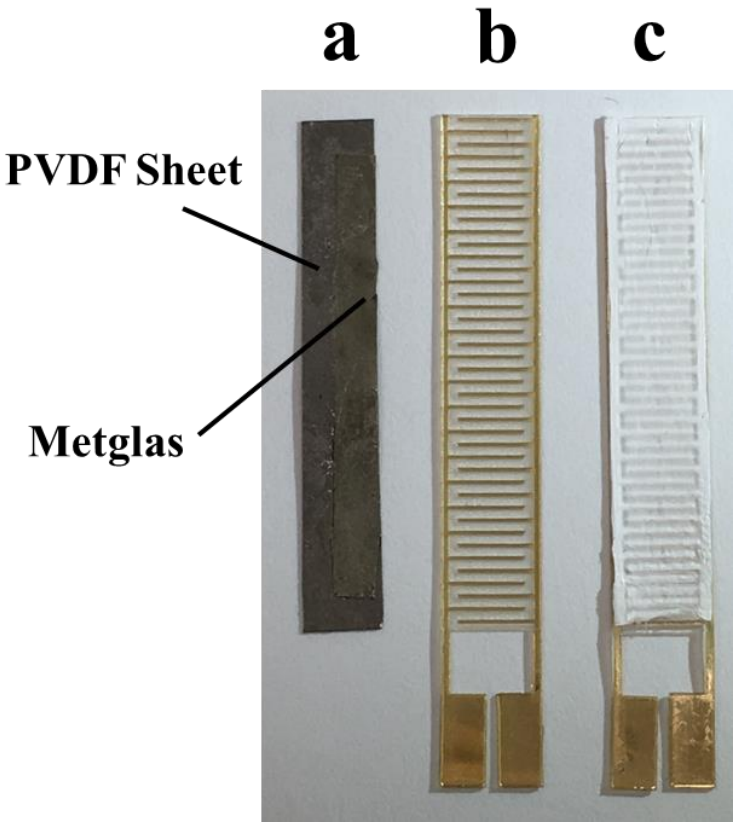


**Figure 5.5** Photographs of (a) PVDF/Metglas laminate, (b) laser-cut interdigitated electrodes and (c) PVDF/$Fe_3O_4$ electrospun nanofibers on the interdigitated electrodes.

### 5.3.2 Fabrication of Aligned PLA Nanofibers

The electrospinning of aligned PLA nanofibers was first studied by adjusting the rotating speed of the drum collector. Figure 5.5 shows the SEM images of PLA nanofibers

electrospun with different parameters. With the speed increasing from 500 rpm (Figure 5.5a) to 1000 rpm (Figure 5.5b) and then to 1500 rpm (Figure 5.5c and 5.5d), the alignment of electrospun nanofibers was improved significantly. At 1500 rpm, very good alignment was achieved for 10 min of electrospinning (Figure 5.5c). To confirm the stability of this process, the electrospinning was carried out for 30 min at 1500 rpm (Figure 5.5d) and the alignment didn't change too much. In the following experiments, PLA composite nanofibers were all electrospun with rotating speed of 1500 rpm.

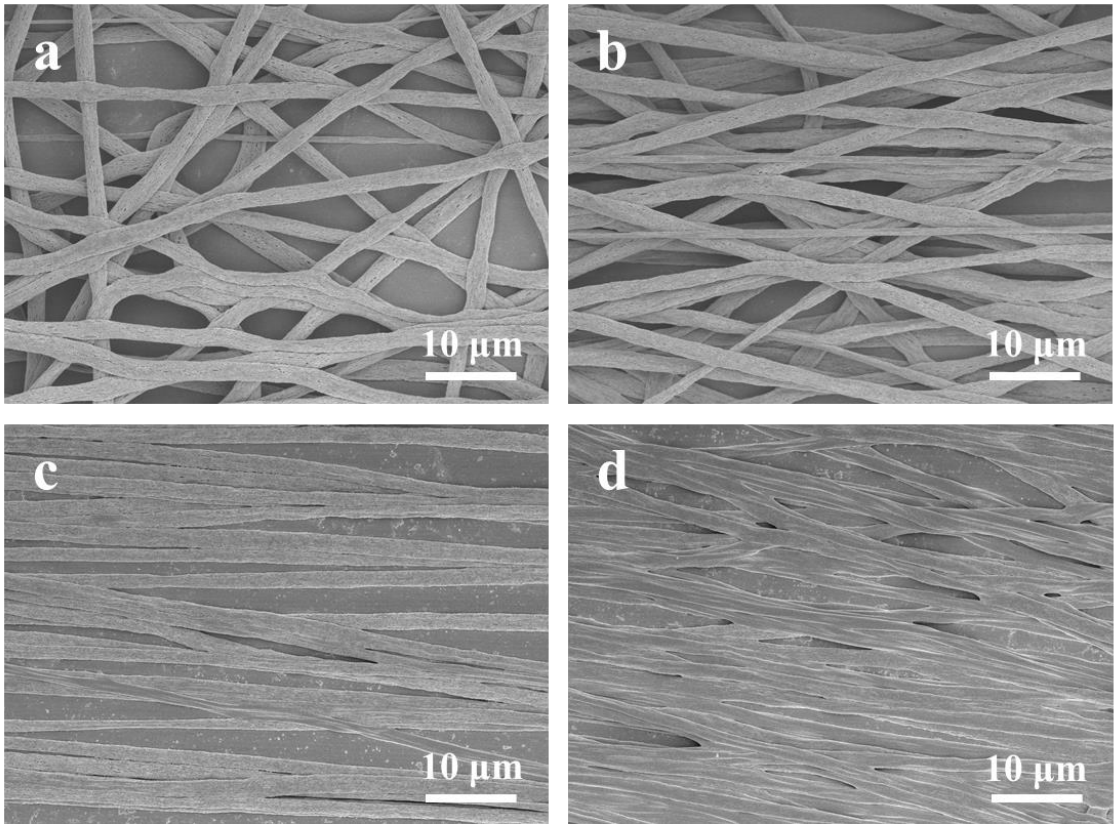


**Figure 5.6** SEM images of aligned PLA nanofibers electrospun with rotating speed and time of (a) 500 rpm and 10 min, (b) 1000 rpm and 10 min, (c) 1500 rpm and 10 min and (d) 1500 rpm and 30 min.

### 5.3.3 Fabrication of PLA-based Samples

Given the optimized rotating speed of collector, aligned PLA/$CoFe_2O_4$ nanofibers were directly electrospun onto interdigitated electrodes for the macroscale ME measurement. Figure 5.7 shows the photographs of ready-to-test devices for the PLA. Figure 5.7a and Figure 5.7c show the random distributed PLA/$CoFe_2O_4$ nanofibers on interdigitated electrodes. Figure 5.7b and Figure 5.7d show the aligned PLA/$CoFe_2O_4$ nanofibers on interdigitated electrodes collected on the rotary drum in high speed.

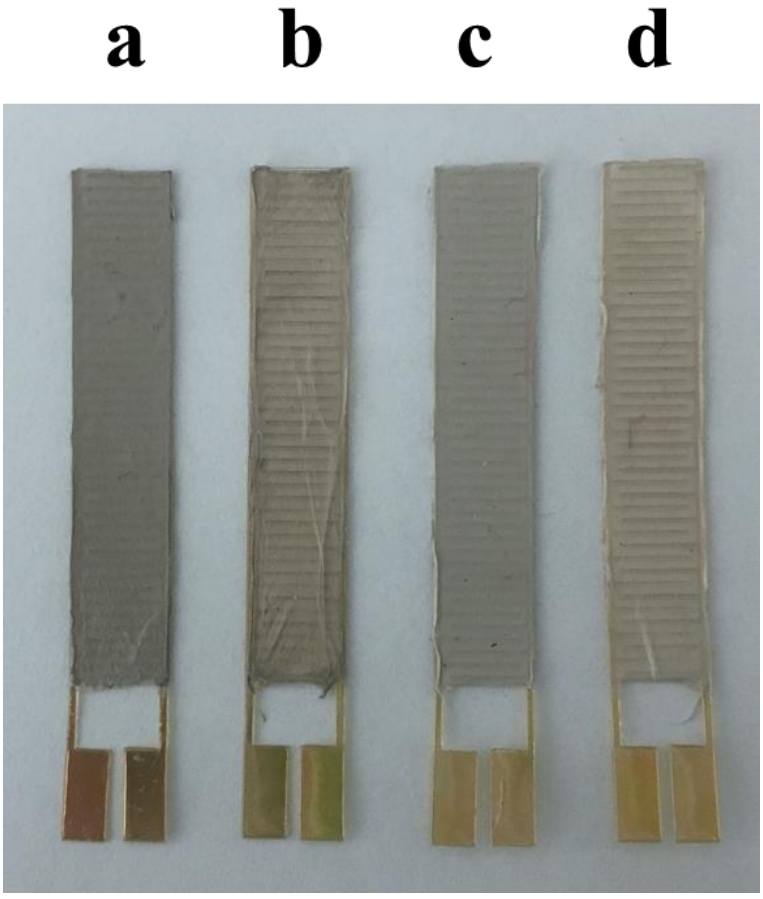


**Figure 5.7** Photographs of PLA-based samples on interdigitated electrodes: (a) PLA/$CoFe_2O_4$ 10-R, (b) PLA/$CoFe_2O_4$ 10-A, (c) PLA/$CoFe_2O_4$ 5-R and (d) PLA/$CoFe_2O_4$ 5-A.

### 5.3.4 Macroscale ME Measurement of Electrospun Nanofiber Sheets

To investigate whether the ME effect could be maintained in electrospun nanofibers macroscopically, ME measurements were conducted on PVDF-based samples, including the PVDF sheet/Metglas, PVDF-NF/Metglas, PVDF/$Fe_3O_4$-NF, IE PVDF/$Fe_3O_4$-NF and PVDF-NF. In particular, the commercial PVDF sheet/Metglas composite was known to produce a significant ME output voltage and thus could be effectively used as a reference sample to calibrate the ME setup. Then, a PVDF-NF/Metglas laminate was tested where the Metglas again provided a known MS response hence leading to a PE response which was expected from the nanofibers [14, 16]. Thus, when combined, an ME effect was expected and represents the first example of an ME device from electrospun nanofibers. To ultimately assess the ME effect from the ME nanofiber composites, electrospun PVDF/$Fe_3O_4$ nanofiber sheets were prepared with either top-and-bottom electrodes (conventional for ME measurement of films [30, 31]) or interdigitated electrode configuration, as illustrated in Figure 5.1 and Figure 5.2b. Finally, PVDF nanofibers without $Fe_3O_4$ nanoparticles were tested as a control and should not produce a signal.

Metglas is attractive due to its low saturation magnetization field and consequently requires a relatively low DC bias magnetic field < 20 Oe [6]. The laminates consisting of Metglas and PVDF was confirmed to generate a giant ME effect with $\alpha_{ME}$ = 310 V $cm^{-1}$ $Oe^{-1}$ [6]. Following this study, the DC and AC magnetic fields were set as 8 Oe and 1 Oe for measurements on the Metglas-based laminates including PVDF sheet/Metglas and PVDF-NF/Metglas. Martins' study [32] on P(VDF-TrFE)-based composites reveals that the most significant ME effect of $Fe_3O_4$/P(VDF-TrFE) and $CoFe_2O_4$/P(VDF-TrFE) films can be achieved at DC magnetic fields of 1500 Oe and 2600 Oe. Though not optimal, both

composites still exhibit certain ME effect at $H_{DC}$ = 2000 Oe, which relates to the MS behaviour of the magnetic phases [32]. Therefore, the DC magnetic field used for measuring the ME effect of PVDF/$Fe_3O_4$ and PLA/$CoFe_2O_4$ samples was set as 2000 Oe. With the limitation of equipment, the measurement was only carried out with $f$ = 10-100 kHz.

During the ME measurement, the samples were tested under a constant DC magnetic field superimposed with a small AC magnetic field. Both magnetic fields were applied along the length of the laminates. Figure 5.8 shows the variation of the ME output voltage with $H_{AC}$ frequency. The use of MS materials with high magnetic permeability and low field saturation, such as Metglas, provides fast mechanical deformation under relatively weak magnetic fields [33]. Combining Metglas with high tensile polymeric PE materials, such as PVDF, gives significant strain transfer and the highest ME output voltage [6]. This is the case in Figure 5.8 (pink curve) for the commercial PVDF sheet/Metglas. It showed an optimized ME output voltage of 43.22 mV with an expected resonance enhancement. The resonance frequency of $f$ = 53 kHz was comparable to other works [6, 34] and the ME coefficient was 15.44 V $cm^{-1}$ $Oe^{-1}$ calculated by the following equation [27].

$$ME\ coefficient = \frac{V_{out}}{h_0 d} \quad (5.1)$$

Where $V_{out}$ is the measured output voltage, $h_0$ is the amplitude of AC field and d is the thickness of the commercial PVDF sheet. This confirmed that the ME testing system was working properly.

However, when the PVDF nanofiber sheet (without magnetic nanoparticles) was combined with the Metglas, there was no response (Figure 5.8, blue curve). Despite this observation, the ME effect of PVDF/$Fe_3O_4$-NF was expected to occur since the PE and MS phases had good coupling, as confirmed in Chapter 2. The red curve in Figure 5.8 shows the output

voltages of PVDF/$Fe_3O_4$-NF though again an ME response was not observed. Alternative to randomly aligned nanofibers, the placement of nanofibers on interdigitated electrodes was purported to enhance higher electrical outputs in scavenging energy due to nanofibers connected in parallel [35]. Thus, PVDF/$Fe_3O_4$ nanofibers were electrospun directly onto a planar interdigitated electrode array for longitudinal measurements of the ME output voltage (IE PVDF/$Fe_3O_4$-NF). The output voltage is shown as the green curve in Figure 5.8. Similar to other electrospun sheets, the curve only had a linear increase due to background noise, with no observation of an ME output signal. The PVDF-NF (black curve) also showed a similar response further confirming the response from the above samples was not from true ME properties, but inherent response from the lock-in system.

In the case of PVDF-NF/Metglas, a cessation of stress transferring from Metglas to PVDF nanofibers appeared to be responsible for the loss of ME response at the macroscale. Alternatively, randomly distributed nanofibers causing anisotropy in the directionality of aligned dipoles or porosity with voids (air) of lower dielectric permittivity, could act as a barrier in measuring the PE output across a nanofiber sheet, as observed from PVDF/$Fe_3O_4$-NF which had a good coupling between the two phases. However, it has been widely reported that the piezoelectricity of electrospun PVDF nanofibers can be directly harnessed to fabricate nanogenerators whether they are random distributed [14, 16] or well aligned [35, 36]. Thus, the exact reason for not observing an ME effect from these devices with electrospun nanofibers is not entirely clear.

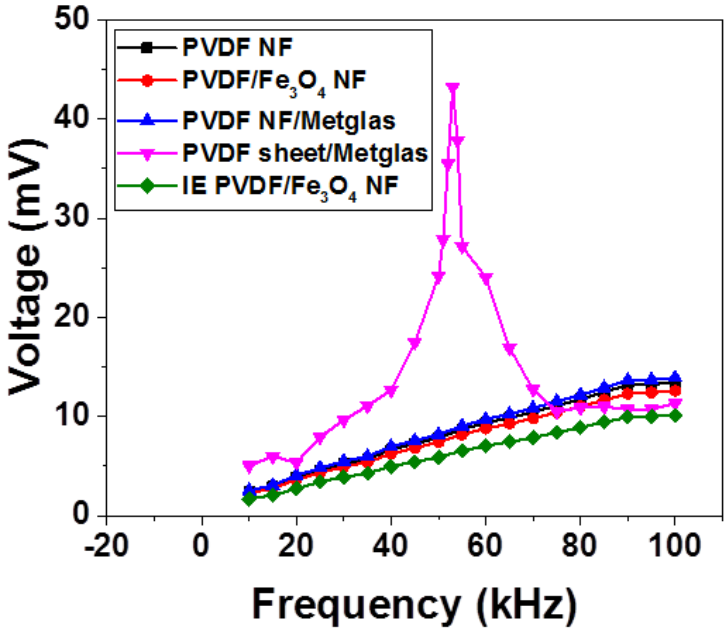


**Figure 5.8** ME output voltage of different PVDF-based ME composite samples as a function of $H_{AC}$ frequency.

Further macroscale ME testing was done on PLA/$CoFe_2O_4$ samples and the results were shown in Figure 5.9. For all the samples, the nanofibers were directly electrospun onto the interdigitated electrodes. The blue and black curves in Figure 5.9 represent for the output voltages from randomly distributed PLA/$CoFe_2O_4$ nanofibers with $CoFe_2O_4$ weight contents of 5% and 10%. Similar to PVDF-based electrospun sheets, no ME response was observed in the samples. Then, aligned PLA/$CoFe_2O_4$ nanofibers on the interdigitated electrodes, fabricated to minimize the effect of random dipoles, were also measured. The output voltages of aligned PLA/$CoFe_2O_4$ nanofibers with $CoFe_2O_4$ weight contents of 5% and 10% are shown as pink and red curves in Figure 5.9. Finally, these samples also showed no ME response.

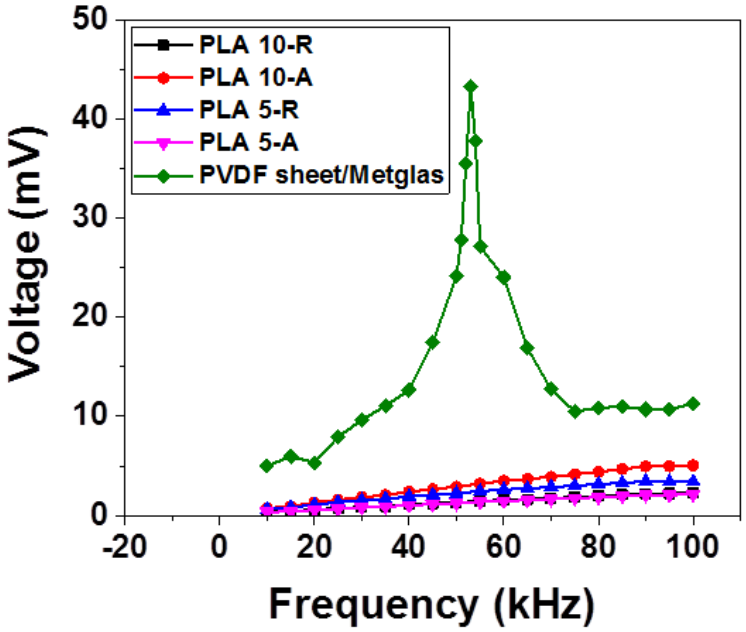


**Figure 5.9** ME output voltage of different PLA/$CoFe_2O_4$ composite samples as a function of $H_{AC}$ frequency.

## 5.4 Conclusions

In this chapter, a macroscale ME testing system was set up based on a lock-in technique. The ME setup was clearly working properly as demonstrated by the PVDF sheet/Metglas laminate. To study the macroscale ME performance of electrospun nanofibers, PVDF electrospun nanofibers were prepared as macroscale ME devices with different MS materials, including Metglas and $Fe_3O_4$ nanoparticles. However, all the samples, even the electrospun PVDF nanofiber sheets with Metglas, showed no ME output measured by the macroscale ME testing system. Then, both random and aligned PLA/$CoFe_2O_4$ nanofibers were electrospun onto interdigitated electrodes for ME testing and similarly no typical ME response was observed for all samples. As the piezoelectricity of both electrospun nanofibers had been widely

confirmed and the nanoscale ME effect of single nanofibers had been demonstrated by PFM in previous chapters, it is difficult to explain the failing of measuring a macroscale ME effect from these electrospun nanofibers. To address this, further optimization of the electrospinning process or new configurations of electrospun devices will need investigation.

## 5.5 References


1. Behera, C., et al., *Development of multiferroism in PVDF with $CoFe_2O_4$ nanoparticles.* Journal of Polymer Research, 2017. **24**(4): p. 1-13.
2. Martins, P., et al., *Optimizing piezoelectric and magnetoelectric responses on $CoFe_2O_4$/P(VDF-TrFE) nanocomposites.* Journal of Physics D-Applied Physics, 2011. **44**(49): p. 495303.
3. Jin, J., et al., *Multiferroic polymer composites with greatly enhanced magnetoelectric effect under a low magnetic bias.* Advanced Materials, 2011. **23**(33): p. 3853-3858.
4. Cai, N., et al., *Large high-frequency magnetoelectric response in laminated composites of piezoelectric ceramics, rare-earth iron alloys and polymer.* Applied Physics Letters, 2004. **84**(18): p. 3516-3518.
5. Nan, C.W., et al., *Large magnetoelectric response in multiferroic polymer-based composites.* Physical Review B, 2005. **71**(1): p. 014102.
6. Zhai, J., et al., *Giant magnetoelectric effect in Metglas/Polyvinylidene-Fluoride laminates.* Applied Physics Letters, 2006. **89**(8): p. 083507.
7. Martins, P., et al., *Polymer-based magnetoelectric materials.* Advanced Functional Materials, 2013. **23**(27): p. 3371-3385.
8. Li, J., et al., *Magnetoelectric effect modulation in a PVDF/Metglas/PZT composite by applying DC Electric fields on the PZT phase.* Journal of Alloys and Compounds, 2016. **661**: p. 38-42.
9. Prabhakaran, T., et al., *Magnetoelectric investigations on Poly(vinylidene fluoride)/$NiFe_2O_4$ flexible films fabricated through a solution casting method.* RSC Advances, 2016. **6**(90): p. 86880-86888.
10. Nan, C.W., et al., *Multiferroic magnetoelectric composites: historical perspective, status, and future directions.* Journal of Applied Physics, 2008. **103**(3): p. 031101.
11. Scott, J., *Applications of magnetoelectrics.* Journal of Materials Chemistry, 2012. **22**(11): p. 4567-4574.
12. Ahn, Y., et al., *Enhanced piezoelectric properties of electrospun Poly(vinylidene fluoride)/multiwalled carbon nanotube composites due to high β-phase formation in Poly(vinylidene fluoride).* The Journal of Physical Chemistry C, 2013. **117**(22): p. 11791-11799.

13. Shao, H., et al., *Effect of electrospinning parameters and polymer concentrations on mechanical-to-electrical energy conversion of randomly-oriented electrospun Poly(Vinylidene Fluoride) nanofiber Mats.* RSC Advances, 2015. **5**(19): p. 14345-14350.

14. Fang, J., et al., *Electrical power generator from randomly oriented electrospun Poly(vinylidene fluoride) nanofibre membranes.* Journal of Materials Chemistry, 2011. **21**(30): p. 11088.

15. Nunes-Pereira, J., et al., *Energy harvesting performance of piezoelectric electrospun polymer fibers and polymer/ceramic composites.* Sensors and Actuators A-Physical, 2013. **196**: p. 55-62.

16. Xin, Y., et al., *Full-fiber piezoelectric sensor by straight PVDF/nanoclay nanofibers.* Materials Letters, 2016. **164**: p. 136-139.

17. Lee, S.J., et al., *Piezoelectric properties of electrospun Poly(L-lactic acid) nanofiber web.* Materials Letters, 2015. **148**: p. 58-62.

18. Ren, G., et al., *Flexible pressure sensor based on a Poly(VDF-TrFE) nanofiber web.* Macromolecular Materials and Engineering, 2013. **298**(5): p. 541-546.

19. Persano, L., et al., *High performance piezoelectric devices based on aligned arrays of nanofibers of Poly(vinylidenefluoride-co-trifluoroethylene).* Nature Communications, 2013. **4**: p. 1633.

20. Nasir, M., et al., *Control of diameter, morphology, and structure of PVPF nanofiber fabricated by electrospray deposition.* Journal of Polymer Science Part B-Polymer Physics, 2006. **44**(5): p. 779-786.

21. Cauda, V., et al., *Confinement in oriented mesopores induces piezoelectric behavior of polymeric nanowires.* Chemistry of Materials, 2012. **24**(21): p. 4215-4221.

22. Kassa, H.G., et al., *Structure and ferroelectric properties of nanoimprinted Poly(vinylidene fluoride-ran-trifluoroethylene).* Macromolecules, 2013. **46**(21): p. 8569-8579.

23. Goncalves, R., et al., *Magnetoelectric $CoFe_2O_4$/Polyvinylidene Fluoride electrospun nanofibres.* Nanoscale, 2015. **7**(17): p. 8058-8061.

24. Goncalves, R., et al., *Development of magnetoelectric $CoFe_2O_4$/Poly(Vinylidene Fluoride) microspheres.* RSC Advances, 2015. **5**(45): p. 35852-35857.

25. Xie, S., et al., *Multiferroic $CoFe_2O_4$-$Pb(Zr_{0.52}Ti_{0.48})O_3$ core-shell nanofibers and their magnetoelectric coupling.* Nanoscale, 2011. **3**(8): p. 3152-3158.

26. Caruntu, G., et al., *Probing the local strain-mediated magnetoelectric coupling in multiferroic nanocomposites by magnetic field-assisted Piezoresponse Force Microscopy.* Nanoscale, 2012. **4**(10): p. 3218-3227.

27. Duong, G.V., et al., *The lock-in technique for studying magnetoelectric effect.* Journal of Magnetism and Magnetic Materials, 2007. **316**(2): p. 390-393.

28. Jalili, R., et al., *Fundamental parameters affecting electrospinning of PAN nanofibers as uniaxially aligned fibers.* Journal of Applied Polymer Science, 2006. **101**(6): p. 4350-4357.

29. Lu, J., et al., *Wideband magnetoelectric measurement system with the application of a virtual multi-channel lock-in amplifier.* Measurement Science and Technology, 2008. **19**(4): p. 045702.

30. Fang, Z., et al., *Enhancing the magnetoelectric response of Metglas/Polyvinylidene Fluoride laminates by exploiting the flux concentration effect.* Applied Physics Letters, 2009. **95**(11): p. 112903.

31. Silva, M., et al., *optimization of the magnetoelectric response of Poly(vinylidene fluoride)/Epoxy/Vitrovac laminates.* ACS Applied Materials & Interfaces, 2013. **5**(21): p. 10912-10919.

32. Martins, P., et al., *Tailored magnetic and magnetoelectric responses of polymer-based composites.* ACS Applied Materials & Interfaces, 2015. **7**(27): p. 15017-15022.

33. Dong, S., et al., *Near-ideal magnetoelectricity in high-permeability magnetostrictive/piezofiber laminates with a (2-1) connectivity.* Applied Physics Letters, 2006. **89**(25): p. 252904.

34. Reis, S., et al., *Electronic optimization for an energy harvesting system based on magnetoelectric Metglas/Poly(vinylidene fluoride)/Metglas composites.* Smart Materials and Structures, 2016. **25**(8): p. 085028.

35. Chang, J., et al., *large array electrospun PVDF nanogenerators on a flexible substrate*. in *Solid-State Sensors, Actuators and Microsystems Conference (TRANSDUCERS), 2011 16th International*. 2011. IEEE.

36. Chang, C., et al., *Direct-write piezoelectric polymeric nanogenerator with high energy conversion efficiency.* Nano Letter, 2010. **10**(2): p. 726-731.

# 6 Conclusions and Outlook

## 6.1 Conclusions

### 6.1.1 PE Measurement of Polymers at the Nanoscale

Poly (vinylidene fluoride) (PVDF) and its copolymer, poly (vinylidene fluoride-co-hexafluoropropylene) (P(VDF-HFP)), were fabricated in the form of nanofibers using electrospinning that demonstrated the ability to induce the formation of the electroactive β-phase and the alignment of dipoles. Piezoresponse Force Microscopy (PFM) measurements revealed a variation in the piezoelectric (PE) response between different nanofibers, suggesting that the nanoscale piezoelectricity depends on variations on the local properties, including polarization and crystalline degree. The P(VDF-HFP) unexpectedly exhibited a higher PE response of 398.3 ± 222.4 pm compared to PVDF (140.9 ± 84.0 pm), which could be explained by the transverse $d_{31}$ response of P(VDF-HFP) contributing to the $d_{33}$ response [1]. The incorporation of magnetic nanoparticles was found to increase the PE response of both PVDF and P(VDF-HFP), indicating that the magnetic nanoparticles improved the crystallinity of the polymers. Finally, the biocompatible and biodegradable polymer, poly (lactic acid) (PLA), was investigated using PFM, with the PLA nanofibers giving a PE response of 186.0 ± 28.1 pm. The piezoelectricity was maintained after the addition of the non-PE, faster degrading polymer, poly (DL-lactide-co-glycolide) (PLGA), demonstrating the ability to tune the biodegradability of a PE polymer. Finally, the PLA nanofibers exhibited a decreased PE response when incorporated with $CoFe_2O_4$ nanoparticles, though still provided a reasonable PE response of 143.4 ± 43.7 pm that could be used for ME coupling.

### 6.1.2 Nanoscale ME Effect of Polymer-based ME Nanofibers

The nanoscale ME effect of electrospun ME nanofibers based on PVDF and P(VDF-HFP) was investigated by PFM/VFM, enabling measurement of changes in the PE response as a function of an applied variable magnetic field. Pure PVDF nanofibers showed no significant change in PE response while PVDF/$Fe_3O_4$ showed decreasing PE response with increasing magnetic fields in the range of 0-2000 Oe, indicating the presence of a nanoscale ME effect. For both P(VDF-HFP)/$Fe_3O_4$ and P(VDF-HFP)/$CoFe_2O_4$ nanofibers, no clear trend in the PE response versus the applied magnetic field was observed. In the positive direction of the magnetic field (0 to 2000 Oe), the P(VDF-HFP)/$Fe_3O_4$ nanofibers showed a significant shift in the PE response (the difference between the maximum and minimum PFM amplitude) as compared to P(VDF-HFP) nanofibers. In the negative direction (0 to -2000 Oe), the shift in the PE response of P(VDF-HFP)/$CoFe_2O_4$ nanofibers was significantly different from that of P(VDF-HFP) nanofibers. Although the reasons for these observations are not clear, they indicate the presence of a nanoscale ME effect in these P(VDF-HFP)-based ME nanofiber composites. However, the PFM/VFM measurement still has some limitations in terms of the nanoscale variations including tip-sample contact, distribution of crystalline and the presence of magnetic nanoparticles. In addition, quantifying the nanoscale ME effect needs to be explored as different methods are used to calculating the ME coefficient [2, 3].

### 6.1.3 Macroscale ME Measurements on Electrospun Nanofibers

Having demonstrated the nanoscale PE and ME effect of electrospun nanofibers in previous chapters [4], the translation of these nanoscale properties to macroscale composites and measurements of their macroscale ME properties were investigated. For the macroscale ME

measurement, an ME testing system based on a lock-in technique [5] was setup and firstly used to confirm the ME response of a laminate composite, consisting of a commercial PVDF sheet and Metglas, that has previously been well-characterized in the literature [6]. The same measurements were done on electrospun sheets of both PVDF/$Fe_3O_4$ and PLA/$CoFe_2O_4$ nanofibers using different configurations such as top-and-bottom electrodes and interdigitated electrodes with and without aligned nanofibers. However, none of the samples showed a macroscale ME effect and reasons for this are unclear at this stage. It is suggested that optimization of the electrospinning process or new configurations of electrospun devices will need further investigation.

## 6.2 Outlook

### 6.2.1 Synthesis of Polymer-based ME Materials

Compared to their ceramic counterparts, research into polymer-based ME materials is still in its infancy [7]. Although the PVDF family of PE polymers has been extensively studied [8], other PE polymers deserve attention due to novel properties they bring to ME composites. PLA is an important scaffold material in tissue engineering due to its biocompatibility and biodegradability [9]. Furthermore, the PE or ME properties of PLA can offer new approaches to electrical stimulation of cells/tissues for tissue regeneration, that is, generating electrical signals from mechanical stress or magnetic stimuli without the need for electrical connections. Similarly, the strategy could be used in controlling drug release profiles by modulating the polymer-drug interactions. In addition to PLA, other bio-derived and biodegradable polymers such as polyhydroxybutyrate (PHB) are also PE polymers [10] though as yet have not been investigated in ME composites. PHB has similar PE properties to natural bones [11] and is

promising for manufacturing a bone fracture fixation since bones can be strengthened and repaired by electrical stimulation [12]. Further to this, remote stimulating bone growth and healing would be possible using PHB-based ME materials.

ME nanomaterials consisting of PLA, or other degradable PE polymers, combined with non-toxic magnetic nanoparticles could also be designed as self-degradable devices; they could "disappear" after delivering electrical stimulation or targeted release of drugs to minimize inflammation or enable clearance of the nanoparticles from the body. Analogous to previous ceramic-based nanoparticle ME composites [13], polymer-based core-shell nanoparticles could be prepared from *in-situ* synthesis using magnetic nanoparticles as a reaction core to initiate formation of a polymer shell. These nanoparticulate ME composites represent dispersible systems that can be directed to target tissues or cells by the application of magnetic fields, as illustrated by Figure 1.1. In this way, tissues may only have to interface with soft polymers instead of hard inorganic materials.

### 6.2.2 Nanoscale Measurement of the Converse ME Effect

The ME polymer nanofiber composites in this thesis also possess a converse ME effect, which is of interest for electrically tuneable devices such as electric-write, non-volatile magnetic memory and electric controlled microwave devices [14]. In this case, the magnetization can be tuned by an electric field through the transfer of stress from the PE polymer to magnetic nanoparticles and is referred to as the electric-field-induced-magnetization effect. Similar to the direct ME effect, there are few studies on the nanoscale converse ME effect. This is a research area that could be explored further using Magnetic Force Microscopy (MFM) that uses a magnetized tip to detect and reconstruct the magnetic

structure of the sample [15]. To elucidate nanoscale converse ME effect, the MFM could be used to monitor magnetization reorientations induced by the application of an electric field. Nanoscale measurements of both direct ME and converse ME effects are very complementary and together they can offer more insight into the mechanisms of the ME effect and a broader range of potential applications, including information storage, multiple-state memories, sensors, actuators and transformers.

### 6.2.3 Macroscale ME Measurement on ME Nanomaterials

ME nanomaterials (e.g. nanoparticles or nanofibers) have the potential to be assembled or integrated into macroscale ME devices such as sensing and memory devices for better performance such as higher sensitivity or larger memory capacity [16]. Though the challenge remains in how to best synthesize, fabricate and assemble the ME nanomaterials so as to preserve and translate their nanoscale ME properties in the final macroscale device and application. It is suggested precise control over the fabrication of the ME nanocomposites are critical and the ability to produce novel electrode configurations may provide an efficient harvesting of induced electric signals. Chapter 5 demonstrates the use of electrospinning to fabricate different configuration, however, it is clear that further investigation is required in order to prove this approach. As nanofibers are much softer than drop-casting films and hence result to lower responsive frequencies, it is worth carrying out the measurement in lower frequency ranges. Further to this, near-field electrospinning could be of merit given its ability to directly "write" fibers on substrates [17]. The state-of-art near-field electrospinning at low-voltage and low-electrical fields can minimize bending instabilities and achieves scalable precision patterning [18]. By shortening the travelling distance of polymer solutions, the dipoles are expected to be aligned with less uncertainty and thus ME microfibers can be

fabricated with tailored piezoelectricity, which is promising for preparing ME nanomaterials for macroscale ME measurement. Other spinning methods to produce micron-sized fibers or yarns are also yet to be explored.

## 6.3 References


1. Kalinin, S.V., et al., *Imaging mechanism of piezoresponse force microscopy in capacitor structures.* Applied Physics Letters, 2008. **92**(15): p. 152906.
2. Xie, S., et al., *Multiferroic $CoFe_2O_4$-$Pb(Zr_{0.52}Ti_{0.48})O_3$ core-shell nanofibers and their magnetoelectric coupling.* Nanoscale, 2011. **3**(8): p. 3152-3158.
3. Caruntu, G., et al., *Probing the local strain-mediated magnetoelectric coupling in multiferroic nanocomposites by magnetic field-assisted piezoresponse force microscopy.* Nanoscale, 2012. **4**(10): p. 3218-3227.
4. Zheng, T., et al., *Local probing of magnetoelectric properties of PVDF/$Fe_3O_4$ electrospun nanofibers by piezoresponse force microscopy.* Nanotechnology, 2017. **28**(6): p. 065707.
5. Duong, G.V., et al., *The lock-in technique for studying magnetoelectric effect.* Journal of Magnetism and Magnetic Materials, 2007. **316**(2): p. 390-393.
6. Zhai, J., et al., *Giant magnetoelectric effect in Metglas/Polyvinylidene-fluoride laminates.* Applied Physics Letters, 2006. **89**(8): p. 083507.
7. Martins, P., et al., *Polymer-based magnetoelectric materials.* Advanced Functional Materials, 2013. **23**(27): p. 3371-3385.
8. Cauda, V., et al., *Nanostructured piezoelectric polymers.* Journal of Applied Polymer Science, 2015. **132**(13).
9. Lasprilla, A.J.R., et al., *Poly-lactic acid synthesis for application in biomedical devices - A review.* Biotechnology Advances, 2012. **30**(1): p. 321-328.
10. Fukada, E., et al., *Piezoelectric properties of poly-β-hydroxybutyrate and copolymers of β-hydroxybutyrate and β-hydroxyvalerate.* International Journal of Biological Macromolecules, 1986. **8**(6): p. 361-366.
11. Holmes, P., *Applications of PHB - a microbially produced biodegradable thermoplastic.* Physics in Technology, 1985. **16**(1): p. 32.
12. Iandolo, D., et al., *Development and characterization of organic electronic scaffolds for bone tissue engineering.* Advanced Healthcare Materials, 2016. **5**(12): p. 1505-1512.
13. Rodzinski, A., et al., *Targeted and controlled anticancer drug delivery and release with magnetoelectric nanoparticles.* Scientific Reports, 2016. **6**: p. 2204.

14. Wang, R.-Q., et al., *Ferroelectric control of in-plane to out-of-plane magnetization switching at poly(vinylidene fluoride)/iron interface.* Journal of Applied Physics, 2014. **115**(4): p. 043909.

15. Hartmann, U., *Magnetic force microscopy.* Annual Review of Materials Science, 1999. **29**(1): p. 53-87.

16. Nan, C.W., et al., *Multiferroic magnetoelectric composites: historical perspective, Status, and Future Directions.* Journal of Applied Physics, 2008. **103**(3): p. 031101.

17. Chang, C., et al., *Direct-write piezoelectric polymeric nanogenerator with high energy conversion efficiency.* Nano Letters, 2010. **10**(2): p. 726-731.

18. Bisht, G.S., et al., *Controlled continuous patterning of polymeric nanofibers on three-dimensional substrates using low-voltage near-field electrospinning.* Nano Letters, 2011. **11**(4): p. 1831-1837.